THE ELECTROCATALYTIC ACTIVITY OF METALLOPHTHALOCYANINES AND THEIR CONJUGATES WITH CARBON NANOMATERIALS AND METAL TUNGSTATE NANOPARTICLES

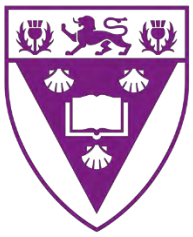

RHODES UNIVERSITY

Where leaders learn

This dissertation is submitted in of the requirements for the degree of

Doctor of Philosophy

of

Rhodes University

by

NOBUHLE NDEBELE

April 2023

DEDICATION

This dissertation is dedicated to my late mother.

🕊 Mrs Thandiwe Ndebele 🕊

Finishing this journey, that we started together, without you has been the greatest challenge.

I hope you are beaming with pride. I did it for you ❤

ACKNOWLEDGEMENTS

“Unkulunkulu emuhle njalo uzongipha amandla” To God be the Glory. It is by grace and grace alone that I have made it this far in life, that I had the strength to finish this PhD despite the challenges I faced in the process.

A huge thank you to my supervisor, Dist. Prof Tebello Nyokong, our very own superstar. Her support and guidance throughout this journey have been invaluable. Working with such a phenomenal woman has been one of the highlights of this challenging journey. I am eternally grateful for the tremendous support, encouragement, and opportunities she has offered and exposed me to these couple of years.

Thank you to the INI staff that always helped me and made sure that things ran smoothly behind the scenes; Dr Jonathan Britton, Prof Mack and Ms Gail Cobus (definitely going to miss randomly coming to your office for a quick chat or rant). Thank you to Dr Pinar Sen for helping me navigate my way through the daunting syntheses and for the collaborations that contributed to this work. To the greatest lab mates and colleagues (S22), thank you so much for making my postgraduate journey memorable.

I also want to thank the National Research Foundation (NRF) of South Africa for funding me from my honours right through to my PhD. Without this funding, my dreams wouldn’t have materialised.

To all my friends 😊 I cannot express how grateful I am to have gone through this journey with you. The love, support, and encouragement you showed me daily did not go unnoticed. I appreciate you all for actively choosing to walk with me every single day.

A big thank you to my maternal family, especially Mam'ncane Musa and Aunty Maggie ❤ Your support throughout has been incredible, and I appreciate you all. I couldn't have picked a better family even if I had tried.

And last but definitely not least, my family. The real pioneers of this journey… My dad Mr Bishop Mbongeni Ndebele, and my siblings, Zandile, Bongiwe and Junior Ndebele 😊 The four of you literally carried me through this journey. We lost our rock in the last year, but you all stayed strong and continuously pushed and motivated me when l felt like giving up. No thank you will ever be enough to express my deepest gratitude for everything you did for me.

ABSTRACT

In this dissertation, seventeen phthalocyanine complexes were synthesised. Of these, only four are known and have been published. These complexes were synthesised using the conventional statistical condensation method that involves refluxing the phthalonitrile(s) (4-((1,3-bis(dimethylamino)propan-2-yl)oxy)phthalonitrile, 4-(4-carboxyphenoxy)phthalonitrile, 4-(4-acetylphenoxy)phthalonitrile, dimethyl 5-(3,4-dicyanophenoxy)-isophthalate, 4-(4-(*tert*-butyl)phenoxy)phthalonitrile, 5-phenoxylpicolinic acid phthalonitrile 4-(4-formylphenoxy) phthalonitrile, and 4-(4-(3-oxo-3-phenylprop-1-enyl) phenoxy) phthalonitrile) with the metal salt and 1,8-diazabicyclo[5.4.0]undecane as a catalyst in a high-temperature solvent. And thereafter (when necessary), isolation and purification of the target compounds were achieved through the use of silica column chromatography.

These compounds were characterised using various analytical techniques such as; ultraviolet-visible absorption, mass spectroscopy, and Fourier transform infrared spectra and elemental analysis. These techniques proved that the complexes were successfully synthesised and isolated as pure compounds.

Carbon-based (graphene quantum dots and nitrogen-doped graphene quantum dots) and metal oxide (bismuth tungsten oxide and nickel tungsten oxide) nanomaterials were synthesised. Together with the purchased single-walled carbon nanotubes, these nanomaterials were conjugated to some of the MPc complexes via non-covalent (carbon-based nanomaterials) and covalent (metal oxides) linkage forming hybrid materials. These nanomaterials and hybrids were characterised using various analytical methods (ultraviolet-visible absorption, X-ray diffraction, Raman spectroscopy, thermographic analysis, and

dynamic light scattering). Nanomaterials were utilised herein to determine their effect on the properties of MPc complexes and provide a synergistic effect in the hope of enhancing these properties.

All complexes synthesised in this work (MPcs, nanomaterials and hybrids) were employed as electrocatalysts in electrochemical sensing. These electrocatalysts were embedded onto the glassy carbon electrode via an adsorption method known as drop-casting. The modified electrode surfaces were characterised using cyclic voltammetry, electrochemical impedance spectroscopy and scanning electrochemical microscopy to determine various electrochemical parameters.

These electrocatalysts were used in the detection of either nitrite, catechol and/or dopamine. The detection limits, sensitivities, kinetics and catalytic constants were among other parameters determined for each electrocatalyst. These electrocatalysts proved to be stable electrocatalysts that could potentially be used for practical applications. The determined parameters were comparable and sometimes better than those obtained in literature.

TABLE OF CONTENTS

DEDICATION ..... **ii**

ACKNOWLEDGEMENTS ..... **iii**

ABSTRACT ..... **v**

TABLE OF CONTENTS ..... **vii**

Abbreviations ..... **xiii**

Symbols ..... **xv**

List of Figures ..... **xvi**

List of Schemes ..... **xxii**

List of Tables ..... **xxiii**

1. INTRODUCTION **2**

1.1 Background on Phthalocyanines **2**

1.1.1 Structural Properties 2

1.1.2 General Phthalocyanine Synthesis 3

1.1.3 Electronic Absorption Spectra of Phthalocyanines 13

1.1.4 General Applications 15

1.2 Electrocatalysis **16**

1.2.1 Modified Electrodes 16

1.2.2 Phthalocyanines as Electrocatalysts 18

1.3 General Overview of Nanomaterials **20**

1.3.1 Carbon-based Nanomaterials 22

1.3.2 Metalic Nanomaterials 28

1.4 Test Analytes 29

1.4.1 Nitrite 30

1.4.2 Dopamine 31

1.4.3 Catechol 32

1.5 Aims of the Dissertation 33

2. EXPERIMENTAL 35

2.1 Materials 35

2.1.1 General Solvents 35

2.1.2 Phthalonitrile and Phthalocyanine Synthesis Reagents 35

2.1.3 Nanomaterial Synthesis and Conjugation Reagents 35

2.1.4 Electrochemical Studies Reagents 36

2.2 Instruments 36

2.3 Synthesis of Phthalonitriles 40

Synthesis of 5-phenoxylpicolinic acid phthalonitrile (**F**), Scheme 3.1 40

2.4 Synthesis of Phthalocyanines 41

2.4.1 Synthesis of tetra-4-((1,3-bis(dimethylamino)propan-2-yl)oxy) phthalocyanato Co(II) (**1-Co**), Scheme 3.2(a) 41

2.4.2 Synthesis of tris-4-((1,3-bis(dimethylamino)propan-2-yl)oxy)mono carboxyphenoxy phthalocyanato Co (II) (**1-Co-As**), Scheme 3.2(b) 41

2.4.3 Synthesis of tetra-[4(4-acetlyphenoxy)phthalocyanato] Co(II) (**2-Co**), Scheme 3.3 ……42

2.4.4 Synthesis of tris-(4-tert-butylphenoxy)-(5-phenoxylpicolinic acid) phthalocyanato Co(II), (**4-Co-As**), Scheme 3.4 ……43

2.4.5 Synthesis of tris-4-((3,17,23-tris(4-(tert-butyl)phenoxy)phthalocyanine-9-yl)oxy)benzaldehyde phthalocyaninato Cu(II) (**4-Cu-As**), Scheme 3.5 ……43

2.4.6 Synthesis of tetra-[(4-formylphenoxy)- phthalocyaninato Cu(II) (**5-Cu**), Scheme 3.6 ……44

2.4.7 Formation of Schiff base substituted phthalocyanines (**6-Cu** and **7-Cu**), Scheme 3.6 ……45

2.4.8 Synthesis of tetra-[4 –(3-(phenyl)-prop-2-en-1-one) phenoxy] phthalocyaninato complexes (**8-Cu**, **8-Mn** and **8-Ni**), Scheme 3.7……46

2.4.9 Synthesis of tetra[(4-formylphenoxy)- phthalocyaninato Mn(III)Cl (**9-Mn**) ……47

2.4.10 Formation of Schiff base substituted phthalocyanines (**10-Mn** and **11-Mn**), Scheme 3.8……48

2.5 Synthesis of Nanomaterials…… 49

2.5.1 Synthesis of GQDs and NGQDs (Scheme 3.9)……49

2.5.2 Synthesis of $NiWO_4$ and Bi_2WO_6 (Scheme 3.10) ……49

2.6 Linking MPcs to nanomaterials…… 50

2.6.1 π-π Stacking……50

2.6.2 Covalent Linkage ……51

2.7 Electrode Modification..... 52

PUBLICATIONS..... 54

3. SYNTHESIS AND CHARACTERISATION 57

3.1 Phthalonitrile Synthesis 57

3.2 Phthalocyanine Synthesis and Characterisation..... 59

3.2.1 Synthesis and Characterisation of **1-Co** and **1-Co-As**.....59

3.2.2 Synthesis and characterisation of **2-Co**.....61

3.2.3 Synthesis and Characterisation of **4-Co-As**.....62

3.2.4 Synthesis and Characterisation of **4-Cu-As**, **5-Cu**, **6-Cu** and **7-Cu**.....63

3.2.5 Synthesis and Characterisation of **8-Co**, **8-Cu**, **8-Mn** and **8-Ni**.....65

3.2.6 Synthesis and Characterisation of **9-Mn**, **10-Mn** and **11-Mn**.....66

3.3 UV-Vis Absorption Spectra **..... 68**

3.4 Nanomaterials and MPc Hybrids 76

3.4.1 Synthesis of GQDs, NGQDs.....76

3.4.2 Synthesis of Bi_2WO_6 and $NIWO_4$.....76

3.4.3 Linkage 78

3.4.4 Characterisation of Nanomaterial and their MPc Hybrids 80

3.5 Conclusions 98

4. ELECTRODE MODIFICATION AND CHARACTERISATION..... 100

4.1 Comparative Cyclic Voltammetry (CV) 100

4.2 Surface Coverage 104

4.3 Scanning Electrochemical Microscopy (SECM) 109

4.4 Electrochemical Impedance Spectroscopy (EIS) 113

4.5 Conclusions 116

5. ELECTROCATALYSIS 118

5.1 Nitrite 118

5.1.1 Comparative Cyclic Voltammetry 118

5.1.2 Mechanism and Kinetics Studies 122

5.1.3 Sensitivity and Detection Limits Studies 129

5.1.4 Stability Studies 138

5.1.5 Interference Studies 140

5.2 Catechol 142

5.2.1 Comparative Cyclic voltammetry 142

5.2.2 Mechanism and Kinetics Studies 144

5.2.3 Sensitivity and Detection Limits Studies 150

5.2.4 Stability Studies 156

5.2.5 Interference Studies 158

5.3 Dopamine 160

5.3.1 Comparative Cyclic voltammetry 160

5.3.2 Mechanism and Kinetics Studies 161

5.3.3 Sensitivity and Detection Limits Studies 166

5.3.4 Stability Studies 169

5.4 Conclusions 171

6. CONCLUSIONS AND RECOMMENDATIONS 175

6.1 Conclusions 175

6.2 Recommendations 176

REFERENCES 177

Abbreviations

Abs	=	Absorbance
AFM	=	Atomic force microscopy
CE	=	Counter electrode
CV	=	Cyclic voltammetry/voltammogram
DBU	=	1,8-diazabicyclo[5.4.0]undec-7-ene
DLS	=	Dynamic light scattering
DMF	=	Dimethylformamide
DMSO	=	Dimethyl sulfoxide
DPV	=	Differential pulse voltammetry
EIS	=	Electrochemical impedance spectroscopy
Ep	=	Peak potential
FT-IR	=	Fourier-transform infrared
GCE	=	Glassy carbon electrode
GCP	=	Glassy carbon plate
GSH	=	Glutathione
GQDs	=	Graphene quantum dots
H_2Pc	=	Unmetalled phthalocyanine
HOMO	=	Highest Occupied Molecular Orbital
LoD	=	Limit of detection
LUMO	=	Lowest Unoccupied Molecular Orbital
NGQDs	=	Nitrogen quantum dots
Pc	=	Phthalocyanine

R_{ct}	=	Charge resistance transfer
RE	=	Reference electrode
Redox	=	Reduction Oxidation
RSD	=	Relative standard deviation
SECM	=	Scanning electrochemical microscopy
SWCNTs	=	Single-walled carbon nanotubes
TGA	=	Thermogravimetric analysis
UME	=	Ultramicroelectrode
UV-Vis	=	Ultraviolet/visible
WE	=	Working electrode
XRD	=	X-ray diffractometer

Symbols

α	=	Peripheral position
A	=	Amperes
A_{eff}	=	Effective electrode area
Γ	=	Surface coverage
D	=	Diffusion coefficient
β	=	Non-peripheral position
k	=	Catalytic rate constant
e^-	=	Electron
ε	=	Molar extinction
ΔEp	=	Peak-to-peak separation
I_{bla}	=	Current of blank/buffer
I_{cat}	=	Current of electrocatalyst
π	=	Pi
λ	=	Wavelength (nm)
Hz	=	Hertz
n	=	Number of electrons
v	=	Scan rate
V	=	Volts
Z’	=	Imaginary impedance
Z”	=	Real Impedance
Z_w	=	Warburg impedance

List of Figures

Figure 1.1: Geometric structure of a phthalocyanine complex.....3

Figure 1.2: Phthalocyanine precursors.....4

Figure 1.3: Electronic absorption spectra of an H_2Pc and MPc.....14

Figure 1.4: Gouterman's 4-orbital model illustrates electronic transitions in, unmetalled and metallophthalocyanine complexes.....14

Figure 1.5: Electrode modification techniques. [35].....17

Figure 1.6: Cyclic voltammogram of the bare and modified GCE.....18

Figure 1.7: Representation of an MPc electrocatalytic reaction at the electrode surface in the analytic solution.....19

Figure 1.8: Top-down and bottom-up nanomaterials synthetic approaches and the synthesis of nanomaterials.....20

Figure 1.9: Nitrogen doping of GQDs using a hydrothermal method yielding to NGQDs. An illustration of the possible N-atom configurations due to N-dopping.....23

Figure 1.10: Typical graphene and possible SWCNTs structures.....25

Figure 1.11: Analytes of interest; catechol, nitrite, and dopamine.....29

Figure 2.1: The Berghof high pressure reactor, autolcave used for the hydrothermal synthesis of GQDs and NGQDs.....37

Figure 2.2: Typical three electrode electrochemical set-up [149].....39

Figure 2.3: Drop casting/drying procedure.....52

Figure 3.1: FT-IR spectra of phthalonitriles **E**, **F** and MPc complex **4-Co-As**.....58

Figure 3.2: UV-Vis absorption spectra of (a) **1-Co** and **1-Co-As,** (b) **2-Co** and **3-Co**, and (c) **4-Co** and **4-Co-As** in DMF.....69

Figure 3.3: UV-Vis absorption spectra of **4-Cu-As**, **5-Cu**, **6-Cu** and **7-Cu** in DMF 70

Figure 3.4: UV-Vis absorption spectra of **8-Co**, **8-Cu**, **8-Mn** and **8-Ni** in DMF.....73

Figure 3.5: UV-Vis absorption spectra of **9-Mn**, **10-Mn** and **11-Mn** in DMF.....74

Figure 3.6: UV-Vis absorption spectra of (a) **GQDs**, **NGQDs** and **SWCNTs** and (b) **Bi_2WO_6** and **$NIWO_4$** 81

Figure 3.7: UV-Vis absorption spectra of (a) **1-Co**, **1-Co-As** and their hybrids; **1-CoπNGQDs** and **1-Co-AsπNGQDs** (b) **2-Co**, **3-Co**, **2-CoπGQDs** and **3-CoπGQDs** and (c) **2-CoπSWCNTs** and **3-CoπSWCNTs** in DMF.....82

Figure 3.8: UV-Vis absorption spectra of (a) **4-Co-As**, **Bi_2WO_6**, **$NiWO_4$**, **4-Co-As@Bi_2WO_6** and **4-Co-As@$NiWO_4$** and (b) **4-Co-AsπGQDs**, **4-Co-AsπNGQDs**, **4-Co-AsπSWCNTs** 85

Figure 3.9: X-ray diffractograms of (a) **4-Co-As**, **Bi_2WO_6** and **$NiWO_4$** and their respective **4-Co-As** conjugates and (b) **GQDs** and **NGQDs** and their respective **4-Co-As** conjugates.....87

Figure 3.10: Raman Spectra of (a) **NGQDs** and (b) **SWCNTs** and their respective **4-Co-As** conjugates.....90

Figure 3.11: Raman spectra for (a) **Bi_2WO_6** and (b) **$NiWO_4$** and their **4-Co-As** conjugates.....91

Figure 3.12: DLS distribution graphs of (a) **NGQDs**, **1-CoπNGQDs** and **1-Co-AsπNGQDs,** (b) **SWCNTs**, **2-CoπSWCNTs** and **3-CoπSWCNTs** (c) **Bi_2WO_6**, **4-Co-As@Bi_2WO_6** and (d) **$NiWO_4$** and **4-Co-As@$NiWO_4$**.....93

Figure 3.13: Thermographic analysis of (a) **Bi_2WO_6** and **$NiWO_4$** and (b) **GQDs**, **NGQDs** and **SWCNTs** and their **4-Co-As** hybrids 94

Figure 3.14: AFM images of (A) **Bi_2WO_6**, (B) **4-Co-As@Bi_2WO_6**, (C) $NiWO_4$, (D) **4-Co-As @$NiWO_4$**. (i) 2D surface topology, (ii) 3D surface topology, and (iii) line profiling.....96

Figure 3.15: AFM images of (a) **SWCNTs**, (b) **2-CoπSWCNTs** and (c) **GQDs**.....97

Figure 4.1: Cyclic voltammograms of (a) Unmodified GCE, (b) **1-Co**, **1-CoπNGQDs**, **1-Co-As**, **1-Co-AsπNGQDs**, **2-Co** and **3-Co**, (c) **8-Co**, **8-Cu**, **8-Mn** and **8-Ni** and (d) **9-Mn**, **10-Mn**, **11-Mn** in 1 mM $[Fe(CN)_6]^{3-/4-}$ (0.1 M KCl). Scan rate = 100 mVs^{-1} 102

Figure 4.2: Cyclic voltammograms of (a) **4-Co-As, GQDs**, **NGQDs**, **SWCNTs** and their respective **4-Co-As** hybrids (b) **4-Cu-As**, **5-Cu**, **6-Cu** and **7-Cu** and (c) **9-Mn**, **10-Mn** and **11-Mn** in 0.1 M PBS buffer at pH 7. Scan rate = 100 mVs^{-1} 105

Figure 4.3: Basic Principles of SECM mechanisms (a) diffusion and approach curves on (b) conducting and (c) insulating substrates 110

Figure 4.4: SECM approach curves of (a) Bare GCP and Teflon (b) **8Co**, **8-Cu**, **8-Mn** and, **8-Ni**, and (c) **1-Co**, **1-Co-As** and their NGQDs hybrids 112

Figure 4.5: Randles equivalent circuit 113

Figure 4.6: Nyquist plots of (a) bare GCE, (b) **NGQDs**, **SWCNTs** and their **4-Co-As** hybrids, (c) **4-Cu-As**, **5-Cu**, **6-Cu** and **7-Cu** and (d) **8-Co**, **8-Cu**, **8-Mn** and **8-Ni** obtained in 1 mM $[Fe(CN)_6]^{3-/4-}$ 115

Figure 5.1: Cyclic voltammograms of (a) **4-Co-As**, **GQDs**, **NGQDs**, **SWCNTs** and their respective hybrids, (b) **8-Co**, **8-Cu**, **8-Mn** and **8-Ni** and (c) **9-Mn**, **10-Mn** and **11-Mn** in 2 mM nitrite solution in 0.1 M pH 7 PBS. Scan rate = 100 mVs^{-1}.....119

Figure 5.2: (a) cyclic voltammograms obtained in 2 mM nitrite (in 0.1 M pH 7 PBS) at varied scan rates, (b) plot of oxidation peak current vs the square root of the scan rate, (c) log of oxidation peak current vs log of scan rate and (d) plot of oxidation peak potential vs log of scan rate. All plots were generated from **4-Co-AsπGQDs**.....125

Figure 5.3: (a) cyclic voltammograms obtained in 2 mM nitrite (in 0.1 M pH 7 PBS) at varied scan rates, (b) plot of oxidation peak current vs the square root of the scan rate, (c) log of

oxidation peak current vs log of scan rate and (d) plot of oxidation peak potential vs log of scan rate. All plots were generated from **9-Mn** 128

Figure 5.4: (a) Chronoamperograms obtained at varied nitrite concentrations (in 0.1 M pH 7 PBS). Insert: calibration curve of the nitrite concentration vs the oxidation current, (b) plots of (I_{cat}/I_{bla}) vs the square root of time and (c) plot of the square root of the slopes vs nitrite concentrations. All plots were generated from **4-Co-AsπGQDs**. 132

Figure 5.5: (a) Chronoamperograms of **9-Mn** obtained at varied nitrite concentrations (in 0.1 M pH 7 PBS). Insert: calibration curve of the nitrite concentration vs the oxidation current, (b) plots of (I_{cat}/I_{bla}) vs the square root of time and (c) plot of the square root of the slopes vs nitrite concentrations, b and c plots were generated from **11-Mn** 133

Figure 5.6: Repetitive cyclic voltammograms of (a) **GQDs** and (b) **4-Co-AsπGQDs** in 2 mM nitrite in PBS pH 7. Scan rate of 100 mVs^{-1}. 138

Figure 5.7: Repetitive cyclic voltammograms of (a) **10-Mn** and b) **11-Mn** in 2 mM nitrite in PBS pH 7. Scan rate of 100 mVs^{-1}.....139

Figure 5.8: Cyclic voltammogram of (a) **8-Co** and (b) **8-Mn** in 2 mM nitrite in PBS pH 7. scan rate = 100 Vs^{-1} 140

Figure 5.9: Differential pulse voltammograms of nitrite in the presence of interfering ions on (a) **GQDs**, (b) **4-Co-AsπGQDs** and (c) **9-Mn** 141

Figure 5.10: Cyclic voltammograms of (a) GQDs, **2-Co**, **2-CoπGQDs** , **3-Co** and **3-Co-GQD**s, (b) GCE, SWCNTs, **2-CoπSWCNTs** and **3-CoπSWCNTs** and (c) **4-Cu-As**, **5-Cu**, **6-Cu** and **7-Cu** obtained in 1 mM catechol in 0.1 M pH PBS. Scan rate = 100 mVs^{-1} 143

Figure 5.11: (a) cyclic voltammograms obtained in 1 mM catechol (in 0.1 M pH 7 PBS) at varied scan rates, (b) plot of oxidation peak current vs the square root of the scan rate, (c) log of

oxidation peak current vs log of scan rate and (d) plot of oxidation peak potential vs log of scan rate. All plots were generated from **2-Co**.....146

Figure 5.12: (a) cyclic voltammograms obtained in 1 mM catechol (in 0.1 M pH 7 PBS) at varied scan rates, (b) plot of oxidation peak current vs the square root of the scan rate, (c) log of oxidation peak current vs log of scan rate .All plots were generated from **6-Cu**.....148

Figure 5.13: (a) Chronoamperograms obtained at varied catechol concentrations (in 0.1 M pH 7 PBS). Insert: calibration curve of the nitrite concentration vs the oxidation current, (b) plots of (I_{cat}/I_{bla}) vs the square root of time and (c) plot of the square root of the slopes vs nitrite concentrations. All plots were generated from **2-CoπGQDs**. 151

Figure 5.14: (a) Chronoamperograms obtained at varied nitrite concentrations (in 0.1 M pH 7 PBS). Insert: calibration curve of the nitrite concentration vs the oxidation current, (b) plots of (I_{cat}/I_{bla}) vs the square root of time and (c) plot of the square root of the slopes vs nitrite concentrations. All plots were generated from **5-Cu**. 152

Figure 5.15: Repetitive cyclic voltammograms of a) **2-CoπGQDs**, b) **4-Cu-As,** and c) **5-Cu** in 1 mM catechol (PBS pH 7) Scan rate = 100 mVs^{-1}. 157

Figure 5.16: Differential pulse voltammograms of **2-CoπGQDs** in the presence of catechol, hydroquinone, resorcinol and a mixture of all three analytes in 0.1 M pH 7 PBS buffer. 158

Figure 5.17: Cyclic voltammograms of **1-Co**, **1-Co-As**, **NGQDs**, **1-CoπNGQDs** and **1-Co-AsπNGQDs.** 160

Figure 5.18: (a) Cyclic voltammograms obtained in 1 mM dopamine (in 0.1 M pH 7 PBS) at varied scan rates, (b) plot of oxidation peak current vs the square root of the scan rate, (c) log of oxidation peak current vs log of scan rate and (d) plot of oxidation peak potential vs log of scan rate. All plots were generated from **1-CoπNGQDs**. 165

Figure 5.19: (a) Chronoamperograms obtained at varied dopamine concentrations (in 0.1 M pH 7 PBS). Insert: calibration curve of the nitrite concentration vs the oxidation current, (b) plots of (I_{cat}/I_{bla}) vs the square root of time and (c) plot of the square root of the slopes vs nitrite concentrations. All plots were generated from **1-CoπNGQDs**. 168

Figure 5.20: Repetitive cyclic voltammograms of a) **1-Co** and b) **1-Co-AsπNGQDs** in 1 mM dopamine in 0.1 M PBS. At a scan rate of 100 mVs^{-1}. 170

List of Schemes

Scheme 1.1: Synthesis of symmetric MPcs using the chemical condensation method.....5

Scheme 1.2: Schematic representation of the statistical method used to synthesise asymmetric MPcs.....7

Scheme 3.1: Synthesis of phthalonitrile **F** 57

Scheme 3.2: Synthesis of **1-Co** and **1-Co-As**.....59

Scheme 3.3: Synthesis of Complex **2-Co** from phthalonitrile **C**.....61

Scheme 3.4: Synthesis of **4-Co-As** from phthalonitriles **E** and **F** 62

Scheme 3.5: Synthesis of **4-Cu-As** 64

Scheme 3.6: Synthesis of **5-Cu**, **6-Cu** and **7-Cu**.....64

Scheme 3.7: Synthesis of **8-Co**, **8-Cu**, **8-Mn** and **8-Ni**.....65

Scheme 3.8: Synthesis of **10-Mn** and **11-Mn** from **9-Mn**.....67

Scheme 3.9: Synthetic route of (a) **GQDs** and (b) **NGQDs** nanomaterials.....77

Scheme 3.10: Synthesis of GSH capped **$NiWO_4$** and **Bi_2WO_6** nanoparticles.....77

Scheme 3.11: Non-covalent π-π stacking of **1-Co** and **NGQDs** to form **1-CoπNGQDs** 78

Scheme 3.12: Covalent linkage **of 4-Co-As** and **Bi_2WO_6** forming **4-Co-As@Bi_2WO_6**.....79

Scheme 5.1: Schematic representation of the mechanism of the electrochemical oxidation Catechol 144

Scheme 5.2: Electrochemical oxidation of dopamine.....162

List of Tables

Table 1.1: Summary of the MPcs synthesised and used in this work as an electrocatalyst, the nanomaterials they were used with and the test analyte of choice 8

Table 1.2: List of a selection of MPc complexes studied as hybrids with carbon-based nanomaterials used as electrocatalysts in electrochemical sensing. 26

Table 3.1: MPc complexes synthesised in this work 71

Table 3.2: Summary of the Q-band and B-band absorption maxima obtained in DMF for all MPc complexes studied herein.....75

Table 3.3: Summary of the data obtained for the nanomaterials and their MPc conjugates 83

Table 3.4: Summary of the Raman spectroscopy data.....89

Table 4.1: Summary of the surface properties of the modified electrode surfaces, obtained in 1 mM $Fe(CN)_6^{3-/4-}$(0.1 M KCl supporting electrolyte).....107

Table 5.1: Summary of the nitrite electrooxidation properties obtained in 2 mM nitrite (in 0.1 M pH 7 PBS) 121

Table 5.2: Summary of the electrocatalytic properties of the electrocatalyst in 2 mM nitrite (0.1 M pH 7 PBS) 136

Table 5.3: Summary of data of the studied electrocatalysts in 1 mM catechol (0.1 M pH 7 PBS) 149

Table 5.4: Comparative sensitivities, LoDs and catalytic rates for catechol (in 0.1 M pH 7 PBS) 155

Table 5.5: Summary of the dopamine electrooxidation properties obtained in 1 mM dopamine in 0.1 M pH 7 PBS.....163

Table 5.6: Summary of the dopamine (in 0.1 M pH 7 PBS) detection parameters.....169

CHAPTER 1

INTRODUCTION

Preface: This chapter gives an overview of the background and synthesis of phthalocyanine complexes and their application as electrocatalysts in electrochemical sensing. It also presents the effect of nanomaterials in enhancing the electrocatalytic properties of phthalocyanine complexes

1. INTRODUCTION

1.1 Background on Phthalocyanines

Phthalocyanine (Pc) complexes are organic molecules that were formed serendipitously in 1927 by a group of Swiss researchers attempting to convert *o*-dibromobenzene into a phthalonitrile [1–3]. These blue-green compounds were only characterised in the 1930s by Linstead and Robertson [1,4,5]. Since their discovery, Pcs have shown great versatility and have been widely studied and used for various applications owing to their remarkable electronic, photochemical, spectral and photophysical properties [1,2,6].

1.1.1 Structural Properties

Phthalocyanines are planar, macrocyclic compounds with an 18-π-electron conjugated system [1,2,6]. Figure 1.1 shows that the phthalocyanine molecule comprises of isoindole units linked together by an azomethine bridge (N atoms) [2,7]. The central cavity (**M**) of the phthalocyanine core can accommodate various metals. The addition of the central metal and the ligand it carries (if any) results in the formation of metallophthalocyanines (MPcs), metal free phthalocyanines are known as H_2Pcs [2,7].

Additional to the central metal, the ring can also accommodate substituents [1,2,7]. These substituents may be attached to the phenyl's α and/or β-positions. Substituents added to the β-positions are known as peripheral substituents, while those at the α-positions are known as non-peripheral substituents [2,6,8]. The phthalocyanine ring is numbered using the International Union of Pure and Applied Chemistry (IUPAC) nomenclature. The α-positions are at 1,4,8,11,15,18,22, and 25, while the β-positions are at 2,3,9,10,16,17,23, and 24 (Figure 1.1) [8]. Using the same substituent at either the α or the β-positions results in the formation of symmetric phthalocyanine complexes.

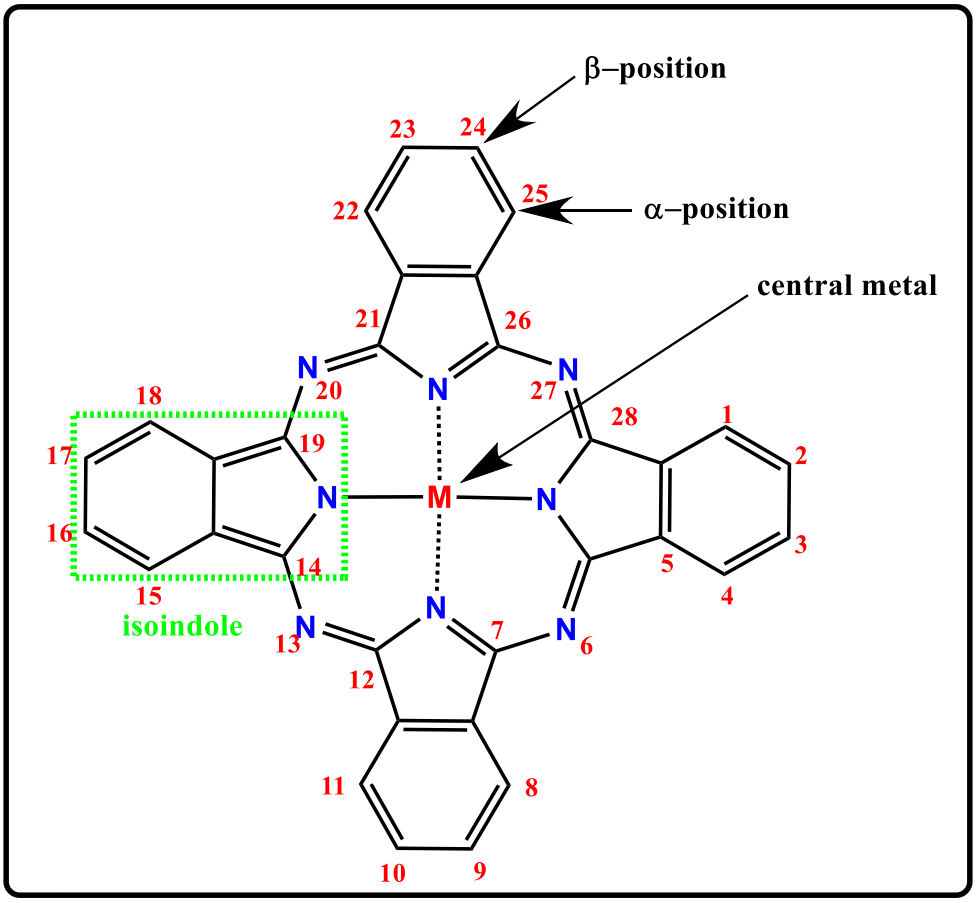

Figure 1.1: Geometric structure of a phthalocyanine complex

Adding the central metal and substituents alters the phthalocyanine complexes' physical, spectral, electronic and chemical properties [2,7,9,10]. Generally, the central metal and the substituents are added onto the core structure to influence the properties of the Pc and, in turn, enhance the properties required for the application of choice.

1.1.2 General Phthalocyanine Synthesis

Phthalocyanine complexes can be synthesised using various precursors (Figure 1.2), such as phthalic anhydrides, phthalic acids, o-cyanobenzamides, phthalimides, dimminoisindolines or phthalonitrile [1,8,9]. Phthalonitrile is the most commonly used precursor for laboratory synthesis. Although phthalonitriles are relatively expensive, they offer great versatility and can be easily synthesised from the relatively inexpensive phthalic anhydride compounds [1,8].

In most cases, the precursors are modified (undergo substitution) before being used as substituents [11–13]. This work explores the use of a 4-nitrophthalonitrile as the precursor of choice.

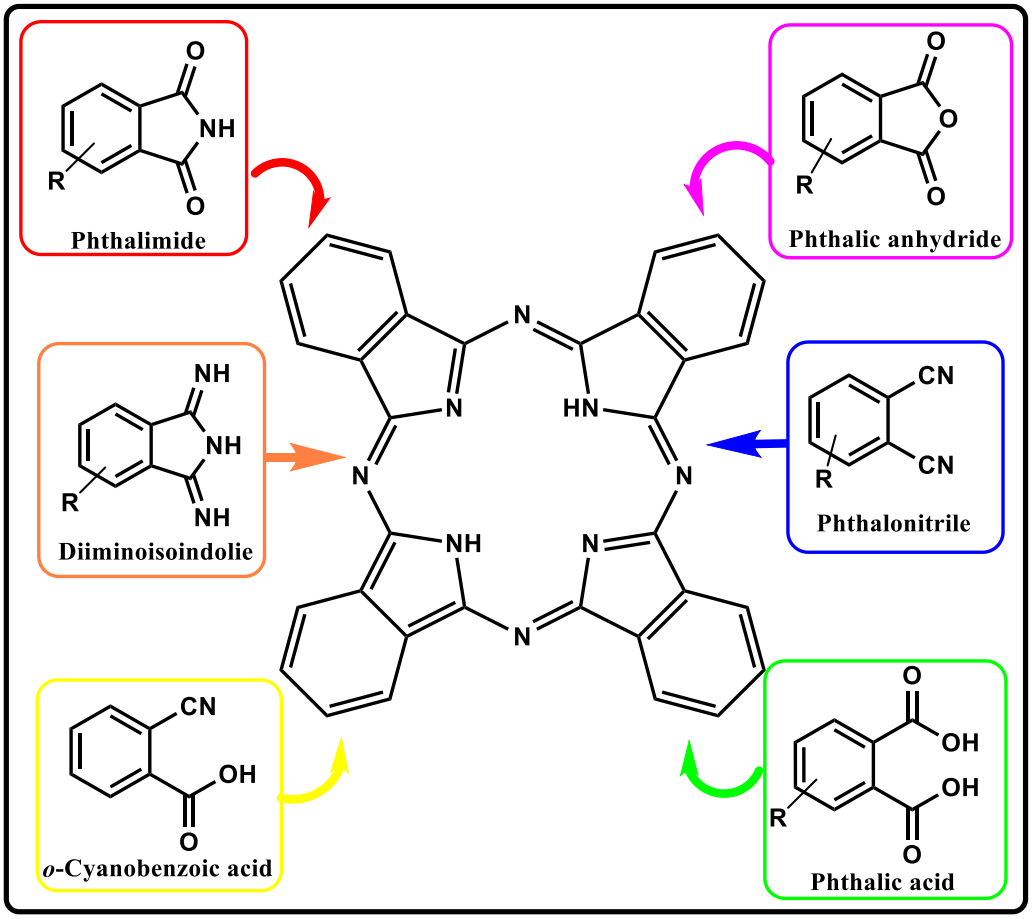

Figure 1.2: Phthalocyanine precursors

Various techniques and or methods such as; chemical (condensation), laser, ultrasonic and microwave radiation can be used to synthesise phthalocyanine complexes [14,15]. The two most common techniques employed are; microwave radiation and the chemical condensation method. This work employed the condensation method.

Scheme 1.1 shows the schematic representation of the synthesis of an MPc using the condensation method. The condensation method typically involves refluxing the substituted phthalonitriles in the presence of high-temperature solvents (pentanol, hexanol or dimethylethanolamine (DMAE)) and a strong organic base catalyst such as 1,8-diazabicyclo[5.4.0]undecane (DBU) (Scheme 1.1) [7,16,17].

When synthesising MPcs, reactive metal salts are added to the above reaction mixture, while they are omitted in the synthesis of the H_2Pc (MPcs can also be synthesised from the H_2Pc[1,2]). During this reaction, cyclotertramization of the substituted phthalonitrile occurs, yielding a tetrasubstituted, symmetric phthalocyanine complex [1,18].

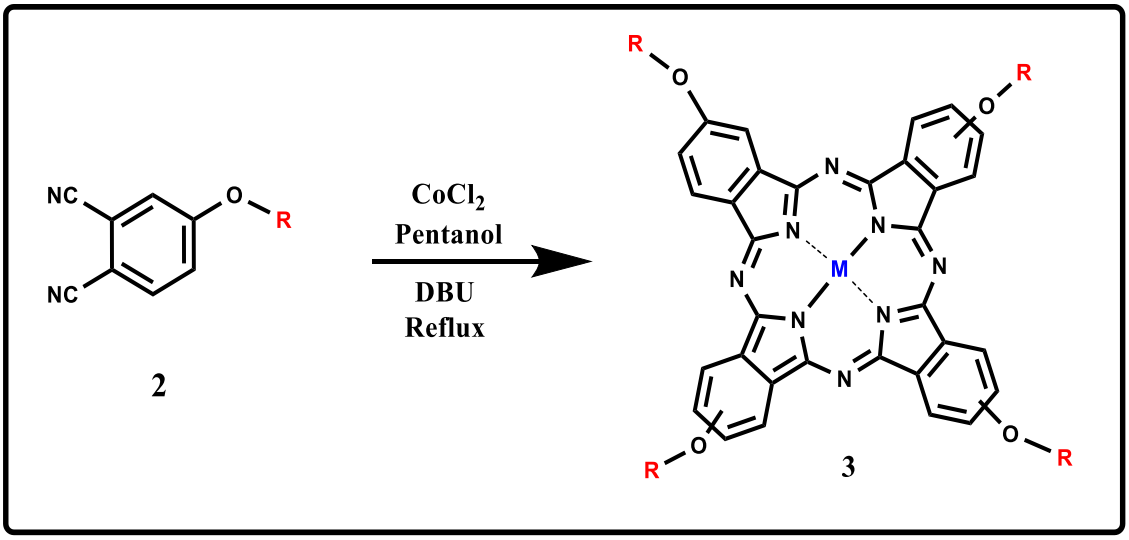

Scheme 1.1: Synthesis of symmetric MPcs using the chemical condensation method

Over the years, there has been an increasing interest in the use of asymmetric phthalocyanine complexes. Research has shown that the decrease in symmetry improves the MPcs' physiochemical properties and enhances the push-pull effect, amongst other properties, thus making them more favourable for use in a wide array of applications [1,8,19,20]. The synthesis

of asymmetric phthalocyanine complexes allows for the use of two dissimilar phthalonitriles, producing a wide range of phthalocyanine complexes (Scheme 1.2). The two substituents are carefully designed (chosen) to suit the application of interest.

Various methods, such as; i) statistical condensation, ii) polymetric-support-based approach, iii) sterically driven cross condensation, and iv) sub-phthalocyanine ring expansion, can be employed for the synthesis of asymmetric MPcs [20–22]. This work focuses on the statistical condensation method due to its simplicity and ability to obtain relatively higher yields.

When synthesising phthalocyanine complexes using the statistical method, the 3:1 or 9:1 ratios (between the two phthalonitriles, A and B) are typically used [20,21,23]. If the reactivities of phthalonitriles are similar, the 3:1 molar ratio can be used to obtain the A_3B complex as the major product, and the other compounds will form as minor side products [20,21]. The ratio could be increased to 9:1 to increase the yields obtained and favour the formation of the A_3B complex if the phthalonitriles have different reactivities [1,20,21,24]. The statistical condensation method is not selective; therefore, six isomers can be formed, two of which are symmetric and four asymmetric, as illustrated in Scheme 1.2 [1,20,21]. Column chromatography is a well-known separation (purification) technique used throughout this work to separate the isomers formed during the synthesis of both symmetric and asymmetric MPc complexes.

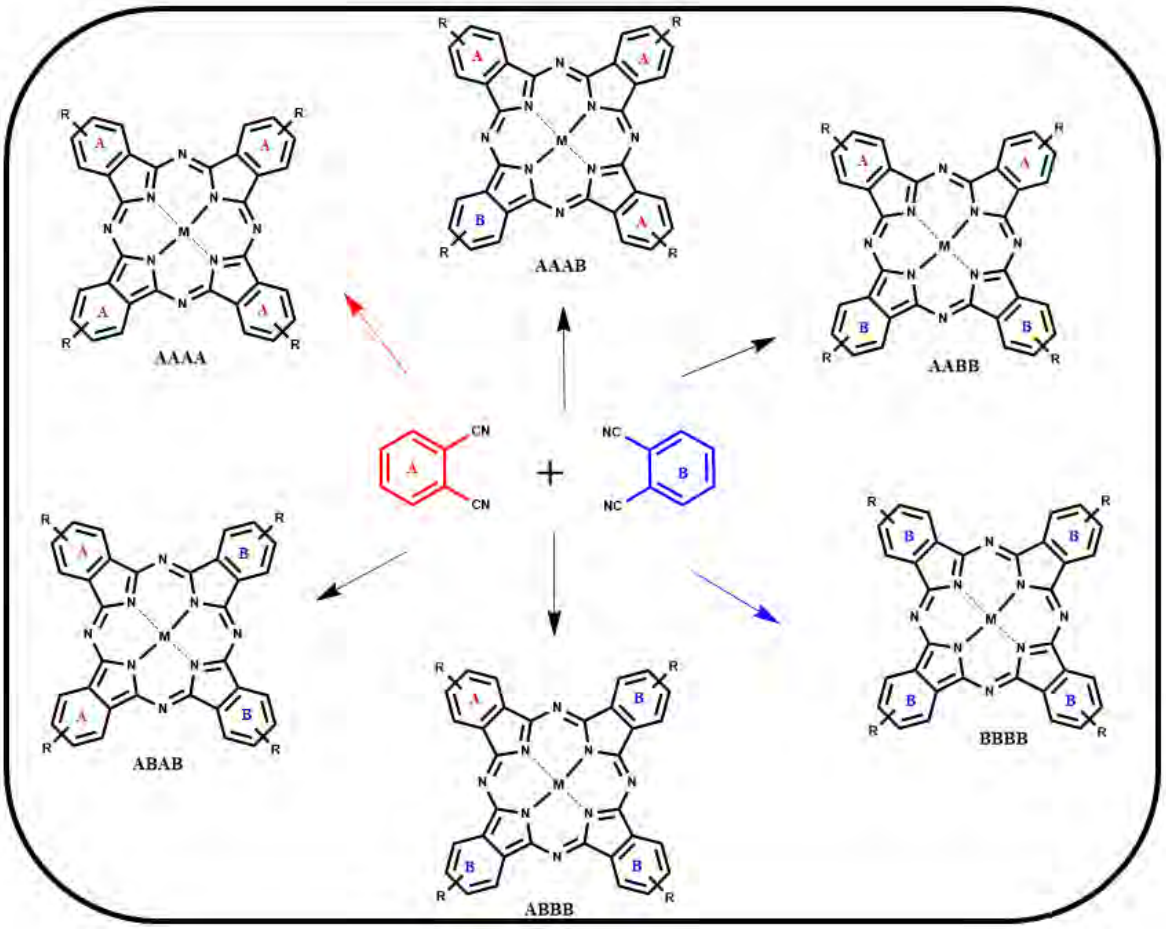

Scheme 1.2: Schematic representation of the statistical method used to synthesise asymmetric MPcs

Table 1.1 summarises the MPcs synthesised and studied in this work as electrocatalysts. The rationale behind the design (of the new MPcs) and use of these complexes is to study the effect of substituents, symmetry and transitional metals on the electrochemical and electrocatalytic properties of MPcs while establishing the impact of the push-pull effect on these properties. In some cases, the MPcs were used in the presence of nanomaterials to determine whether nanomaterials enhance the electroactivity of MPcs. All MPcs synthesised in this work are new except for **3-Co**, **4- Co**, **8-Co** and **9-Mn** [25–28].

Table 1.1: Summary of the MPcs synthesised and used in this work as an electrocatalyst, the nanomaterials they were used with and the test analyte of choice

MPc	Nanomaterial (conjugation)	Test analyte
1-Co 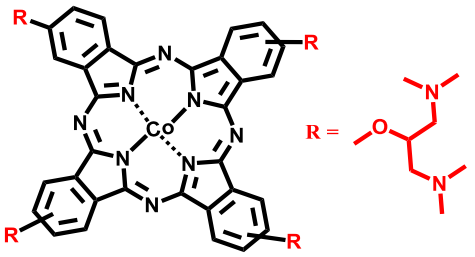 **tetra-4-((1,3-bis(dimethylamino)propan-2-yl)oxy) phthalocyanato Co(II)** New	NGQDs (π-π staking)	Dopamine
1-Co-As 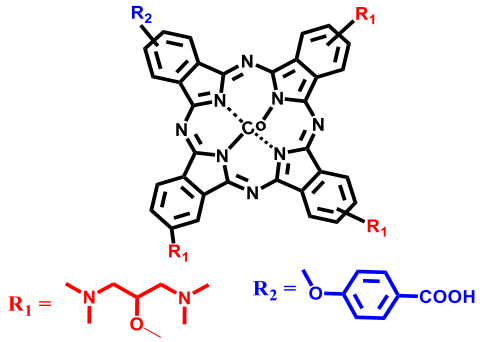 **tris-4-((1,3-bis(dimethylamino)propan-2-yl)oxy) mono carboxyphenoxy phthalocyanato Co(II)** New	NGQDs (π-π staking)	Dopamine
2-Co 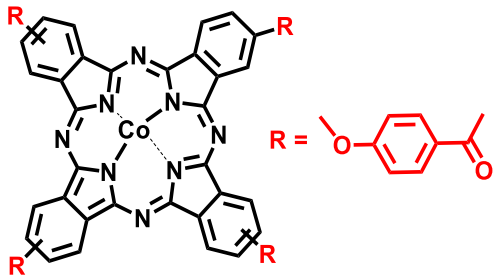 **tetra[4(4-acetylphenoxy) phthalocyanato] Co(II)** New	GQDS and SWCNTs (π-π staking)	Catechol

3-Co 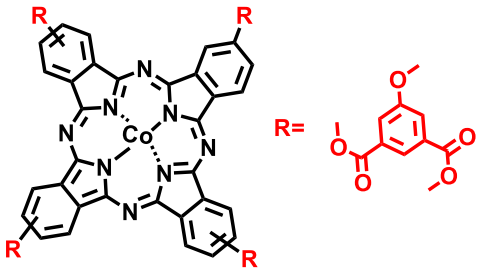 **tetra[dimethyl-5-(phenoxy)isophthalate phthalocyaninato] Co(II)** [25]	GQDS and SWCNTs (π-π staking)	Catechol
4-Co 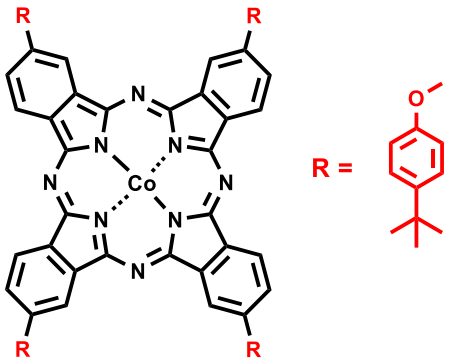 **tetra(4-(tert-butyl)phenoxy)phthalocyanato Co(II)** [26]	-	Nitrite
4-Co-As 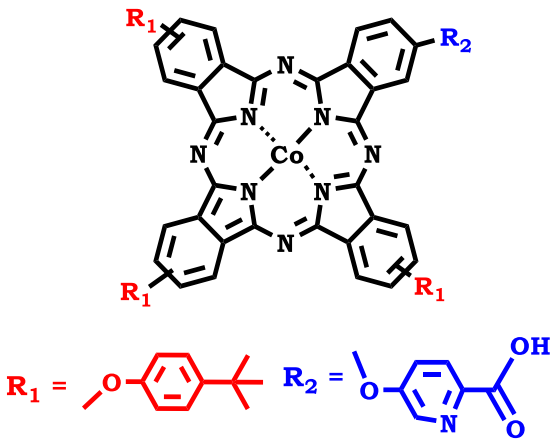 **tris(4-tert-butylphenoxy)-(5-phenoxylpicolinic acid) phthalocyanato Co(II)** New	Bi_2WO_6 and $NiWO_4$ (amide) NGQDs, GQDs and SWCNTs (π-π staking)	Nitrite

4-Cu-As 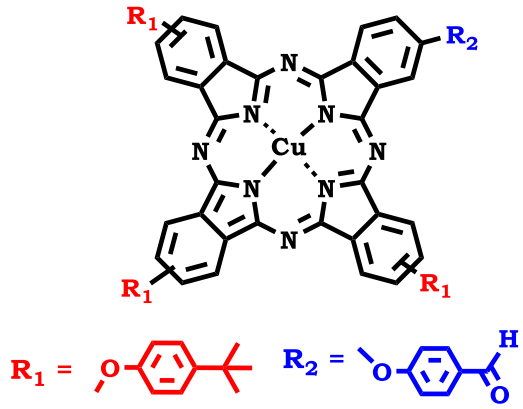 **4-((3,17,23-tris(4-(tert-butyl)phenoxy)phthalocyanine-9-yl)oxy)benzaldehyde phthalocyaninato Cu(II)** New	-	Catechol
5-Cu 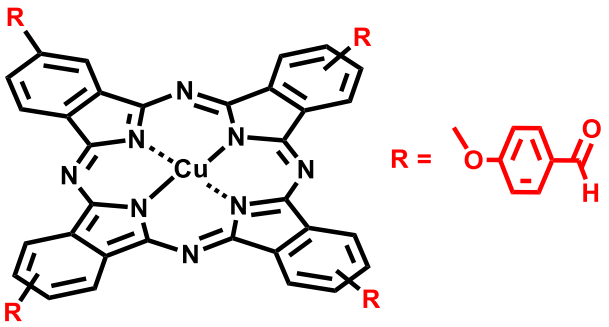 **tetra [(4-formylphenoxy)- phthalocyaninato Cu(II)** New	-	Catechol
6-Cu 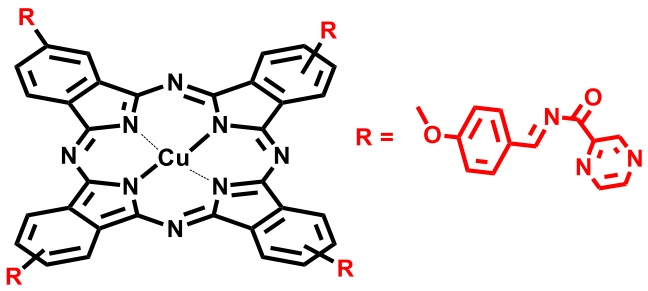 **tetra(oxy))tetra(benzene-4,1-diyl))tetra(methanylylidene))tetra(pyrazine-2-carboxamide) phthalocyaninato Cu(II)** New	-	Catechol

7-Cu 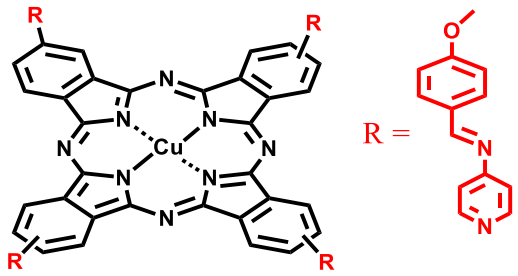 **tetra(oxy))tetra(benzene-4,1-diyl))tetra(N-(pyridin-4-yl)methanimine) phthalocyaninato Cu(II)** New	-	Catechol
8 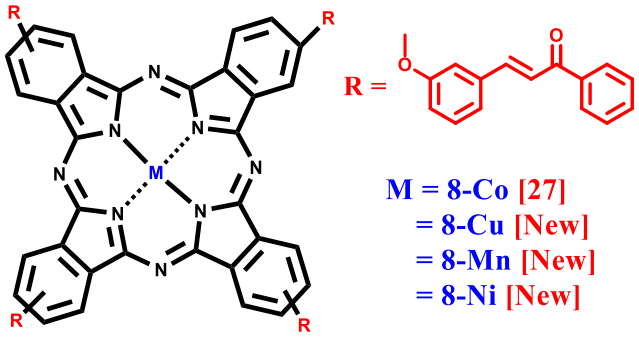 **Tetra–[4 –(3-(phenyl)-prop-2-en-1-one) phenoxy] phthalocyaninato (Metal)**	-	Nitrite
9-Mn 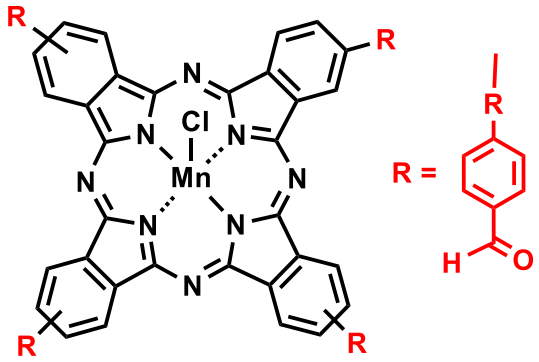 **tetra[(4-formylphenoxy)phthalocyaninato Mn(III)Cl** [28]	-	Nitrite

10-Mn 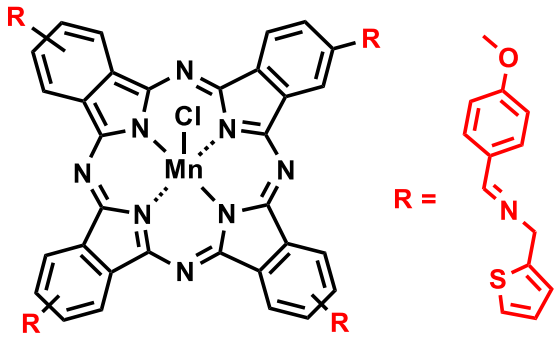 **tetra-4-(4-thio-thiophene-2-ylmethanamino)phthalocyaninato Mn(III)Cl New**	-	Nitrite
11-Mn 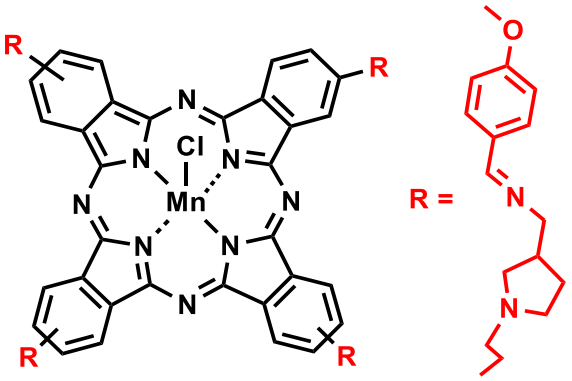 **tetra-4-(3-(pyrrolidine-1-yl)propan-1-amino)phthalocyaninato Mn(III)Cl New**	-	Nitrite

GQDs = Graphene doped quantum dots, NGQDs =Nitrogen-doped quantum dots, SWCNTs = Single-walled carbon nanotubes and As = Asymmetric MPcs

1.1.3 Electronic Absorption Spectra of Phthalocyanines

The occurrence of two absorption bands characterises the electronic absorption spectra of phthalocyanine complexes. The highly intense band (Q-band) is observed in the visible to near-infrared region of the electromagnetic spectrum between 600 – 1000 nm, and the less intense band, known as the Soret and or B-band, is typically observed in the UV (blue) region (300 – 400 nm) [2,29–31]. Figure 1.3 illustrates the electronic absorption spectra obtained for an H_2Pc (green) and MPc (blue). The observed absorption spectra are theorised using the Goutermans 4-orbital model (Figure 1.4) [1,2,29,32]. The model describes the transfer/transition of electrons from the highest occupied molecular orbital (HOMO, π) to the lowest unoccupied molecular orbital (LUMO, π*) [2,29].

The Q-band observed in the electrotonic absorption spectra of the phthalocyanine complexes is due to the π→π* transition from the a_{1u} at the HOMO to the e_g of the LUMO (Figure 1.4). Figure 1.3 shows that the H_2Pc has a split Q-band while the MPc has one solid band; this is attributed to the fact that H_2Pcs have a relatively lower symmetry (D_{2h}) [1,2].

The electronic transitions that MPcs undergo are not limited to the π-π* transitions. There are other vibronic components and charge transfers transitions (CTT), such as the metal-to-ligand charge transfer (MLCT) and the ligand-to-metal charge transfer (LMCT), that occur and result in the occurrence of additional absorption bands between 300 nm and 500 nm [2,29,32]. These CTTs, which involve the central metal, are attributed to the d-orbital/energy levels lying between the HOMO and LUMO gap of the MPc ring [2,29]. Charge transfer transitions affect the position of the main absorption band and solubility, which may result in aggregation [29]. Charge transfer transitions are common amongst cobalt, iron, manganese and chromium-metallated phthalocyanines.

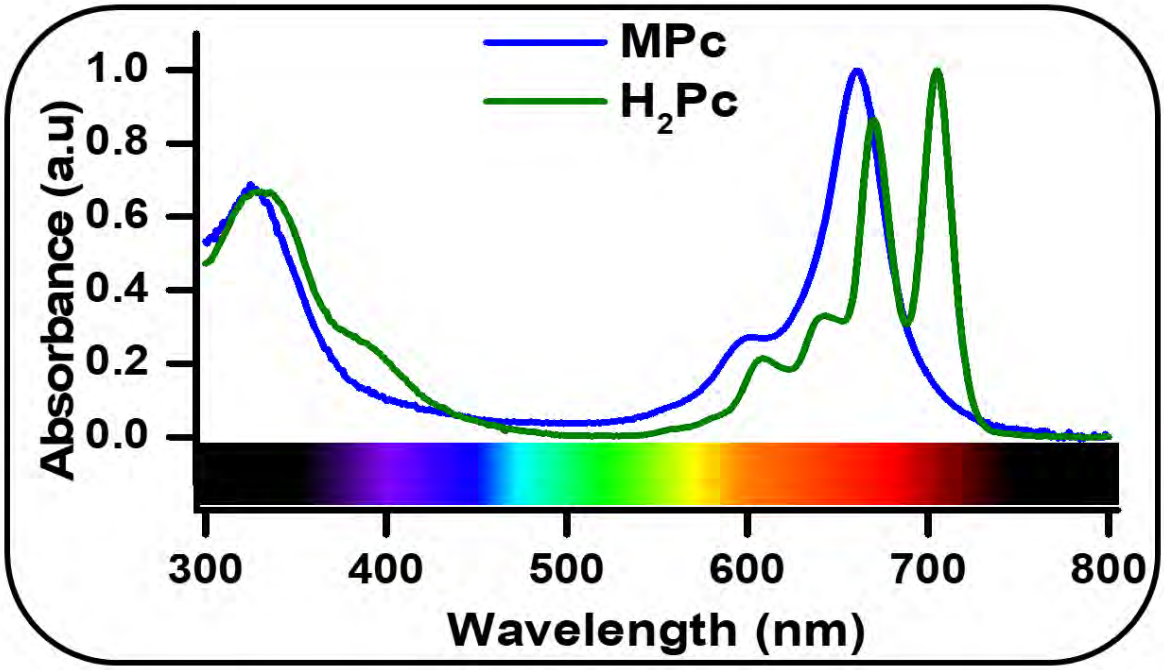

Figure 1.3: Electronic absorption spectra of an H_2Pc and MPc

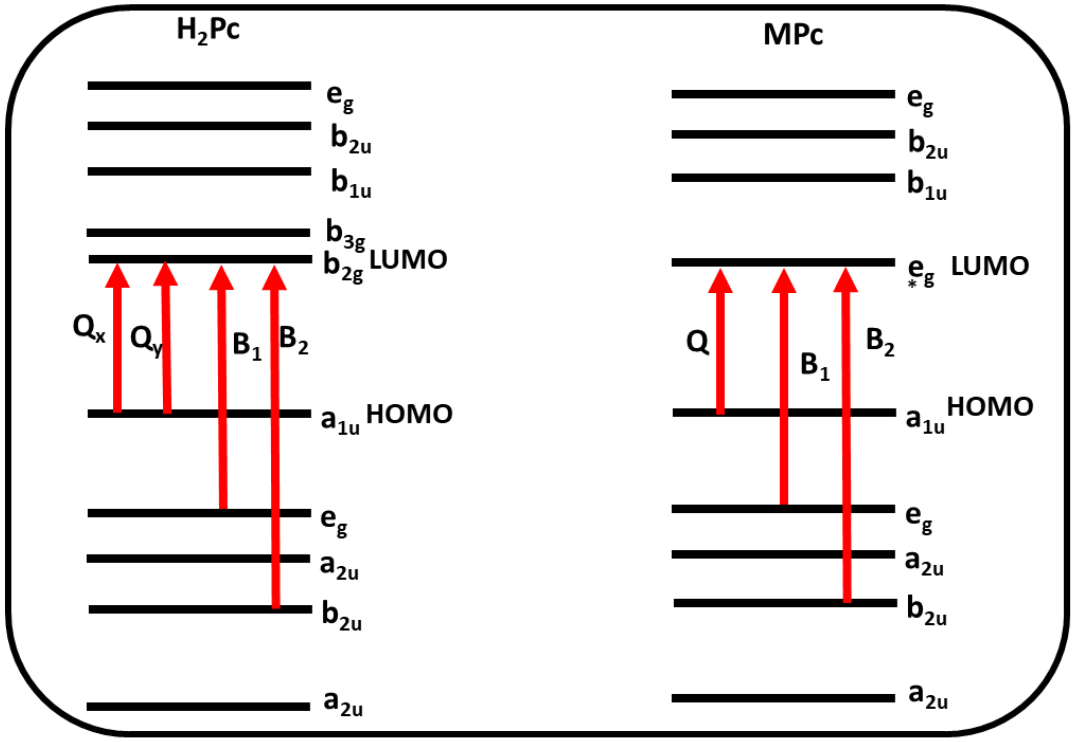

Figure 1.4: Gouterman's 4-orbital model illustrates electronic transitions in, unmetalled and metallophthalocyanine complexes.

1.1.4 General Applications

Phthalocyanines owe their applications to the flexibility of their chemical structure, chemical-thermal- and-photo stability, and excellent electronic properties. MPcs were initially synthesised and employed as dyes and pigments in the textile, paint, paper and printing industries [33,34]. Over the years, phthalocyanines have emerged to be among the most researched molecules in chemistry. MPcs are most commonly employed as catalysts for chemical reactions by large-scale industrial companies and in the degradation of various organic pollutants [35–37]. MPcs and their analogues have been used in dye-sensitised solar cells, electrochemical water electrolysis, and in batteries due to their excellent electronic and redox properties [38–41]. Over the past few decades, there has been an increasing trend in the use of MPc complexes in non-linear optics (NLO) [38,42–44]. Phthalocyanines have been applied in the medical industry as an alternative cancer treatment in photodynamic therapy (PDT) and photodynamic antimicrobial chemotherapy (PACT), in these applications, MPcs are used as photosensitisers [45–47].

The work described in this dissertation is based on the use of phthalocyanine complexes as electrocatalysts in electrochemical sensing. MPcs have been used as electrocatalysts in chemical and electrochemical sensors over the years owing to their excellent redox properties [38,48,49].

1.2 Electrocatalysis

This work explores the use of MPcs listed in Table 1.1 as electrocatalysts. It also investigates whether the use of nanomaterials enhances the electrocatalytic properties of MPcs.

Electrocatalysts are generally used to modify the working electrode surface in order to increase the rate constants, increase the current, and reduce over potentials [50,51].

1.2.1 Modified Electrodes

The glassy carbon electrode (GCE) was used throughout this work as the working electrode of choice because of its inertness, cost-effectiveness, broad active potential window, good electrochemical conductivity and ease of modification [52,53]. Despite the listed advantages, the bare GCE has very low sensitivity, the electron transfer reactions are relatively slow, and these reactions occur at relatively high over potentials. These limitations have led to the need for and rise in chemically modified electrodes (CMEs).

A modified electrode is a bare electrode whose surface has been coated with an electrocatalyst. Modification results in changes in the properties of the bare electrodes (optical, chemical and electrochemical) [54–56]. Modification allows for the electrode surface properties to be tuned and/or enhanced in favour of the intended application. In electrochemical sensing, electrode modification increases sensitivity. The bare electrode surfaces can be modified using electrostatic interactions, covalent bonding, grafting and adsorption (Figure 1.5) [35].

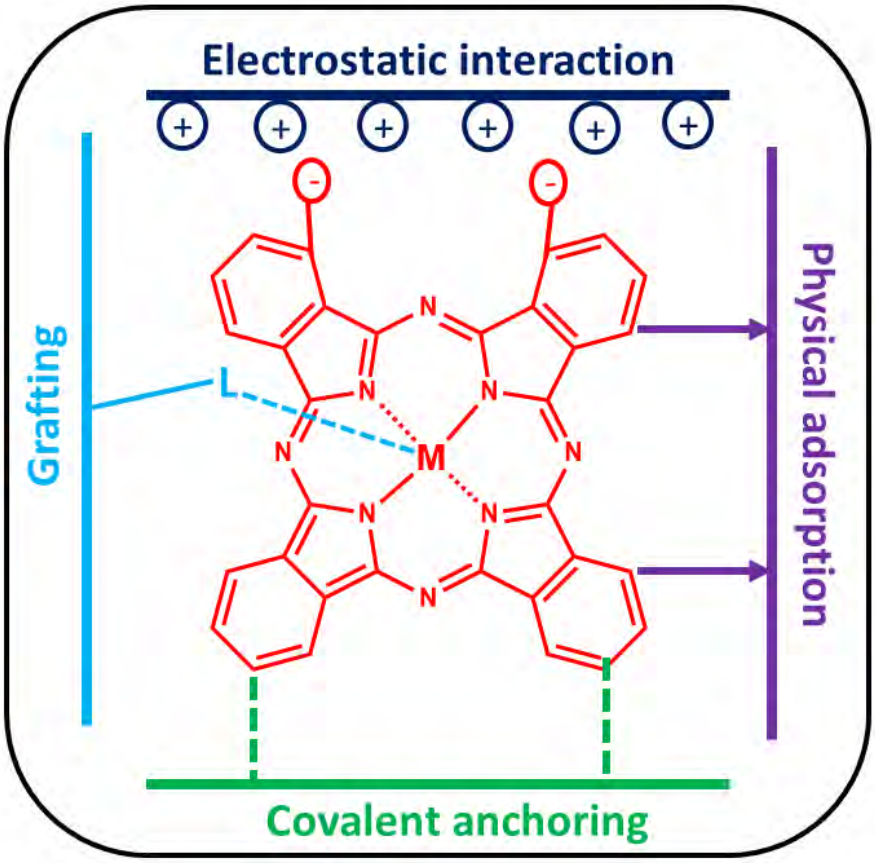

Figure 1.5: Electrode modification techniques. [35]

The physical adsorption (drop casting) method was used in this work to modify the working electrode surface. Drop casting is a straightforward method, cost-effective, and does not alter the chemical composition (therefore properties) of the MPcs (or other material used) and because MPcs have an affinity for the carbon surface, it makes adsorption on the GCE surface easy to achieve [35,57].

Figure 1.6 illustrates the cyclic voltammogram obtained before and after the GCE has been modified with an electrocatalyst. The figure shows that using a modified electrode results in relatively reduced over potentials and increased faradaic currents (sensitivity), which typically translates into low detection limits.

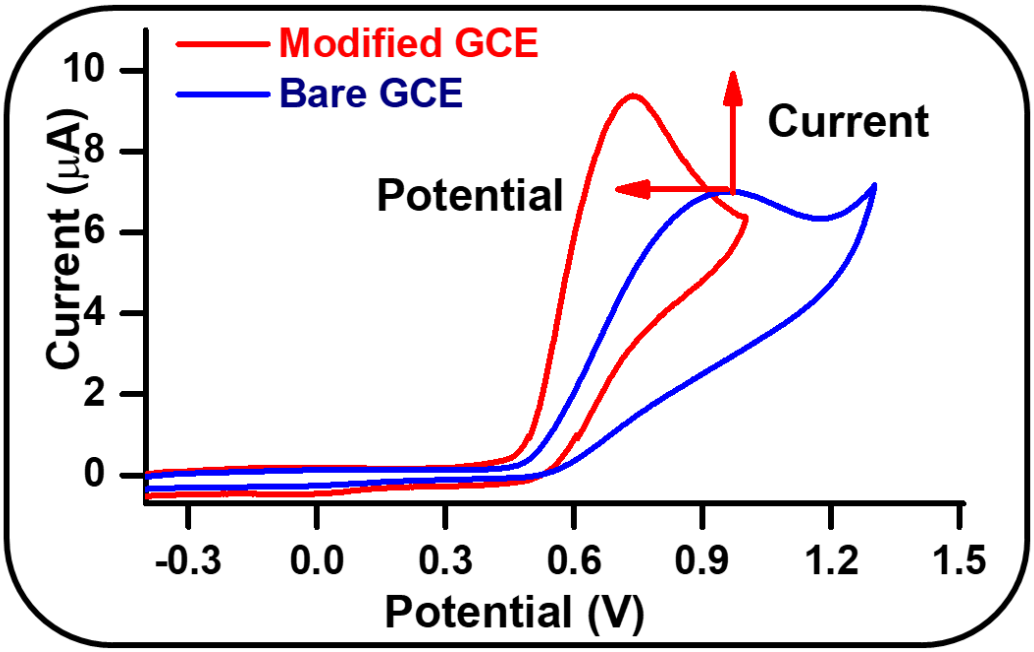

Figure 1.6: Cyclic voltammogram of the bare and modified GCE

1.2.2 Phthalocyanines as Electrocatalysts

Metallated phthalocyanine complexes exhibit good electrocatalytic activity, which can be utilised for the reduction and/or oxidation of various analytic species. MPcs owe most of their catalytic activity to their central metals (and the aromatic rings and substituents) [58,59]. The most commonly used transitional metals for electrocatalytic applications are iron, cobalt, manganese, copper and nickel (the order refers to the favourability of their electrocatalytic activity) [60]. In this work, Co, Mn, Cu and Ni phthalocyanine complexes were used for the electrochemical detection of various analytes. Oxidative reactions catalysed by redox processes on the central metal are described by Equations 1.1 and 1.2, while the mechanism of oxidation due to redox processes on the ring are summaries by Equations 1.3 to 1.5: (A is the analytic species)

$M^{(II)}Pc(-2) \rightarrow M^{(III)}Pc(-2) + e^-$ (**1.1**)

$M^{(III)}Pc(-2) + A \rightarrow M^{(II)}Pc(-2) + A^+_{ox}$ (**1.2**)

Figure 1.7 illustrates the basic electrocatalytic mechanism of the redox reactions followed by MPcs in the presence of the analytical species.

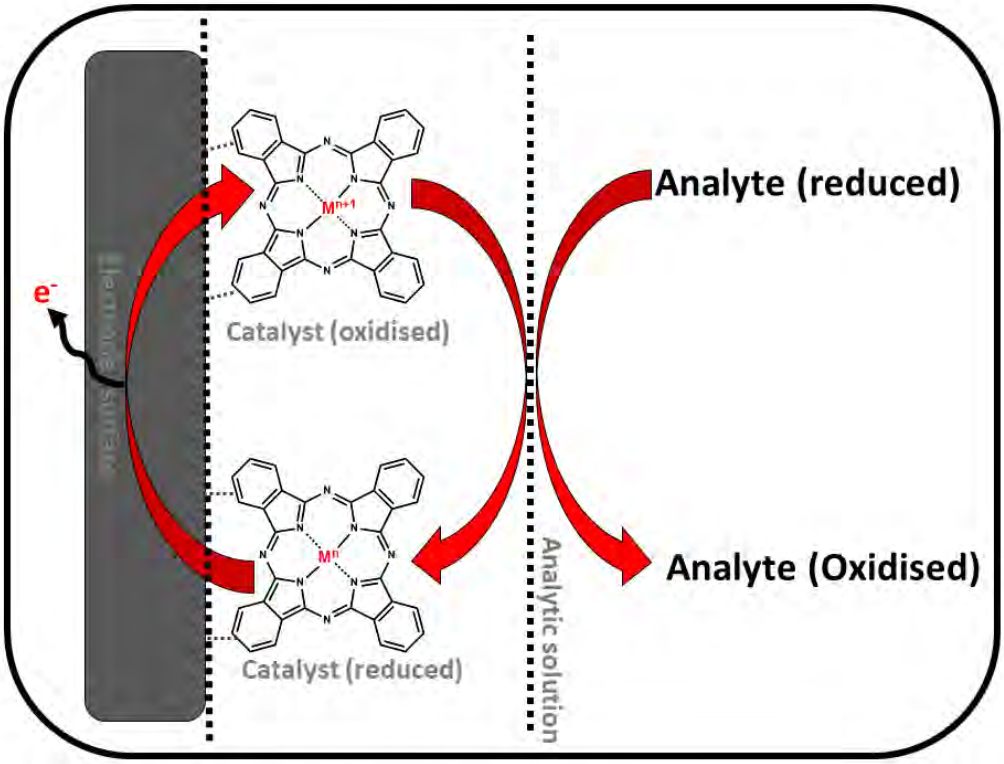

Figure 1.7: Representation of an MPc electrocatalytic reaction at the electrode surface in the analytic solution

The oxidation state of the MPc changes when it interacts with the analyte. The MPc regains its oxidation state by donating an electron to the electrode surface. The electrocatalytic activity of MPcs can be enhanced (achieve reduced potentials, high currents and detection limits) by incorporating other materials with good electrocatalytic properties, such as polymers and nanomaterials [59,61,62].

1.3 General Overview of Nanomaterials

Nanomaterials are nano-sized particles with sizes within the nanometer range (1 to 100 nm) [63]. The nanomaterials' shape, size, composition and synthetic method influence their chemical, physical and electrical properties [64]. Nanomaterials are typically synthesised using two main approaches, top-down and bottom-up (Figure 1.8).

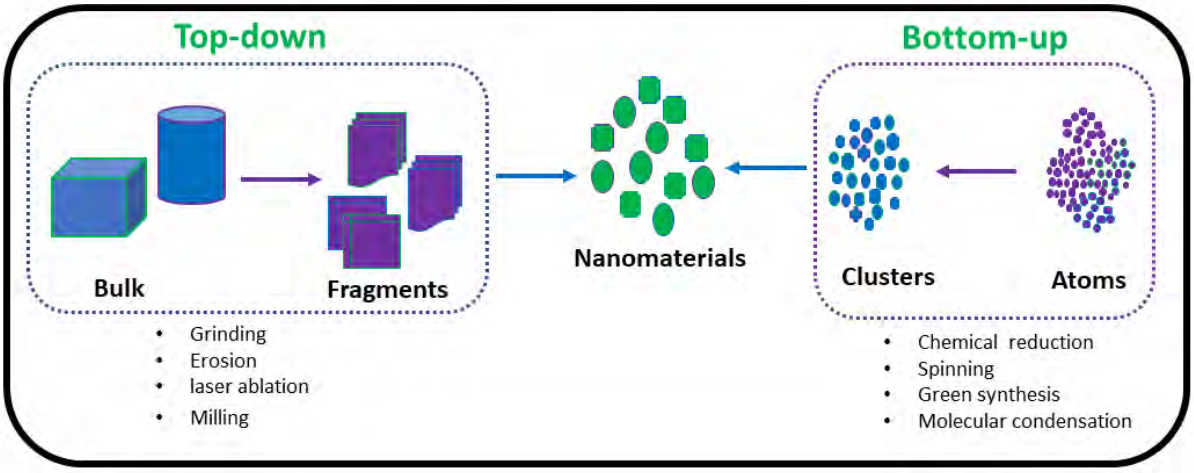

Figure 1.8: Top-down and bottom-up nanomaterials synthetic approaches and the synthesis of nanomaterials

In the top-down approach, bulk materials are broken down/reduced to produce nano-sized materials [64–66]. This approach typically uses physical/mechanical and chemical methods such as mechanical grinding and milling, laser ablation, electrolysis, pyrolysis and co-precipitation. On the other hand, the bottom-up approach mainly uses biological and chemical methods such as electrospinning, electrolysis, molecular condensation, chemical reduction, and green synthesis to produce and "grow" the nanoparticles from smaller molecules [64,66]. Various analytical techniques and instruments can be used to characterise nanomaterials and determine their key parameters [64,67,68].

Nanomaterials have several unique properties that are relatively enhanced compared to bulk materials. These include (not limited to) high surface area, antimicrobial activity, quantum effects, good mechanical properties, high thermal and electrical conductivity and excellent support for catalysts [68,69]. It is mainly due to these properties that nanomaterials have been used commercially in various fields, such as; drug delivery, water purification, fuel cells, photothermal therapies, electrocatalysis and sensors [70,71]. Nanomaterials are typically used with other materials to have a synergistic effect, thus enhancing the key properties required for the specified applications [58].

This work explores the use of carbon (graphene) and metal-based nanomaterials to enhance the electrocatalytic activity of MPcs. These nanomaterials will be studied as single entities and as hybrids when conjugated to MPcs to determine their effect on the electrochemical (electrocatalytic) activity and sensing ability of MPcs.

Nanomaterials can be linked with or added to phthalocyanine complexes via conjugation. Conjugation techniques can be classified as either covalent or non-covalent. Covalent linkage involves chemically linking two or more molecules together, allowing them to share a pair of electrons [72,73]. Covalent bonds are typically irreversible. While non-covalent linkage on the other hand, does not involve direct bonding by sharing electrons but rather electrostatic interactions. Non-covalent interactions linkage typically involves; hydrogen, ionic bonding, and Van der Waal interactions [72,74].

1.3.1 Carbon-based Nanomaterials

Carbon has various forms with changeable morphologies, such as fullerenes, diamonds, carbon nanotubes (CNTs) and graphene, giving rise to numerous carbon-based nanomaterials [69,75,76]. Throughout this work, graphene and carbon nanotubes nanomaterials were studied.

Carbon-based nanomaterials have been utilised to synthesise nanomaterials that have been used in a wide range of applications such as; medicinal, energy conversion, optical devices, sensing and environmental monitoring [77–79]. These nanomaterials have gained popularity in electrochemical applications, particularly in electrochemical sensing because they have; (i) high surface-to-volume ratio, (ii) high electrical conductivity, (iii) excellent chemical and thermal stability, (iv) fast electron transfer rate and (v) are robust [69,75,76].

Herein, three carbon-based nanomaterials (from two forms), graphene quantum dots (GQDs), nitrogen-doped quantum dots (NGQDs) and single-walled carbon nanotubes (SWCNTs), were used in conjunction with phthalocyanine complexes in electrochemical sensing.

Graphene is a monolayer carbon sheet comprised of sp^2 hybridised carbon atoms arranged in a hexagonal “honeycomb” lattice [72,75]. It is the basic structural element for carbon nanotubes, fullerene and graphite [75]. The chemical structure and shape of graphene (and consequently graphene-derived nanomaterials) results in graphene having more advantageous properties compared to other nanomaterials hence its widespread application in various fields such as; drug delivery, bioimaging, sensing, electronics and energy [69,80].

Graphene-based nanomaterials are used in electrochemical sensors mainly because they are cost-effective and do not contain metallic impurities, unlike other carbon-based nanomaterials [63,81].

1.3.1.1 Graphene Quantum Dots

GQDs are semi-conductor, two-dimensional graphene sheets with a diameter <100 nm their average size is 20 nm [69,82]. Graphene quantum dots have a prominent absorption peak in the UV region between 350 – 500 nm [83]. This absorption peak is due to the excitation of the sp^2 aromatic electrons from $\pi \rightarrow \pi^*$ [65,83]. Their absorption spectra are also influenced by their size and composition (addition of functional groups) [84].

Nitrogen-doped quantum dots are functionalised graphene quantum dots. These are GQDs that have been doped with nitrogen atoms [85]. Nitrogen doping can be achieved using ultrasonic, hydrothermal, thermal annealing and solvothermal methods, to name a few [82,85]. Figure 1.9 shows the addition of the N atoms using dicyandiamide as the nitrogen source via a hydrothermal reaction.

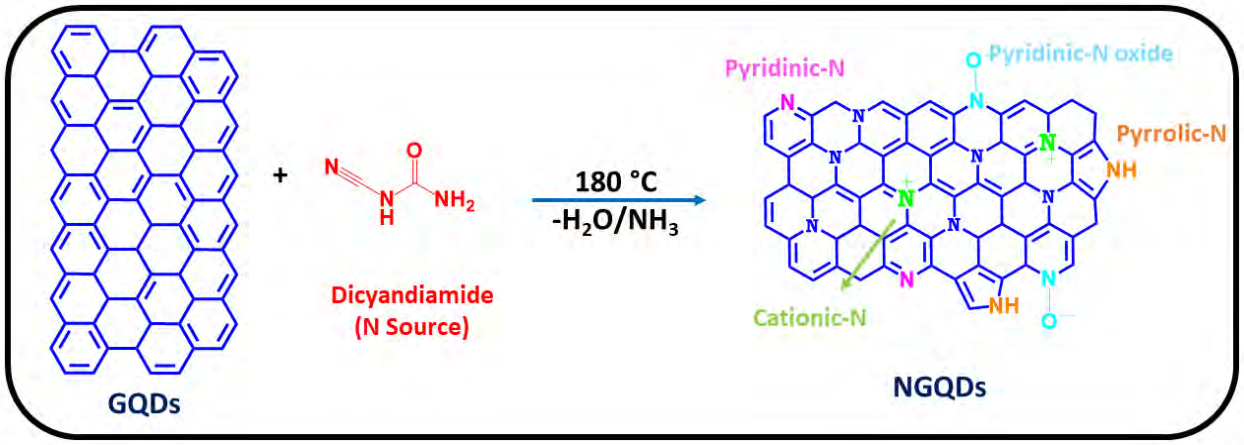

Figure 1.9: Nitrogen doping of GQDs using a hydrothermal method yielding to NGQDs. An illustration of the possible N-atom configurations due to N-dopping

The nitrogen atoms can be added in three different bonding configurations in graphene, pyrrolic, pyridinic, and graphitic (inner surface of the aromatic ring) (Figure 1.9) [85]. Controlling where the atoms attach is a challenge. The addition of N-atoms to the graphene

structure improves its properties, especially its electrocatalytic properties, therefore, broadening the applicability of GQDs [82,85]. Nitrogen-doped quantum dots have been extensively used in optical and electrical applications [85]. In this work, GQDs and NGQDs will be used to enhance the electrochemical sensing of MPcs, by being conjugated to MPcs.

1.3.1.2 Carbon nanotubes

Carbon nanotubes are rolled sheets of sp^2 hybridised carbon (or graphene) atoms arranged in hexagons (Figure 1.10) [75,76]. The atomic arrangement, length, diameter and morphology of the nanotubes influence the properties observed [86]. CNTs can be classified based on the number of carbon sheets; single-walled (SWCNTs), double-walled (DWCNTs) and multi-walled carbon nanotubes (MWCNTs) [87,88]. This work utilised single-walled carbon nanotubes conjugated to MPcs in electrochemical sensing.

SWCNTs are one-dimensional nanomaterials that only contain one graphitic layer [63,86]. Three possible SWCNTs (chiral, armchair and zig-zag) can be formed based on how the graphene sheet was rolled (Figure 1.10) [63,75,76]. Their average diameter is between 0.4 nm and 2.5 nm. Their size, length and diameter are influenced by the synthetic route, amongst other factors [63,88]. SWCNTs have remarkable properties such as high electrical conductivity and good and fast electron transfer reactions that have led to them being widely used in sensing and, most significantly, electrochemical sensing [76,89,90].

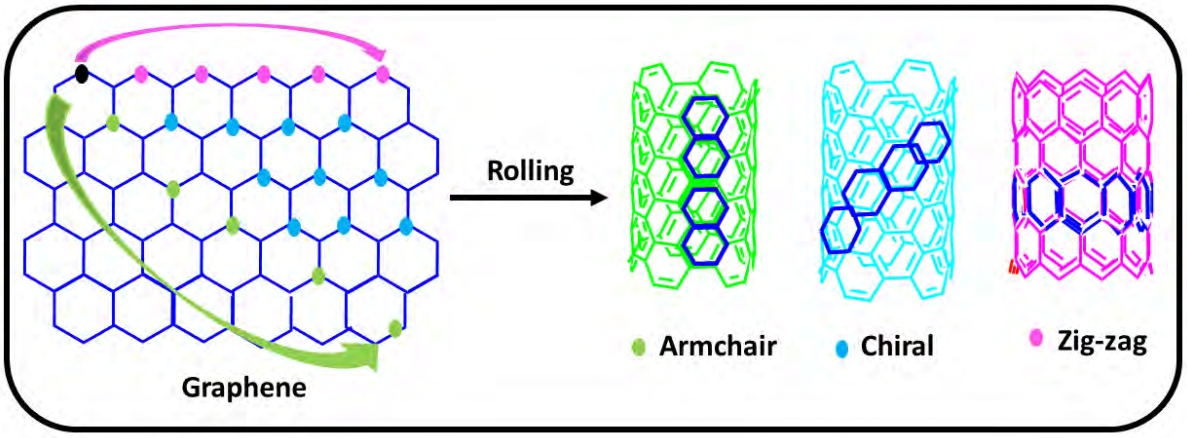

Figure 1.10: Typical graphene and possible SWCNTs structures

Table 1.2 shows a summary of MPcs linked to the carbon-based nanomaterials (hybrid materials) that have been used in literature as electrocatalysts in electrochemical sensing [91–97]. The table shows that the most commonly used MPcs are cobalt MPcs, this is attributed to their remarkable redox properties. Minimal work has been published using these hybrid complexes (MPcs with carbon-based nanomaterials) in electrochemical sensing, especially involving the use of asymmetric MPc hybrids. This work introduces a wide array of novel MPcs (Co, Cu, Ni and Mn Pcs) and new MPc-nanomaterial hybrids, extensively studied and employed as electrocatalysts in electrochemical sensing (Table 1.1).

Table 1.2: List of a selection of MPc complexes studied as hybrids with carbon-based nanomaterials used as electrocatalysts in electrochemical sensing.

MPc	Nanomaterial (conjugation)	Analyte	Reference
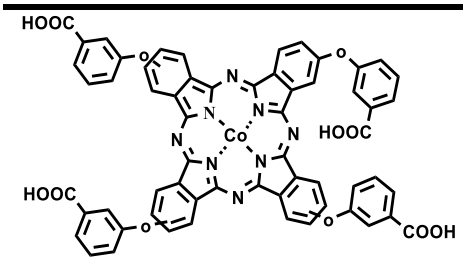	Gold nanoparticles and GQDs (Amide)	catecholamine	[91]
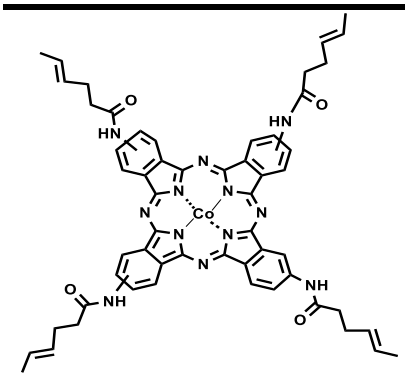	MWCNTs (Amide)	2-amino phenol	[92]
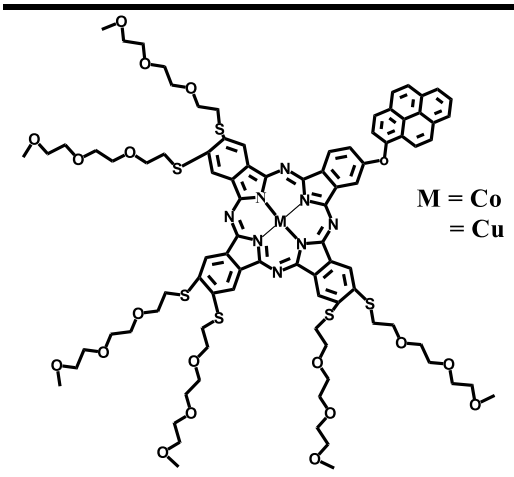	NGQDs (π-π staking) NGQDs (Amide)	Nitrite Nitrite	[93]

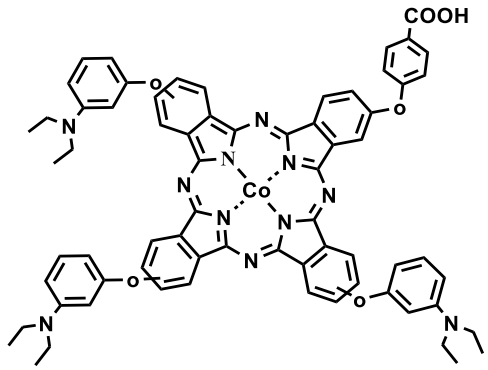	SWCNTs (π-π stacking)	Gas	[94]
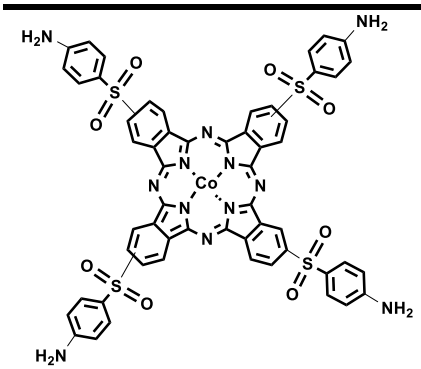	SWCNTs (Amide)	Thiochlorine	[95]
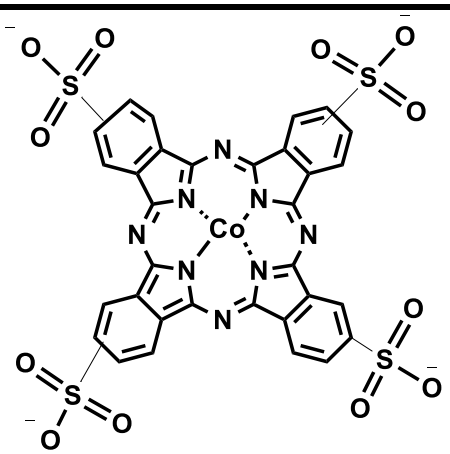	Graphene (π-π stacking)	Dopamine, uric acid and ascorbic acid	[96]
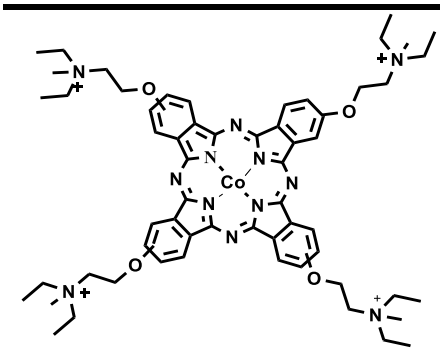	Graphene oxide (π-π stacking)	Catechol	[97]

1.3.2 Metalic Nanomaterials

Metallic nanomaterials have gained great popularity in various applications due to their remarkable properties, such as; good antimicrobial activity, electrical conductivity, and optical polarizability, amongst other properties [98–101]. This work focuses on the use of metal oxide nanomaterials.

The metal oxide nanomaterials used herein are tungstate oxide nanomaterials, bismuth tungstate oxide (Bi_2WO_6) and nickel tungstate oxide ($NiWO_4$). Tungstates are ternary metal oxides generally denoted as MWO_x, where M is the bivalent cation [102–104]. Tungstate nanomaterials are synthesised into various crystal structures such as spheres, hollow structures, and nanorods, amongst other forms [105,106].

Tungsten-based materials are commonly used in luminescence, electronics, catalysis, sensing and energy storage applications [102,104,107,108]. They are exploited in these fields primarily because they have self-activating fluorescence and remarkable catalytic properties due to their high surface area and sensitivity and are environmentally friendly [103,104,108,109]. $NiWO_4$ has been used in catalytic and electrocatalytic processes and in supercapacitors [109]. Bi_2WO_6 has been extensively studied as a photocatalyst [110].

There are no literature findings of MPc-tungstate hybrids in electrochemical sensing. Therefore, this work is the first to report on the use of tungstate nanoparticles to enhance the electrochemical and electrocatalytic properties of MPcs and their use in electrochemical sensing.

1.4 Test Analytes

This work uses catechol, nitrite and dopamine as test analytes when studying the electrochemical and electrocatalytic properties of MPcs (Figure 1.11). The detection of these analytical species is of great importance for diagnostic and environmental monitoring purposes as they all pose potential threats to aquatic, plant and human life. These analytic species were used as test analytes due to their availability, sensitivity, and selectivity of the MPc (or hybrid MPc-nanomaterials) towards their detection.

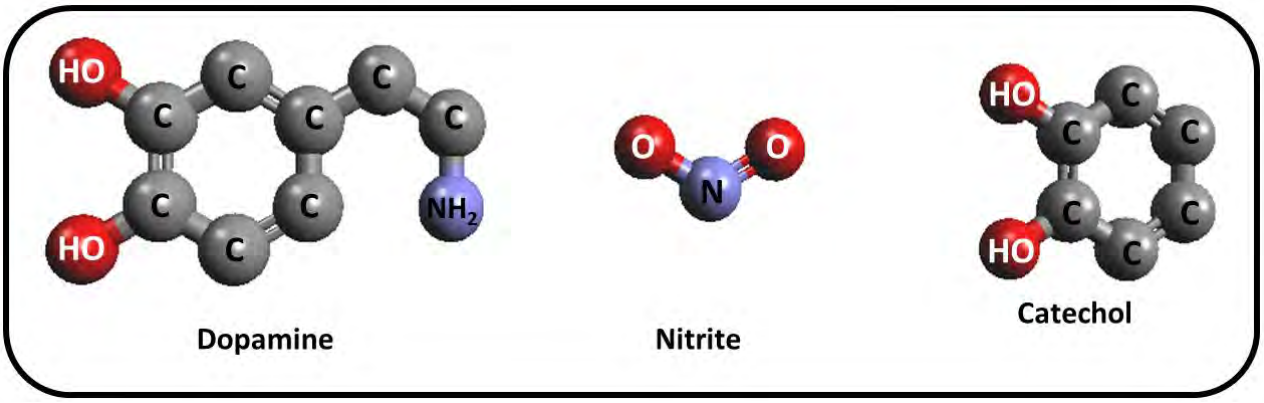

Figure 1.11: Analytes of interest; catechol, nitrite, and dopamine

Table 1.2 lists work published using MPcs in the presence of carbon-based nanomaterials to detect these analytes. The low citations indicate that very minimal work has been done in this subject matter. This work significantly contributes to this discipline by introducing new MPc as electrocatalysts and studying the effect nanomaterials have on their electrocatalytic activity when detecting these analytic species.

1.4.1 Nitrite

Nitrite is a naturally occurring component of the nitrogen cycle, readily found in humans and certain foods such as fruits and vegetables [111–113]. Nitrite can also be added to processed foods to combat the growth of harmful bacteria while adding flavour [114]. Nitrite plays a significant role in several physiological processes and industrial systems [115].

In the human body, nitrite can lose an oxygen molecule and become nitric oxide, which is an important molecule that causes blood vessels to dilate and lower one's blood pressure. Thus reducing the risk of having high blood pressure, which could lead to heart disease, stroke and even death [116,117]. Although nitrite has health benefits, at high concentrations, it poses a significant threat to plant and aquatic life. In humans, it has been associated with various ailments and diseases such as; Parkinson's disease, rheumatoid arthritis, meningitis and nephritic syndrome in children [111,118–121]. Capillary electrophoresis, spectrophotometry, chemiluminescence, and electrochemistry are among the numerous techniques and technologies used to detect nitrite [115,122–124].

Table 1.1 shows the MPcs synthesised and utilised as electrocatalysts to detect nitrite. Two low-symmetry CoPcs (**4-Co** and **4-Co-As**) were used to investigate the effect of symmetry on the detection of nitrite and the push-pull effect on the electrochemical and electrocatalytic properties. **4-Co-As** was further conjugated to functionalised metal oxide nanoparticles, Bi_2WO_6 and $NiWO_4$ via amide bond and to GQDs, NGQDs and SWCNTs via π-π stacking to investigate the effect of nanomaterials, on the electrocatalytic properties of MPcs and towards nitrite detection. MPcs and tungstate nanoparticle hybrids were reported herein for the first time for electrochemical sensing in general.

A chalcone substituted CoPc series (**8**) was employed to study the effect of the central metal of MPcs, their electrocatalytic properties and their ability to detect nitrite. Schiff base manganese phthalocyanine complexes **Mn-10** and **Mn-11**, derived from **Mn-9,** were the first Schiff base MPcs complexes to be reported as electrocatalysts in the detection of nitrite. These complexes were used to investigate whether Schiff bases (Schiff base phthalocyanine complexes) could be potentially used as electrocatalysts. They were also used to study the effect of heteroatoms on the electrocatalytic activity of MPcs.

1.4.2 Dopamine

Dopamine (4-(2-aminoethyl)benzene-1,2-diol) plays a significant role in the central nervous, renal, cardiovascular and hormonal systems and metabolism [125–127]. It controls reward-motivated behaviours such as memory, movement, attention and moods, to name a few [128–130]. Abnormally high or low concentrations of dopamine can lead to neurological disorders and diseases such as Schizophrenia, Parkinsons' disease, Alzheimer's, epilepsy and attention deficit hyperactive disorder. Hence the need to develop materials and or technologies that can detect dopamine.

Numerous methods and technologies, such as high-performance liquid chromatography, spectrophotometry, fluorometry, colourimetry and electrochemistry, have been used to detect dopamine [131–133]. Electrochemical sensing has been widely employed in detecting dopamine, and it is advantageous over other techniques because it offers high selectivity, sensitivity and low detection limits [131,134–136]. Over the years, MPc complexes, nanomaterials and MPc-nanomaterial hybrid molecules have been used in the electrochemical detection of dopamine. These systems have exhibited highly favourable detection properties such as high sensitivity, selectivity and low detection limits [96,137,138].

In this work, two cobalt phthalocyanine complexes (**1-Co** and **1-Co-As**) (Table 1.1) were employed as electrocatalysts to detect dopamine. These CoPcs were studied alone and as hybrids with NGQDs conjugated via π-π stacking. These complexes aid in studying the effect of symmetry and the addition of nanomaterials in electrochemical sensing, particularly towards nitrite detection.

1.4.3 Catechol

Catechol (1,2-dihydroxybenzene) is a widely studied naturally occurring phenolic compound [97,139]. Catechol has also been used commercially in cosmetics, plastics, photography, dyes, antioxidants, textiles, agricultural chemicals and medicine [97,140]. It is commonly released into the environment as a toxic industrial by-product [97]. In high concentrations, catechol can be very harmful to aquatic, plant and human life [97,140]. Over (high concentration) exposure of catechol generally affects the heart, lungs and central nervous system in humans [97,141].

Various analytical methods, such as; high-performance liquid chromatography, capillary electrophoresis, gas chromatography, and chemiluminescence electrochemical methods, have been used to determine and detect catechol [140,142–144]. This work focuses on the use of electrochemistry in detecting catechol, using MPcs and their nanomaterial conjugates as electrocatalysts. MPcs-nanomaterial hybrids have not been extensively explored in the detection of catechol, this work offers new insight into this [97,145].

Herein, six MPcs (Table 1.1) were used as electrocatalysts to detect catechol. The two symmetric CoPcs (**2-Co** and **3-Co**) were synthesised and conjugated to GQDs and SWCNTs, to study the effect of substituents. The addition of nanomaterials and the effect of the nature of the nanomaterials structure (planar graphene sheet vs rolled-up graphene). The CuPc

series (**4-Cu-As**, **5-Cu**, **6-Cu** and **7-Cu**) was not studied with nanomaterials. The CuPc complex series was used to determine the effect of substituents on the electrocatalytic properties of the MPcs for the detection of catechol.

1.5 Aims of the Dissertation

The aims of the dissertation are summarised below:

i. Design, synthesise, and characterise phthalocyanine complexes (symmetric and asymmetric). Study their spectral and electrochemical properties.

ii. Synthesise and characterise nanomaterial; graphene quantum dots, nitrogen-doped quantum dots, nickel and bismuth tungsten and study their properties (spectral, electrochemical and physical)

iii. Conjugate the phthalocyanine complexes and the nanomaterials, creating complex hybrid systems. Characterise these conjugates by studying their physical and electrochemical properties.

iv. Use the conjugates and the individual phthalocyanine complexes and nanomaterial to modify the glassy carbon electrode surface and study their electrochemical properties.

v. Use the modified electrodes to detect nitrite, catechol, and dopamine. Study the reaction kinetics associated with the electrochemical detection of these analytes.

vi. Investigate the modified electrodes' stability, sensitivity, and selectivity.

CHAPTER 2

EXPERIMENTAL

Preface: This chapter lists the materials and instruments used throughout this dissertation. While providing a summary of the synthetic routes followed during the synthesis of phthalonitriles, phthalocyanines and nanomaterials. It also provides the linkage/conjugation (MPc-nanomaterials) methods and electrode modification techniques used.

2. EXPERIMENTAL

2.1 Materials

2.1.1 General Solvents

1-Pentanol, dimethylethanolamine (DMAE), dimethylformamide (DMF), dimethyl sulfoxide (DMSO), tetrahydrofuran (THF), cyclohexane, petroleum ether, dichloromethane (DCM), methanol, ethanol, chloroform and acetone were purchased from Merck.

2.1.2 Phthalonitrile and Phthalocyanine Synthesis Reagents

4-Nitrophtalonitrile, potassium carbonate, cobalt(II) acetate tetrahydrate ($Co(OAc)_2 \cdot 4H_2O$), copper (II) chloride, manganese(II) chloride, nickel(II) acetate tetrahydrate ($Ni(OAc)_2 \cdot 4H_2O$), 1,8-diazobicyclo [5.4.0] undec-7-ene (DBU), 5-hydroxypicolinic acid, pyrazine-2-carboxamide, 4-aminopyridine, thiophene-2-ylmethylamine and 3-(pyrrolidine-1-yl)propane-1-amine were purchased from Sigma-Aldrich.

2.1.3 Nanomaterial Synthesis and Conjugation Reagents

N,N'-dicyclohexylcarbodiimide (DCC), glutathione (GSH), thioglycolic acid (TGA), urea, citric acid, nickel acetate tetrahydrate ($Ni(OAc)_2 \cdot 4H_2O$), sodium hydroxide, sodium tungstate dihydrate ($Na_2WO_4 \cdot 2H_2O$) and bismuth oxide (Bi_2O_3) were purchased from Sigma-Aldrich. Single-walled carbon nanotubes (SWCNTs-COOH), 1–5 nm in diameter and 1–5 μm in length) were purchashed from Nanolab. Graphene quantum dots [146], nitrogen-doped quantum dots [147], nickel and bismuth tungstate oxide nanoparticles [148] were prepared according to literature.

2.1.4 Electrochemical Studies Reagents

Tetrabutylammonium tetrafluoroborate ($TBABF_4$) and alumina nanopowder (<10 μm) were purchased from Sigma-Aldrich. The 1 mM $[Fe(CN)_6]^{3-/4-}$ redox couple solution was prepared using weighed amounts of; $K_3[Fe(CN_6)]$, $K_4[Fe(CN_6)]$ and KCl. The 0.1 M phosphate saline buffer (PBS), pH 7, was prepared using weighed amounts of Na_2HPO_4, KH_2PO_4, KCl and NaCl. Type II Elga water, obtained from an Elga PURE LAB Chorus 2 (Ro/di) system. Nitrite, dopamine and catechol solutions were prepared using sodium nitrite (Sigma-Aldrich), dopamine hydrochloride (Sigma-Aldrich) and catechol (Merck).

2.2 Instruments

The following equipment were used in the characterisation of the phthalonitriles, phthalocyanines, nanomaterials and hybrids/conjugates synthesised and used throughout this work:

- The **Ultraviolet-Visible** (UV–Vis) absorption spectra were recorded using a Shimadzu UV-2250 spectrophotometer
- The **Infrared spectra** were recorded using a Bruker Alpha-model FT-IR Spectrometer with platinum-ATR.
- The **mass spectra** data were measured on a Bruker AutoFLEX III Smart beam TOF/TOF mass spectrometer, α-cyano-4-hydrocinnamic acid was selected as the MALDI matrix while a 355 nm Nd: YAG laser was used as the ionising source.
- **Elemental analyses** were obtained using a Vario-Elementar Microcube ELIII.

- The **proton nuclear magnetic resonance** (^{1}H-NMR) spectra were recorded on a Bruker AMX Advance 600 MHz NMR spectrometer using tetramethylsilane as an internal reference
- **Hydrothermal synthesis** was carried out using a Berghof (Germany) High Pressure Laboratory Reactor **Autoclave** BR-300, V.3.0 equipped with PT-100 temperature and pressure sensors, BTC-300 Temperature regulator and manometer and PTFE lining (Figure 2.1)

Figure 2.1: The Berghof high pressure reactor, autolcave used for the hydrothermal synthesis of GQDs and NGQDs

- The **Raman** spectral data was collected using the Bruker Vertex 70-Ram II Raman spectrometer (equipped with a 1064 nm Nd: YAG laser and liquid nitrogen-cooled germanium detector).
- The **X-ray powder diffraction** (XRD) patterns were measured on a Bruker D8 Discover equipped with a Lynx Eye detector (proportional counter) using Cu Kα radiation (l = 1.5405 A°, nickel filter).
- For **thermogravimetric analysis** (TGA), the thermal decomposition profiles were recorded over a temperature range of 50–700 °C on a Perkin Elmer TGA 8000 Thermogravimetric Analyzer.
- **Atomic force microscopy** (AFM) measurements were carried out in the tapping mode with MFP-3D Origin supplied by Asylum research.
- **Dynamic light scattering** (DLS) experiments were done on a Malvern Zetasizer nanoseries, Nano-ZS90.
- All **electrochemical studies**; cyclic voltammetry (CV), differential pulse voltammetry (DPV) chronoamperometry, and electrochemical impedance spectroscopy (EIS), were performed using Autolab potentiostat PGSTAT30 equipped with Nova software version 2.1 A three-electrode electrochemical cell (Figure 2.2) comprising of a glassy carbon electrode (GCE) as the working electrode, platinum wire as the counter electrode and silver|silver chloride wire (Ag|AgCl) (3 M KCl) as reference electrode was used.

  EIS experiments carried out using an additional manual control, FRA2 module. These studies were performed between 0.1 Hz and 10 KHz using a 5 mV rms sinusoidal modulation.

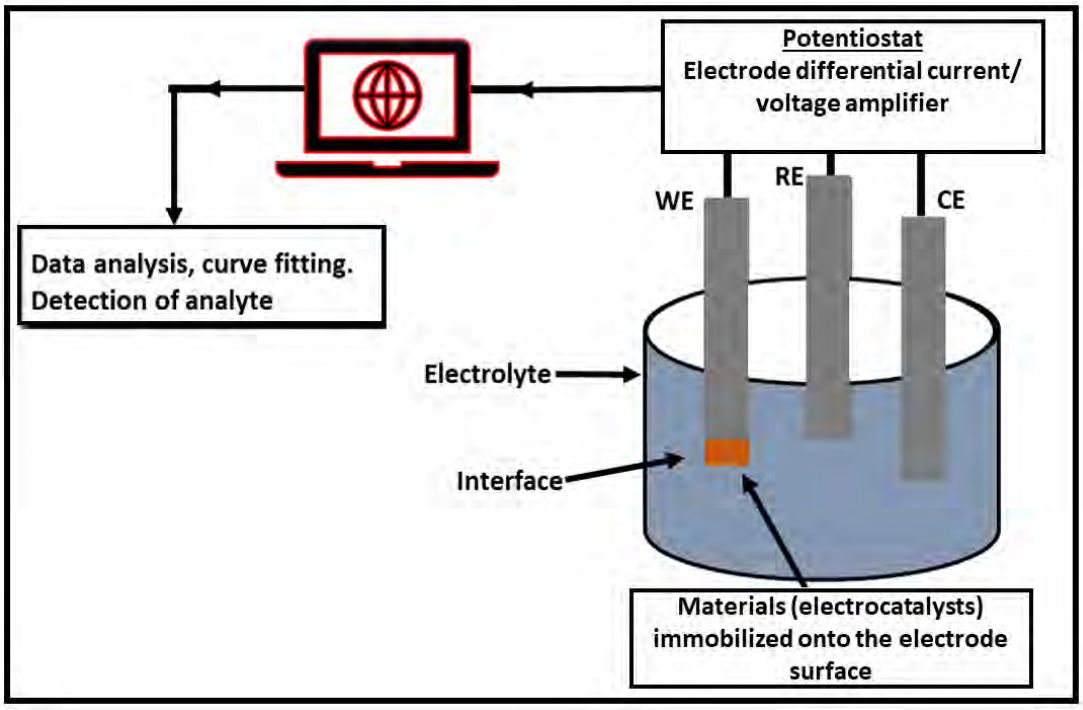

Figure 2.2: Typical three electrode electrochemical set-up [149]

- **Scanning electrochemical microscopy** (SECM) measurements were conducted on the Uniscan Model 370 equipment and a 10 µm Pt microelectrode (Uniscan) as the tip. SECM approach curves were obtained using the Pt microelectrode with a Pt counter electrode and Ag|AgCl wire as the pseudo-reference electrode. Glassy carbon plates (Goodfellow, UK) of 1 × 1 cm and 2 mm thick were used as substrates for the SECM measurements.

2.3 Synthesis of Phthalonitriles

Phthalonitriles; 4-((1,3-bis(dimethylamino)propan-2-yl)oxy)phthalonitrile (**A**) [150], 4-(4-carboxyphenoxy)phthalonitrile (**B**) [151], 4-(4-acetylphenoxy)phthalonitrile (**C**) [152], dimethyl 5-(3,4-dicyanophenoxy)-isophthalate (**D**) [25], 4-(4-(*tert*-butyl)phenoxy)phthalonitrile (**E**) [153], 4-(4-formylphenoxy) phthalonitrile (**G**) [154], and 4-(4-(3-oxo-3-phenylprop-1-enyl) phenoxy) phthalonitrile (**H**) [155] are all known and were prepared according to literature.

Synthesis of 5-phenoxylpicolinic acid phthalonitrile (**F**), Scheme 3.1

4-Nitrophthalonitrile (1.5 g, 8.67 mmol) and 5-hydroxypicolinic acid (1.21 g, 8.67 mmol) were dissolved in DMF (60 mL) and degassed under argon flow. The mixture was stirred for 20 min, and then potassium carbonate (4 g, 28.9 mmol) was added. The resulting suspension was stirred for 48 h at room temperature. The product was precipitated out in ice and filtered under reduced pressure. The resultant product (**F**) was then purified with water and washed with hot ethanol.

Yield = 68%. IR (cm^{-1}): 3068-3034 (Ar C-H), 2858 (Aliph. C-H), 2288 (C≡N), 1671 (C=O), 1578 (C=C), 1487-1357 (C-C), 1248 (Asymmetric Ar-O-), 1093 (Symmetric Ar-O-), 952, 912 ^{1}H NMR (600 MHz in DMSO – d_6). δ(ppm), 8.78 (s, OH), 8.62 (d, Ar, 1H), 8.38 (d, Ar, 1H), 7.88(s, Ar, 1H), 7.74(d, Ar, 1H), 6.75(d, Ar, 2H).

2.4 Synthesis of Phthalocyanines

Phthalocyanine complexes **3-Co**, **4-Co**, and **8-Co** and are known, and were synthesised according to literature [25–27]. Complex **9-Mn** is known however, it was synthesised differently from the complex cited in literature.

2.4.1 Synthesis of tetra-4-((1,3-bis(dimethylamino)propan-2-yl)oxy) phthalocyanato Co(II) (**1-Co**), Scheme 3.2(a)

Phthalonitrile **A** (200 mg, 0.734 mmol) and cobalt (II) acetate tetrahydrate (91 mg, 0.367 mmol) were dissolved in dry 1-pentanol (4 mL) in the presence of DBU (0.5 mL), the reaction mixture was heated at reflux temperature (140˚C) for approximately 18 h under inert conditions and thereafter cooled to room temperature. The resultant product was centrifuged in DMSO several times and centrifuged in water, and thereafter washed in ethanol several times, the supernatant was dried under vacuum yielding to **1-Co**.

Yield: 45%. IR (cm^{-1}): 3106 (Ar C-H), 2928-2860 (Aliph. C-H), 1591 (C=C), 1400-1385 (C-C), 1200,1064 (Ar-O-), 724. UV/Vis (DMF), λ_{max} nm (log ε): 676 (4.64), 620 (4.03), 332 (4.38). MALDI-TOF-MS(m/z): Found = 1150.19 amu; Calc = 1148.34 amu $[M - 2H]^-$. Anal. Calc. for $C_{60}H_{80}CoN_{16}O_4.5H_2O$: C, 58.15%, H, 6.46%, N, 18.09%. Found: C, 59.22 %, H, 6.09%, N, 16.04%.

2.4.2 Synthesis of tris-4-((1,3-bis(dimethylamino)propan-2-yl)oxy)mono carboxyphenoxy phthalocyanato Co (II) (**1-Co-As**), Scheme 3.2(b)

Complex **1-Co-As** was obtained through the mixture of two phthalonitriles; **A** (250 mg, 0.918 mmol) and **B** (80 mg, 0.306 mmol) with cobalt (II) acetate tetrahydrate (114 mg, 0.459 mmol) in 1-pentanol (4 mL) in the presence of DBU (0.5 mL). The mixture was refluxed for 18 h, under

inert conditions. The blue product was cooled to room temperature and centrifuged in DMSO several times. The product was dried under a vacuum and further purified using silica column chromatography with chloroform. The polarity of the eluent system was gradually increased by adding ethyl acetate (up to 5%) yielding, **1-Co-As**.

Yield: 20%. IR (cm^{-1}): 3100 (Ar. C-H), 2928-2860 (C-H), 1659 (C=O), 1520 (C=C), 1413,1385 (C-C), 1254, 1088 (Ar-O-), 864, 655. UV/Vis (DMF), λ_{max} nm (log ε): 660 (4.90), 587 (4.51), and 332 (4.97). MALDI-TOF-MS(m/z): Found = 1140.19; Calc = 1139.48 amu $[M + 1H]^+$. Anal. Calc. for $C_{60}H_{68}CoN_{14}O_6$. $3H_2O$:C, 60.35%, H, 5.70%, N, 16.43%. Found: C, 59.77 %, H, 6.02%, N, 16.53%.

2.4.3 Synthesis of tetra-[4(4-acetlyphenoxy)phthalocyanato] Co(II) (**2-Co**), Scheme 3.3

Complex **2-Co** was synthesised using the same synthetic procedure followed for the synthetic of complex **1-Co** as follows: $Co(OAc)_2.4H_2O$ (0.338 g, 1.36 mmol) and phthalonitrile **C** (0.350 g, 1.33 mmol) were dissolved in 1-pentanol (5 mL). An aliquot amount of DBU was added and the reaction mixture was refluxed for 18 h at 140 °C. The formed product was cooled to room temperature and then precipitated in ethanol via centrifugation. The final product was washed with boiling methanol and purified further using silica-packed column chromatography using $CHCl_3$/THF:9/1 as the eluting solvent mixture.

Yield: 84%. IR (cm^{-1}): 3061 (Ar C-H), 2916-2824 (Aliph. C-H), 1672 (C=O), 1586 (C=C), 1465-1347 (C-C), 1230 (Asymmetric Ar-O-), 1092 (Symmetric Ar-O-), 950, 832. UV/Vis (DMF), λ_{max} nm (log ε): 661 (4.53), 598 (4.14), 329 (4.62). MALDI-TOF-MS(m/z): Found = 1107.13 amu; Calc = 1107.23 amu [M]. Anal. Calc. for $C_{64}H_{40}CoN_8O_8$: C, 69.38%, H, 3.64%, N, 10.11%. Found: C, 69.31 %, H, 3.81%, N, 9.96%.

2.4.4 Synthesis of tris-(4-tert-butylphenoxy)-(5-phenoxylpicolinic acid) phthalocyanato Co(II), (**4-Co-As**), Scheme 3.4

Phthalonitriles **F** (250 mg, 0.943 mmol) and phthalonitrile **E** (742 mg, 2.83 mmol) were added into a round bottom flask containing 8 mL of 1-hexanol and cobalt acetate tetrahydrate (0.350 g, 1.98 mmol), an aliquot of DBU was added dropwise. The reaction mixture was refluxed for approximately 16 h. The product was precipitated using methanol via centrifugation and washed with ethanol. The target product was isolated using silica column chromatography and eluted using tetrahydrofuran/cyclohexane (5:1 v/v).

Yield: 36%. IR (cm^{-1}): 3059 (Ar C-H), 2858-2919 (Aliph. C-H), 1661 (C=O), 1586 (C=C), 1465-1348 (C-C), 1225 (Asymmetric Ar-O-), 1157-1088 (Symmetric Ar-O-), 951, 835. UV/Vis (DMF), λ_{max} nm (log ε): 673 (4.21), 607 (3.78), 336 (4.53). MALDI-TOF-MS(m/z): Calc = 1152.36 amu. Found = 1152.27 amu [M]; Anal. Calc. for $C_{68}H_{55}CoN_9O_6.2H_2O$: C, 68.66 %, H, 4.63%, N, 10.60%. Found: C, 68.86 %, H, 4.56%, N, 10.51%.

2.4.5 Synthesis of tris-4-((3,17,23-tris(4-(tert-butyl)phenoxy)phthalocyanine-9-yl)oxy)benzaldehyde phthalocyaninato Cu(II) (**4-Cu-As**), Scheme 3.5

A mixture of phthalonitriles **E** (315 mg, 1.14 mmol), and **G** (100 mg, 0.38 mmol), and $CuCl_2$ (102.5 mg, 0.76 mmol) were dissolved in 1-pentanol (5 mL) and heated to reflux under inert conditions, an aliquot of DBU (100 µL) was added dropwise. The resulting product was precipitated out in methanol and washed using a water: methanol mixture (1:1) then purified using column silica chromatography using petroleum ether and dichloromethane (DCM) as eluents.

Yield: 45%. IR (cm^{-1}): 3057 (Ar C-H), 2922-2858 (Aliph. C-H), 1698 (C=O), 1588 (C=C), 1464-13323 (C-C), 1224 (Asymmetric Ar C-O), 1155-1044 (Symmetric Ar C-O-), 941, 825. UV/Vis (DMF), λ_{max} nm (log ε): 674 (4.85), 614 (4.64), 345 (5.02). MALDI-TOF-MS m/z calc.: 1139.37, Found: 1138.62 $[M - 1H]^-$. Anal. Calc. for $C_{69}H_{56}CuN_8O_5$: C, 72.7 %, H, 4.95%, N, 9.82%. Found: C, 71.8 %, H, 3.01 %, N, 9.63 %.

2.4.6 Synthesis of tetra-[(4-formylphenoxy)- phthalocyaninato Cu(II) (**5-Cu**), Scheme 3.6

Phthalonitrile **G** (400 mg, 1.53 mmol) and copper chloride (103 mg, 0.763 mmol) were dissolved in DMAE (5 mL), an aliquot of DBU was added dropwise. The reaction mixture was heated to reflux for 18 h under inert conditions. The mixture was allowed to cool to room temperature, and the product was precipitated out in methanol. The product was then washed and centrifuged using a water-methanol mixture (1:1). The resultant blue product (**5-Cu**) was dried under a vacuum.

Yield: 63%. IR (cm^{-1}): 3056 (Ar C-H), 2918-2849 (Aliph. C-H), 1698 (Aldehyde C=O), 1163-1588 (C=C), 1487-1401 (C-C), 1225-1155 (Asymmetric Ar-O-), 1087-1048 (Symmetric Ar-O-), 942, 828. UV/Vis (DMF), λ_{max} nm (log ε): 675 (4.61), 614 (4.23), 343 (4.62). MALDI-TOF-MS m/z calc: 1055.16. Found: 1056.21 $[M + 1H]^+$. Anal. Calc. for $C_{60}H_{32}CuN_8O_8.4H_2O$: C, 63.81 %, H, 3.55%, N, 9.94%. Found: C, 62.7 %, H, 3.07 %, N, 10.50%.

2.4.7 Formation of Schiff base substituted phthalocyanines (**6-Cu** and **7-Cu**), Scheme 3.6

Solutions of pyrazine-2-carboxamide (51.23 mg, 0.416 mmol, for **6-Cu**) in THF (10 mL) and 4-aminopyridine (39.14 mg, 0.416 mmol, for **7-Cu**) in THF (10 mL) were added to complex **5-Cu** (100 mg, 0.0947 mmol, for **6-Cu**), (100 mg, 0.0947 mmol, for **7-Cu**). The reaction mixtures were stirred at room temperature for 48 h under inert conditions. The reactions were monitored using thin-layer chromatography (TLC). The products were washed in methanol, thereafter the solvent was evaporated to a lower volume, the resultant products were obtained by filtration. The final products were washed several times and allowed to dry under vacuum, yielding to complexes **6-Cu** and **7-Cu**.

6-Cu: tetra-(oxy))tetra(benzene-4,1-diyl))tetra(methanylylidene))tetra(pyrazine-2-carboxamide) phthalocyaninato Cu(II),

Yield: 42%. IR (cm^{-1}): 3055 (Ar C-H), 2922-2852 (Aliph. C-H), 1691 (C=O), 1583 (C=C), 1462-1325 (C-C), 1224 (Asymmetric Ar-O-), 1165 (C-N), 1045 (Symmetric Ar-O-), 944, 830. UV/Vis (DMF), λ_{max} nm (log ε): 674 (4.81), 614 (3.78), 343 (4.57). MALDI-TOF-MS m/z calc.: 1475.29 amu. Found: 1471.83 amu $[M - 4H]^-$. Anal. Calc. for $C_{80}H_{44}CuN_{20}O_8.2H_2O$: C, 63.51%, H,3.20%, N, 18.74%. Found: C, 63.4 %, H, 2.24 %, N, 17.40 %.

7-Cu: tetra-(oxy))tetra(benzene-4,1-diyl))tetra(N-(pyridin-4-yl)methanimine) phthalocyaninato Cu(II):

Yield: 38%. IR (cm^{-1}): 3079 (Ar C-H), 2917-2854 (Aliph. C-H), 1646 (C=N), 1578 (C=C), 1496-1333 (C-C), 1230 (Asymmetric Ar-O), 1156 (C-N), 1051 (Symmetric Ar-O-), 982, 953. UV/Vis (DMF), λ_{max} nm (log ε): 674 (4.85), 614 (4.64), 345 (5.02). MALDI-TOF-MS m/z calc.: 1359.33

amu, Found: 1362.04 amu $[M + 3H]^+$. Anal. Calc. for $C_{81}H_{50}CuN_{16}O_4$: $6H_2O$: 65.41% C, 4.12% H, 15.30% N; Found: C, 64.62 %, H, 4.52 %, N, 14.01 %.

2.4.8 Synthesis of tetra-[4 –(3-(phenyl)-prop-2-en-1-one) phenoxy] phthalocyaninato complexes (**8-Cu**, **8-Mn** and **8-Ni**), Scheme 3.7

8-Co is known and was synthesised according to literature [27]. Phthalonitrile **H** (0.1 g, 0.285 mmol) and the respective metal salts: copper chloride (57.7 mg, 0.428 mmol), manganese chloride (53.9 mg, 0.428 mmol) and nickel acetate (75.3 mg, 0.426 mmol) were dissolved in 5 mL pentanol. Thereafter, aliquots of DBU (100 µL) were added dropwise to the respective reaction mixtures, followed by refluxing for 18 h. The resultant products were washed in methanol and dried in a vacuum overnight.

8-Cu: Tetra-[4 –(3-(phenyl)-prop-2-en-1-one) phenoxy] phthalocyaninato Cu(II):

Yield: 63%. IR (cm^{-1}): 3065 (Ar. C-H), 2924, 2865 (Aliph. C-H), 1651 (C=O), 1589 (C=C), 1466, 1369 (C-C), 1221 (Asym Ar. C-O),1158 (Sym Ar. C-O), 982, 837. UV-Vis (DMF), λ_{max} nm (log ε): 675 (4.63), 609 (4.17), 316 (4.62). MALDI-TOF-MS (m/z): Calc = 1464.36 amu, Found = 1466.61 $[M +2H]^+$ amu. Anal. Calc for $C_{92}H_{56}CuN_8O_8.2H_2O$: C, 73.62 %, H, 4.00 %, N, 7.47 % Found: C, 73.20 %, H, 4.27 %, N, 7.21.

8-Mn: Tetra-[4 –(3-(phenyl)-prop-2-en-1-one) phenoxy] phthalocyaninato Mn(II)Cl:

Yield: 45%. IR (cm^{-1}): 3064 (Ar. C-H), 2926, 2861 (Aliph. C-H), 1655 (C=O), 1590 (C=C), 1486, 1397 (C-C), 1229 (Asym Ar. C-O),1161 (Sym Ar. C-O), 951, 883. UV-Vis (DMF), λ_{max} nm (log ε): 720 (4.83), 642 (4.54), 312 (4.67), MALDI-TOF-MS (m/z): Calc = 1490.33 amu, Found = 1486 amu $[M -4H]^-$. Anal. Calc for $C_{92}H_{56}ClMnN_8O_8.3H_2O$: C, 71.50 %, H, 4.01 %, N, 7.25% Found: C, 71.30 %, H, 4.12 %, N, 7.06.

8-Ni: Tetra-[4 –(3-(phenyl)-prop-2-en-1-one) phenoxy] phthalocyaninato Ni(II):

Yield: 52%. IR (cm^{-1}): 30264 (Ar. C-H), 2963, 2870 (Aliph. C-H), 1652 (C=O), 1591 (C=C), 1462, 1409 (C-C), 1221 (Asym Ar. C-O),1159 (Sym Ar. C-O), 958, 882. UV-Vis (DMF), λ_{max} nm (log ε): 668 (4.51), 613 (4.48), 313 (4.72). MALDI-TOF-MS (m/z): Calc = 1460.20 amu, Found = 1459.09 amu $[M - 1H]^-$. Anal. Calc for $C_{92}H_{56}NiN_8O_8.2H_2O$: C, 73.86 %, H, 4.01 %, N, 7.47 %, Found: C, 73.40 %, H, 4.50 %, N, 7.41 %.

2.4.9 Synthesis of tetra[(4-formylphenoxy)- phthalocyaninato Mn(III)Cl (**9-Mn**)

Complex **9-Mn** is known [28], the method described by Sen *et* al involved the deprotonation of a previously synthesised acetal MnPc complex [28]. Herein, **9-Mn** was synthesised via cyclotetramerisation, following the same procedure used for the synthesis of **5-Cu** as follows: A reaction mixture of phthalonitrile **G** (300 mg, 1.2 mmol) and manganese chloride (38 mg, 0.3 mmol) was heated to reflux in DMAE (3 mL). Thereafter, an aliquot of DBU was added dropwise and the reaction was refluxed overnight. The product was precipitated out in a 1:1 (v/v) mixture of water: ethanol and washed several times in pure ethanol and thereafter dried under vacuum. The resultant brown/red product was purified using silica column chromatography using chloroform: methanol (9:1) as an eluant.

Yield: 65%. FT-IR ν max/cm^{-1}: 3295 (OH), 3080 (Ar. C-H), 2925, 2855 (Aliph. C-H), 1731 (C=O), 1589 (C=C), 1500, 1421, 1360 (C-C), 1224 (Asym Ar. C-O), 1107, 1089 (Sym Ar. C-O), 944, 849, 578. UV-Vis (DMF), λ_{max} nm (log ε): 733 (4.85), 657 (4.12), 350 (3.53). MALDI-TOF-MS (m/z): Calc = 1083.14 amu, Found = 1085 amu $[M +2]^+$. Anal. Calc for $C_{60}H_{32}ClMnN_8O_8$: C, 66.5 %, H, 2.98 %, N, 10.34 % Found: C, 64.9 %, H, 3.24 %, N, 9.62 %

2.4.10 Formation of Schiff base substituted phthalocyanines (**10-Mn** and **11-Mn**), Scheme 3.8

Complex 9-Mn (70 mg, 0.0668 mmol) was added to a reaction vessel containing primary amines; thiophene-2-ylmethenamine (0.0302 mL, 0.294 mmol) or 3-(pyrrolidine-1-yl)propan-1-amine (0.294 mmol, 0.0372 mL). The mixtures were dissolved in ethanol (10 mL) and refluxed overnight under inert conditions. The reaction mixtures were then cooled to room temperature, and the bulk of the solvent evaporated using a rotary evaporator. The resultant products were precipitated in methanol, washed several times in methanol via centrifugation, and dried in a vacuum, yielding to **10-Mn** and **11-Mn** from primary amines thiophene-2-ylmethanamine and 3-(pyrrolidine-1-yl)propan-1-amine, respectively.

10-Mn: 2,9,16,23-tetra-4-(4-thio-thiophene-2-ylmethanamino)-phthalocyaninato Mn(III)Cl

Yield: 56%. IR (cm^{-1}): 3330 (OH), 3082 (Ar. C-H), 2930, 2865 (Aliph. C-H), 1590 (C=C), 1508, 1364 (C-C), 1127 (Asym Ar. C-O), 1159-1098 (Sym Ar. C-O), 945, 830, 703. UV-Vis (DMF), λ_{max} nm (log ε): 738 (4.76), 658 (3.59), 343 (4.20). MALDI-TOF-MS (m/z): Calc = 1462.22 amu, Found = 1464.03 amu $[M + 2H]^+$. Anal. Calc for $C_{80}H_{52}ClMnN_{12}O_4S_4$. C, 66.63 %, H, 3.58 %, N, 11.48 % Found: C, 65.43%, H, 3.21%, N, 12.03%

11-Mn: 2,9,16,23-tetra-4-(3-(pyrrolidine-1-yl)propan-1-amino)phthalocyaninato Mn(III)Cl

Yield: 63%. IR (cm^{-1}): 3297 (OH), 3066 (Ar. C-H), 2931, 2868 (Aliph. C-H), 1581 (C=C), 1502-1360 (C-C), 1222 (Asym Ar. C-O), 1159-1095 (Sym Ar. C-O), 946, 828, 492. UV-Vis (DMF), λ_{max} nm (log ε): 733 (4.85), 657 (4.34), 360 (4.17). MALDI-TOF-MS (m/z): Calc = 1522.62 amu, Found = 1522.35 amu [M]. Anal. Calc for $C_{88}H_{88}MnClN_{16}O_4$. $4H_2O$: C, 66.22 %, H, 6.06 %, N, 14.04 % Found: C, 66.59 %, H, 5.19 %, N, 16.11%.

2.5 Synthesis of Nanomaterials

2.5.1 Synthesis of GQDs and NGQDs (Scheme 3.9)

The Synthesis of both GQDs and NGQDs has been reported [146].

Briefly, graphene quantum dots were prepared by dissolving citric acid (4.2 g, 1 mmol) and sodium hydroxide (2.4 g, 3 mmol) in water (100 mL). After constant stirring the mixture was transferred into a Teflon lined stainless autoclave. The resultant product was re-dispersed into water and was dialysed for 48 h using a dialysis membrane (MW 1.5 kDa) to remove excess salts.

The nitrogen-dopped quantum dots were prepared using the same procedure as the GQDs. However, urea (3.6 g, 3 mmol) was used (instead of NaOH) as a source of nitrogen.

2.5.2 Synthesis of $NiWO_4$ and Bi_2WO_6 (Scheme 3.10)

The synthesis of $NiWO_4$ nanoparticles has been reported [148].

Briefly, $Ni(OAc)_2$ (1.2 g, 4.82 mmol) and thioglycolic acid (TGA, 0.62 mL, 0.0125 M) were dissolved in purified water (200 mL). The pH was adjusted to 11 using NaOH under constant stirring and deaerated under inert conditions for 30 min. Thereafter, $Na_2WO_4{\cdot}2H_2O$ (0.64 g, 1.94 mmol) was added to the reaction mixture. The reaction mixture was refluxed at 100 °C for 1 h. GSH (50 mL, 0.0250 M) was added to the reaction mixture to facilitate ligand exchange between TGA and GSH. The mixture was heated for approximately 20 min and then cooled to room temperature and precipitated out with ethyl alcohol and purified using acetone. The resultant product ($NiWO_4$) was dried under vacuum and stored in the dark.

Bi_2WO_6 nanoparticles were prepared using the same procedure. However, bismuth oxide (1.8 g, 3.86 mmol) was used in place of $Ni(OAc)_2$.

2.6 Linking MPcs to nanomaterials

Throughout this work, graphene-based nanomaterials were conjugated to MPc complexes via non-covalent bonding. π-π Staking was achieved by taking advantage of the rich π-electrons that both MPcs and graphene-based materials possess. The procedure used has been reported, minor modifications were made for this work [156,157]. The metallic nanoparticles were conjugated via covalent linkage, forming amide bonds.

2.6.1 π-π Stacking

2.6.1.1 Linking **1-Co** and **1-Co-As** with NGQDS, Scheme 3.11

Complexes **1-Co** (10 mg, 8.71×10^{-3} mmol) and **1-Co-As** (8.77×10^{-3} mmol) were dissolved in 2 mL THF. NGQDs (5 mg) in water (1 mL) were added to the reaction vessel and sonicated at room temperature for 24 h. After 24 h the mixtures were stirred at room temperature for 96 h. The formed hybrid materials (**1-CoπNGQDs** and **1-Co-AsπNGQDs**) were precipitated and washed in ethanol, then dried under vacuum.

2.6.1.2 Linking **2-Co** and **3-Co** with GQDs and SWCNTs

Complexes **2-Co** and **3-Co** (20 mg, 1.81×10^{-1} mmol and 1.43×10^{-1} mmol, respectively) were dissolved (separately) in DMF (2 mL). GQDs (10 mg) in water (1 mL) were added to each complex's reaction vessel. The mixtures were sonicated at room temperature for 24 h, and then stirred at room temperature for 96 h. The products were precipitated and washed in ethanol, then dried under vacuum. The formed hybrids are represented as **2-CoπGQDs** and **3-CoπGQDs**.

The same amounts of complex **2-Co** and **3-Co** were employed for their linkage to SWCNTs using 10 mg (in 1 mL DMSO) of the latter, followed by sonication for 24 h and stirring at 70˚C for 96 h. The formed hybrid materials were purified as explained above for GQDs conjugates. The conjugates are represented as **2-CoπSWCNTs** and **3-CoπSWCNTs**.

2.6.1.3 Linking **4-Co-As** with GQDs, NGQDs, SWCNTs

A stock solution of **4-Co-As** (30 mg, 2.60 $\times 10^{-2}$ mmol) was prepared in DMF (6 mL). While in parallel vessels, the 5 mg of the respective nanomaterials were dissolved in a 1 mL water (for NGQDs and GQDs) and DMF (for SWCNTs), followed by sonication for 24 h at room temperature. Then, a **4-Co-As** solution (2 mL) was added to each reaction vessel containing the nanomaterial and the mixtures were stirred at room temperature for approximately 96 h to yield π-stacked hybridised materials. The hybrids were washed in a water-ethanol mixture (50:50 v/v), and precipitated in ethanol, and dried in an inert vacuum. These conjugates were labelled **4-Co-AsπGQDs**, **4-Co-AsπNGQDs** and **4-Co-AsπSWCNTs**.

2.6.2 Covalent Linkage

2.6.2.1 Conjugation of **4-Co-As** to Bi_2WO_6 and $NiWO_4$, Scheme 3.12

The conjugates were prepared by dissolving **4-Co-As** (30 mg, 0.026 mmol) and DCC (45 mg, 0.218 mmol) in DMF (3 mL). The reaction mixture was stirred at room temperature under nitrogen flow for 48 h. Thereafter, Bi_2WO_6 (or $NiWO_4$) (50 mg) were added, and the mixtures were stirred for a further 48 h. The resultant products were precipitated out in methanol in the centrifuge and purified with ethanol. The conjugates formed are labelled as **4-Co-As@Bi_2WO_6** and **4-Co-As@$NiWO_4$**.

2.7 Electrode Modification

Throughout this work, the glassy carbon electrode was employed as the working electrode of choice. The glassy carbon electrode surfaces were polished on a Buehler-felt polishing pad in an alumina nanopowder (<10 µm) slurry (with Elga Type II purified water). The electrodes were rinsed several times using the purified water.

The electrode surfaces were modified using the conventional drop-casting/drop-drying method [35], where, an aliquot from a solution of 1 mg of the electrocatalyst (in 1 mL DMF) were deposited onto the electrode surface and later dried in an oven at 60°C overnight before use. Figure 2.3 is an illustration of the drop-casting mechanism.

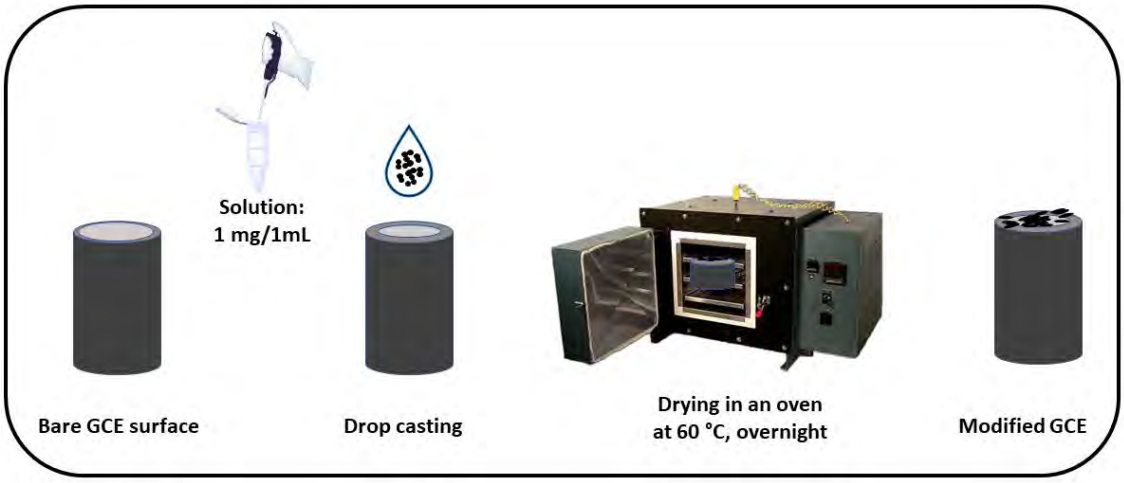

Figure 2.3: Drop casting/drying procedure

RESULTS AND DISCUSSION

PUBLICATIONS

The publications listed below are summarised under the result and discussion in Chapters 3 to 6

1. **Nobuhle Ndebele**, Pinar Sen, Tebello Nyokong, Electrochemical detection of dopamine using phthalocyanine-nitrogen-doped graphene quantum dot conjugate, J. Electroanal. Chem. 886 (2021) 115111.
2. **Nobuhle Ndebele**, Sithi Mgidlana, Tebello Nyokong Electrocatalytic activity of cobalt phthalocyanines revisited: Effect of the number of oxygen atoms and conjugation to carbon nanomaterials, Electrocatalysis, 12 (2021) 499-515.
3. **Nobuhle Ndebele**, Sithi Mgidlana, Tebello Nyokong, Electrochemical Detection of Nitrite Using Cobalt Phthalocyanine Conjugated to Metal Tungstate Nanoparticles, Electroanalysis 34 (2022) 1348-1362.
4. **Nobuhle Ndebele**, Pinar Sen, Tebello Nyokong, Electrocatalytic activity of Schiff base containing copper phthalocyanines towards the detection of catechol: Effect of heteroatoms and asymmetry, Polyhedron 210 (2021) 115518.
5. **Nobuhle Ndebele** and Tebello Nyokong, Electrocatalytic behaviour of Chalcone Substituted Co, Cu, Mn and Ni Phthalocyanines towards the detection of nitrite, J. Electranal. Chem. 926 (2022) 116951.
6. **Nobuhle Ndebele** and Tebello Nyokong, The Electrochemical Detection of Nitrite Using Manganese Schiff Base Phthalocyanine Complexes, Electrocatalysis 13 (2022) 663-674.

7. **Nobuhle Ndebele** and Tebello Nyokong, The Use of Carbon-Based Nanomaterials Conjugated to Cobalt Phthalocyanine Complex in The Electrochemical Detection of Nitrite, Diam. Relat. Mater. (2022) Accepted with revisions.

Side Publications:

Bunin A. Dmitry, **Nobuhle Ndebele**, Alexander G. Martynov, John Mack, Yulia G. Gorbunova, and Tebello Nyokong, Low-Symmetry Phthalocyanines Bearing Carboxy-Groups: Synthesis, Spectroscopic and Quantum-Chemical Characterization, Molecules 27 (2022).

CHAPTER 3

SYNTHESIS AND CHARACTERISATION

Preface: This chapter provides the complete characterisation of the phthalocyanine complexes, nanomaterials and the MPc-nanomaterial hybrid/conjugate materials studied in this dissertation.

3. SYNTHESIS AND CHARACTERISATION

3.1 Phthalonitrile Synthesis

Phthalonitriles **A**-**E**, **G,** and **H** are known and were synthesised according to literature [25,150–155]. Phthalonitrile **F** was synthesised herein for the first time by reacting 4-nitrophthalonitrile and 5-hydroxypicolinic acid using dry dimethylformamide (DMF) as a solvent in the presence of potassium carbonate (K_2CO_3) at room temperature. Scheme 3.1 shows the synthetic route followed during the synthesis of phthalonitrile **F**. An overall yield of 68% was obtained following the purification of the phthalonitrile and hot ethanol. The synthesis of the phthalonitrile was confirmed using FT-IR (Figure 3.1).

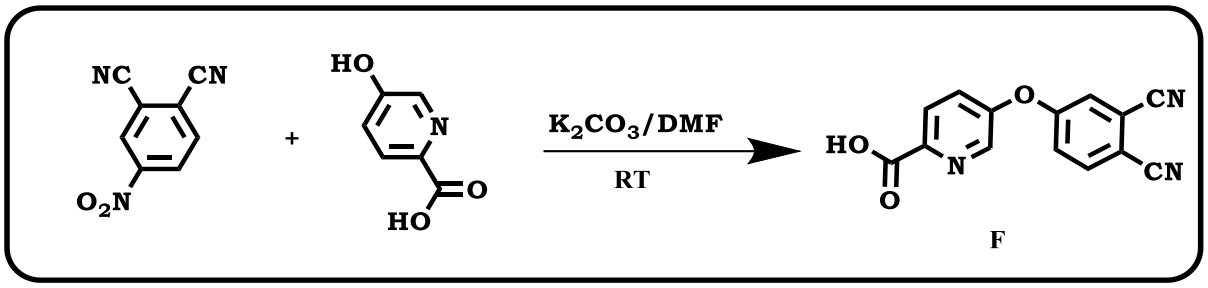

Scheme 3.1: Synthesis of phthalonitrile **F**

Figure 3.1 shows the FT-IR spectra obtained for phthalonitriles **E**, **F** and the MPc complex **4-Co-As**. The distinctive cyano (C≡N) stretch is observed from the spectra at approximately 2227 cm^{-1} for the phthalonitriles. The occurrence of this stretch is indicative of the successful synthesis of **F**. This stretch will be expected to disappear upon cyclisation to form MPc complexes.

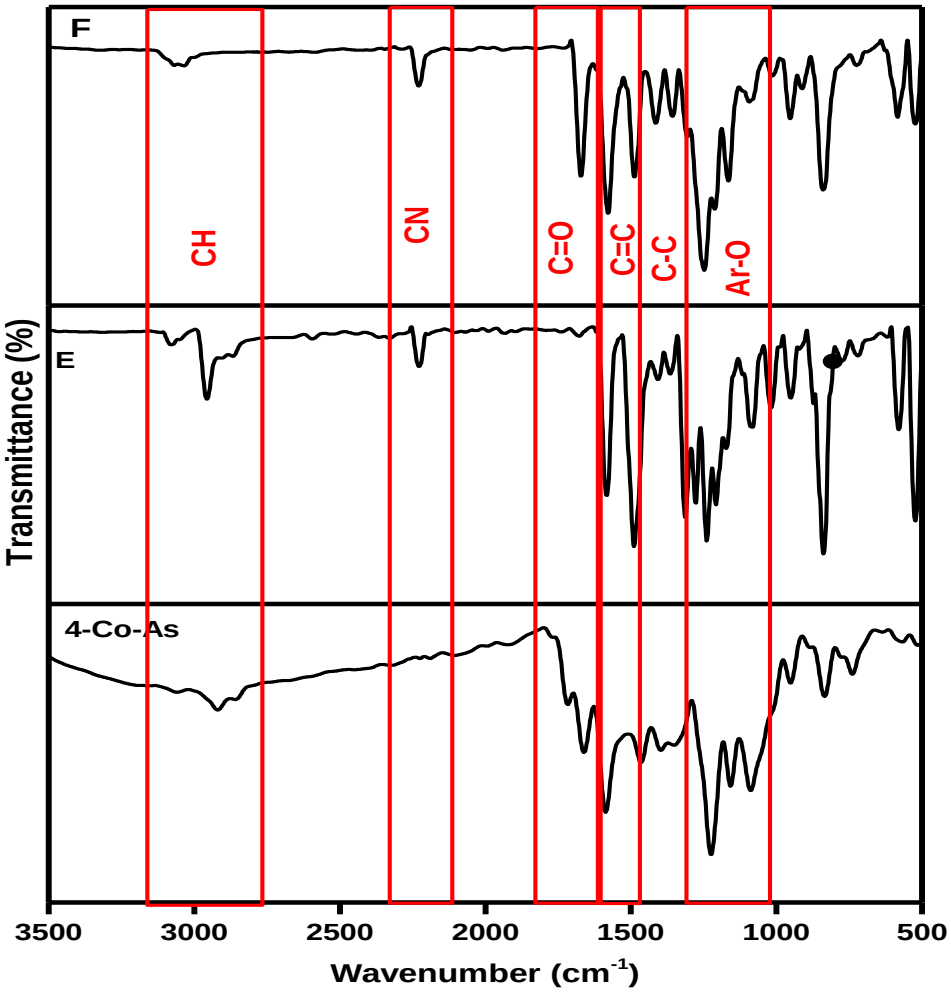

Figure 3.1: FT-IR spectra of phthalonitriles **E**, **F** and MPc complex **4-Co-As**

3.2 Phthalocyanine Synthesis and Characterisation

The phthalocyanine complexes studied in this work were synthesised using the statistical condensation method. MPcs **3-Co**, **4-Co**, and **8-Co** are known, they have been previously synthesised, characterised and published [25–27]. Although **9-Mn** is known and has been published [28], it was synthesised differently in this work.

3.2.1 Synthesis and Characterisation of **1-Co** and **1-Co-As**

Scheme 3.2 shows the synthetic route followed during the synthesis of the symmetric (**1-Co**) and asymmetric (**1-Co-As**) complexes.

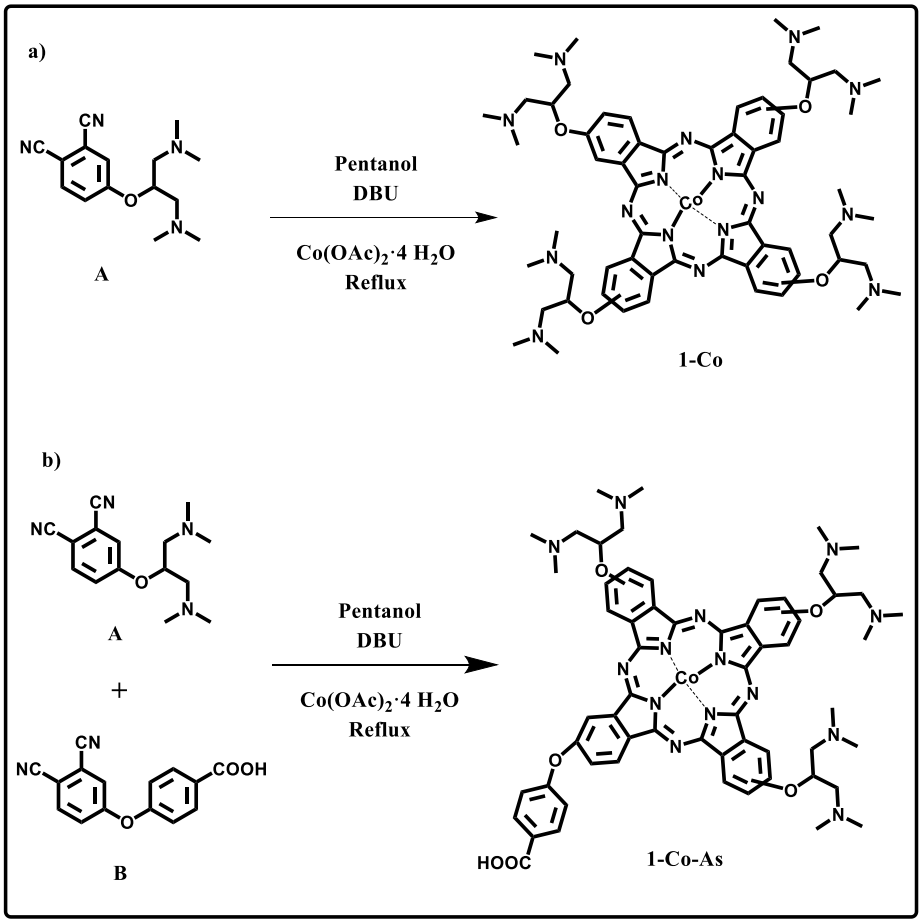

Scheme 3.2: Synthesis of **1-Co** and **1-Co-As**

The synthesis of **1-Co** involves the cyclotetramerisation of known phthalonitrile **A** with cobalt acetate. While the synthesis of asymmetric **1-Co-As**, on the other hand, required the use of two phthalonitriles, **A** and **B** (3:2). Complexes **1-Co** and **1-Co-As** were synthesised under the same conditions in 1-pentanol with an aliquot of DBU added dropwise, followed by refluxing under inert conditions for approximately 18 h. Complex **1-Co** was obtained as a pure compound, which is typical of simple symmetric MPcs. While **1-Co-As** was isolated and purified via silica column chromatography using chloroform as the eluent solvent. The respective yields obtained were 45% and 20% for the symmetric and asymmetric MPc complexes, respectively. It is typical of the asymmetric MPc complexes to be obtained in relatively smaller yields than the symmetric MPc complexes, this is attributed to the isomers formed and the extra purification steps required. The formation of these complexes was further characterised by mass spectra, FTIR, elemental analysis and UV-Vis absorption.

The experimental masses obtained for **1-Co** and **1-Co-As** were 1148.34 amu and 1139.48 amu. These masses agreed with the expected theoretical masses (1150.19 amu and 1140.19 amu), confirming the successful synthesis of both **1-Co** and **1-Co-As**. The elemental analysis data obtained experimentally was also in agreement with the theoretical data, however, with the addition of $5H_2O$ and $3H_2O$ for the two complexes, respectively. MPcs are often isolated as hydrates [158].

3.2.2 Synthesis and characterisation of **2-Co**

Complex **2-Co** was obtained via the cyclisation of phthalonitrile **C** (Scheme 3.3). Cyclotetramerisation was achieved in the presence of 1-pentanol, DBU and cobalt acetate. The complex was purified using silica column chromatography, obtaining a total yield of 84%.

The experimental mass values obtained via MALDI TOF mass spectroscopy were 1107.13 amu for **2-Co**, the mass was in agreement with the theoretically calculated values. The experimental elemental analysis results were in agreement with the theoretical values. Indicating the successful synthesis of the complex.

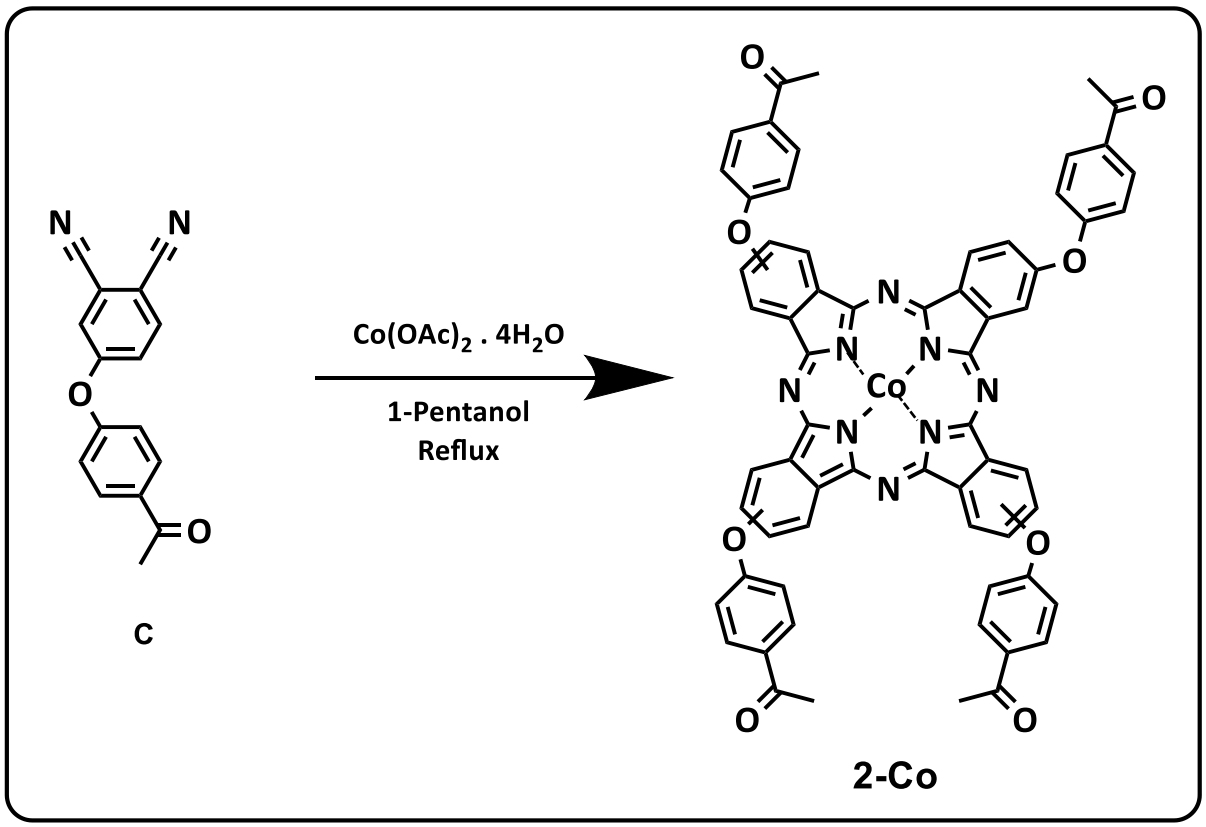

Scheme 3.3: Synthesis of Complex **2-Co** from phthalonitrile **C**

3.2.3 Synthesis and Characterisation of **4-Co-As**

The asymmetrical phthalocyanine complex (**4-Co-As**) was obtained using the statistical condensation method, where phthalonitriles **E** and **F** were reacted together using the 3:1 ratio (Scheme 3.4). The phthalonitriles underwent cyclotetramerisation in hexanol using cobalt acetate as the metal salt, and aliquots of DBU (100 µL) were added drop wise. The target complex was isolated using silica column chromatography and eluted using tetrahydrofuran/cyclohexane, obtaining a yield of 36%. The complex was characterised by FT-IR, elemental analysis, mass spectra and UV-vis. The experimental mass and elemental analysis data obtained were in agreement with the expected values, confirming the successful synthesis of **4-Co-As**.

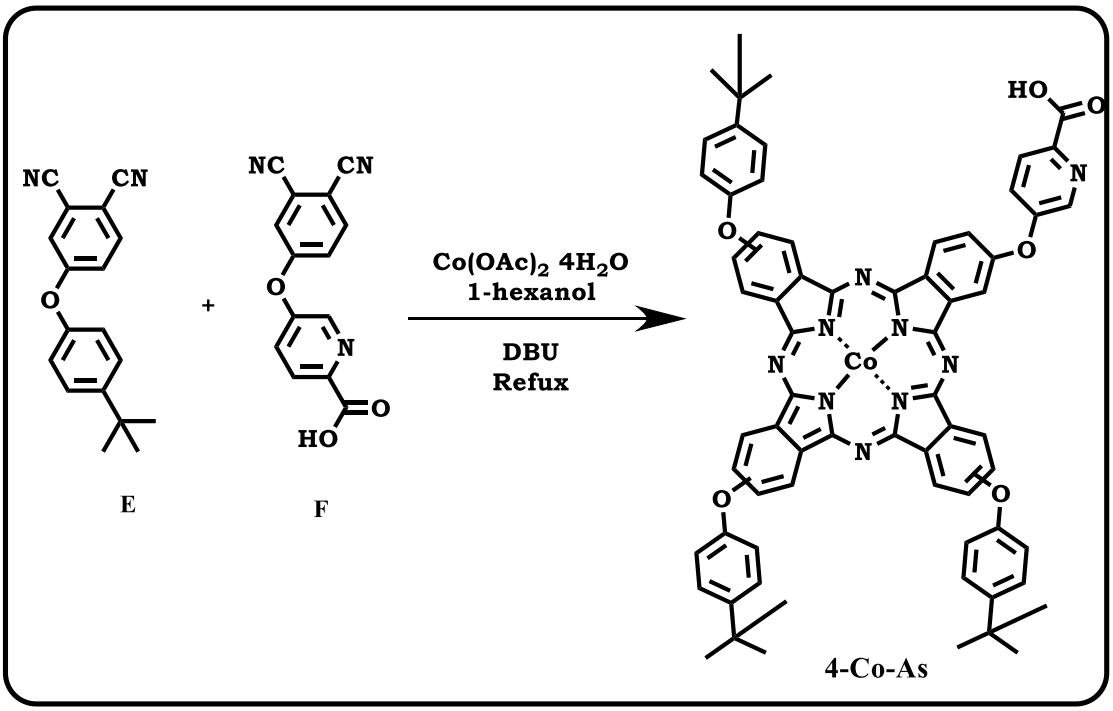

Scheme 3.4: Synthesis of **4-Co-As** from phthalonitriles **E** and **F**

From Figure 3.1, the cyano (C≡N) stretches were observed at approximately 2228 cm^{-1} and 2227 cm^{-1} for phthalonitriles **E** and **F**, respectively. The observed stretched disappeared upon the cyclisation of the phthalonitriles to form **4-Co-As**. Indicating that **4-Co-As** was successfully synthesised as there were no residual phthalonitriles in the sample. It can also be observed that **E** does not have a carbonyl stretch as it is a *tert*-butyl phthalonitrile. However, the carbonyl stretch is observed at 1671 and 1661 cm^{-1} for **F** and **4-Co-As,** respectively. The stretch is attributed to the carbonyl stretch from the picolinic acid.

3.2.4 Synthesis and Characterisation of **4-Cu-As**, **5-Cu**, **6-Cu** and **7-Cu**

The synthesis of asymmetric complex **4-Cu-As** involves the cyclisation of precursors; **E** and **G** (Scheme 3.5) at a ratio of 1:3 using 1-pentanol as the solvent of choice in the presence of copper chloride with constant stirring at reflux temperature. The target product was isolated via silica column chromatography using petroleum ether and dichloromethane as the eluent solvents.

Scheme 3.6 illustrates the synthetic route followed during the synthesis of copper metallated phthalocyanine complexes **5-Cu**, **6-Cu** and **7-Cu**. The symmetric complex **5-Cu** was synthesised through the cyclotetramerisation of phthalonitrile **G** in DMAE for approximately 18 h. The complex was used as a precursor in the synthesis of Schiff base MPc complexes **6-Cu** and **7-Cu**. These two complexes were synthesised via the condensation of **5-Cu** with pyrazine-2-carboxamide (**6-Cu**) and 4-aminopyridine (**7-Cu**) in THF. The synthesis of these complexes was confirmed by UV-Vis absorption, elemental analysis and mass spectroscopy.

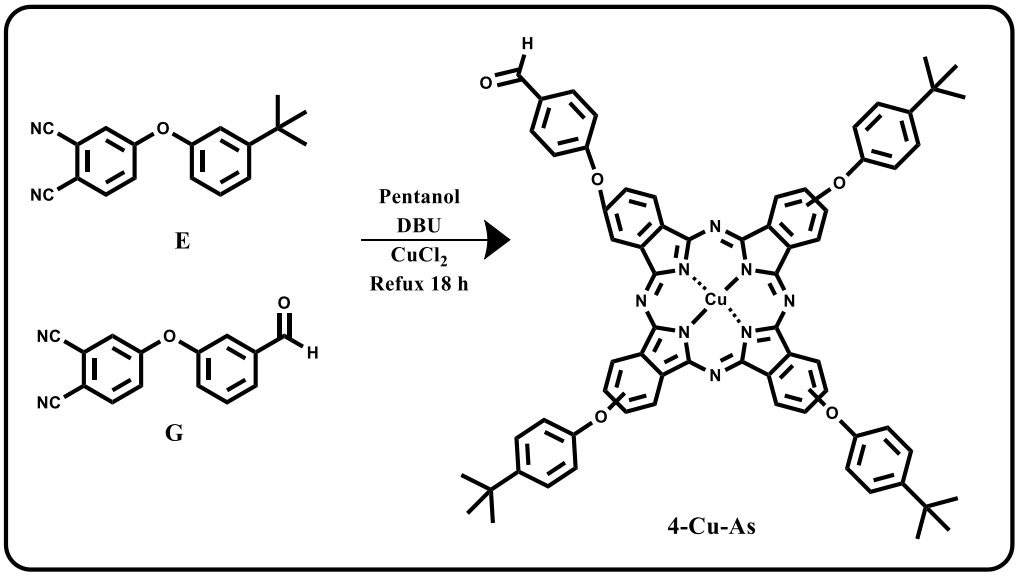

Scheme 3.5: Synthesis of **4-Cu-As**

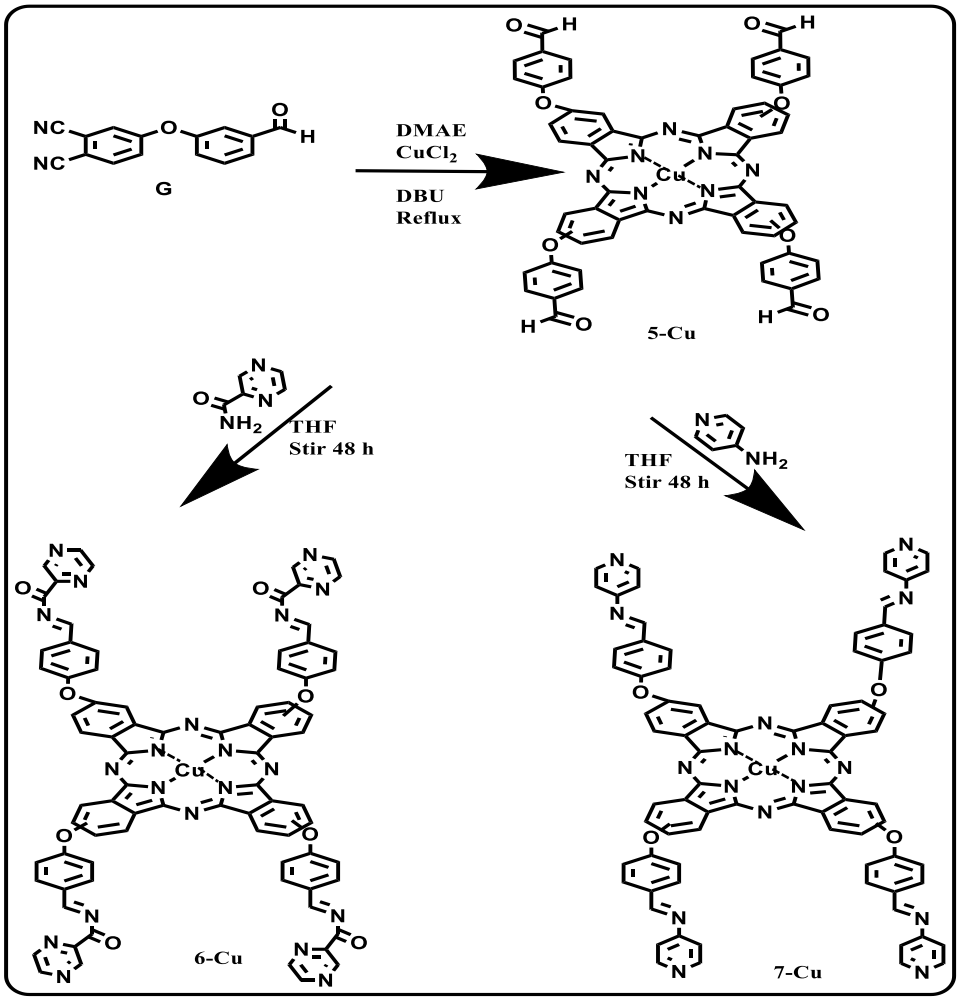

Scheme 3.6: Synthesis of **5-Cu**, **6-Cu** and **7-Cu**

Mass spectroscopy was used to confirm the mass of the synthesised copper phthalocyanine complexes. The mass peaks obtained were at m/z 1138.62, 1056.21, 1471.83, 1362.04 amu for complexes **4-Cu-As**, **5-Cu**, **6-Cu** and **7-Cu**, respectively. These experimental masses were in agreement with the theoretically calculated values.

3.2.5 Synthesis and Characterisation of **8-Co**, **8-Cu**, **8-Mn** and **8-Ni**

The synthesised chalcone derivative phthalonitrile **H** underwent cyclotetramerisation with different metal salts;, copper chloride, manganese chloride and nickel acetate (individually) in 1-pentanol under reflux for approximately 18 h, yielding three symmetrical phthalocyanine complexes namely, **8-Cu**, **8-Mn** and **8-Ni** (Scheme 3.7). **8-Co** is known [27], while the other complexes are reported herein for the first time.

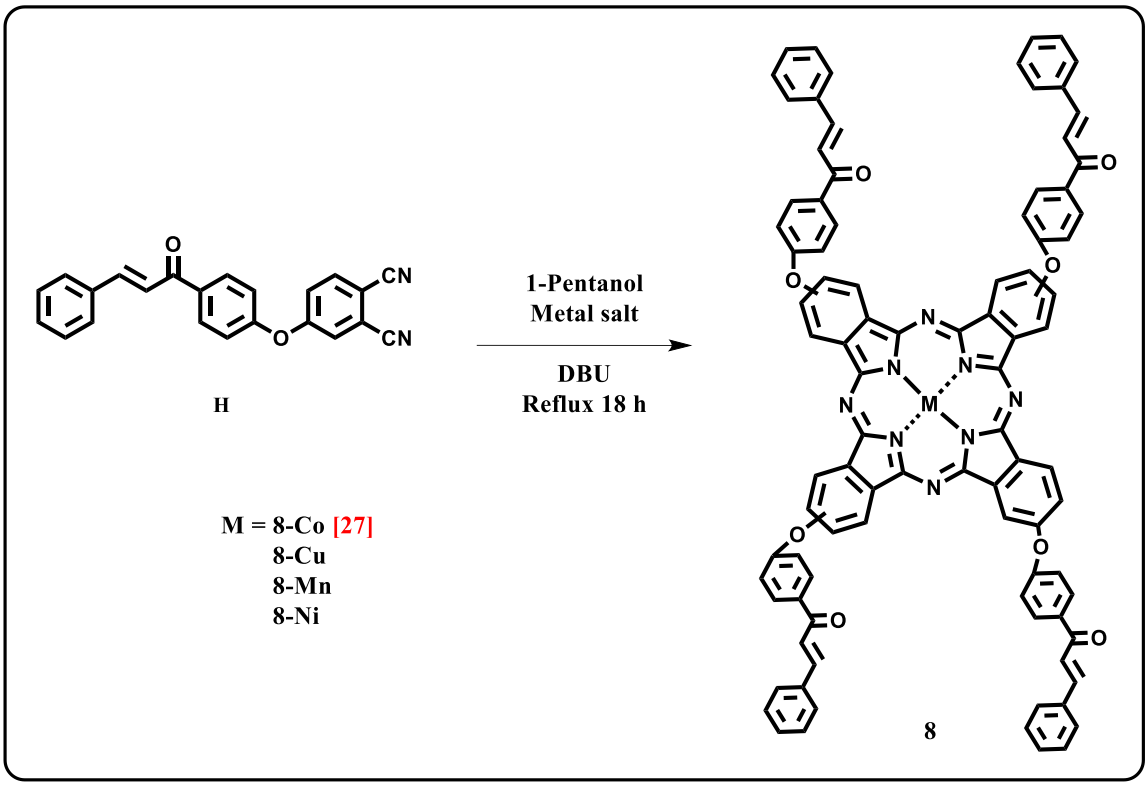

Scheme 3.7: Synthesis of **8-Co**, **8-Cu**, **8-Mn** and **8-Ni**

The yields obtained were above 45%. The elemental analysis results were in agreement with observations that some Pcs were isolated as hydrates [158]. The theoretical masses were in agreement with those obtained experimentally.

An interesting observation made after the synthesis of these compounds was the different colour compounds obtained. The **8-Co** and the **8-Ni** complexes were blue, the **8-Cu** was green, and the **8-Mn** was “red-brown". Since the same phthalonitrile (substituent) was used for the synthesis of these complexes, all spectral changes (and colour) observed are due to the central metal.

3.2.6 Synthesis and Characterisation of **9-Mn**, **10-Mn** and **11-Mn**

Complex **9-Mn** is known [28]. However, it was not synthesised following the synthetic route followed by Sen *et al* as the procedure followed there involves the deprotonation of an acetyl phthalocyanine complex to form the aldehyde complex [28]. Herein **9-Mn** was synthesised following the same synthetic procedure used in the synthesis of **5-Cu** (and other MPc complexes synthesised herein). Which involved the cyclotetramerisation of a phthalonitrile (**G**) in the presence of a metal salt (manganese chloride). Schiff base complexes **10-Mn** and **11-Mn** were formed according to Scheme 3.8. Where the active carbonyl from **9-Mn** was reacted with the primary amines; thiophene-2-ylmethanamine (**10-Mn**) and 3-(pyrrolidine-1-yl)propan-1-amine (**11-Mn**). The condensation reactions involving the primary amine and complex **9-Mn** were carried out in ethanol (Scheme 3.8).

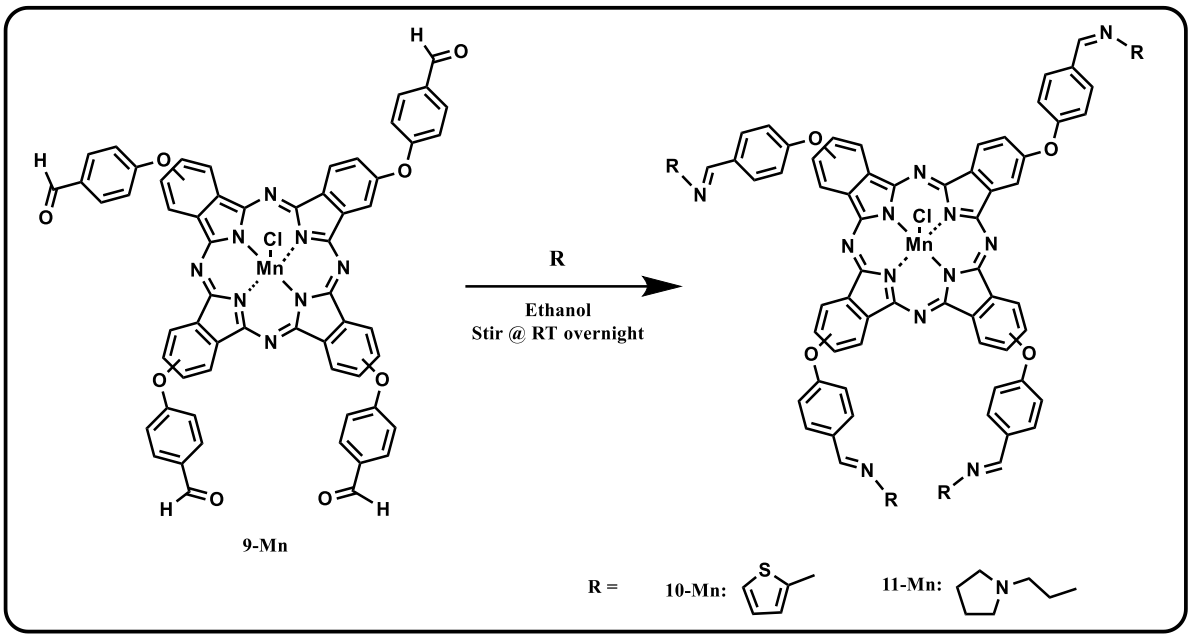

Scheme 3.8: Synthesis of **10-Mn** and **11-Mn** from **9-Mn**

3.3 UV-Vis Absorption Spectra

The synthesised MPc complexes are listed in Table 3.1 (for ease of reference). Phthalocyanines have two characteristic absorption bands, namely: the Q and B bands (Table 3.2). Figures 3.2 – 3.5 show the UV-Vis absorption spectra obtained in DMF for all the MPc complexes. In these figures, both characteristic bands were observed.

Figure 3.2 illustrates the UV-Vis absorption spectra obtained for the cobalt phthalocyanine complexes synthesised and studied in this work (except for **8-Co**, represented in Figure 3.4). Figure 3.2(a) is an illustration of the normalised UV-Vis absorption spectra obtained for **1-Co** and **1-Co-As**. From the figure, the two prominent MPc characteristic absorption bands were observed. The Q-bands were observed at 676 and 660 nm for **1-Co** and **1-Co-As**, respectively, while the B-bands are observed at 332 nm for both complexes (Table 3.2). Complex **2-Co** exhibited a relatively blue shift absorption maxima compared to **3-Co**. The blue shift is attributed to the reduction in dimethylamino groups. Nitrogen-containing groups are known to result in red shifting in MPc complexes [159].

Figure 3.2(b) shows the UV-Vis absorption spectra obtained for symmetric cobalt phthalocyanine complexes, **2-Co** and **3-Co**. The Q and B characteristic MPc absorption bands were observed at 661 nm and 666 nm for the two complexes, respectively (Table 3.2). **3-Co** appeared to be relatively red shifted, this could be attributed to the notable presence of more oxygen atoms on its structure. Figure 3.2(c) illustrates the UV-vis absorption spectra obtained for **4-Co** and **4-Co-As**. **4-Co** displayed a Q-band at 666 nm, while **4-Co-As**'s Q-band was observed at 673 nm. Herein, the decrease in symmetry from **4-Co** to **4-Co-As** resulted in a red shifting and broadening of the Q-band. The red shift is due the addition of nitrogen containing group when reducing symmetry in **4-Co-As** as stated above.

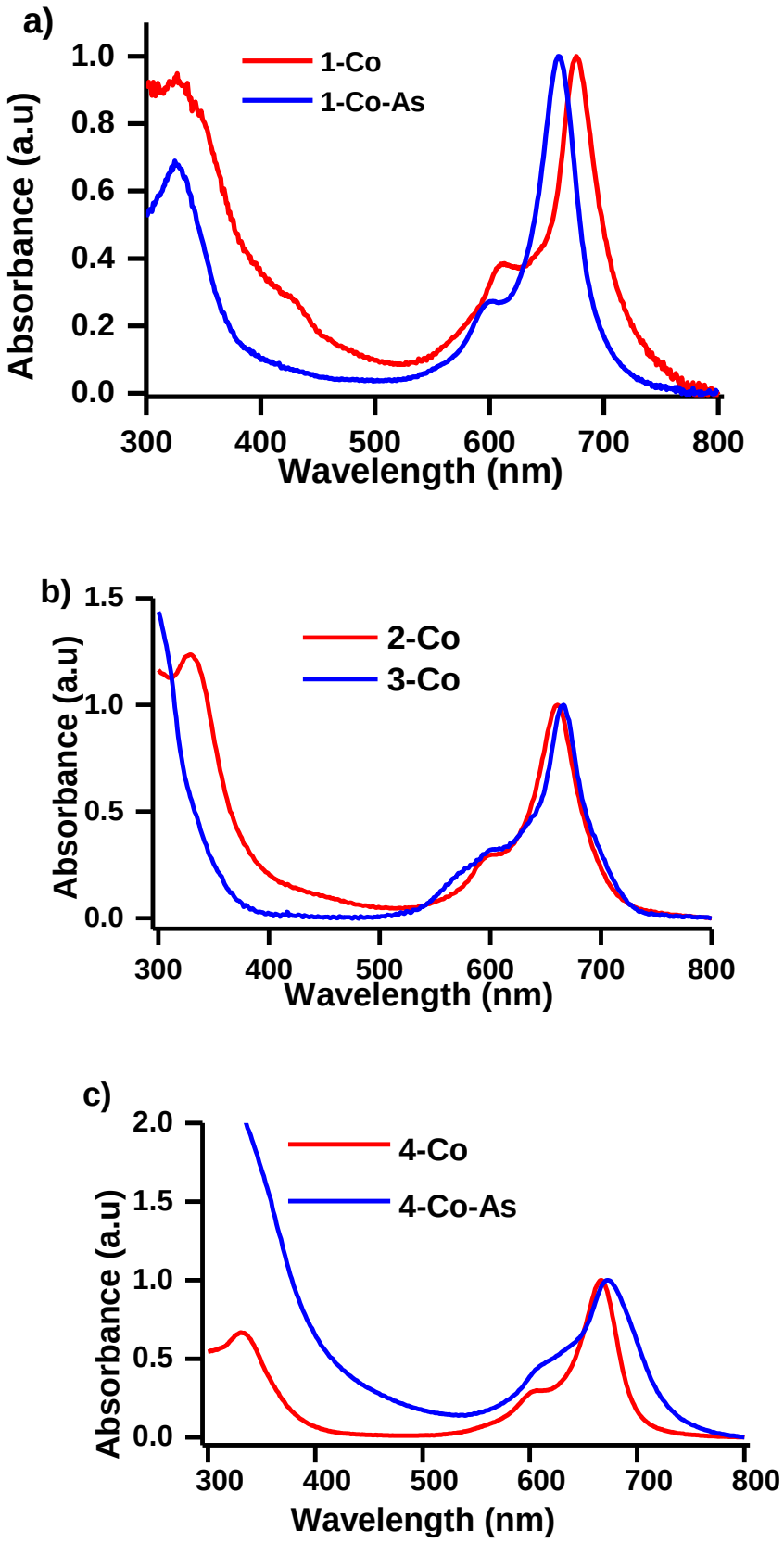

Figure 3.2: UV-Vis absorption spectra of (a) **1-Co** and **1-Co-As,** (b) **2-Co** and **3-Co**, and (c) **4-Co** and **4-Co-As** in DMF. ~ Concentration = 1×10^{-6} M.

From the figure, it can be observed that the average Q band absorption for the cobalt phthalocyanine complexes is at approximately 660 nm. It is inconclusive whether lowering the symmetry of the MPc leads to a blue or red shift. As a 16 nm blue shift was observed when the symmetry of **1-Co** was lowered to **1-Co-As** and a 10 nm red shift was observed between **4-Co** and **4-Co-As**.

The UV-Vis absorption spectra obtained for the copper MPcs are represented in Figure 3.3. From the figure, it can be clearly observed that all complexes exhibited the characteristic Q and B, absorption bands. The Q-band was observed between 674 and 675 nm for all four complexes. The change in symmetry and condensation to form Schiff base CuPcs did not affect the main absorption bands. The B-bands observed between 345 and 343 nm showed varied absorption intensities.

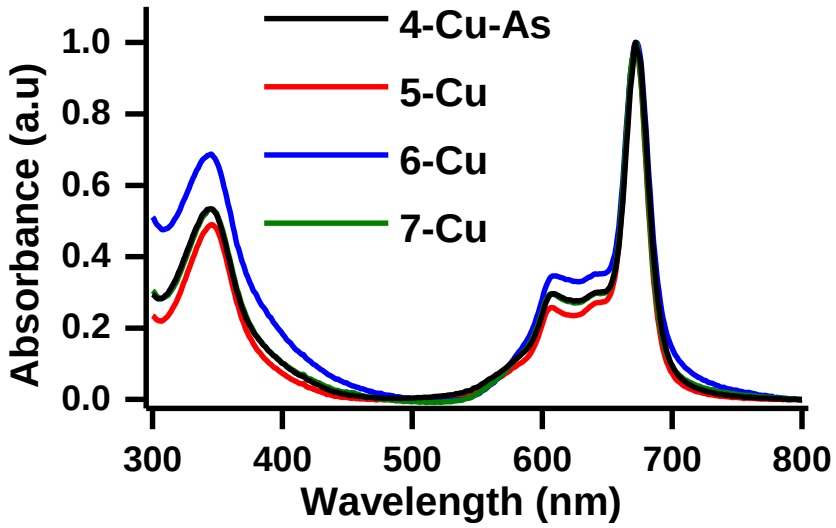

Figure 3.3: UV-Vis absorption spectra of **4-Cu-As**, **5-Cu**, **6-Cu** and **7-Cu** in DMF. **~** Concentration = 1×10^{-6} M.

Table 3.1: MPc complexes synthesised in this work

Symmetric MPcs	
Core ring	**R Substituents**
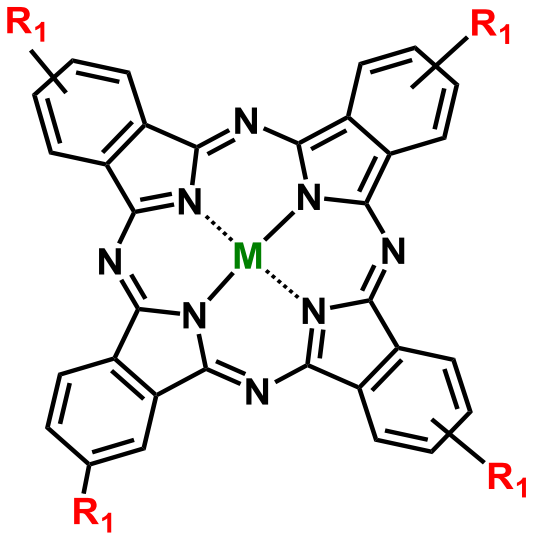	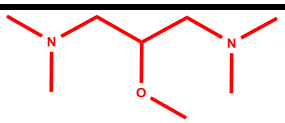 **1-Co**
	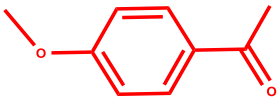 **2-Co**
	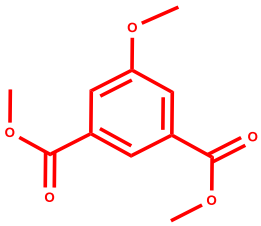 **3-Co**
	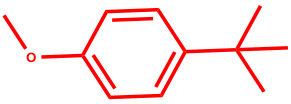 **4-Co**
	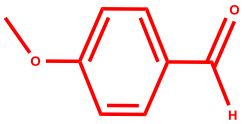 **5-Cu & 9-Mn**
	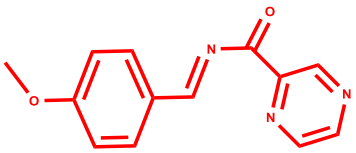 **6-Cu**
	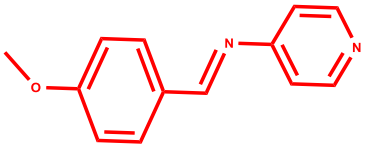 **7-Cu**
	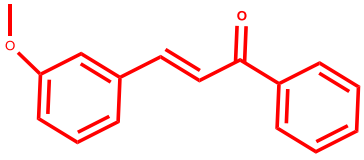 **8-Co 8-Cu 8-Mn 8-Ni**

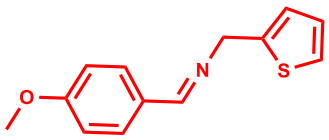

10-Mn

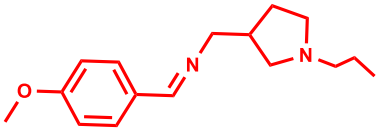

11-Mn

Asymmetric MPcs	
Core ring	R_1 and R_2 Substituents
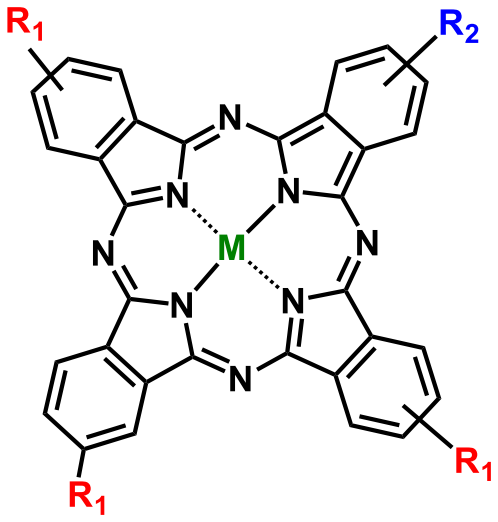	R_1 = 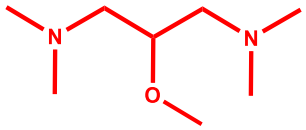 1-Co-As R_2 = 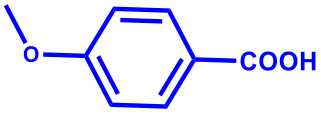 R_1 = 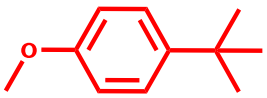 4-Co-As R_2 = 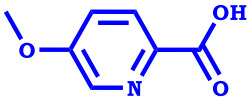 R_1 = 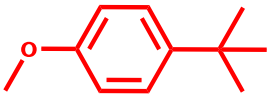 4-Cu-As R_2 = 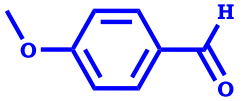

Figure 3.4 illustrates the UV-vis absorption spectra obtained for the **8**-series complexes. The main absorption bands for **8-Co** and **8-Cu** were observed at 668 nm and 675 nm, respectively (Table 3.2). The figure shows that the **8-Ni** absorption spectra differed from the other complexes in that there were two distinct absorption bands at 668 nm and 614 nm. This was attributed to aggregation, NiPc derivatives are known for their aggregation [160].

The low energy absorption band is due to the monomer, and the high energy absorption band is due to the aggregate. Aggregation in phthalocyanines is highly dependent on the concentration, temperature, nature of the substituents attached to the molecule, the solvent the compound is dissolved in and complexed metal ions. **8-Mn** showed more monomeric behaviour with a narrower Q band, while **8-Co** showed a broadened Q band typical of CoPcs [161]. **8-Mn** displayed the most red-shifted Q band in the near-infrared at 720 nm. This is typical of manganese (III) phthalocyanine complexes [162,163]. Some aggregation was observed for **8-Mn** and **8-Co**, but not as severe as for **8-Ni**.

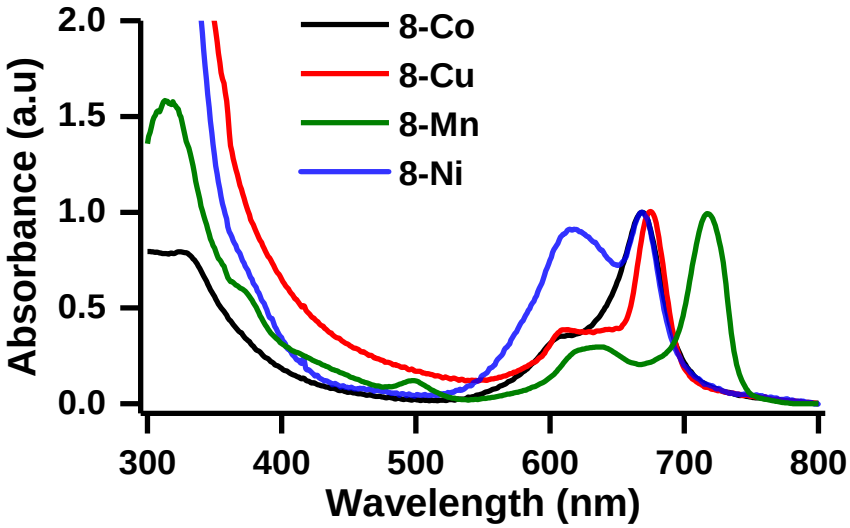

Figure 3.4: UV-Vis absorption spectra of **8-Co**, **8-Cu**, **8-Mn** and **8-Ni** in DMF. ~ Concentration = 1×10^{-6} M.

Figure 3.5 is an illustration of the UV-Vis absorption spectra obtained for **9-Mn**, **10-Mn** and **11-Mn**. The two MPc characteristic bands were observed for all three complexes indicating that the MPcs were successfully synthesised. The Q-bands were observed at 732 nm, 738 nm and 733 nm for three complexes, respectively. A slight red shift in the Q-band was observed for **10-Mn** compared to the two MPcs. The red shift is attributed to the thiol in the substituents, as sulphur-containing complexes exhibit slightly red shifted absorptions. This is because sulphur atoms tend to mix with the π orbitals of the aromatic system and thus result in the main absorption band shifting to the red [31].

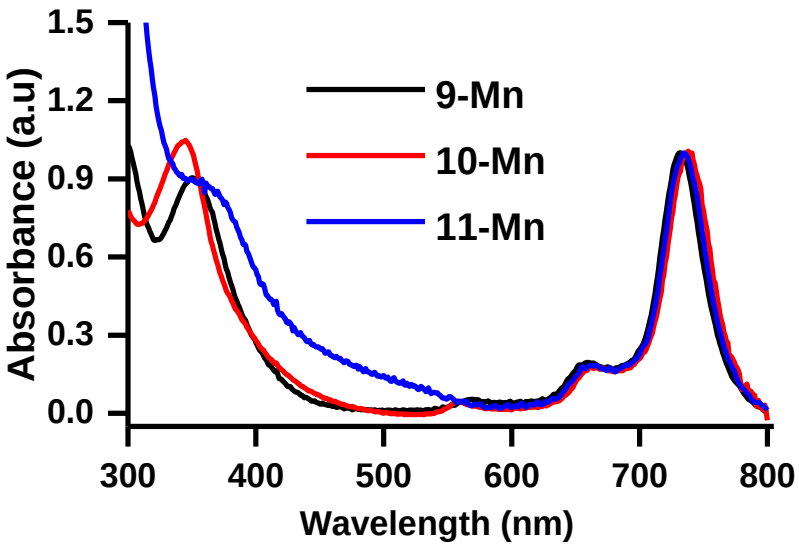

Figure 3.5: UV-Vis absorption spectra of **9-Mn**, **10-Mn** and **11-Mn** in DMF. ~ Concentration = 1×10^{-6} M.

Table 3.2: Summary of the Q-band and B-band absorption maxima obtained in DMF for all MPc complexes studied herein

	Q-band λ_{max} (nm)	B -Band λ_{max} (nm)
1-Co	676	332
1-Co-As	660	332
2-Co	661	329
3-Co	666	315
4-Co	663	334
4-Co-As	673	336
4-Cu-As	674	335
5-Cu	675	343
6-Cu	674	343
7-Cu	674	335
8-Co	668	328
8-Cu	675	316
8-Mn	720	312
8-Ni	668 and 613	313
9-Mn	733	350
10-Mn	738	343
11-Mn	733	360

3.4 Nanomaterials and MPc Hybrids

Carbon-based nanomaterials (GQDs, NGQDs and SWCNTs) and metallic nanoparticles ($NiWO_4$ and Bi_2WO_6) were used in this work. These nanomaterials were used in conjunction with MPc complexes to study their effect on the electrochemical and electrocatalytic properties of MPcs. All nanomaterials studied herein, except for SWCNTs, were synthesised. SWCNTs were purchased from Nanolab. All nanomaterials and their synthesised MPc-hybrid materials were analysed using various analytical techniques.

3.4.1 Synthesis of GQDs, NGQDs

The synthesis of GQDs and NGQDs has been reported [146]. These two graphene-based nanomaterials were synthesised via the bottom-up approach using the hydrothermal treatment. Where citric acid was reacted with NaOH in water to yield GQDs (Scheme 3.9(a)). The same procedure was used in the synthesis of NGQDs. However, urea was used as a nitrogen source (Scheme 3.9(b)).

3.4.2 Synthesis of Bi_2WO_6 and $NIWO_4$

Scheme 3.10 illustrates the synthetic route followed in the synthesis of $NiWO_4$ and Bi_2WO_6 nanomaterials, which has been reported [148]. The same procedure was followed when synthesising both these metal oxide nanoparticles. However, $Ni(OAC)_2$ was used as the starting material for $NiWO_4$, and Bi_2O_3 was used for Bi_2WO_6. Glutathione (GSH) was used to cap the nanoparticles.

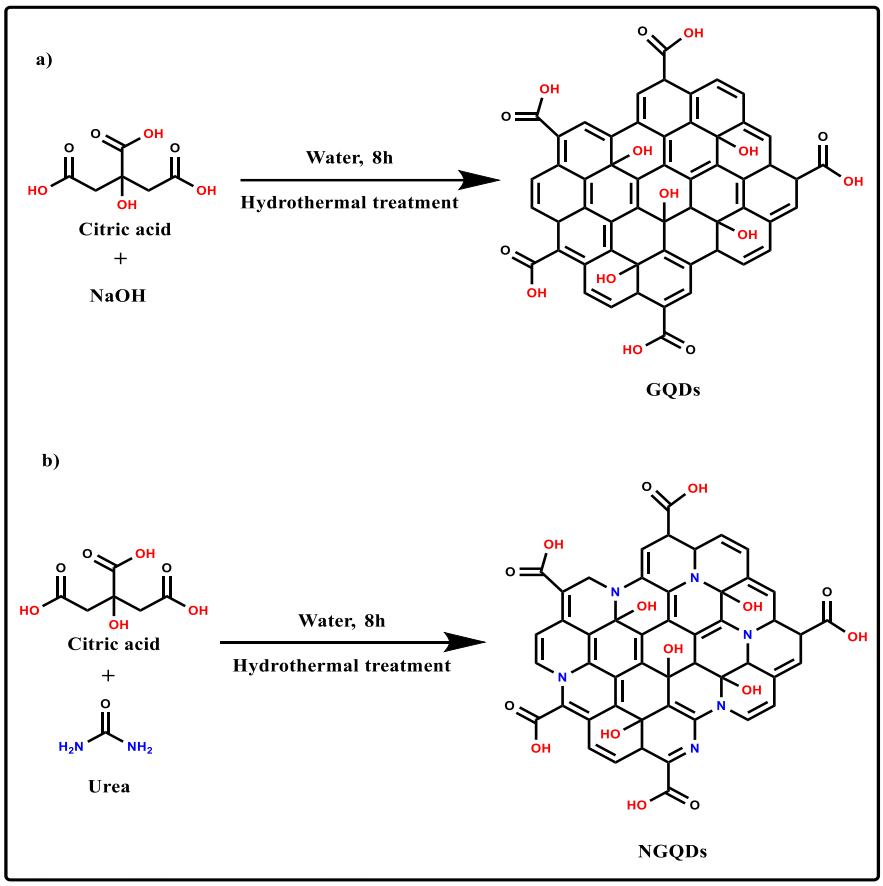

Scheme 3.9: Synthetic route of (a) **GQDs** and (b) **NGQDs** nanomaterials

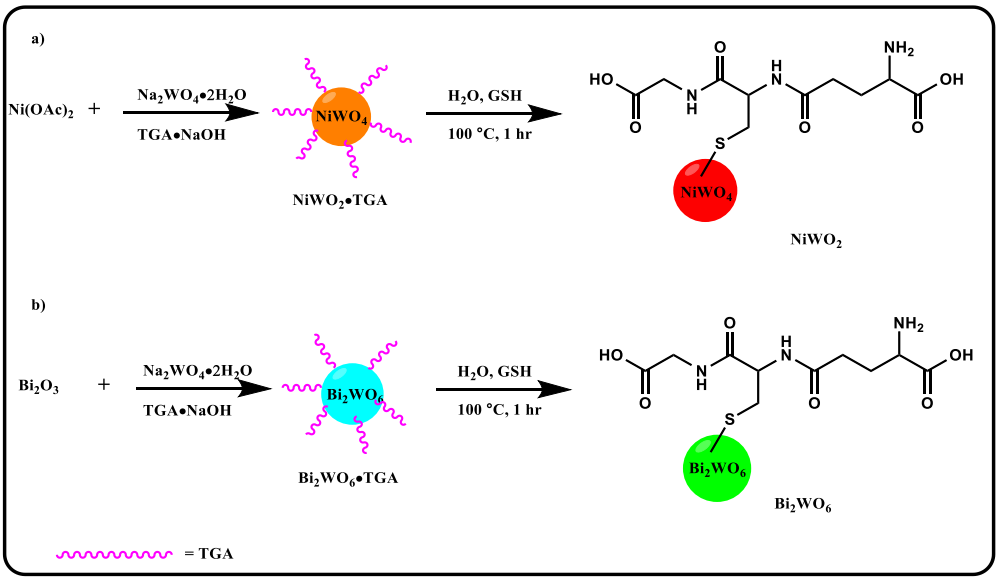

Scheme 3.10: Synthesis of GSH capped **$NiWO_4$** and **Bi_2WO_6** nanoparticles

3.4.3 Linkage

Herein carbon-based nanomaterials and metallic nanomaterials were used in conjunction with phthalocyanine complexes. These molecules were conjugated (covalent linkage involving metallic nanoparticles) or hybridised (π-π stacking involving carbon-based nanomaterials) using non-covalent bonding (for carbon-based nanomaterials) and covalent linkage via an amide bond (for metallic nanomaterials). Schemes 3.11 and 3.12 show how hybridisation(conjugation) of the MPcs and nanomaterials was achieved using N**GQDs** and **Bi_2WO_6** as examples in the two schemes, respectively.

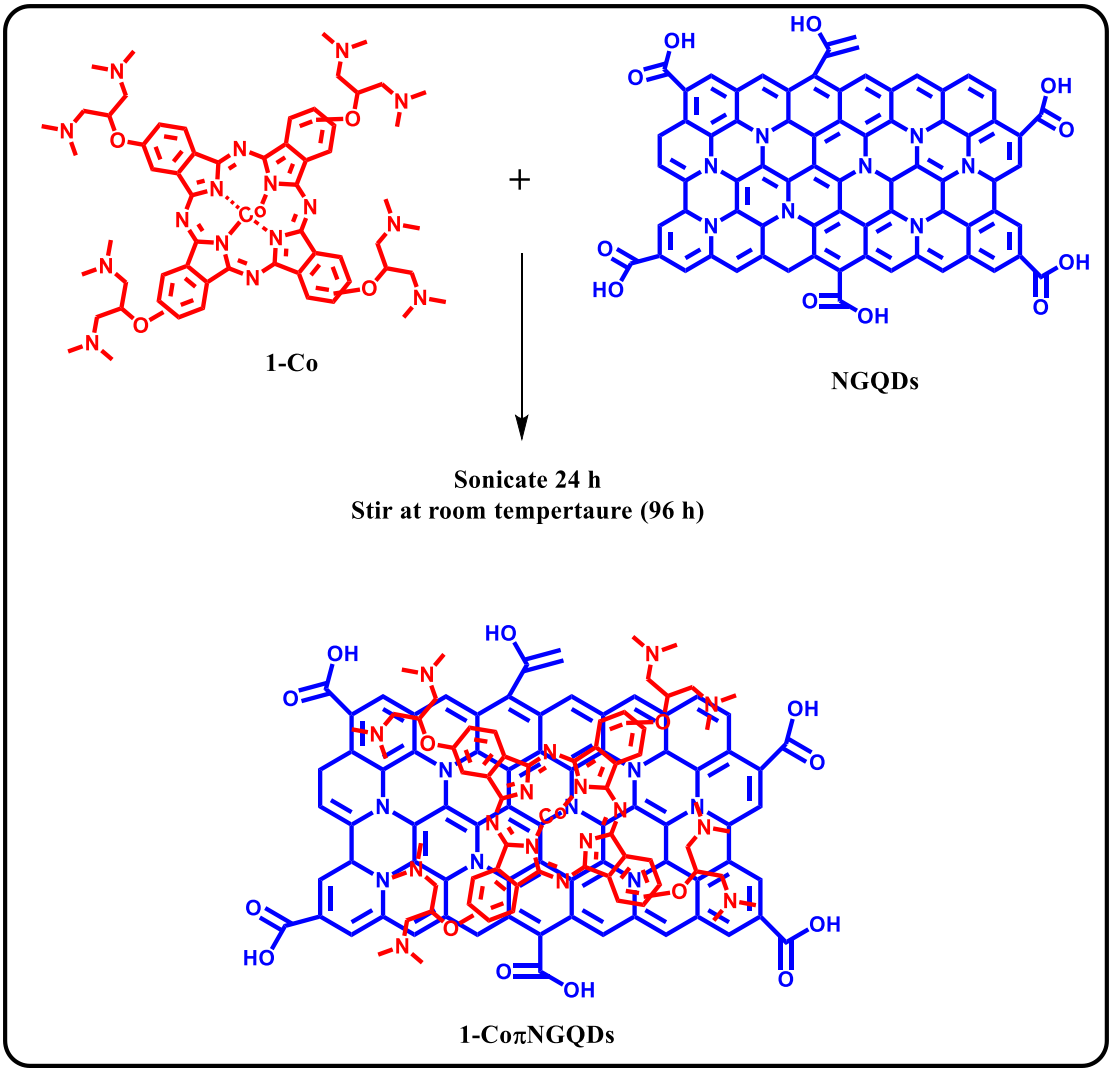

Scheme 3.11: Non-covalent π-π stacking of **1-Co** and **NGQDs** to form **1-CoπNGQDs**

Non-covalent linkage was achieved via π-π stacking. Since the carbon-based nanomaterials and the synthesised phthalocyanine complexes all have rich π-electrons, their hybridisation was achieved by exploiting these π-electrons. The MPcs and nanomaterial(s) were immersed in THF/DMF, sonicated for approximately 24h and then stirred constantly (96 h). Scheme 3.10 illustrates the π-π staking of **1-Co** and **NGQDs** forming **1-CoπNGQDs**. Scheme 3.12 represents the covalent linkage of **4-Co-As** and **Bi_2WO_6** to form **4-Co-As@Bi_2WO_6**.

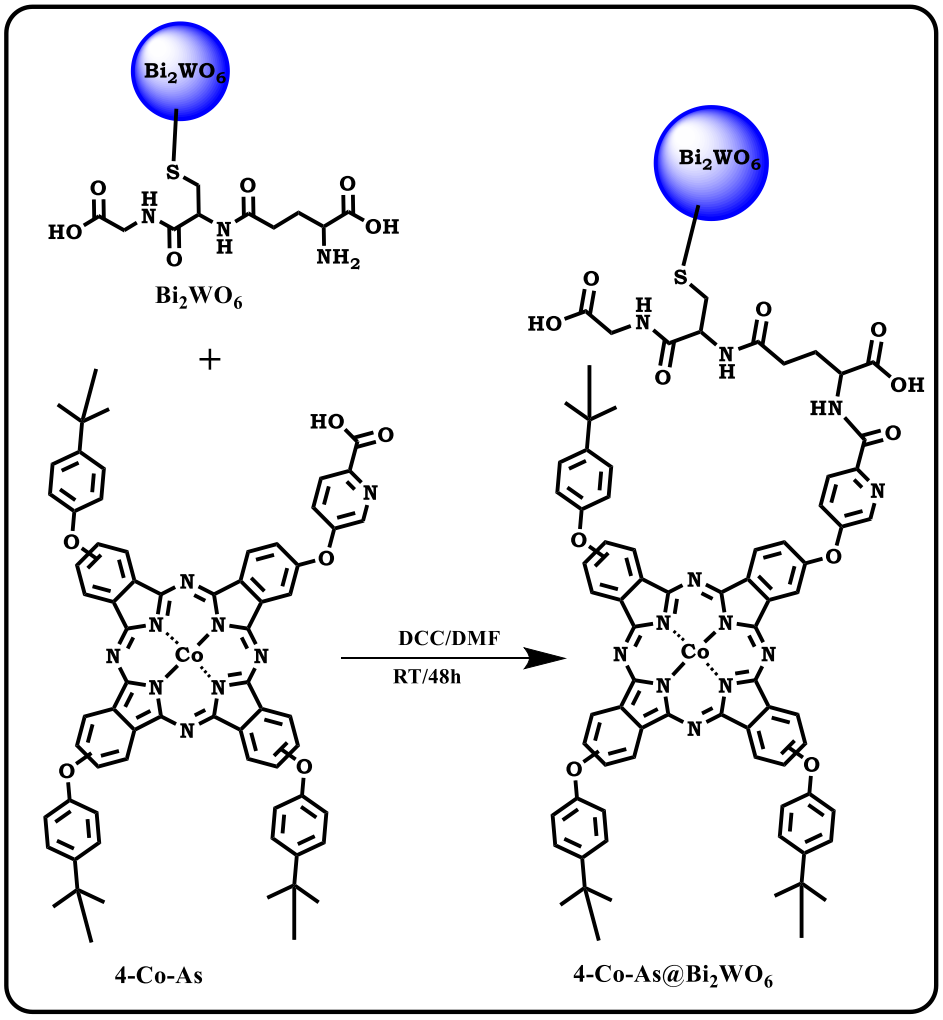

Scheme 3.12: Covalent linkage **of 4-Co-As** and **Bi_2WO_6** forming **4-Co-As@Bi_2WO_6**

3.4.4 Characterisation of Nanomaterial and their MPc Hybrids

The hybridisation of MPcs complexes to nanomaterials was confirmed using various analytical and microscopic techniques

3.4.4.1 UV-Vis Absorption Spectral Properties

Herein, UV-Vis absorption spectra were used to characterise the nanomaterials and their conjugates (UV-vis absorption spectra of MPc complexes were discussed in *Section 3.3*). Like MPcs, nanomaterials have distinct absorption bands, typically observed between 300 – 500 nm [164,165].

Figure 3.6 is an illustration of the UV-Vis absorption spectra obtained for the graphene-based nanomaterials (a) and the metallic nanomaterials (b). Graphene-based materials typically have well-established absorption bands in the UV region due to the π-π transitions of the sp^2 domains [164,166]. Their absorption band depends on the method used in their preparation and not their size [164,165]. The main absorption bands (Table 3.3) were observed at 387 nm (**GQDs**), 348 nm (**NGQDs**) and 324 nm (**SWCNTs**); GQDS and NGQDs were measured in water while SWCNTs were in DMF. It has been reported that the Q band absorptions of MPc complexes are sensitive to π-π interactions and that the strong π-π interactions result in the formation of complexes between Pcs and nanomaterials in the ground state hence spectral shifts are observed upon linkage [167] (Table 3.3).

Bi_2WO_6 and **$NiWO_4$** were absorbed at 448 nm and 330 nm (Table 3.3), these absorption bands are in agreement with those obtained in literature [105]. **Bi_2WO_6** exhibited a relatively broader and longer wavelength absorption band. The broadness was attributed to aggregation.

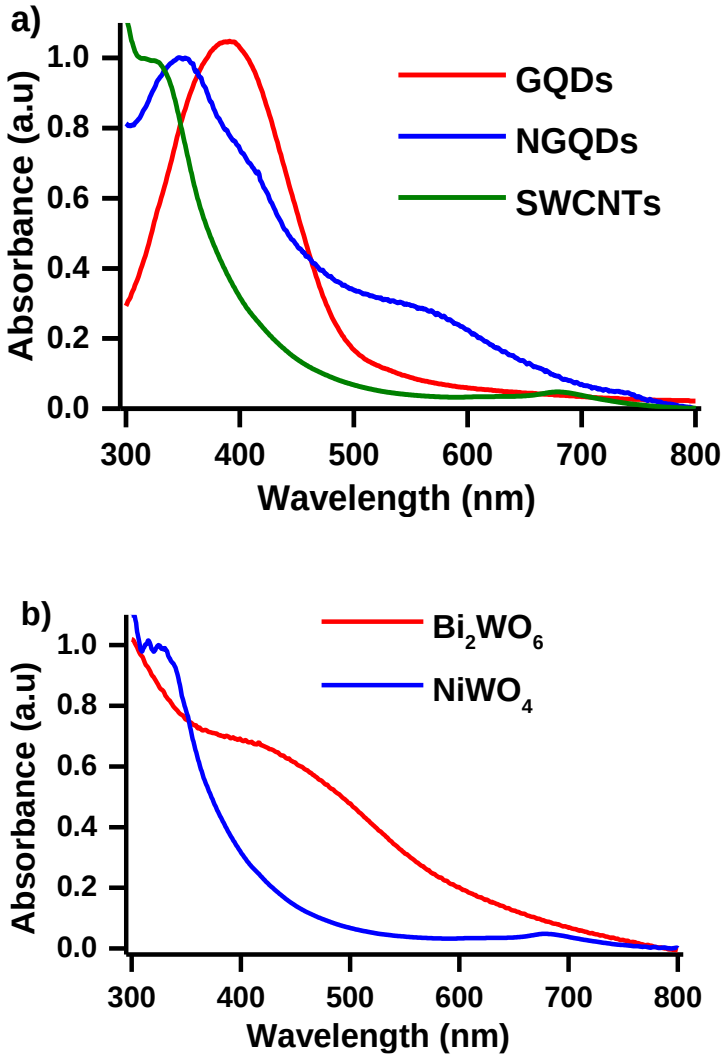

Figure 3.6: UV-Vis absorption spectra of (a) **GQDs**, **NGQDs** and **SWCNTs** and (b) **Bi_2WO_6** and **$NIWO_4$**

Figure 3.7(a) is an illustration of the UV-Vis absorption spectra of **1-Co**, **1-Co-As** and their π-π stacked hybrids **1-CoπNGQDs** and **1-Co-AsπNGQDs**. A 10 nm blue shift in the Q band was observed for **1-Co** upon hybridisation with **NGQDs**. While the conjugation of **1-Co-As** to **NGQDS** resulted in a 16 nm red shift. The UV-Vis absorption spectra of the two symmetric MPc complexes **2-Co** and **3-Co** and their GQDs and SWCNTs hybrids are illustrated in Figure 3.7(b and c).

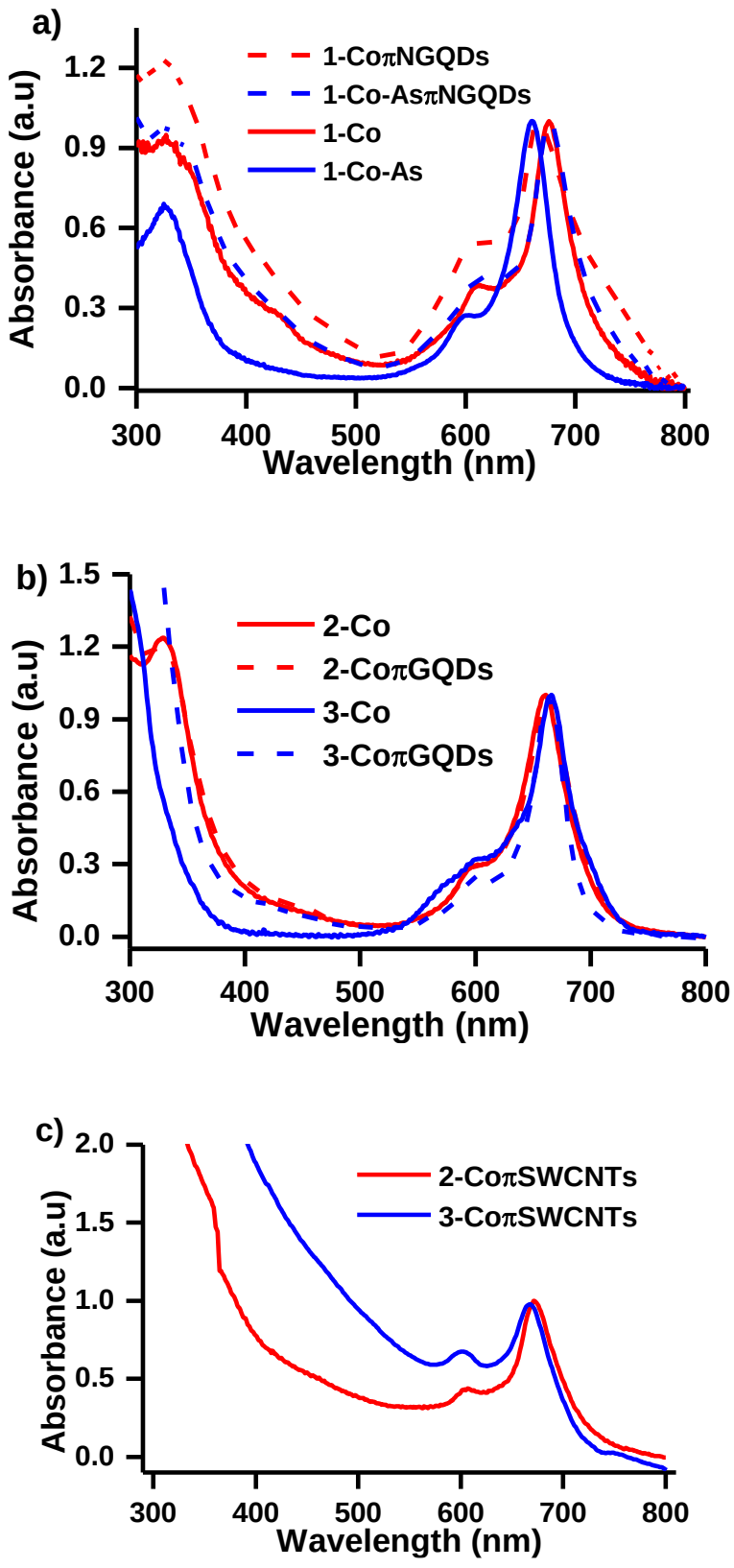

Figure 3.7: UV-Vis absorption spectra of (a) **1-Co**, **1-Co-As** and their hybrids; **1-CoπNGQDs** and **1-Co-AsπNGQDs** (b) **2-Co**, **3-Co**, **2-CoπGQDs** and **3-CoπGQDs** and (c) **2-CoπSWCNTs** and **3-CoπSWCNTs** in DMF

Table 3.3: Summary of the data obtained for the nanomaterials and their MPc conjugates

	Abs maxima (nm)	DLS Size (nm)	Loading (µg/mg)
GQDs	387[a]	5.61	-
NGQDs	348[a]	4.96	-
SWCNTs	324	15.3	-
Bi_2WO_6	448[a]	13.5	-
$NiWO_4$	330[a]	32.7	-
1-Co	676	-	-
1CoπNGQDs	666	19.2	506
1-Co-As	660	-	-
1-Co-AsπNGQDs	676	23.5	596
2-Co	661	-	-
2-CoπGQDs	663	15.7	300
2-CoπSWCNTs	672	21.5	430
3-Co	666	-	-
3-CoπGQDs	664	18.2	270
3-CoπSWCNTs	670	26.3	450
4-Co-As	673	-	-
4-Co-AsπGQDs	663	19.5	642
4-Co-AsπNGQDs	664	21.3	607
4-Co-AsπSWCNTs	667	20.3	528
4-Co-As@Bi_2WO_6	666	28.2	98

4-Co-As@$NiWO_4$	674	48.3	184

[a]Spectra obtained in water, all others in DMF

Red shifts have been attributed to the flattening of porphyrins in porphyrins-graphene oxide nanoconjugates [168,169]. Blue spectral shifts have also been reported for porphyrin-graphene oxide conjugate [169]. These spectral changes are attributed to strong interactions between MPcs and the graphitic sheet. The increase in intensity of the B band observed upon hybridisation was attributed to the intense absorption of the nanomaterials within the region. The observed broadening of the Q bands upon hybridisation suggests that aggregation occurred.

Figure 3.8 illustrates the UV-vis absorption spectra obtained for complex **4-Co-As** alone and when linked to the studied nanomaterials. As indicated above, **4-Co-As** displayed a Q-band absorption maxima at 673 nm, Tables 3.2 and 3.3. The Q-bands (wavelengths) obtained for the hybrid complexes are summarised in Table 3.3. A 7 nm blue shift in the Q band maxima was observed upon the hybridisation of **4-Co-As** with Bi_2WO_6. Blue shifts have been previously reported for porphyrinoid conjugates with graphene oxide and have been attributed to strong interactions between the components, as stated above. With regards to hybridisation of **4-Co-As** with carbon-based nanomaterials, 6 – 10 nm blue shifts in the Q-band were observed.

Upon hybridisation, a general increase in the absorption intensity of the B band of the MPc complex was observed. This can be attributed to the influence of the nanomaterials with absorption profiles within that region.

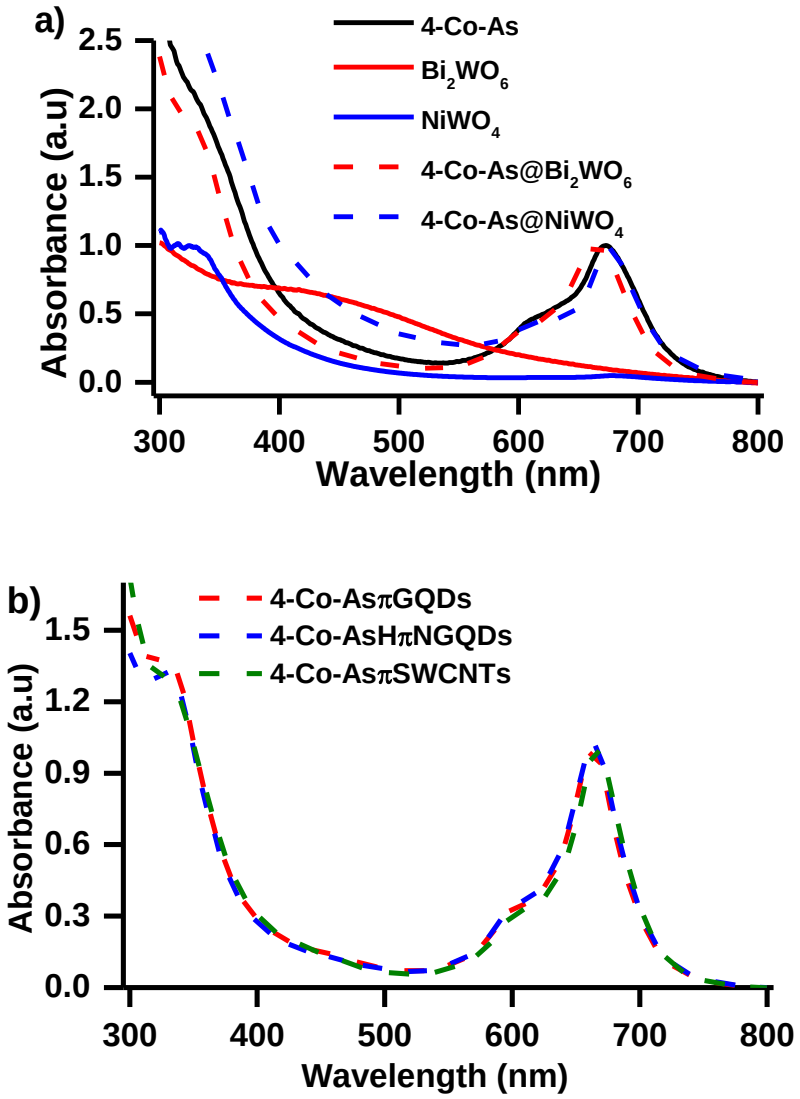

Figure 3.8: UV-Vis absorption spectra of (a) **4-Co-As**, **Bi_2WO_6**, **$NiWO_4$**, **4-Co-As@Bi_2WO_6** and **4-Co-As@$NiWO_4$** and (b) **4-Co-AsπGQDs**, **4-Co-AsπNGQDs**, **4-Co-AsπSWCNTs**

3.4.4.2 X-Ray Diffraction

X-ray powder diffraction (XRD) was used to study the morphology and crystallinity of the nanomaterials and the respective MPc hybrid materials (conjugates) used in this work. Figure 3.9 shows the X-ray powder diffractogram of the nanomaterials and their conjugates recorded from 2θ between 5° and 100°. MPcs complexes are known to show broad XRD peaks at approximately 20° due to their amorphous nature, as observed in Figure 3.9(a) [170]. This

peak is observed in the diffractograms obtained for the conjugates as well. However, in some cases, it may overlap with that of the graphene-based nanomaterials (**GQDs**, **NGQDs** and **SWCNTs**), as graphene structures have prominent peaks at between 25° and 43°C (Figure 3.9(b)). These peaks were attributed to the reflection of the carbon on the graphitic layer of the structure, respectively [171,172].

The $NiWO_4$ nanoparticles showed diffraction peaks with 100, 110, 111, 200, 130, 113, 311 and 302 (JCPDS no. 15-0755) planes. While the Bi_2WO_6 XRD patterns observed were in accordance with the JCPDS no 39-0256 with diffraction peaks at 131, 002, 202, 133, 262, 204 [173–175] (Figure 3.9(a)). The presence of these diffraction peaks in the conjugates confirms their presence.

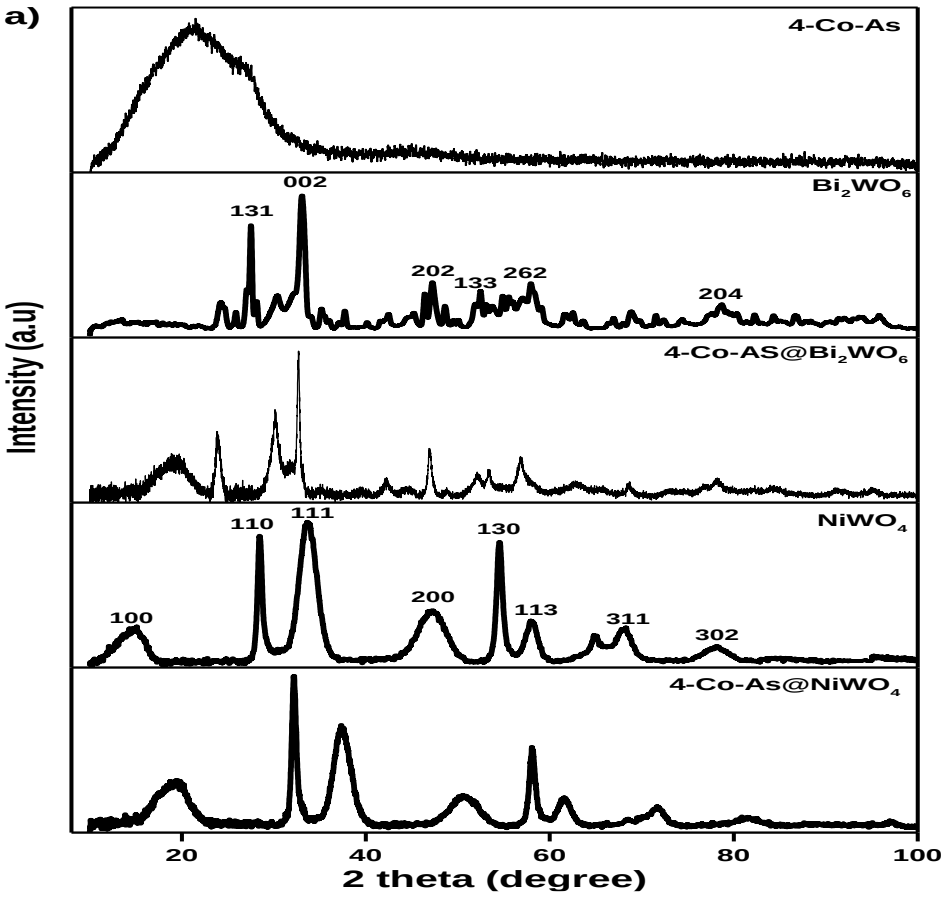

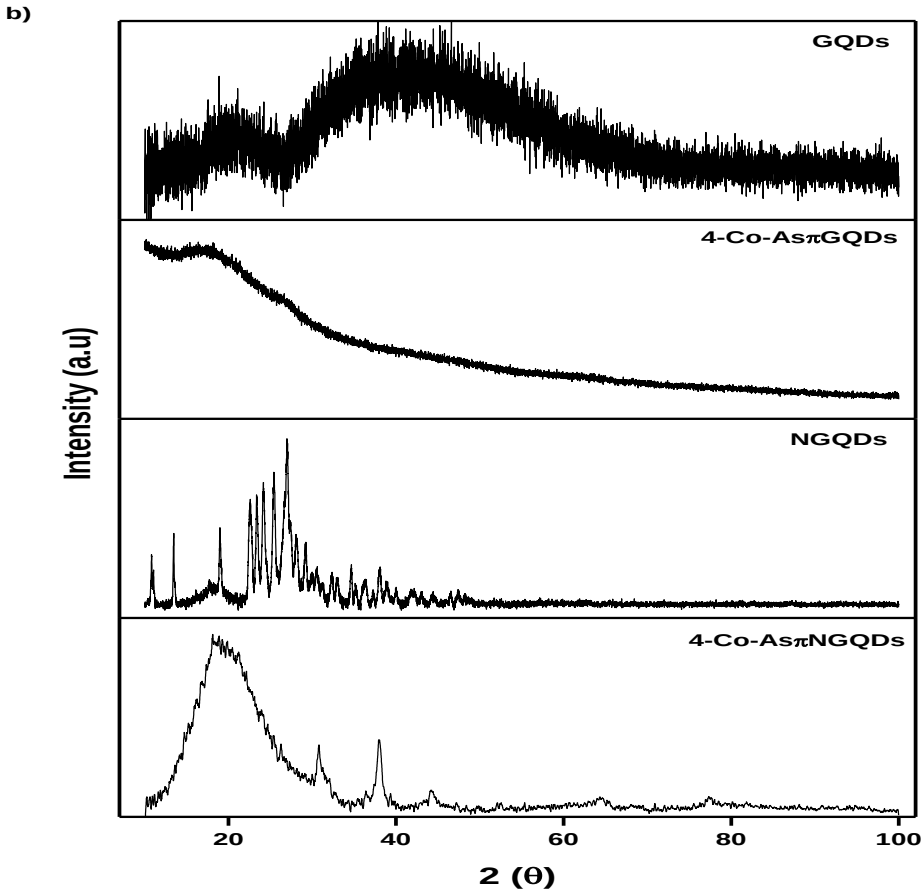

Figure 3.9: X-ray diffractograms of (a) **4-Co-As**, **Bi_2WO_6** and **$NiWO_4$** and their respective **4-Co-As** conjugates and (b) **GQDs** and **NGQDs** and their respective **4-Co-As** conjugates

3.4.4.3 Raman Spectroscopy

Raman spectroscopy was used herein to determine the vibrational modes of the nanomaterials and their respective conjugates as well as to investigate whether the structural fingerprints of the nanomaterials were maintained after conjugation (Figures 3.10 and 3.11). The G bands observed in the Raman spectra are attributed to the in-plane vibrations of the sp^2 bonded carbon atoms. While the D bands are due to the out-of-plane vibrations caused by structural defects, sp^3 carbon atoms [176–178]. The G and D bands (wavenumbers) are tabulated in Table 3.4.

The G band associated with **GQDs** was observed at 1586 cm^{-1}. Upon hybridisation with **2-Co** and **4-Co-As**, no significant changes in the G band were observed for the formed hybrids. However, a 17 cm^{-1} shift in the G band was observed after hybridisation with **3-Co**. The **GQDs** exhibited a D vibrational band at approximately 1354 cm^{-1}, after conjugation < 5 cm^{-1}, shifts were observed for **3-CoπGQDs** and **4-Co-AsπGQDs**. While **2-CoπGQDs** showed a more significant shift, with the D band at 1315 cm^{-1}.

NGQDs exhibited G and D vibrational bands at 1605 cm^{-1} and 1171 cm^{-1}, respectively (Figure 3.12(a)). **1-CoπNGQDs** is the only hybridised material that exhibited a significant (12 cm^{-1}) change in the G band upon hybridisation. While the only noticeable difference in the D band was the 20 cm^{-1} shift observed for **1-Co-AsπNGQDs**. Hybrid **4-Co-AsπNGQDs** exhibited < 3 cm^{-1} for both the G and D bands from the original G and D bands obtained for **NGQDs**.

Figure 3.10(b) shows the Raman spectra obtained for **SWCNTs** and the MPc hybrid, **4-Co-AsπSWCNTs**. The figure shows that unlike the other carbon-based nanomaterials studied, **SWCNTs** have an additional and relatively less intense vibrational band, the 2D band, observed at higher wavenumbers. The 2D band is an overtone of the D band [179,180]. The three prominent SWCNTs vibrational bands were observed at 1600 cm^{-1} (G band), 1303 cm^{-1} (B band) and 2595 cm^{-1} (2D band). After hybridisation, the average shifts were < 8 cm^{-1} for all the G and D vibrational bands. Relatively larger shifts were observed for the 2D band for **2-CoπSWCNTs** (2675 cm^{-1}, 80 cm^{-1} shift) and **3-CoπSWCNTs** (2632 cm^{-1}, 37 cm^{-1}).

Shifts in the G band indicate a strong interaction between an MPc and the coplanar graphitic sheet of the nanomaterial, this is attributed to a charge transfer between the MPcs and the nanomaterials [179,181]. The lack of change in the D band suggests that the central graphene sheet was intact during π-π stacking and that the structural integrity was preserved. Raman

shifts have also been reported to indicate a change in size and strain effect on nanoparticles [182,183].

Upon hybridisation, the order of the graphene framework is disrupted, and a change in the I_D/I_G ratio is expected [184]. The I_D/I_G ratios were calculated (Table 3.4). No apparent trends were observed in the I_D/I_G ratios after conjugation, as both increases and decreases in the ratios were observed.

Table 3.4: Summary of the Raman spectroscopy data

	G (cm^{-1})	D (cm^{-1})	2D (cm^{-1})	I_D/I_G
GQDs	1586	1354	-	0.59
2-CoπGQDs	1586	1315	-	0.44
3-CoπGQDs	1603	1351	-	0.57
4-Co-AsπGQDs	1585	1357	-	0.88
NGQDs	1605	1171	-	0.42
1-CoπNGQDs	1593	1171	-	0.80
1-Co-AsπNGQDs	1605	1191	-	0.67
4-Co-AsπNGQDs	1602	1170	-	0.53
SWCNTs	1600	1303	2595	0.39
2-CoπSWCNTs	1595	1300	2675	0.68
3-CoπSWCNTs	1593	1307	2632	0.37
4-Co-AsπSWCNTs	1604	1298	2593	0.90

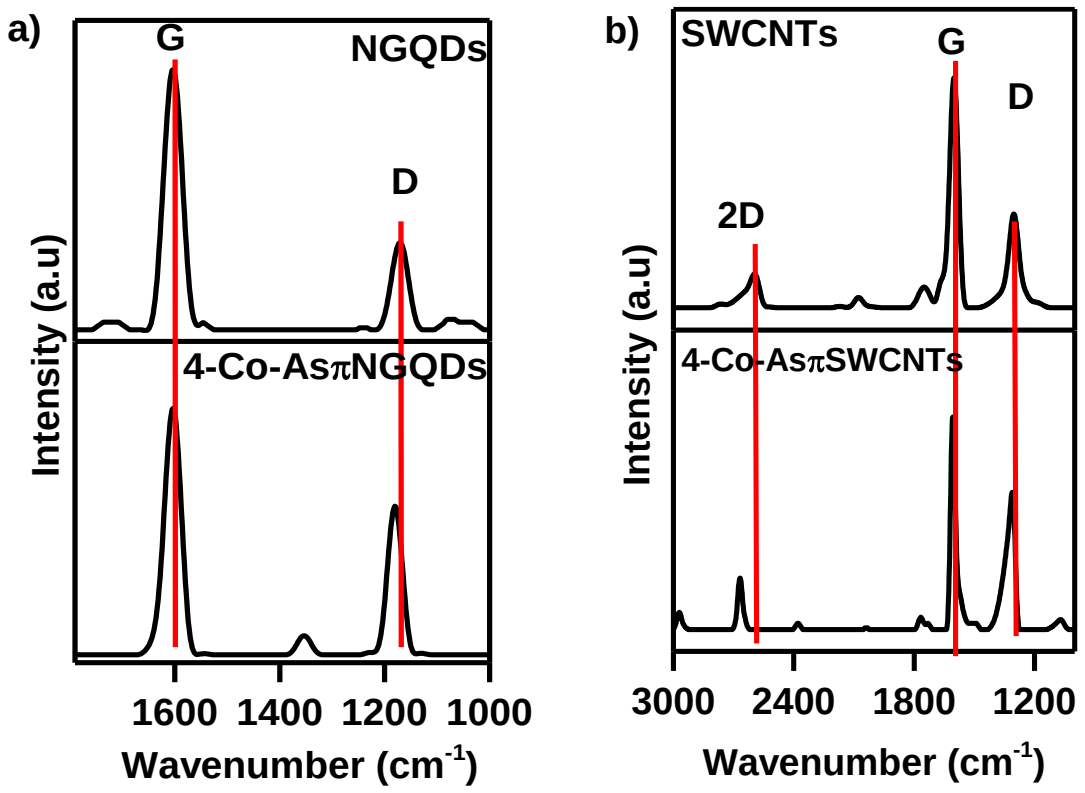

Figure 3.10: Raman Spectra of (a) **NGQDs** and (b) **SWCNTs** and their respective **4-Co-As** conjugates

Raman spectroscopy was also used to determine the vibrational modes of the metallic nanomaterials studied herein (Figure 3.11(a and b)). The W=O band typically has a Raman fingerprint at 874 cm^{-1} with a standard deviation of 55 cm^{-1} [105,185].

The Bi_2WO_6 nanoparticles displayed two intense vibrational bands at 791 cm^{-1} and 303 cm^{-1} and two relatively weak bands at 687 cm^{-1} and 380 cm^{-1}. The vibrational peak at 791 cm^{-1} is attributed to the symmetrical and asymmetrical W=O octahedral stretches, and the band observed at 687 cm^{-1} is due to the asymmetrical WO_6 stretch [102,186]. The vibrational bands at 303 cm^{-1} and 380 cm^{-1} are assigned to the bending modes of the bismuth-oxygen polyhedral

[102,186]. Similar Raman fingerprints were observed for the conjugates with slight shifts in the wavenumbers.

The $NiWO_4$ nanoparticles (Figure 3.11(b)) displayed three strong prominent vibrations at 877 cm^{-1}, 739 cm^{-1} and 699 cm^{-1}. The band observed at 877 cm^{-1} was assigned to the symmetrical W=O vibrational stretch [105,186]. The peaks at 739 cm^{-1} and 699 cm^{-1} and the relatively weaker band observed at 1018 cm^{-1} are assigned to the W-O vibrational bands of the WO_6 octahedra. The vibrational bands obtained for the $NiWO_4$ nanoparticles and corresponding conjugates were within the range of the vibrations observed in literature [105,185,187].

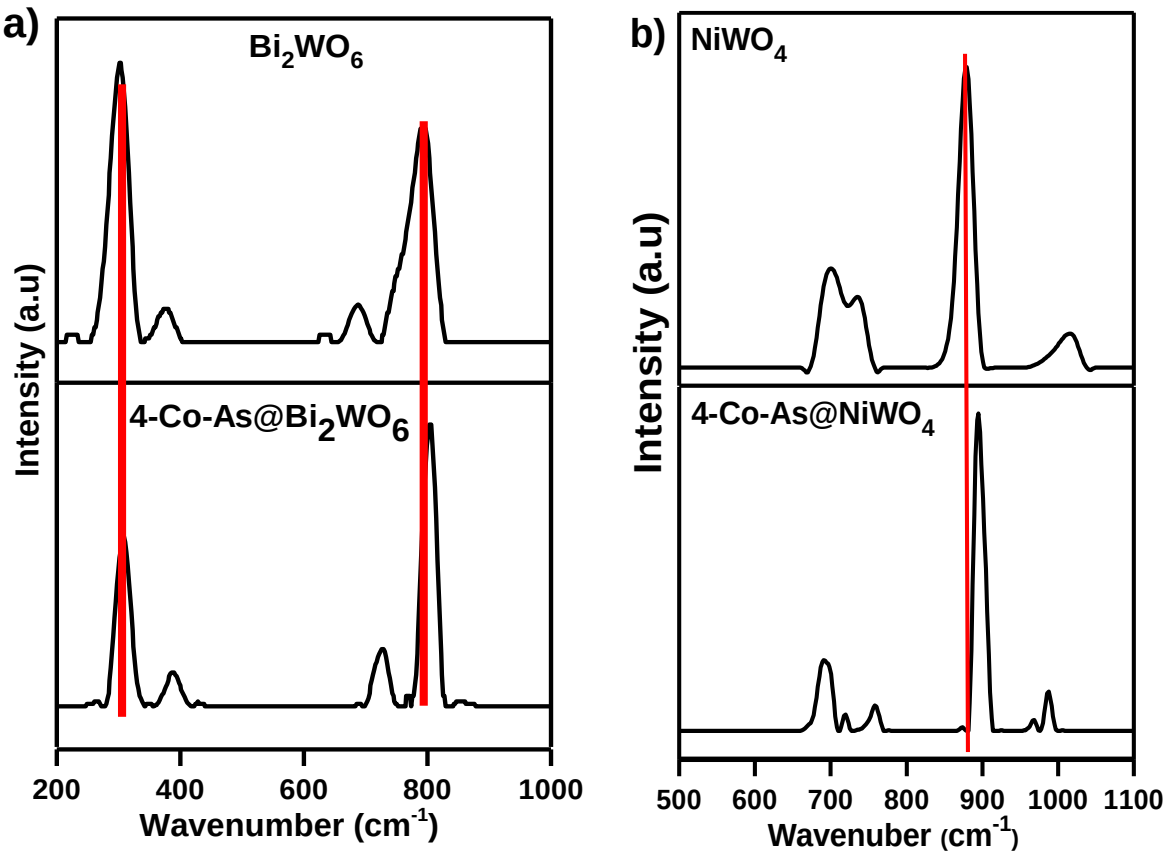

Figure 3.11: Raman spectra for (a) **Bi_2WO_6** and (b) **$NiWO_4$** and their **4-Co-As** conjugates

3.4.4.4 Dynamic Light Scattering

Dynamic light scattering was used to determine the average particle size of the nanomaterials and the MPc-nanomaterial hybrids (Figure 3.12, Table 3.3).

The nitrogen-doped graphene quantum dots exhibited the smallest size of all the nanomaterials studied herein, with their average size being 4.96 nm. The average size of GQDs and SWCNTs was determined to be 5.61 nm and 15.3 nm, respectively (Table 3.3). The metallic nanomaterials had relatively large sizes; 13.5 nm (Bi_2WO_6) and 32.7 nm ($NiWO_4$). An important observation made, was that there was an increase in the average size after linkage, as expected. The increase in particle size confirms the possible supramolecular assembly formation between to (or more) materials.

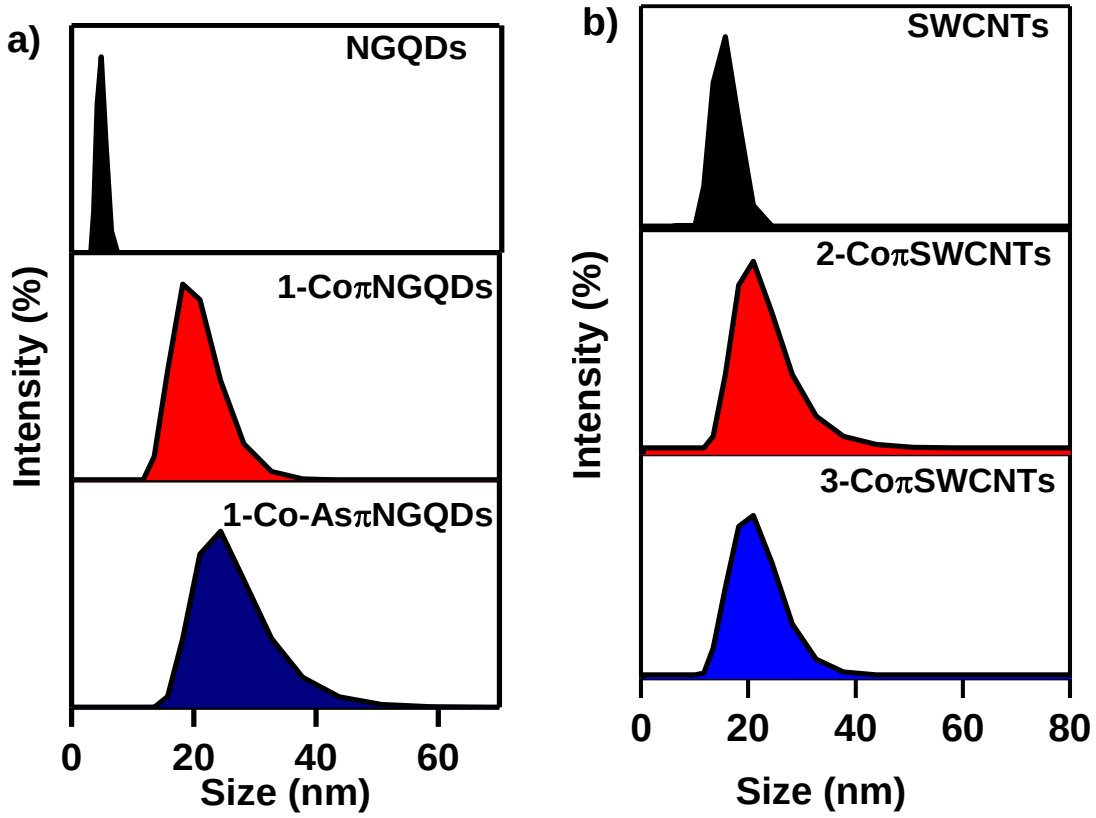

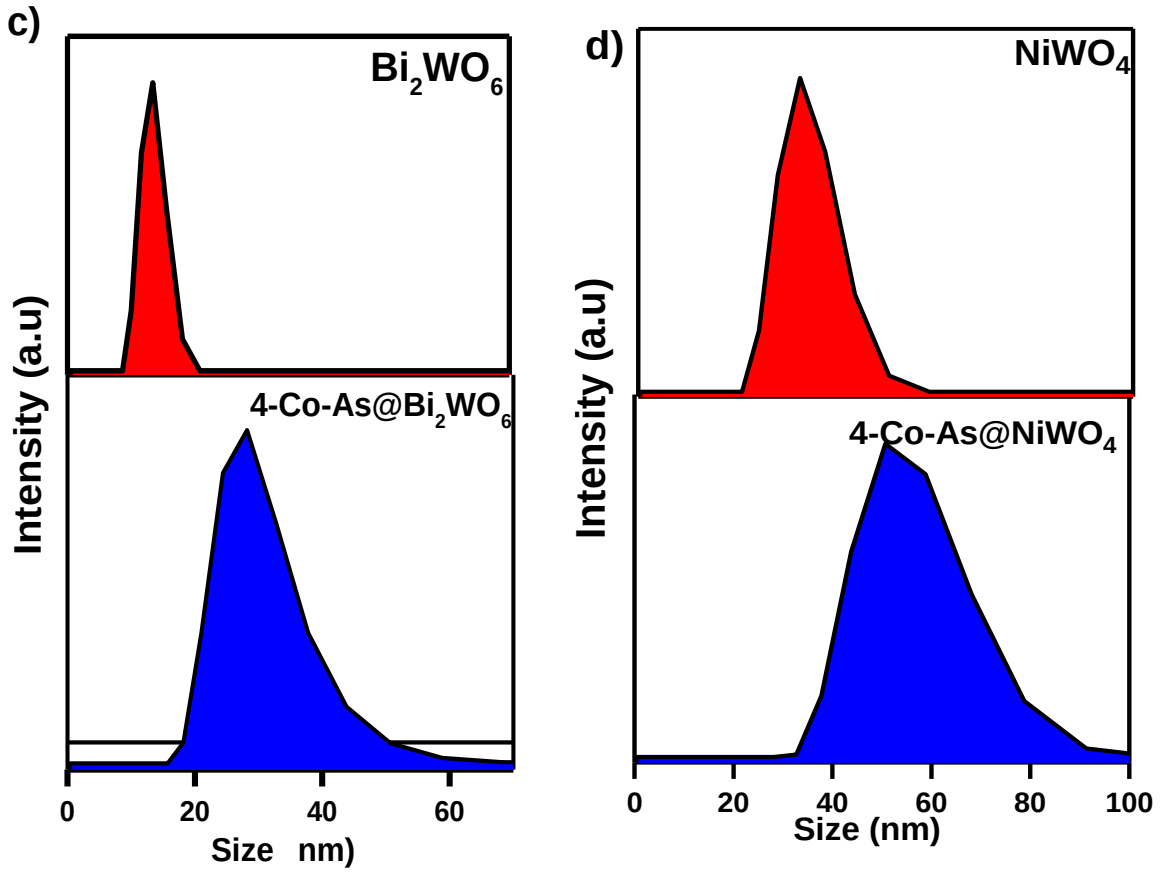

Figure 3.12: DLS distribution graphs of (a) **NGQDs**, **1-CoπNGQDs** and **1-Co-AsπNGQDs,** (b) **SWCNTs**, **2-CoπSWCNTs** and **3-CoπSWCNTs** (c) **Bi_2WO_6**, **4-Co-As@Bi_2WO_6** and (d) **$NiWO_4$** and **4-Co-As@$NiWO_4$**

3.4.4.5 Thermographic Analysis

Thermographic analysis, TGA, was conducted to determine the thermal stability of the phthalocyanine complexes, nanomaterials, and the hybrids. Figure 3.13 shows the thermograms (decay curves) obtained for **4-Co-As**, the nanomaterials studied in this work and the **4-Co-As** hybrid materials (as an example). The results show that the MPc complex was the most thermally unstable material studied herein, with 68% of the complex being degraded at 700 °C.

The nanomaterials alone were relatively more stable compared to **4-Co-As** and the hybrids/conjugates.

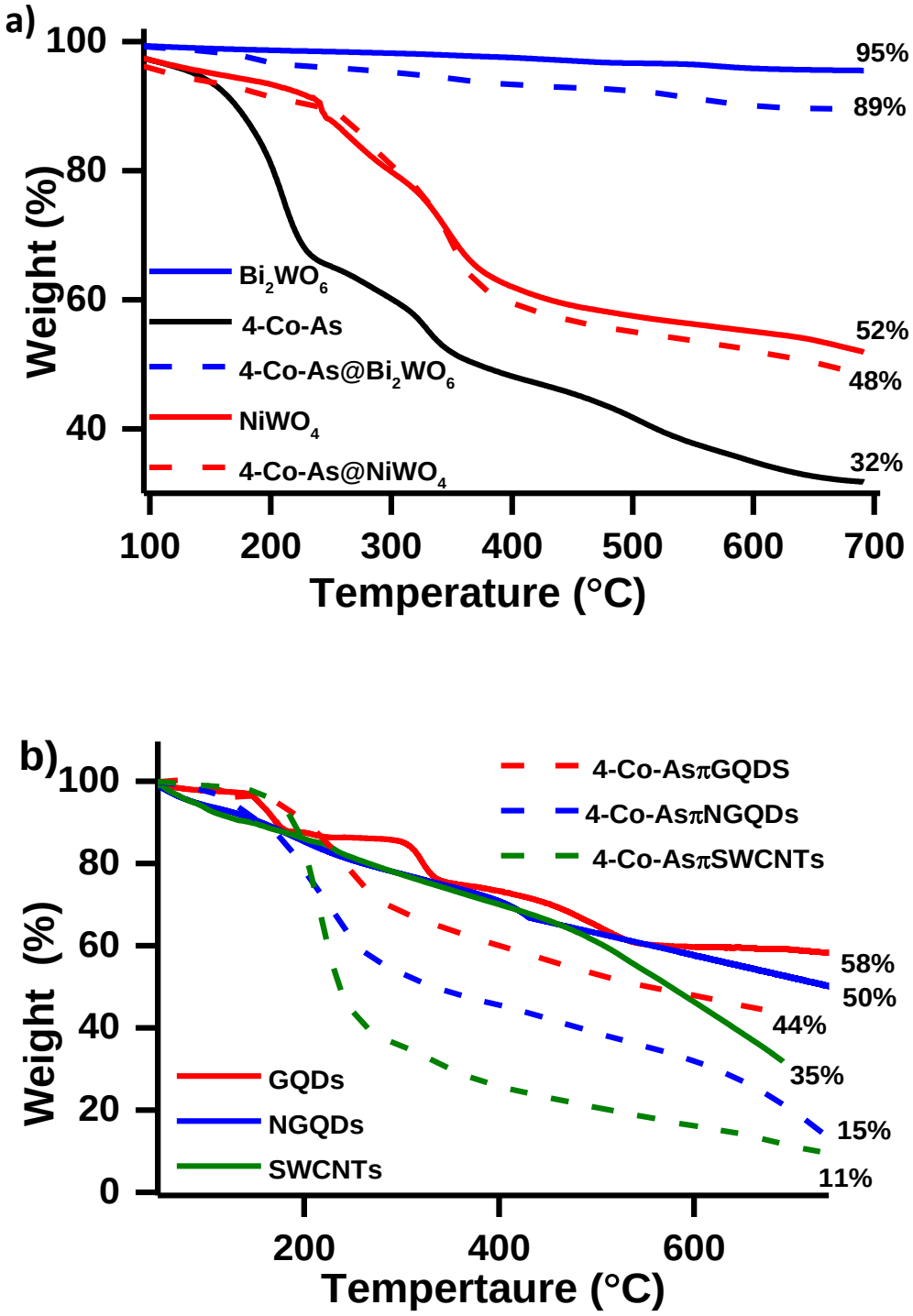

Figure 3.13: Thermographic analysis of (a) **Bi_2WO_6** and **$NiWO_4$** and (b) **GQDs**, **NGQDs** and **SWCNTs** and their **4-Co-As** hybrids

Generally, tungsten nanoparticles are thermally stabile up to 800 °C [188]. Bi_2WO_6 and **4-Co-As@Bi_2WO_6** were the most stable materials studied herein, with more than 80% of the materials retaining their integrity at 700 ˚C. Graphene-based materials are thermally stable as they comprises of sp^2 hybridised carbons held together via covalent bonds and van de Waal forces which are strong and not easily decomposed (reduced) [189]. Hence, herein GQDs exhibited good thermal stability as they had only degraded by just above 58% at 700 °C. with **4-Co-AsπSWCNTs** showing the lowest thermal stability with approximately 90% degradation at 700°C. NGQDs are less stable than GQDs because the additional nitrogen atoms readily decompose, compromising the nanomaterials' thermal stability.

TGA was also used to determine the loading of the various MPc complexes onto the respective nanomaterials, this was accomplished using a method reported in literature [190]. The method involves comparing the thermal decomposition of the MPc in their hybrids with that of the initial MPc before conjugation with reference to the thermal decomposition of the metallic nanoparticle [190]. The calculated loading values are tabulated in Table 3.3. The loading values will be briefly used to explain electrocatalysis in chapter 5.

3.4.4.6 Atomic Force Microscopy

The AFM characterisation was also undertaken. Figure 3.14 illustrates the profiles obtained for **Bi_2WO_6**, **$NiWO_4$** and their conjugates with **4-Co-As.** The nanoparticles were dispersed in water/ethyl alcohol Figure 3.14(A, C). The topographic image in Figure 3.14 (B) demonstrates the spherical flattened and polydispersed particles following the conjugation of MPcs to the nanomaterials. Figure 3.14 (B, D) shows that the introduction of MPcs to the nanomaterials resulted in aggregates and agglomerated particles.

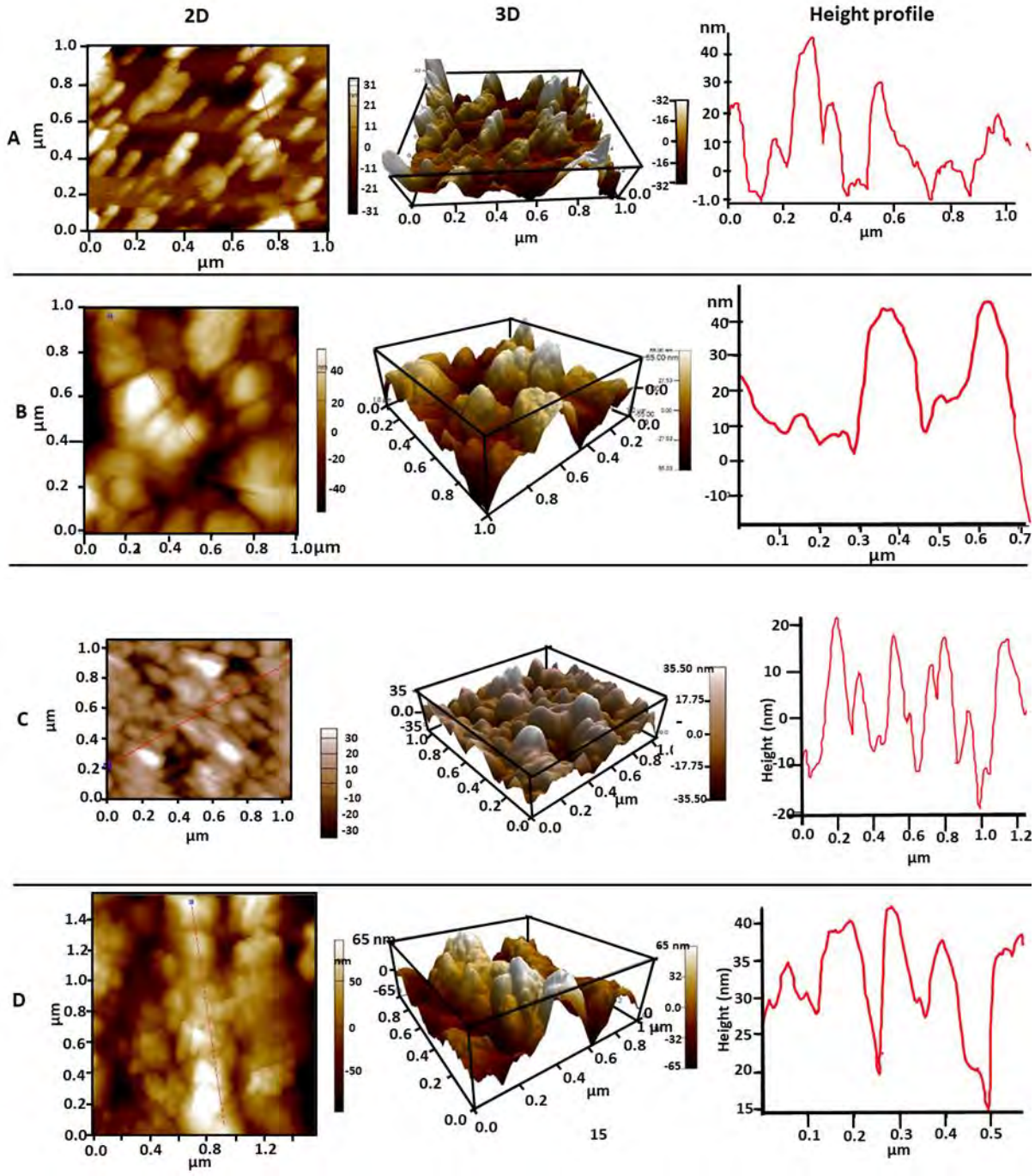

Figure 3.14: AFM images of (A) **Bi_2WO_6**, (B) **4-Co-As@Bi_2WO_6**, (C) $NiWO_4$, (D) **4-Co-As @$NiWO_4$**. (i) 2D surface topology, (ii) 3D surface topology, and (iii) line profiling.

Figure 3.15 is an illustration of the visual profiles obtained for **SWCNTs**, **GQDs and 2-CoπSWCNTs**. The 2-dimensional image reveals the **SWNCTs,** which look spherical with 60 nm height, Figure 3.15(A). The spherical look could be due to the fact that **SWCNTs** may lie on the surface in various directions [191]. However, the 3-dimensional image illustrates the cylindrical shape of **SWCNTs**. Correlation in topographic morphology between **SWCNTs** alone and when conjugated to phthalocyanine is demonstrated in Figure 3.15(B). Similarly, Figure 3.15(C) illustrates the distribution and thickness of the **GQDs**. The figures demonstrate dispersed particles, and the height shows an average thickness of 4 nm, suggesting that **GQDs** are multi-layered [178,192].

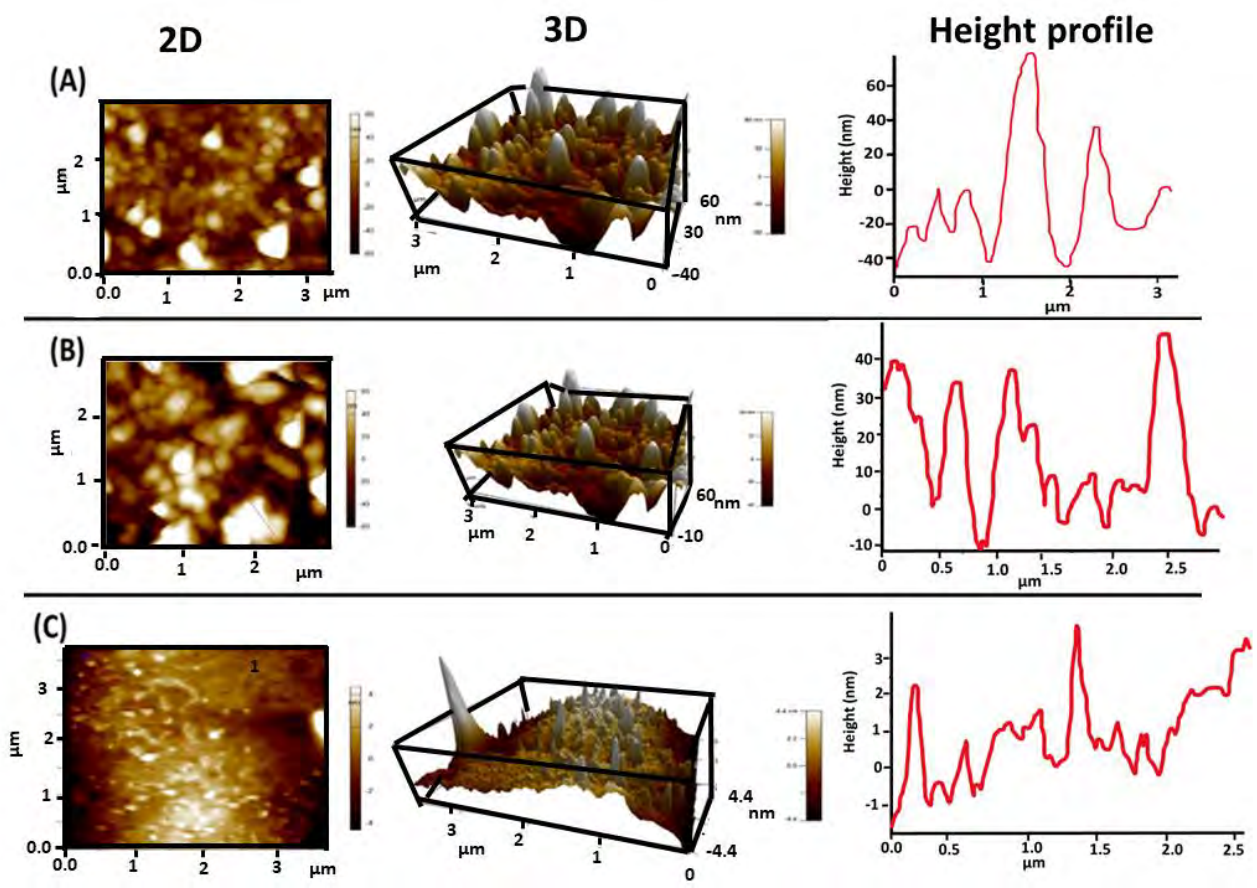

Figure 3.15: AFM images of (a) **SWCNTs**, (b) **2-CoπSWCNTs** and (c) **GQDs**

3.5 Conclusions

Seventeen phthalocyanine complexes were synthesised in this work, only four are known. These complexes were grouped as series based on either their central metal or substituents. This chapter gave an overview of the synthesis and characterisation of these complexes. Phthalocyanine complexes studied herein were synthesised using the condensation method, which requires refluxing a mixture of the desired phthalonitrile(s) with the metal salt and DBU in high boiling point solvents. The complexes were successfully characterised using UV-Vis absorption spectra, elemental analysis and FT-IR.

This chapter also characterised the nanomaterials synthesised in this work and the MPc-nanomaterial hybrids and conjugates. The carbon-based nanomaterials were successfully conjugated to the MPcs via non-covalent linkage, while the metallic nanomaterials were conjugated via covalent linkage. The hybridised complexes were characterised using various analytical techniques such as; Raman spectroscopy, DLS, AFM, XRD, and UV-Vis absorption.

CHAPTER 4

ELECTRODE MODIFICATION AND CHARACTERISATION

Preface: This chapter summarises the working electrode modification technique and the characterisation of the modified electrode surfaces using various electrochemistry techniques and principles.

4. ELECTRODE MODIFICATION AND CHARACTERISATION

Herein, the glassy carbon electrode was used as the working electrode of choice due to its chemically inert nature, the wide active potential window and the ease with which it can be modified to enhance these properties and achieve greater sensitivity and selectivity [52,53].

The bare (unmodified) GCE was modified with the synthesised MPc complexes, nanomaterials, and MPc-nanomaterial hybrids (employed as electrocatalysts) using the conventional drop-casting method. Drop casting is an adsorption method where a measured aliquot of the electrocatalyst is deposited onto the electrode surface and dried (in an oven) before use [35,193].

The modified electrode surfaces can be characterised using various analytical and electrochemical techniques. Herein, cyclic voltammetry, electrochemical impedance spectroscopy and scanning electrochemical microscopy were used to study surface modification and determine key parameters such as surface coverage and conductivity.

4.1 Comparative Cyclic Voltammetry (CV)

Figure 4.1(a) is an illustration of the cyclic voltammograms obtained for the bare glassy carbon electrode in 1 mM ferricyanide solution ($[Fe(CN)_6]^{3-/4-}$) using 0.1 M KCl as the supporting electrolyte. The observed CV is typical of a reversible reaction, characterised by the occurrence of both the anodic (E_{pa}) and cathodic (E_{pc}) peaks [194,195]. The peak-to-peak separation ($\Delta Ep = E_{pc} - E_{pa}$) of a clean GCE in a reversible system should be approximately 59 mV at 25 °C to indicate good, fast electron transfer at the electrode surface [195–197]. The ΔEp value obtained for the unmodified GCE used in this work was calculated to be 64 mV (Table 4.1), which is within range and indicative of good electron transfer.

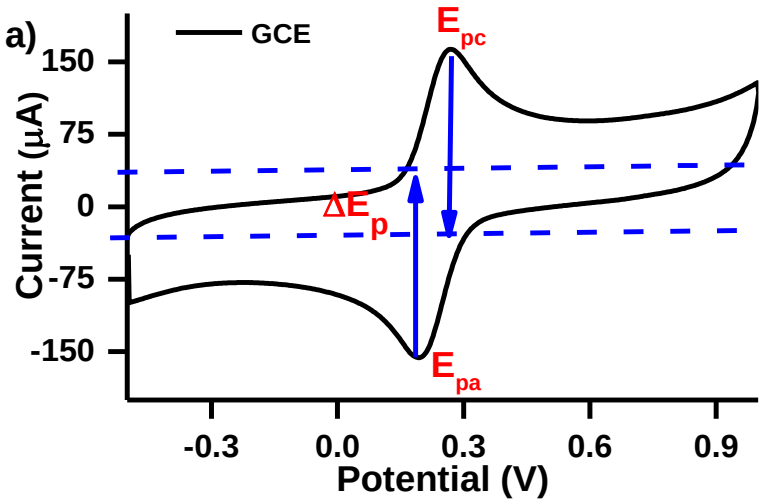
a)
GCE
E_{pc}
ΔE_p
E_{pa}
Current (μA)
150
75
0
-75
-150
-0.3
0.0
0.3
0.6
0.9
Potential (V)

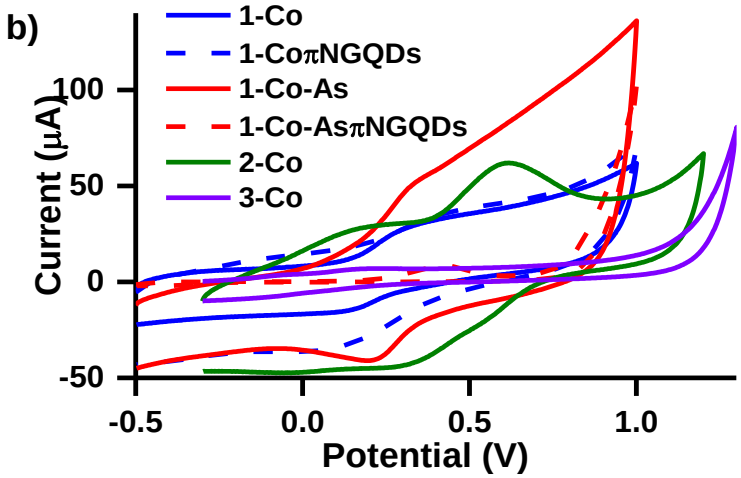
b)
1-Co
1-CoπNGQDs
1-Co-As
1-Co-AsπNGQDs
2-Co
3-Co
Current (μA)
100
50
0
-50
-0.5
0.0
0.5
1.0
Potential (V)

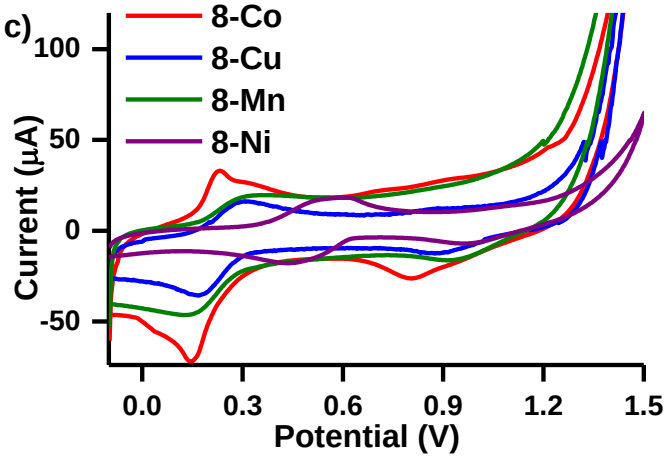
c)
8-Co
8-Cu
8-Mn
8-Ni
Current (μA)
100
50
0
-50
0.0
0.3
0.6
0.9
1.2
1.5
Potential (V)

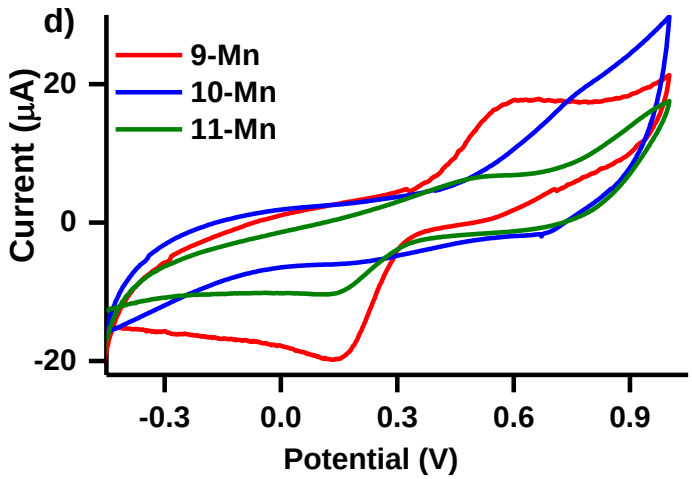

Figure 4.1: Cyclic voltammograms of (a) Unmodified GCE, (b) **1-Co**, **1-CoπNGQDs**, **1-Co-As**, **1-Co-AsπNGQDs**, **2-Co** and **3-Co**, (c) **8-Co**, **8-Cu**, **8-Mn** and **8-Ni** and (d) **9-Mn**, **10-Mn**, **11-Mn** in 1 mM $[Fe(CN)_6]^{3-/4-}$ (0.1 M KCl). Scan rate = 100 mVs^{-1}

Figures 4.1(b-d) show the cyclic voltammograms obtained for the modified electrode surfaces in the ferrocyanide redox couple solution at a scan rate of 100 mVs^{-1}. It can be observed that each electrode employed in this work behaved uniquely in the redox couple solution as each electrode surface had a unique CV profile. This is an indication that each modified surface has unique electron transfer capabilities [195,198]. Hence, each electrocatalyst studied in this work had a different ΔEp value (Table 4.1) and current.

In some cases, ΔEp could not be calculated due to the absence of the return peak (E_{pa}), meaning that the reaction at the electrode surface was either irreversible or oxidation occurred at a higher potential than the one studied herein. This was observed for **1-Co-AsπNGQDs**, **2-CoπSWCNTs**, **3-Co**, **3-CoπGQDs**, **3-CoπSWCNTs**, and **GQDs**. The lack of peaks in the redox couple solution is often correlated with poor charge transfer activity. This however, provides no information as to how the seemingly passivated electrode surface will interact with the analyte.

A lower ΔEp is highly desired in electrochemistry as it indicates that the electrode has good electron transfer abilities. However, this does not directly translate to the electron transfer properties of the electrocatalysts in the presence of the analyte. The following conclusions were drawn with regard to the electron transfer abilities of the unmodified and modified electrodes studied in the redox couple solution (Figure 4.1, Table 4.1):

i. An increase in the ΔEp value was observed upon modification. This is attributed to the electrode surface being modified (blocked) by the electrocatalysts [195].

ii. Lowering the symmetry of the MPc complex improved the electron transfer ability of the MPc (lower ΔEp).

iii. No apparent trend was observed with regard to the effect of the nanomaterials on the electron transfer abilities of the MPcs. Complex **4-Co-As** was conjugated to all nanomaterials used in this work. It was observed that incorporating nanomaterials enhanced the electron transfer abilities (a lower ΔEp was obtained) for all hybrids except for **4-Co-AsπSWCNTs** and **4-Co-AsπNGQDs**. However, for other hybridised materials, the change in ΔEp upon the incorporation of nanomaterials was inconsistent. For example, **1-Co** (170 mV) < **1-CoπNGQDs** (294 mV) and **2-Co** (309 mV) > **2-CoπGQDs** (88 mV).

iv. Regarding the substituents, the CuPc series showed that the formation of Schiff bases from the precursor, **5-Cu**, improved the electron transfer abilities. This is apparent from the relatively lower ΔEp values obtained for Schiff bases **6-Cu** and **7-Cu** compared to **5-Cu**. This was also observed with MPc Schiff base complex **11-Mn** formed from **9-Mn**. However, Schiff base **10-Mn** displayed a relatively higher

ΔEp than its precursor **9-Mn,** this is attributed to the sulphur atoms as they are generally oxidised at higher over potentials.

v. MnPcs displayed relatively higher and unfavourable ΔEp values compared to other MPcs. The ΔEp values of the **8**-series MPcs complexes were ranked as follows: **8-Co** < **8-Ni** < **8-Cu** < **8-Mn**.

4.2 Surface Coverage

Cyclic voltammetry was also used to determine the effective electrode area (surface roughness) and average surface coverage.

The effective electrode area was calculated using data obtained from Figure 4.1 fitted into the Randles-Sevcik Equation 4.1, for reversible systems, applied on the $[Fe(CN)_6]^{3-/4-}$ redox couple.

$$I_p = (2.69 \times 10^5)\, n^{3/2} A D^{1/2} C v^{1/2} \qquad (\mathbf{4.1})$$

where I_p, n, A, D, C and v represent the peak current, the number of electrons transferred (~ 1), the electrode area (cm^2), the diffusion coefficient of the electroactive species, the concentration of the redox couple solution ($K_3[Fe(CN)_6]^{3-/4}$), and the scan rate (Vs^{-1}) respectively. The diffusion coefficient for the redox couple employed was 7.6×10^{-6} $cm^2\ s^{-1}$. [199].

The calculated effective electrode area and the total charge of the electrocatalysts were calculated using CV scans in the buffer solution (Figure 4.2). Equation 4.2 was used to calculate the total surface coverage of the respective modified electrodes [200].

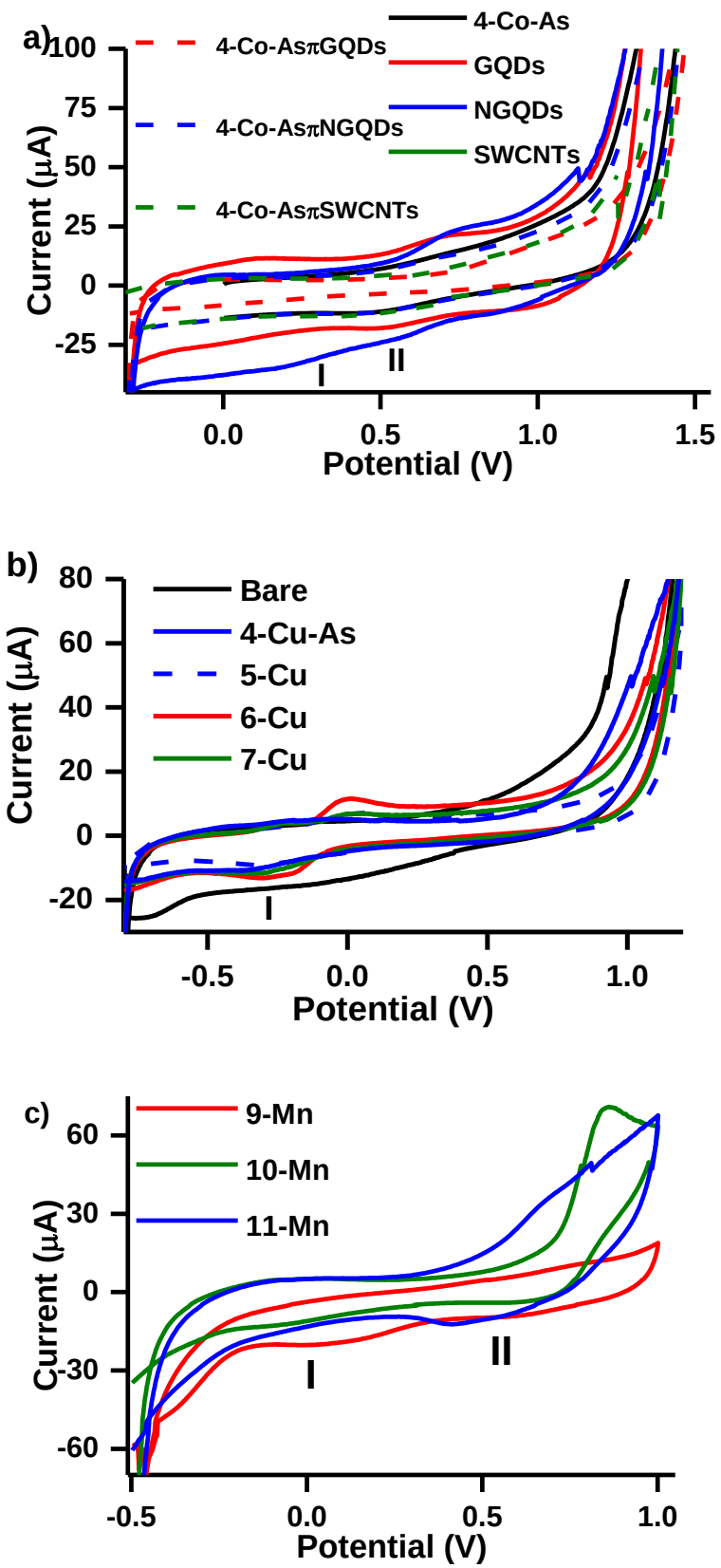

Figure 4.2: Cyclic voltammograms of (a) **4-Co-As, GQDs**, **NGQDs**, **SWCNTs** and their respective **4-Co-As** hybrids (b) **4-Cu-As**, **5-Cu**, **6-Cu** and **7-Cu** and (c) **9-Mn**, **10-Mn** and **11-Mn** in 0.1 M PBS buffer at pH 7. Scan rate = 100 mVs^{-1}

$$\Gamma = \frac{Q}{nFA} \quad (\mathbf{4.2})$$

where Γ is the surface coverage (mol.cm^{-2}), n is the number of electrons transferred (~ 1), F is the Faraday constant (96 485 C mol^{-1}), and A is the effective surface area obtained from Equation 4.1. The peak areas obtained in the buffer (Figure 4.2, labelled I and II) were integrated due to the broadness of the anodic peak. From the data obtained it was observed that for the **8**-series complexes, **8-Cu** has a relatively larger Γ value (Table 4.1) and this could be attributed to copper being relatively flatter. The Γ values (Table 4.1) will be discussed in chapter 5.

Table 4.1: Summary of the surface properties of the modified electrode surfaces, obtained in 1 mM $Fe(CN)_6^{3-/4-}$(0.1 M KCl supporting electrolyte)

Complex/Complex	**ΔEp (mV)**	**Γ (x 10^{-10} molcm^{-2})**	**R_{ct} (KΩ)**
GCE	64		0.7
1-Co	170	3.00 x 10^{-10}	5.67
1-CoπNGQDs	294	-[b]	12.3
1-Co-As	107	-[b]	16.8
1-Co-AsπNGQDs	-[a]	-[b]	15.4
2-Co	309	-[b]	4.38
2-CoπGQDs	88	-[b]	19.9
2-CoπSWCNTs	-[a]	-[b]	11.0
3-Co	-[a]	-[b]	6.95
3-CoπGQDs	-[a]	-[b]	13.1
3-CoπSWCNTs	-[a]	-[b]	13.8
4-Co	280	-[b]	7.20
4-Co-As	267	-[b]	24.7
4-Co-AsπGQDs	152	2.81 x 10^{-11}	6.58
4-Co-AsπNGQDs	-[a]	7.69 x 10^{-11}	28.8
4-Co-AsπSWCNTs	346	2.40 x 10^{-10}	116
4-Co-As@$NiWO_4$	123	-[b]	16.3
4-Co-As@Bi_2WO_6	251	-[b]	24.2

4-Cu-As	220	1.36×10^{-10}	11.6
5-Cu	214	1.87×10^{-10}	3.25
6-Cu	158	1.36×10^{-10}	28.0
7-Cu	60	1.95×10^{-10}	30.3
8-Co	77	1.07×10^{-10}	18.0
8-Cu	137	1.90×10^{-10}	14.0
8-Mn	190	1.29×10^{-10}	23.0
8-Ni	132	3.34×10^{-11}	22.0
9-Mn	446	6.24×10^{-10}	18.3
10-Mn	586	2.79×10^{-10}	22.6
11-Mn	375	1.85×10^{-10}	24.5
GQDs	-[a]	8.12×10^{-11}	6.17
NGQDs	188	2.59×10^{-11}	43.3
SWCNTs	127	1.95×10^{-10}	16.4
$NiWO_4$	105	-[b]	6.0
Bi_2WO_6	151	-[b]	32.0

[a] = No return peak, [b] = no peaks

4.3 Scanning Electrochemical Microscopy (SECM)

Scanning electrochemical microscopy is a microscopic technique used to characterise the electrode surface. An ultramicroelectrode (UME) tip is used as the probe. Throughout the study, the tip current is monitored. The current is affected by the; i) electroactive species at the probe, ii) conductivity of the electrocatalyst, and iii) distance between the tip and the electrode surface [201]. These factors determine the electrochemical, conductivity and topographic properties of the electrocatalysts.

Figure 4.3 illustrates the possible SECM mechanisms due to electron transfer at the tip perturbated by the electrode surface. The current observed depends on the nature of the electrode surface. If the surface is conductive, then diffusion of the electroactive species is enhanced, and the current increases due to the influx of redox species (Figure 4.3(b)). Whereas if the electrode surface is insulating, diffusion is blocked (movement of electrons is hindered) and therefore, the current decreases (Figure 4.3(c)) [201,202]. Figure 4.3(a) shows how diffusion typically occurs.

This work employed the SECM approach curves to characterise the electrode surfaces and determine the conductivity of the electrocatalysts. The approach curves (Figure 4.4) illustrate the changes in tip current as the ultra-micro electrode (UME) tip approaches the substrate in a feedback mode experiment in the presence of the Fe^{3+}/Fe^{2+} redox mediator. The approach curves were obtained in a 5 mM $[Fe(CN)_6]^{3-/4-}$ solution (0.1 M KCl), where d/a is the normalised distance, (µm), and I/I_{Lim} is the normalised current. Approach curves are obtained by lowering the tip towards the surface. Data obtained from the approach curves illustrates the conductivity of the surface in relation to the distance from the electrode surface [202,203].

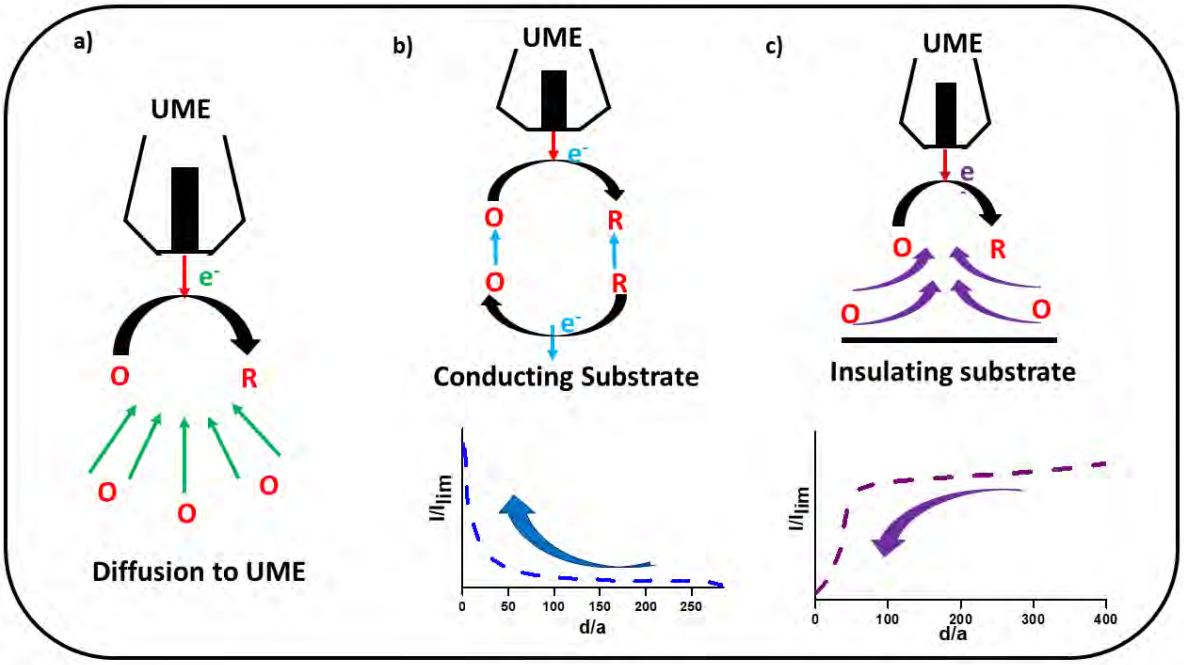

Figure 4.3: Basic Principles of SECM mechanisms (a) diffusion and approach curves on (b) conducting and (c) insulating substrates

Figure 4.4(a) is a representation of the typical approach curves obtained for the bare carbon plate (BCP) and Teflon. It can be observed that the current increases as the tip approaches the bare electrode and proving that the bare electrode is an electron conductor [204,205]. The Teflon surface is insulating, and non-conductive. Therefore, it hinders diffusion resulting in a decrease in current, as observed in Figure 4.4(a) [204–206]. The MPcs, nanomaterials, and their hybrid materials are generally electron-conducting complexes/materials.

Figure 4.4(b) is an illustration of the SECM approach curve obtained for the chalcone MPcs, where the effect of the central metal was studied. From the figure, it can be observed that **8-Co**, **8-Cu**, **8-Mn** and **8-Ni** are all relatively good electron conductors, better than the unmodified electrode surface as judged by d/a values at 0, contradicting the ΔEp values obtained. **8-Mn** displayed the lowest conductivity (at d/a = 0), with the overall conductivity

results obtained in the redox couple solution being as follows; **8-Co**>**8-Cu**>**8-Ni**>**8-Mn**. This trend could be related to conductivity (Siemens/m) of the central metals: Cu = 6.0×10^7 > Co = 1.6×10^7, > Ni = 1.5×10^7 > Mn = 6.2×10^5 [207].

Figure 4.4(c) shows the approach curves obtained for symmetric complex **1-Co**, asymmetric complex **1-Co-As**, **NGQDs** and the hybrids obtained from the two complexes with NGQDs. This study was conducted to investigate whether nanomaterials enhance the conductivity of MPcs and whether symmetry influences electron conductivity. The MPc complexes and their hybrid materials exhibited relatively reduced electron conductivity compared to the unmodified electrode. This confirmed the ΔEp results obtained from the CVs in Figure 4.1 (summarised in Table 4.1). **1-Co** exhibited relatively higher electron conductivity compared to **1-Co-As**, thus lowering the symmetry of the complex did not enhance its electron conductivity behaviour. However, no obvious trend was observed with regard to the effect of nanomaterials on the electron conductivity of MPc complexes.

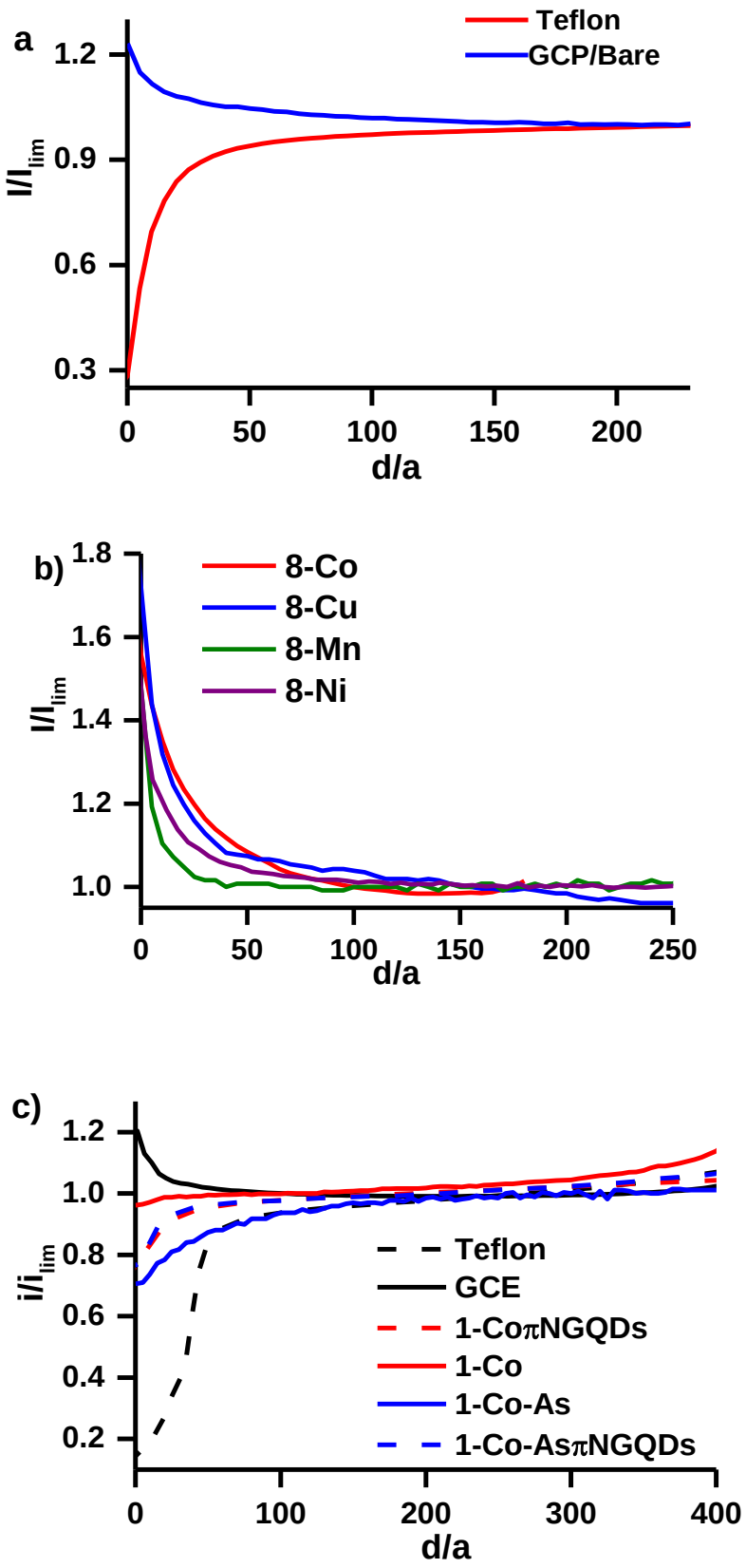

Figure 4.4: SECM approach curves of (a) Bare GCP and Teflon (b) **8-Co**, **8-Cu**, **8-Mn** and, **8-Ni**, and (c) **1-Co**, **1-Co-As** and their NGQDs hybrids

4.4 Electrochemical Impedance Spectroscopy (EIS)

Electrochemical impedance spectroscopy is one of the most important techniques used to study the electrochemical systems and processes at the electrode surface [194,208]. EIS was conducted to characterise the working electrode surfaces (bare and modified) by determining the transfer kinetics in the ferrocyanide redox couple solution.

EIS data is interpreted using models with equivalent electrical current elements, the elements are attributed to physical processes in the system, such as charge transfer resistance (R_{ct}) and the double layer capacitance (C_{dl}) or constant phase element (CPE) [208,209]. The model used in this work is the Randles circuit equivalent (Figure 4.5), where R_s is the solution resistance, and Z_W is the Warburg impedance [209].

EIS data is most commonly represented using Nyquist plots (Figure 4.6). In the Nyquist plots, frequency is plotted as the imaginary part (Z") versus the real part (Z') in Ohms [210]. These Nyquist plots were used to determine the R_{ct} values, which in the plots is the size of semi-circle [210].

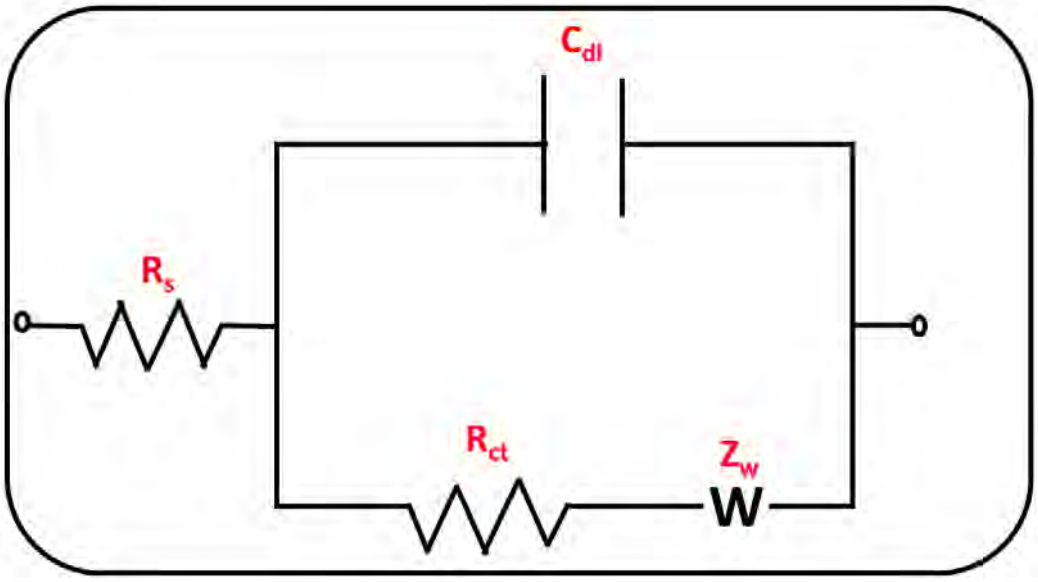

Figure 4.5: Randles equivalent circuit

R_{ct} values obtained in this work are tabulated in Table 4.1. A low R_{ct} value is indicative of good electron transfer. The lowest R_{ct} value of 0.7 kΩ, was calculated for the unmodified electrode. This confirms the ΔEp values obtained where the bare electrode accounted for the lowest ΔEp, which translates to the best electron transfer abilities compared to the studied complexes, nanomaterials and hybrids. Upon electrode modification, the R_{ct} values obtained increased as expected since the electrode surface had been modified/blocked. R_{ct} values generally follow the same trend as ΔEp.

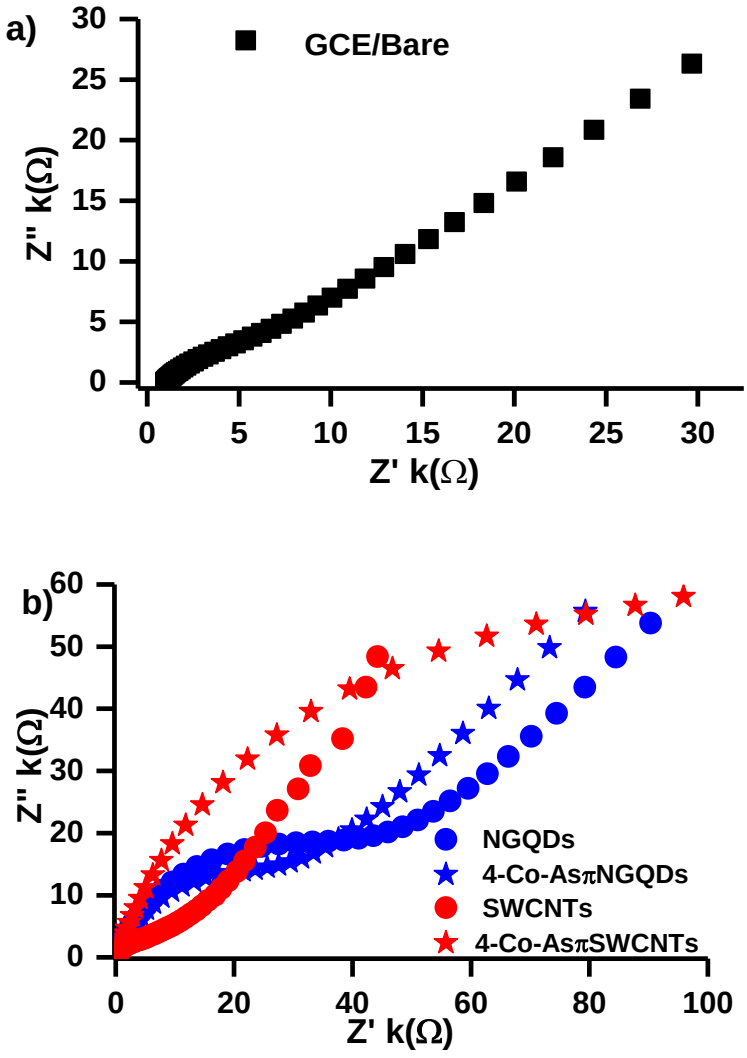

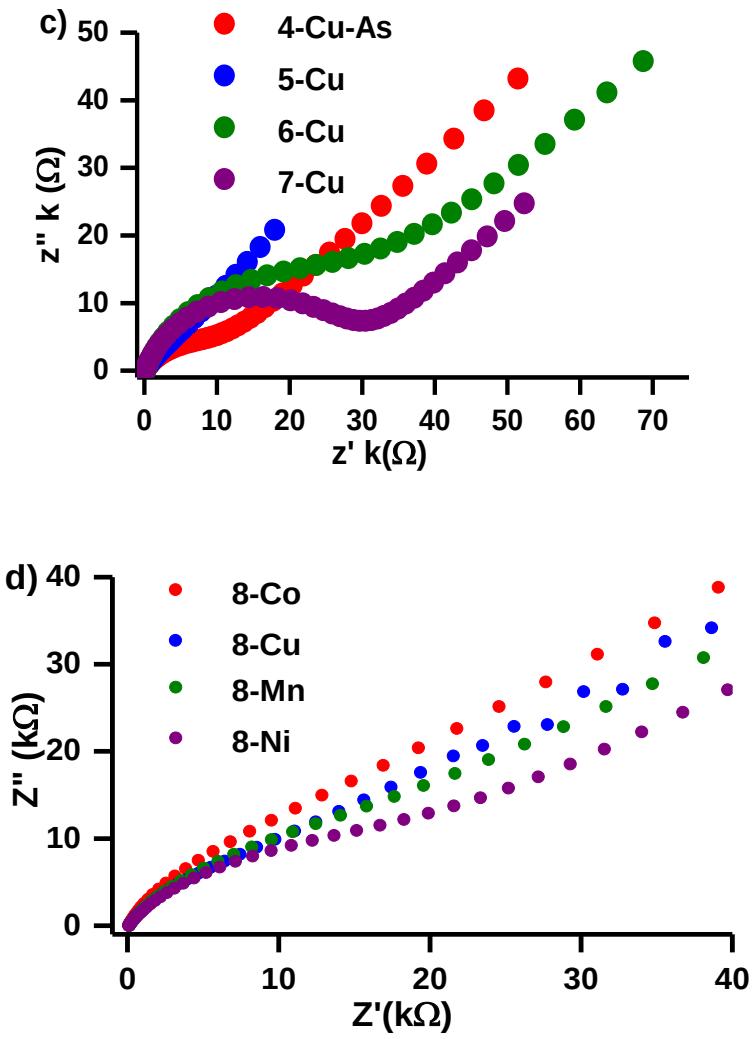

Figure 4.6: Nyquist plots of (a) bare GCE, (b) **NGQDs**, **SWCNTs** and their **4-Co-As** hybrids, (c) **4-Cu-As**, **5-Cu**, **6-Cu** and **7-Cu** and (d) **8-Co**, **8-Cu**, **8-Mn** and **8-Ni** obtained in 1 mM $[Fe(CN)_6]^{3-/4-}$

4.5 Conclusions

This chapter was based on characterising the working electrode surface and determining key parameters. The glassy carbon electrode (glassy carbon plate for SECM experiments) was used as the working electrode of choice and modified using the conventional drop-casting method. The electrode surface was modified with the synthesised phthalocyanine complexes, nanomaterials and their respective hybrids, which were used as electrocatalysts. The modified electrode surfaces were primarily characterised in the ferrocyanide redox couple solution.

Cyclic voltammetry was used to determine the peak-to-peak separation and whether the GCE was indeed modified, and its ability to transfer electrons after modification. An expected increase in the ΔEp value was observed upon electrode modification for most electrodes but in some cases no return peaks were observed. This is because all these complexes did not show the cathodic (reverse) peak.

CV scans in both the redox couple solution and the buffer were used to calculate the effective electrode area and the surface coverage. Electrochemical impedance spectroscopy and scanning electrochemical microscopy were successfully used to determine the conductivity of the studied electrocatalysts.

CHAPTER 5

ELECTROCATALYSIS

Preface: This chapter summarises the electrocatalytic properties of the studied electrocatalysts (MPcs, nanomaterials and hybrids). It also provides the detection properties of the electrocatalysts when employed in the electrochemical detection of nitrite, catechol, and dopamine.

5. ELECTROCATALYSIS

5.1 Nitrite

5.1.1 Comparative Cyclic Voltammetry

Cyclic voltammetry was employed to study the electrocatalytic behaviour of the electrocatalysts employed in this work. MPc complexes **4-Co**, **4-Co-As** and its MPc-nanomaterial hybrids, and **8-11** were employed as electrocatalysts to detect nitrite. Figure 5.1 is an illustration of the cyclic voltammograms obtained in the presence of nitrite. The electrocatalysts studied herein exhibited different CV profiles in nitrite. This suggests that each electrocatalyst responded uniquely to nitrite and exhibited different nitrite detection properties. From the figure, it can be observed that the studied complexes only showed oxidation peaks. Therefore, it can be concluded that the electrooxidation of nitrite using MPc complexes (and nanomaterials) is irreversible.

The nitrite oxidation peak potentials (Ep) obtained in this work ranged between 0.65 V and 1.09 V (Table 5.1). These were in accordance with the peak potentials obtained in literature for the electrochemical oxidation of nitrite [211–219]. Generally, in electrochemistry, a good electrocatalyst is classified by its ability to detect the analyte of interest at low oxidation peak potentials and high currents. The following observations were drawn from the cyclic voltammograms in Figure 5.1(a-c) about the oxidation peak potentials and currents obtained from the electrooxidation of nitrite (Table 5.1):

i. The unmodified glassy carbon electrode did not display a nitrite oxidation peak, indicating that it could not detect nitrite at the studied potential window. However, upon modification, nitrite oxidation peaks were observed.

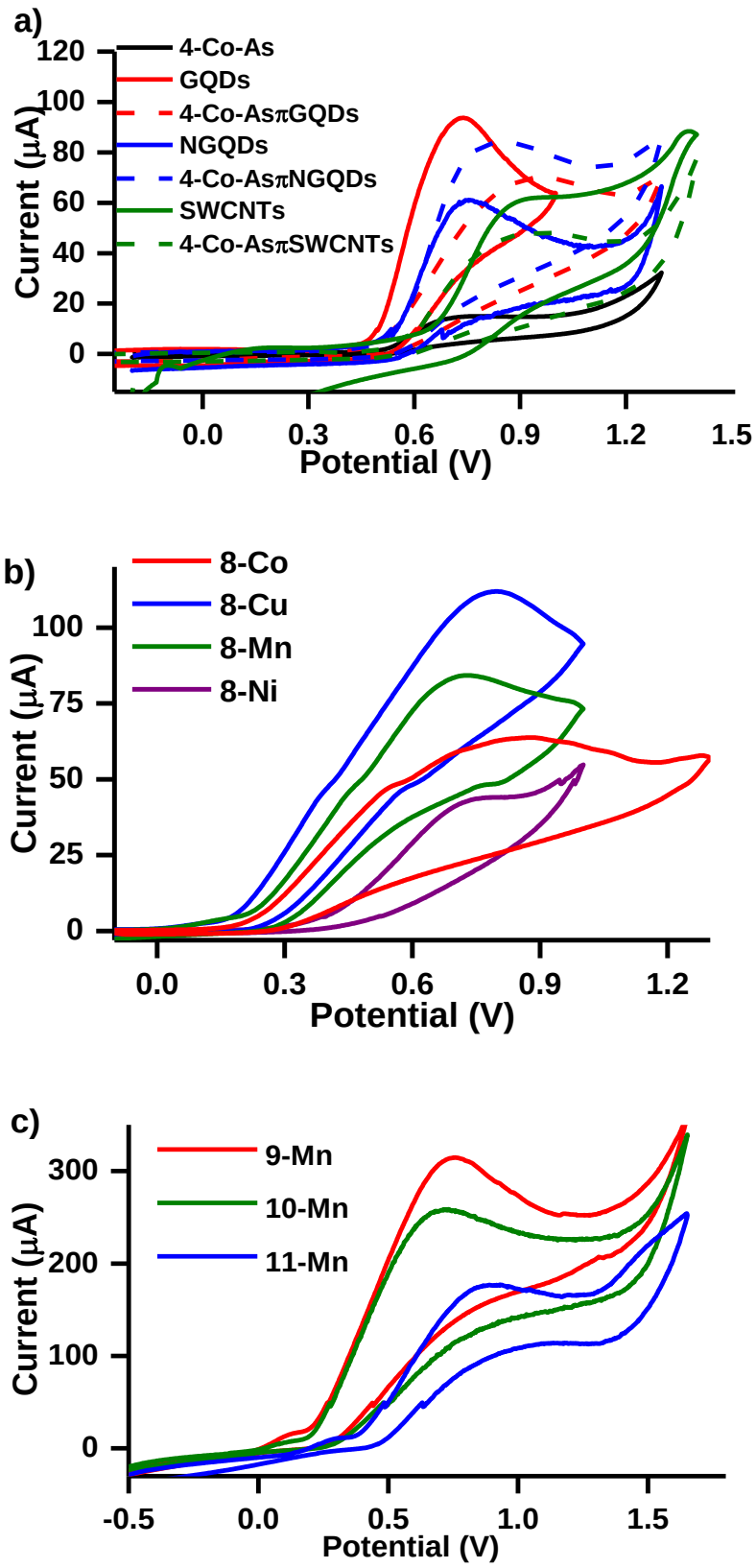

Figure 5.1: Cyclic voltammograms of (a) **4-Co-As**, **GQDs**, **NGQDs**, **SWCNTs** and their respective hybrids, (b) **8-Co**, **8-Cu**, **8-Mn** and **8-Ni** and (c) **9-Mn**, **10-Mn** and **11-Mn** in 2 mM nitrite solution in 0.1 M pH 7 PBS. Scan rate = 100 mVs^{-1}

ii. **Symmetry**: Herein, the symmetric MPc complex (**4-Co**) exhibited more favourable nitrite detection properties than the asymmetric complex (**4-Co-AS**) as it gave a lower oxidation peak potential and higher current. This suggests that lowering the symmetry of an MPc does not necessarily enhance its electrocatalytic properties

iii. **Effect of nanomaterials**: With regard to the oxidation peak potentials, the incorporation of nanomaterials did not enhance the ability of **4-Co-As** to detect nitrite at low potentials. Electrocatalyst **4-Co-As** alone displayed a nitrite oxidation peak at 0.68 V. Upon conjugation with the studied nanomaterials, the oxidation peak potential increased to potentials as high as 1.09 V (for **4-Co-As@$NiWO_4$**). However, the incorporation of nanomaterials did enhance the sensitivity of the MPc electrocatalyst, as the obtained oxidation peak currents increased upon conjugation from 7 μA to currents as high as 84 μA.

Of the nanomaterials employed herein, **Bi_2WO_6** alone exhibited the most favourable and lowest oxidation peak potential (0.65 V), while **GQDs** exhibited the highest faradic oxidation peak current (94 μA).

iv. **Central metal**: Overall, the manganese phthalocyanine complexes employed as electrocatalysts in this work (except **8-Mn**) displayed the highest oxidation peak current towards nitrite. This is evident in their ability to detect nitrite in relatively higher faradic currents (82 μA to 316 μA) compared to other MPcs studied herein.

Table 5.1: Summary of the nitrite electrooxidation properties obtained in 2 mM nitrite (in 0.1 M pH 7 PBS)

Electrode	Ep (V)	Background corrected oxidation peak current (μA)	Tafel slope (mV decade^{-1})
GCE	-	-	-
4-Co	0.65	32	165
4-Co-As	0.68	7	237
GQDs	0.74	94	138
4-Co-AsπGQDs	0.94	70	434
NGQDs	0.75	61	171
4-Co-AsπNGQDs	0.93	84	378
SWCNTs	0.86	59	140
4-Co-AsπSWCNTs	0.91	48	563
Bi_2WO_6	0.65	10	84
4-Co-As@Bi_2WO_6	0.97	38	442
$NiWO_4$	0.79	14	330
4-Co-As@$NiWO_4$	1.09	45	912
8-Co	0.86	64	530
8-Cu	0.80	112	442
8-Mn	0.72	82	264
8-Ni	0.75	44	-[a]
9-Mn	0.74	316	582
10-Mn	0.84	177	710
11-Mn	0.70	270	252

[a]No oxidation peak below 50 mVs^{-1}

v. **Substituents**: Schiff bases complexes, **10-Mn** and **11-Mn,** were formed from **9-Mn** to investigate whether Schiff bases enhance the electrocatalytic behaviour of MPc complexes. Figure 5.1(c) (Table 5.1) illustrates that there was a decrease in the oxidation peak current. The effect of Schiff bases on the oxidation peak potential was inconclusive, as the peak potential increased for **10-Mn** and decreased for **11-Mn**. The increase in oxidation peak potential of **10-Mn** can be attributed to the thiol on the Schiff base. Sulphur atoms generally result in oxidation peaks at high over potentials.

5.1.2 Mechanism and Kinetics Studies

Herein, kinetic studies were conducted to determine the reaction kinetics, parameters and mechanisms of the electrocatalyst's reaction towards the electrooxidation of nitrite. These experiments were conducted using cyclic voltammetry by varying the scan rates while keeping each electrocatalyst's concentration and potential window constant.

The mechanism of nitrite oxidation is well-studied and understood. Equations 5.1 and 5.2 summarise the reaction mechanism of the electrooxidation of nitrite [220–222].

$$NO_2^- \leftrightarrow + NO_2 + e^- \quad (\mathbf{5.1})$$

$$2NO_2 + H_2O \leftrightarrow 2H^+ + NO_2^- + NO_3^- \quad (\mathbf{5.2})$$

Equation 5.1 shows the heterogenous transfer of an electron, from nitrite, forming nitrogen dioxide. While Equation 5.2 shows the formed nitrogen dioxide undergoing homogenous disproportion forming nitrite and nitrate ions.

Although not much research has been done with regard to studying the electrochemical interaction of nitrite and phthalocyanine complexes. It is understood that ring-based redox processes are involved in the electrocatalytic processes with phthalocyanine complexes that contain an electro-inactive central metal. The following mechanisms have been proposed (Equations 5.3 and 5.4) [223]:

$$MPc(-2) \rightarrow [MPc(-1)]^{+\cdot} + e^- \quad (\mathbf{5.3})$$

$$[MPc(-1)]^{+} + O \rightarrow MPc(-2) + R \quad (\mathbf{5.4})$$

Where O and R denote oxidised and reduced species, respectively. Studies have shown that cobalt phthalocyanine complexes interact with nitrite ions in aqueous media [224,225]. Equations 5.5 – 5.7 summarise the proposed mechanisms for the electrooxidation of nitrite involving cobalt phthalocyanine complexes [224,226,227].

$$Co^{II}Pc + NO_2^- \leftrightarrow [Co^{II}Pc(NO_2^-)]^- \quad (\mathbf{5.5})$$

$$[Co^{II}Pc(NO_2^-)]^- \leftrightarrow [Co^{III}Pc(NO_2^-)] + e^- \quad (\mathbf{5.6})$$

$$[Co^{III}Pc\ (NO_2^-)] + H_2O \rightarrow Co^{II}Pc + NO_3^- + 2H^+ + e^- \quad (\mathbf{5.7})$$

Equation 5.5 is suggested since the coordination of nitrite to $M^{II}Pc$ was confirmed by UV-visible studies for CoPc complexes [226]. Equation 5.6, on the other hand, involves the electrooxidation of $Co^{II}Pc$ to $Co^{III}Pc$ since nitrite undergoes oxidation in the presence of $Co^{III}Pc$ species. Equation 5.7 is proposed because nitrate is the most common nitrite oxidation product and the total number of electrons involved is two [227].

Equations 5.8 – 5.10 have been proposed for the electrooxidation of nitrite using manganese (II) phthalocyanine complexes as electrocatalysts [228]:

$(L^{-})Mn^{III}Pc + NO_2^{-} \rightarrow (NO_2^{-})Mn^{III}Pc + L^{-}$ (**5.8**)

$(NO_2^{-})Mn^{III}Pc \rightarrow [Mn^{II}Pc] + NO_2$ (**5.9**)

$[Mn^{II}Pc] \rightarrow [Mn^{III}Pc]^{+} + e^{-}$ (**5.10**)

Equation 5.8 is proposed since the linkage of nitrite to Mn(III)Pc and the displacement of the axial ligand have been reported [226]. Equation 5.9 is suggested since the reduction of the Mn(III)Pc to $[Mn(II)Pc]^{-}$ by nitrite is known [226]. Equation 5.10, on the other hand, is suggested since the $[Mn(II)Pc]^{-}$ is oxidised back to Mn(III)Pc [226].

Since CuPcs and NiPcs only utilise ring-based redox processes. Equations 5.3 and 5.4 are the proposed mechanisms for their electrocatalytic reactions with nitrite.

Figures 5.2(a) and 5.3(a) are an illustration of the cyclic voltammograms obtained for **4-Co-AsπGQDs** and **9-Mn,** respectively (as examples), in 2 mM nitrite solutions, at varied scan rates.

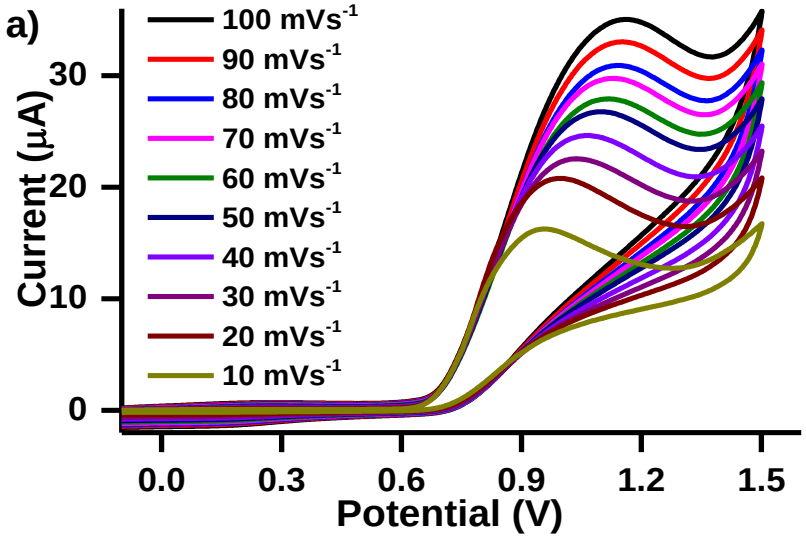

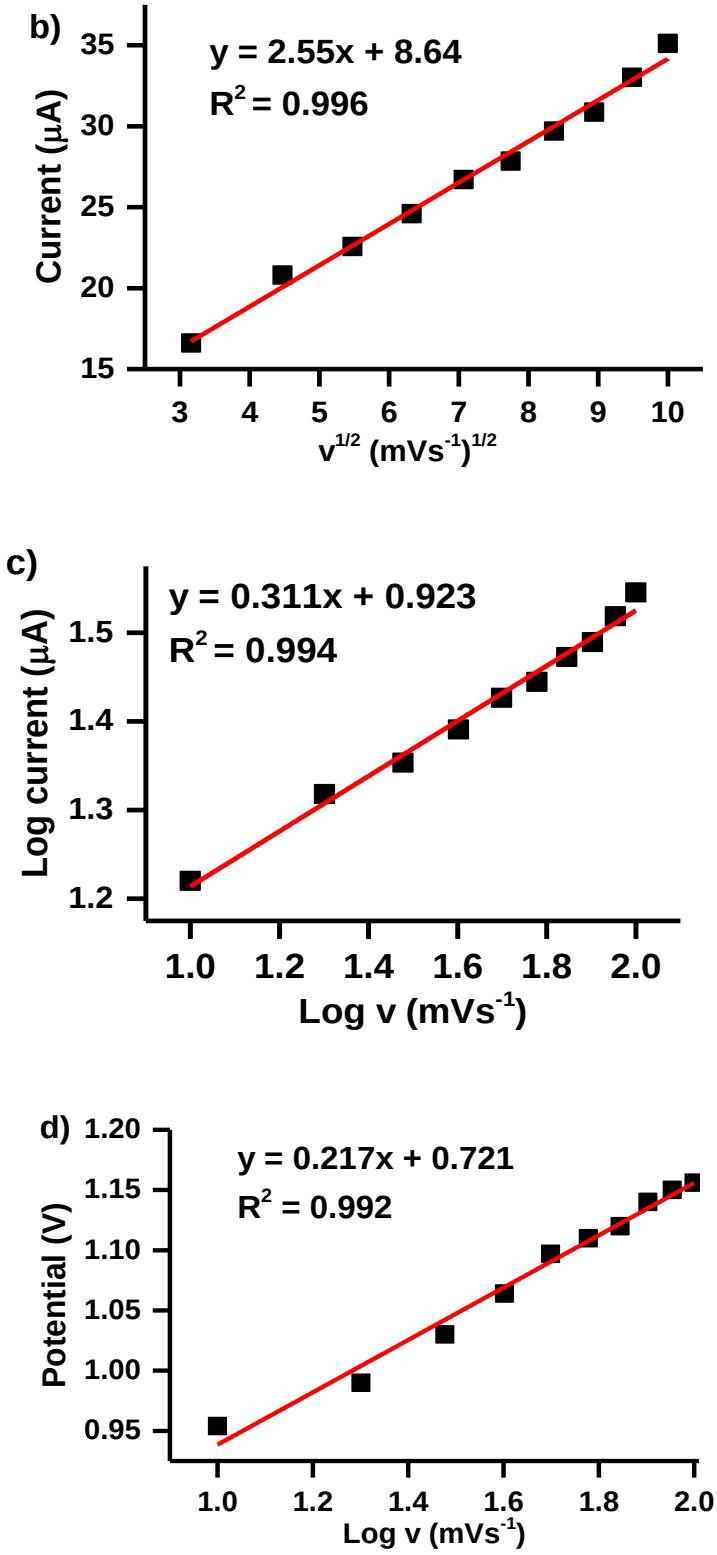

Figure 5.2: (a) cyclic voltammograms obtained in 2 mM nitrite (in 0.1 M pH 7 PBS) at varied scan rates, (b) plot of oxidation peak current vs the square root of the scan rate, (c) log of oxidation peak current vs log of scan rate and (d) plot of oxidation peak potential vs log of scan rate. All plots were generated from **4-Co-AsπGQDs**.

For all the CVs obtained in this study, an increase in the scan rate resulted in an increase in the oxidation peak current and a shift in the oxidation peak potential (to the more positive values). This confirms the irreversibility of the nitrite oxidation reaction at the modified electrode surface.

Figures 5.2(b) and 5.3(b) show the linear relationship between the oxidation peak current and the square root of the corresponding scan rate (data extrapolated from Figures 5.2(a) and 5.3(a). Figures 5.2(b) and 5.3(b) were used to determine the reaction mechanism between nitrite and the electrocatalysts on the electrode surface. The linearity of the plots suggests that an irreversible diffusion-controlled reaction occurred at each electrode surface [195,229].

Figures 5.2(c) and 5.3 (c) were used to additionally confirm whether the electrode surfaces' reaction processes were diffusion or adsorption-controlled. These figures are plots of the log of the oxidation peak current against the log of the scan rate and are the most accurate measure of electrochemical reaction processes. A slope below 0.5 suggests that the reaction at the electrode surface is diffusion-controlled, and slopes above 0.5 are attributed to adsorption occurring at the electrode surface [229,230]. The slopes obtained herein were below 0.5, indicating that the electrochemical reactions involving nitrite and the electrocatalysts studied in this work were diffusion-controlled, as suggested by the data obtained from Figures 5.2(b) and 5.3(b).

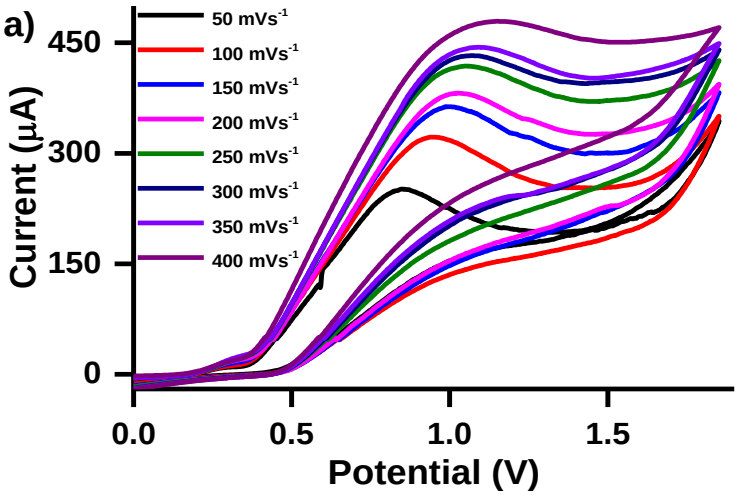
a)
50 mVs-1
100 mVs-1
150 mVs-1
200 mVs-1
250 mVs-1
300 mVs-1
350 mVs-1
400 mVs-1
Current (μA)
450
300
150
0
0.0
0.5
1.0
1.5
Potential (V)

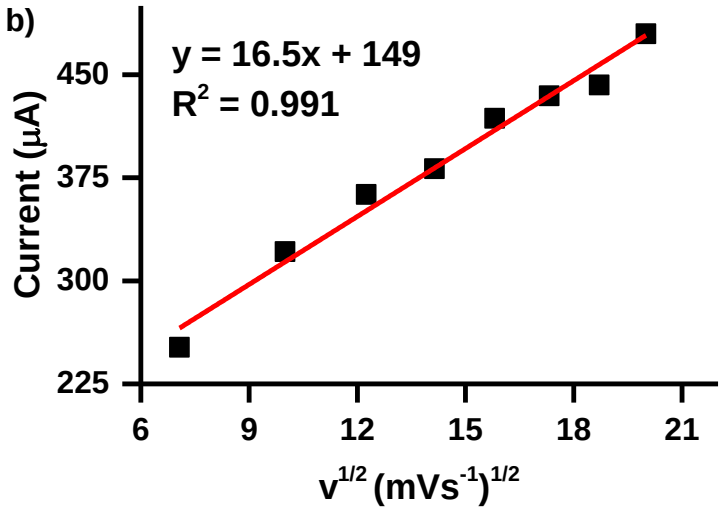
b)
y = 16.5x + 149
R2 = 0.991
Current (μA)
450
375
300
225
6
9
12
15
18
21
v1/2 (mVs-1)1/2

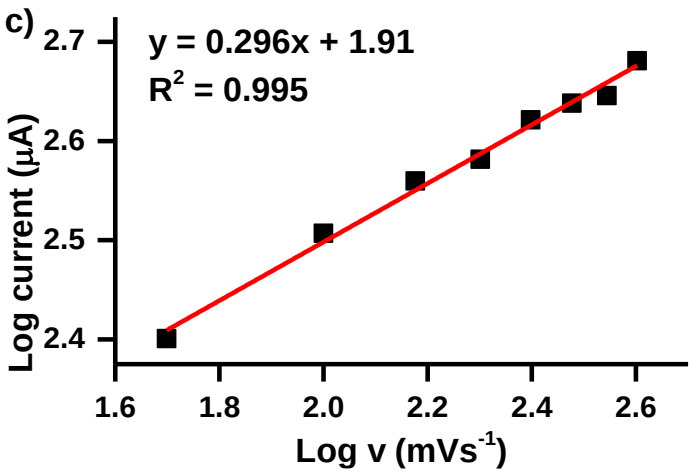
c)
y = 0.296x + 1.91
R2 = 0.995
Log current (μA)
2.7
2.6
2.5
2.4
1.6
1.8
2.0
2.2
2.4
2.6
Log v (mVs-1)

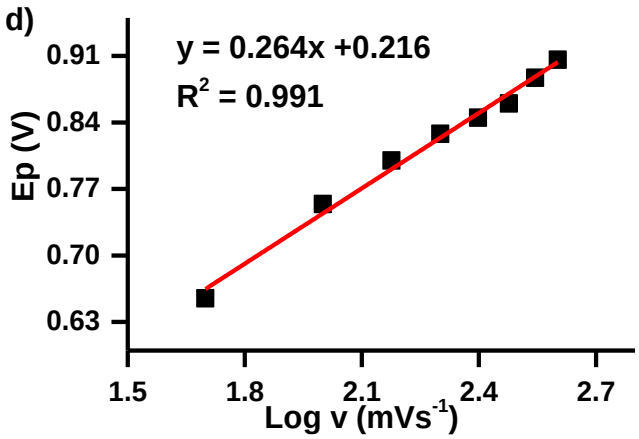

Figure 5.3: (a) cyclic voltammograms obtained in 2 mM nitrite (in 0.1 M pH 7 PBS) at varied scan rates, (b) plot of oxidation peak current vs the square root of the scan rate, (c) log of oxidation peak current vs log of scan rate and (d) plot of oxidation peak potential vs log of scan rate. All plots were generated from **9-Mn**

Tafel slopes are a graphical point used to measure the efficiency with which an electrode can produce a current in response to the change in potential [231]. Herein, Tafel slopes were calculated using Figures 5.2(d) and 5.3(d), linear plots representing the oxidation peak potential against the log of the scan rate. The data were fitted into Equation 5.11 to calculate the Tafel slopes [225,232].

$$E_p = \frac{b}{2}\log v + K \qquad \textbf{(5.11)}$$

where; b is equivalent to the Tafel slope, K is a constant and v represents the scan rate. Tafel slopes between 60 and 120 mVdecade^{-1} are highly favourable as they indicate the occurrence of a one-electron transfer process during the rate-determining step, where the electron transfer coefficient (α) = 1 [233–235].

The Tafel slopes obtained in this work ranged between 84 mVdecade^{-1} and 912 mV decade^{-1} (Table 5.1). Tafel slopes above 120 mV decade^{-1} have no kinetic meaning and suggest the possibility of chemical complications on the surface of the electrode [233]. However, factors other than the reaction mechanism have been reported to affect the reaction kinetics, resulting in high Tafel slope values [236,237]. Factors such as; electrode surface defects, potential window, solvent environment, temperature and the number of active sites also influence the Tafel slope. An increase in the Tafel slopes was observed upon the conjugation of MPcs to nanomaterials.

5.1.3 Sensitivity and Detection Limits Studies

Chronoamperometry was used to study the catalytic reaction kinetics and determine the limits of detection (LoD). Chronoamperometry involves the study of current as a function of time at a specified potential. The potential applied for each electrocatalyst is the nitrite oxidation peak potential obtained from the cyclic voltammograms in *Section 5.1.1*. Figures 5.4 and 5.5 illustrate the chronoamperograms obtained for **4-Co-AsπGQDs**, **9-Mn** and **11-Mn** (as examples).

These chronoamperograms were obtained from running chronoamperometry scans for 30s at varied nitrite concentrations. The concentration of nitrite was increased by 0.1 mM for each subsequent scan. The linear concentration range used throughout this work was 0 µM to 1000 µM. From the figures, it can be observed that an increase in the current was detected upon the increase in nitrite concentration. This was the case for all studied electrocatalysts.

The inserts in Figures 5.4(a) and 5.5(a) are calibration plots of the concentration vs the corresponding currents obtained from the chronoamperograms of each electrocatalyst. The

LoDs were calculated using these calibration curves. When calculating the LoD, the slope of the calibration curve (electrocatalyst sensitivity) was utilised in Equation 5.12.

$$LoD = \frac{3\delta}{S} \quad \textbf{(5.12)}$$

where S is the slope of the calibration curve, and δ represents the standard deviation of 30 chronoamperograms run in the buffer (blank scans). Table 5.2 provides a summary of the sensitivities, limits of detection and catalytic rate constants obtained from the electrocatalysts studied herein. The following observations and comparisons can be made from the results obtained:

i. **Symmetry**: **4-Co**, Bi_2WO_6 and **4-Co-As@Bi_2WO_6** exhibited the lowest and most favourable LoDs of 0.12/0.13 µM. While **4-Co-As** had the second-highest detection limit (1.7 µM, **8-Ni** had the highest LoD, 1.8 µM). **4-Co** also had a relatively higher sensitivity of 21 µA.µM^{-1} value when compared the sensitivity of 7 µA.µM^{-1} calculated for **4-Co-As**. This suggests that the decrease in symmetry did not improve the electrocatalytic properties of **4-Co-As**.

ii. **Central metal**: **8-Ni** performed the worst as an electrocatalyst towards the detection of nitrite, giving the highest LoD in this work (1.8 µM). Its sensitivity of 12 µA.µM^{-1} was the lowest and least favourable in its chalcone complex **8**-series. The order based on detection limits for this series is as follows; **8-Ni** > **8-Cu** > **8-Mn** > **8-Co**, these results are in line with the electrocatalytic activity ranking reported by Ding and colleagues based on the favourability of central metal for electrocatalysis [60]. **8-Co** outperformed the other electrocatalysts obtaining the highest sensitivity (59 µA.µM^{-1}) and lowest detection limit (0.18 µM).

iii. **Substituents**: Forming Schiff base complexes **10-Mn** and **11-Mn** from complex **9-Mn**, enhanced the detection limit and sensitivity towards nitrite. This is observed in a favourable decrease in the detection limit by almost just above two folds from 0.59 µM (**9-Mn**) to 0.16 and 0.24 for **10-Mn** and **11-Mn,** respectively. An increase in sensitivity was also observed upon the formation of Schiff bases. Schiff bases showed good nitrite detection abilities.

iv. **Effect of nanomaterials**: The tabulated results show that the MPc-nanomaterial hybrids generally outperformed their precursor MPc (**4-Co-As**). A favourable decrease in the detection limit and an increase in the sensitivity were observed upon hybridisation/conjugation, when using **4-Co-As** as a point of reference. Therefore, incorporating nanomaterials into the MPc enhanced its nitrite detection ability (LoD and sensitivity). However, unlike other studied hybrids, **4-Co-AsπSWCNTs** (1.0 µM) and **4-Co-As@NiWO$_4$** (0.80 µM) exhibited LoD values relatively higher than their nanomaterials whose LoD were calculated to be 0.44 µM and 0.41 µM respectively. This can be attributed to SWCNTs and Bi_2WO_6 having relatively lower loading values (lower than GQDs).

v. **Comparison with literature:** The LoDs and sensitivities obtained in this work are similar and in some cases better than those obtained in literature for similar complexes and hybrids (Table 5.2) [211–218,238].

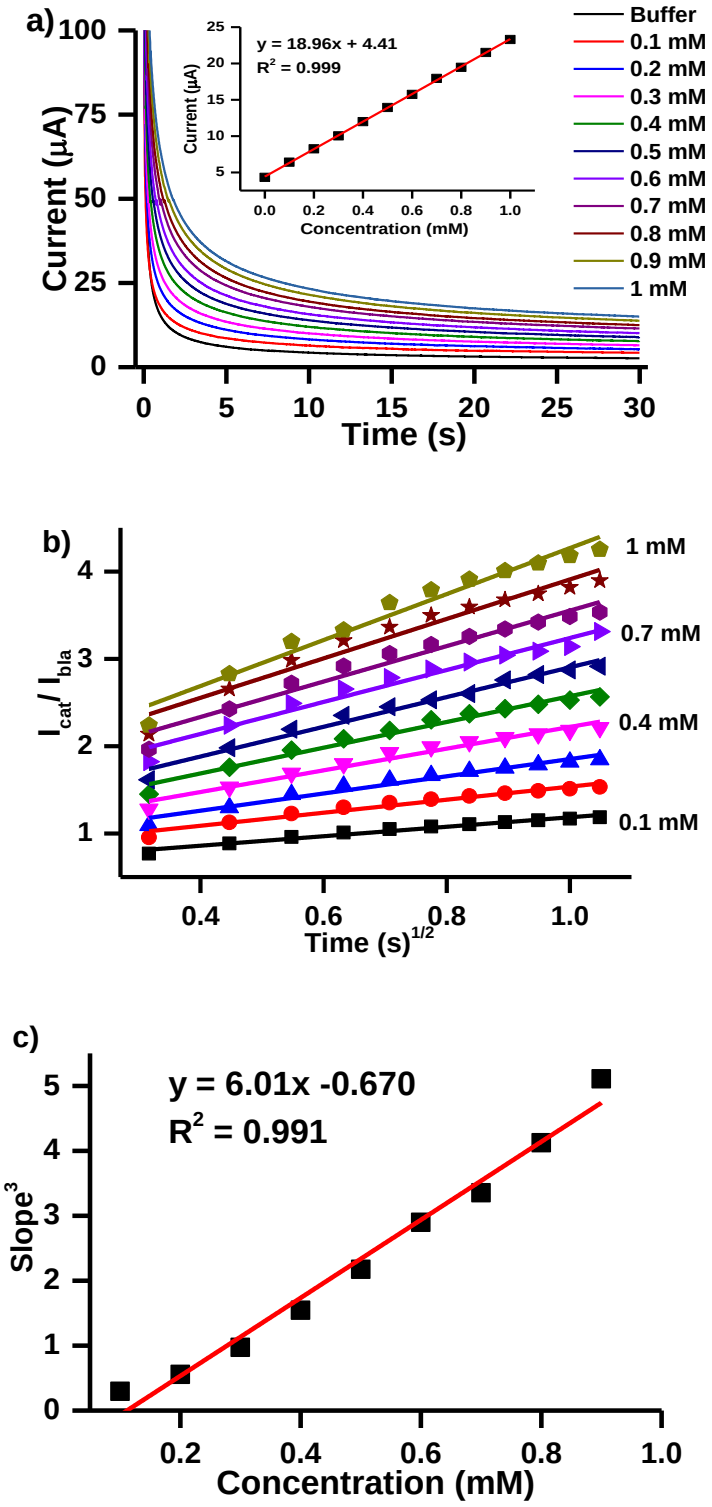

Figure 5.4: (a) Chronoamperograms obtained at varied nitrite concentrations (in 0.1 M pH 7 PBS). Insert: calibration curve of the nitrite concentration vs the oxidation current, (b) plots of (I_{cat}/I_{bla}) vs the square root of time and (c) plot of the square root of the slopes vs nitrite concentrations. All plots were generated from **4-Co-AsπGQDs**.

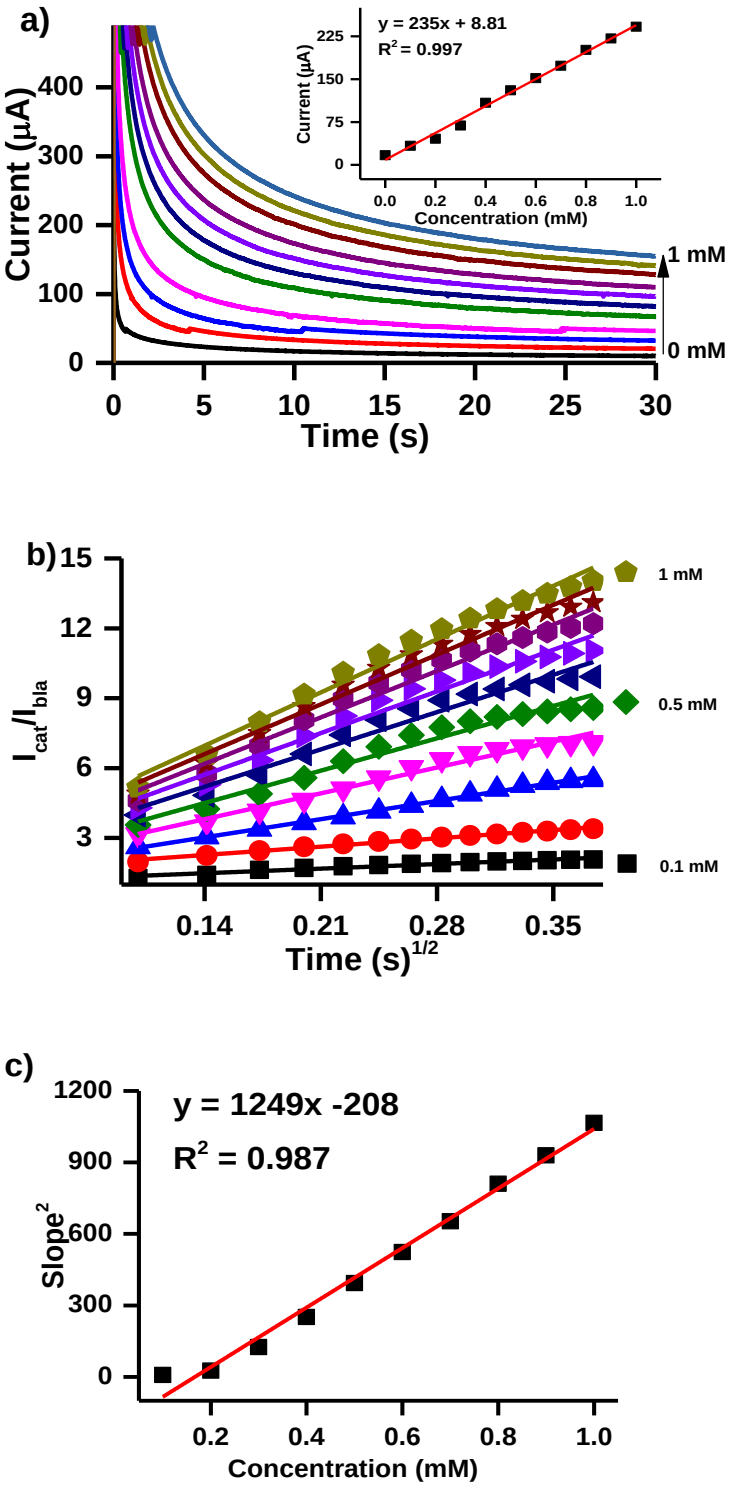

Figure 5.5: (a) Chronoamperograms of **9-Mn** obtained at varied nitrite concentrations (in 0.1 M pH 7 PBS). Insert: calibration curve of the nitrite concentration vs the oxidation current, (b) plots of (I_{cat}/I_{bla}) vs the square root of time and (c) plot of the square root of the slopes vs nitrite concentrations, b and c plots were generated from **11-Mn**

The electrocatalytic rate constants of the studied electrocatalysts were calculated using data obtained from the chronoamperograms. Figures 5.4(b) and 5.5(b) show linear plots that represent the ratio of the oxidation current obtained in the presence of nitrite (I_{cat}) against the current in the buffer only (I_{bla}) against the square root of the time lapsed. The gradients (slopes) obtained from these linear pots were fitted into Equation 5.13 and used to calculate the catalytic rate constants. Equation 5.13 has been described in literature and used to determine the catalytic rate constant [239,240].

$$\frac{I_{cat}}{I_{bla}} = y^{\frac{1}{2}}\pi^{\frac{1}{2}} = \pi^{\frac{1}{2}}(KCt)^{\frac{1}{2}} \quad \textbf{(5.13)}$$

where C, k and t represent the concentration of nitrite, catalytic rate constant and time lapsed, respectively. The gradients obtained were squared and plotted against their respective concentrations to afford the linear plots in Figures 5.4(c) and 5.5(c). The slopes obtained in Figures 51.4(c) and 5.5(c) were then used to calculate the catalytic rate of each electrocatalyst towards the oxidation of nitrite using Equation 5.14:

$$Slope = \pi k \quad \textbf{(5.14)}$$

The linear equations obtained for the electrocatalysts (from Figures 5.4(c) and 5.5(c)) are represented in Equation 5.15 (i-xv):

$$y = \ Slope\ (nitrite\ concentration\ )\frac{s^{-1}}{mM} + constant \quad (\mathbf{5.15})$$

4-Co: (i)

y = 1.57x -235 (R^2 = 0.996)

4-Co-As: (ii)

y = 0.3101x – 0.068 (R^2 = 0.959)

GQDs: (iii)

y = 56.71x – 10.2 (R^2 = 0.986)

4-Co-AsπGQDs: (iv)

y = 6.01x – 0.670 (R^2 = 0.991)

NGQDs: (v)

y = 81.8x – 11.0 (R^2 = 0.962)

4-Co-AsπNGQDs: (vi)

y = 7.86x – 1.77 (R^2 = 0.976)

SWCNTs: (vii)

y = 0.621x + 0.208 (R^2 = 0.961)

4-Co-AsπSWCNTs: (viii)

y = 1.70x – 0.225 (R^2 = 0.980)

Bi_2WO_6: (ix)

y = 157.47x – 18.71 (R^2 = 0.991)

4-Co-As@Bi_2WO_6: (x)

y = 724.08x – 253.46 (R^2 = 0.971)

$NiWO_4$: (xi)

y = 409.19x –46.49 (R^2 = 0.992)

4-Co-As@$NiWO_4$: (xii)

y = 24.56x – 428 (R^2 = 0.966)

9-Mn: (xiii)

y = 151x – 40.2 (R^2 = 0.982)

10-Mn: (xiv)

y = 1474x – 300 (R^2 = 0.998)

11-Mn: (xv)

y = 1249x -208 (R^2 = 0.987)

Table 5.2: Summary of the electrocatalytic properties of the electrocatalyst in 2 mM nitrite (0.1 M pH 7 PBS)

Sample[a]	Sensitivity ($\mu A.\mu M^{-1}$)	LoD (µM)	k ($M^{-1} s^{-1}$)	Reference
4-Co	21	0.12	4.9×10^1	This work
4-Co-As	7	1.7	9.87×10^1	This work
GQDs	18	0.19	1.80×10^2	This work
4-Co-AsπGQDs	19	0.17	1.19×10^3	This work
NGQDs	14	0.41	2.06×10^2	This work
4-Co-AsπNGQDs	20	0.25	2.49×10^3	This work
SWCNTs	28	0.44	1.98×10^4	This work
4-Co-AsπSWCNTs	3	1.0	5.42×10^4	This work
Bi_2WO_6	21	0.13	5.02×10^2	This work
4-Co-As@Bi_2WO_6	76	0.12	2.30×10^1	This work
$NiWO_4$	13	0.41	1.30×10^1	This work
4-Co-As@$NiWO_4$	58	0.80	7.82×10^3	This work
8-Co	59	0.18	1.71×10^3	This work
8-Cu	52	0.67	2.57×10^3	This work
8-Mn	32	0.20	1.31×10^4	This work
8-Ni	12	1.8	3.34×10^3	This work
9-Mn	235	0.59	4.86×10^2	This work
10-Mn	257	0.16	4.69×10^1	This work

11-Mn	276	0.24	3.98×10^1	This work
[TMPyPcCo/aCNTs]$_{12}$	18	2.6		[211]
12/MWCNTs	-	0.5	-	[212]
CoTM-QOPc/CNP	1	0.06	-	[213]
13πNGQDs	-	5.27	7.46×10^3	[214]
14πNGQDs	-	0.70	1.10×10^2	[214]
CoPc/MWCNTs	4	2.1		[215]
p-NiPTAPc	-	0.1		[216]
Fe(III)Pc/MCNNTs	0.0272	0.5		[217]
Pd/CoPc	0.01	0.1		[218]
2D-NiPc-MOF	-	2.3		[238]

[a]TMPy = 2,9,16,23-tetra[4-(N-methyl)pyridinyloxy], aCNT = acid-treated carbon nanotubes; MWCNT = multiwalled carbon nanotubes; TM-QOPc = tetra methyl substituted-quinoline oxy bridged phthalocyanine; CNP = carbon nanoparticles; **12** = chloro [3,7,12,17-tetramethyl-8,13-divinylporphyrin-2,18-dipropanoato (2−) Fe(III); **13** = N,N',N''-(((23-(4-aminophenoxy)phthalocyanine-2,9,16-triyl)tris(oxy))tris(benzene-4,1-diyl))triaceta-mide cobalt (II); **14** = tetrakis [phenoxyacetamide)-phthalocyaninato] cobalt (II), p-NiTA = polymeric nickel tetraamino; MOF = metal-organic framework

The catalytic rates obtained herein range between 3.98×10^1 $M^{-1}s^{-1}$ and 1.98×10^4 $M^{-1}s^{-1}$ (Table 5.2). No clear trend was observed with regard to the catalytic rate constants across the group classifications that were previously explored in the other nitrite electrocatalytic properties. And no correlation can be made between the obtained catalytic rates and the other determined parameters. This could be attribute to the fact that the catalytic rate is not only dependent on the activity of the electrocatalysts in the nitrite solution but equally its response and/or stability in the buffer.

5.1.4 Stability Studies

Figures 5.6 – 5.8 show examples of repetitive cyclic voltammograms obtained under the same respective conditions per electrocatalysts (concentration, scan rate and potential window). These scans were conducted to determine the stability of the electrocatalysts in the presence of the analyte and the reproducibility of the results obtained overall. For each electrocatalyst, multiple consecutive scans were run.

Figure 5.6 is an illustration of the CVs obtained for **GQDs**, and **4-Co-AsπGQDs**. The figure shows that the electrocatalysts were stable, as no significant changes were observed in the oxidation peak potentials when analysing the multiple scans. The decrease in peak currents were calculated to be below 30% for **4-Co-As**, the nanomaterials and the hybrids, indicating that the electrocatalysts studied herein were stable in nitrite. The relative standard deviations calculated ranged between 2 and 5.

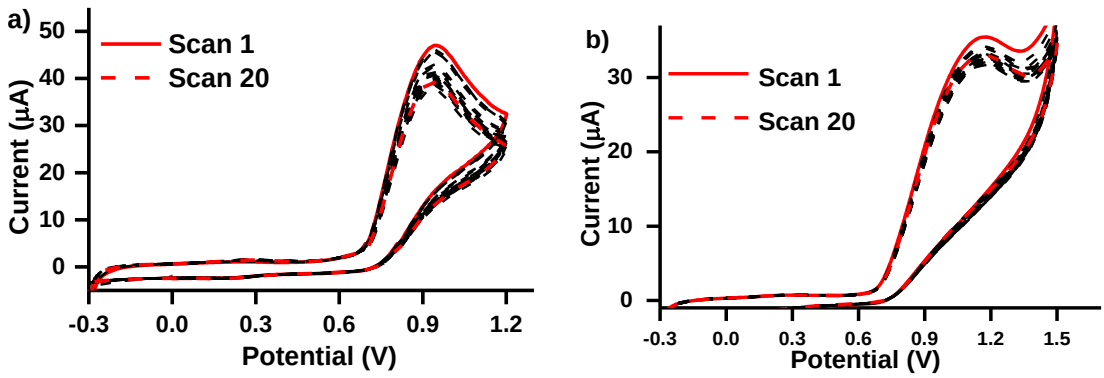

Figure 5.6: Repetitive cyclic voltammograms of (a) **GQDs** and (b) **4-Co-AsπGQDs** in 2 mM nitrite in PBS pH 7. Scan rate of 100 mVs^{-1}.

Figure 5.7 is an illustration of the CV scans obtained for **10-Mn** and **11-Mn**. The oxidation peak currents for **9-Mn** and **11-Mn** decreased by 15% and 9%, respectively. While **10-Mn**, showed approximately a 14% increase in the oxidation peak current after 20 scans. All three

electrocatalysts exhibited incredible stability, with the average change in the oxidation peak current being below 20%. After multiple scans over a couple of days, the three electrocatalysts maintained approximately 85%, 86%, and 91% of their oxidation peak currents, respectively. The oxidation peak potentials did not shift significantly, suggesting that the electrocatalysts were stable under the studied conditions and that the results were reproducible.

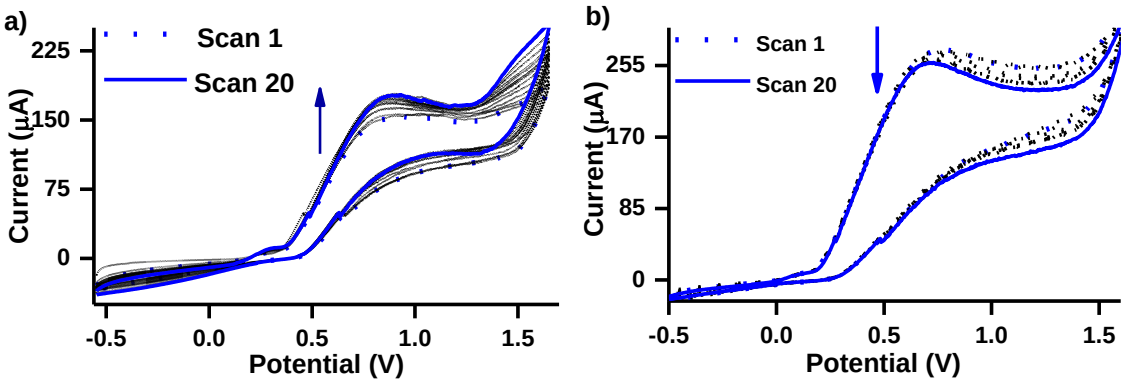

Figure 5.7: Repetitive cyclic voltammograms of (a) **10-Mn** and b) **11-Mn** in 2 mM nitrite in PBS pH 7. Scan rate of 100 mVs^{-1}

Figure 5.8 illustrates the stability studies conducted for **8-Mn** and **8-Co.** It can be observed from the figure that both electrocatalysts were reasonably stable, with no change in the oxidation peak potentials being observed and slight decreases in the oxidation peak currents for the first few scans. The oxidation peak currents stabilised and remained constant after fifteen consecutive scans. Similar trends were also observed for **8-Cu**. The change in the oxidation peak currents were calculated to be 30%, 22% and 14% for **8-Co**, **8-Cu** and **8-Mn**, respectively. The relatively low percentage change in the oxidation peak currents obtained

for **8-Co**, **8-Cu** and **8-Mn** indicate that these three electrocatalysts were stable in 2 mM nitrite and that this work can be reproduced and used for practical applications. **8-Ni** was, however, not stable after a few consecutive scans, the oxidation peak disappeared.

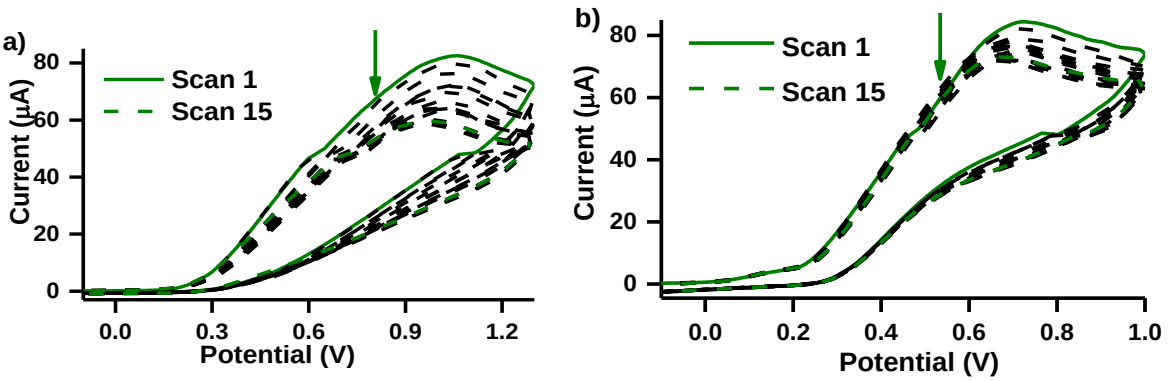

Figure 5.8: Cyclic voltammogram of (a) **8-Co** and (b) **8-Mn** in 2 mM nitrite in PBS pH 7. scan rate = 100 Vs^{-1}

5.1.5 Interference Studies

Interference studies were used to determine the sensitivity of the electrocatalysts towards the detection of nitrite in the presence of other analytes (interfering species). The following ions; NO_3^{2-}, Cl^- and SO_4^{2-}, were selected and used as the interferants of choice. These ions tend to co-exist (especially in water) with nitrite and are known to influence the detection of nitrite [241–243]. For this study, differential pulse voltammetry (DPV) was used as it is a highly sensitive technique (compared to CV) and can detect substances in trace concentrations.

Figure 5.9 illustrates the differential pulse voltammograms that were obtained in this work. The figure shows that neither of the anionic species displayed a detection peak that overlapped with that of nitrite. Slight changes in the peak potential were observed when

nitrite was studied in the presence of the anionic species. These changes were, however, below 5% and are therefore negligible.

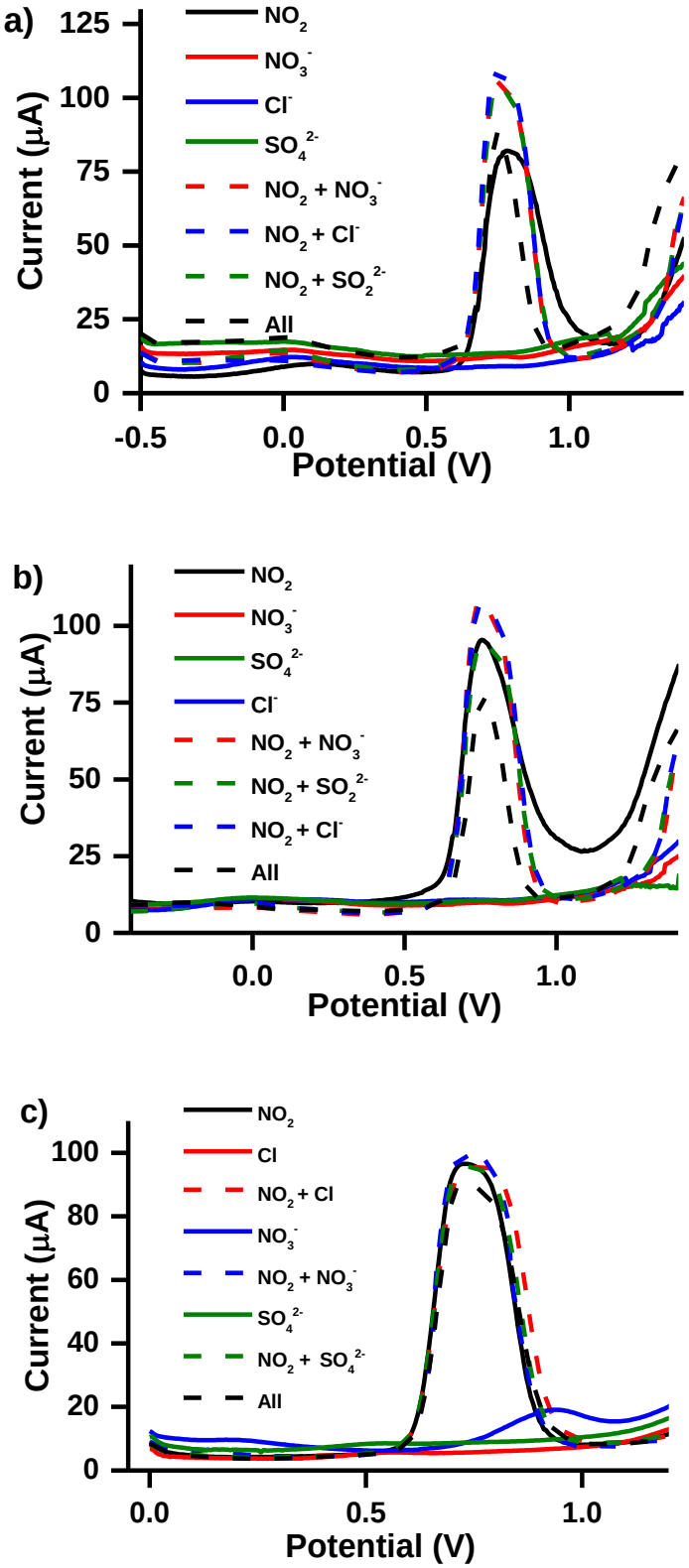

Figure 5.9: Differential pulse voltammograms of nitrite in the presence of interfering ions on (a) **GQDs**, (b) **4-Co-AsπGQDs** and (c) **9-Mn**

5.2 Catechol

5.2.1 Comparative Cyclic voltammetry

Cyclic voltammetry was employed to investigate the electrocatalytic behaviour of the following electrocatalysts; **2-Co**, **2-CoπGQDs**, **2-CoπSWCNTs**, **3-Co**, **3-CoπGQDs**, **3-CoπSWCNTs**, **4-Cu-As**, **5-Cu**, **6-Cu** and **7-Cu**, in the presence of catechol (Figure 5.10). The electrocatalysts studied herein exhibited oxidation and reduction peaks, typical of catechol [244].

The studied electrocatalysts were responsive towards catechol; however, the degree of responsiveness (oxidation peak potential and current) was unique for each electrocatalyst, as observed in Figure 5.10. The studied electrocatalysts exhibited oxidation peak potentials between 0.21 V (**4-Cu-As**) and 0.72 V (**2-Co**), and the oxidation peak currents ranged from 15 µA to 177 µA (Table 5.3).

With the exception of **2-Co**, it was observed that the modification of the bare electrode improved the detection of catechol as relatively lower Ep values were obtained upon modification. The following observations were drawn from the oxidation peak potentials and their respective currents obtained from the electrooxidation of catechol:

i. **Substituents**: **2-Co** displayed a relatively higher and favourable oxidation peak current compared to **3-Co**. However, **3-Co** exhibited the most favourable oxidation peak potential. Complex **4-Cu-As** was the only asymmetrical complex studied in this work. Despite having the lowest and most favourable catechol oxidation peak, **4-Cu-As** had the lowest oxidation peak current. Therefore, it was the least sensitive towards catechol.

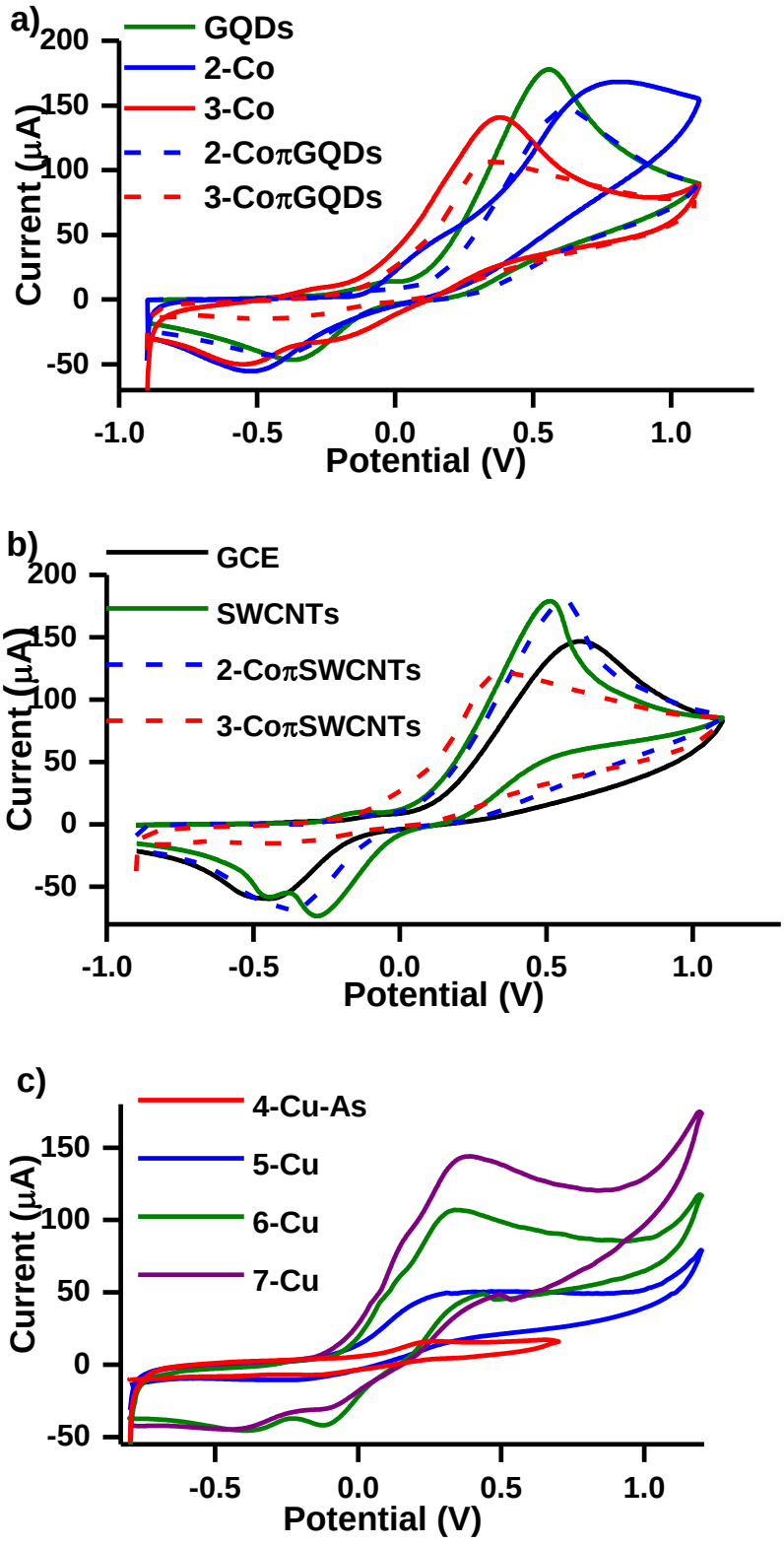

Figure 5.10: Cyclic voltammograms of (a) GQDs, **2-Co**, **2-CoπGQDs** , **3-Co** and **3-Co-GQD**s, (b) GCE, SWCNTs, **2-CoπSWCNTs** and **3-CoπSWCNTs** and (c) **4-Cu-As**, **5-Cu**, **6-Cu** and **7-Cu** obtained in 1 mM catechol in 0.1 M pH PBS. Scan rate = 100 mVs^{-1}

The formation of Schiff base complexes **6-Cu** and **7-Cu** from **5-Cu** enhanced activity towards catechol detection as higher oxidation peak currents were obtained after their formation.

ii. **Nanomaterials**: The two nanomaterials (SWCNTs and GQDs) showed relatively higher faradic oxidation currents than the MPcs alone. This suggests that the nanomaterials were more sensitive toward the detection of catechol. However, the addition of nanomaterials to the MPcs did not enhance the sensitivity of the MPcs toward catechol, as the oxidation peak currents obtained after hybridisation were relatively lower except for **2-CoπSWCNTs**.

iii. A general inverse relationship between the oxidation peak potential and the oxidation peak currents was observed in this work.

5.2.2 Mechanism and Kinetics Studies

The electrochemical oxidation of catechol has been described and reported as a two-electron ($2e^-$), and two proton ($2H^+$) quasi-reversible electrochemical process (Scheme 5.1) [244,245].

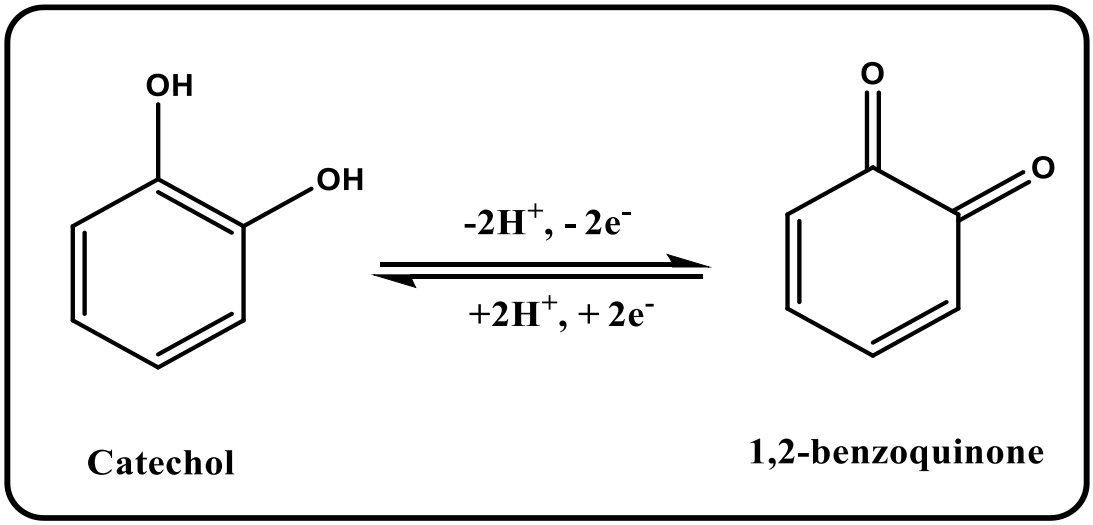

Scheme 5.1: Schematic representation of the mechanism of the electrochemical oxidation Catechol

The mechanism of catechol oxidation involving phthalocyanine complexes is not well understood. The electrocatalytic mechanism of MPcs containing electro-inactive central metal(s) is mediated by ring processes explored in Equations 5.3 and 5.4, and this the case for CuPcs.

Figures 5.11(a) and 5.12(a) illustrate the cyclic voltammograms obtained in 1mM catechol at different scan rates (10 mVs^{-1} to 100 mVs^{-1}). These voltammograms were used to determine the reaction kinetics and parameters of the electrocatalysts at the electrode surface. The figures show that for all the electrocatalysts studied in this work, there was a shift in the oxidation peak potential to more positive values with the increase in scan rate. This trend is attributed to the irreversibility of the redox reaction between catechol and the electrocatalysts at the electrode surface.

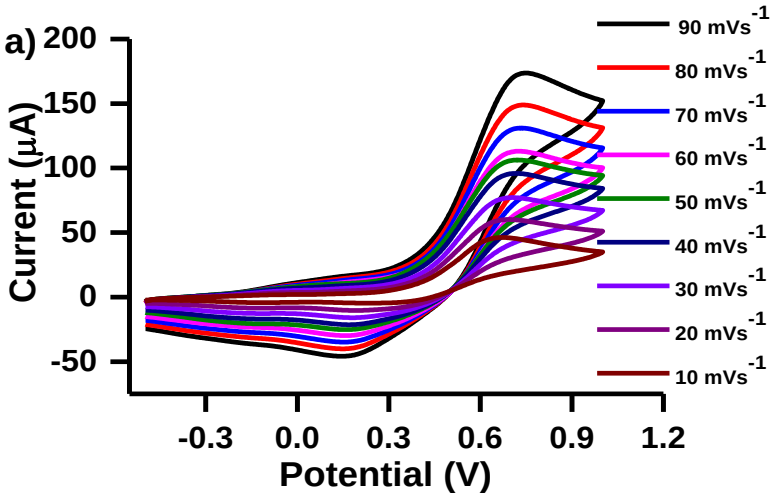

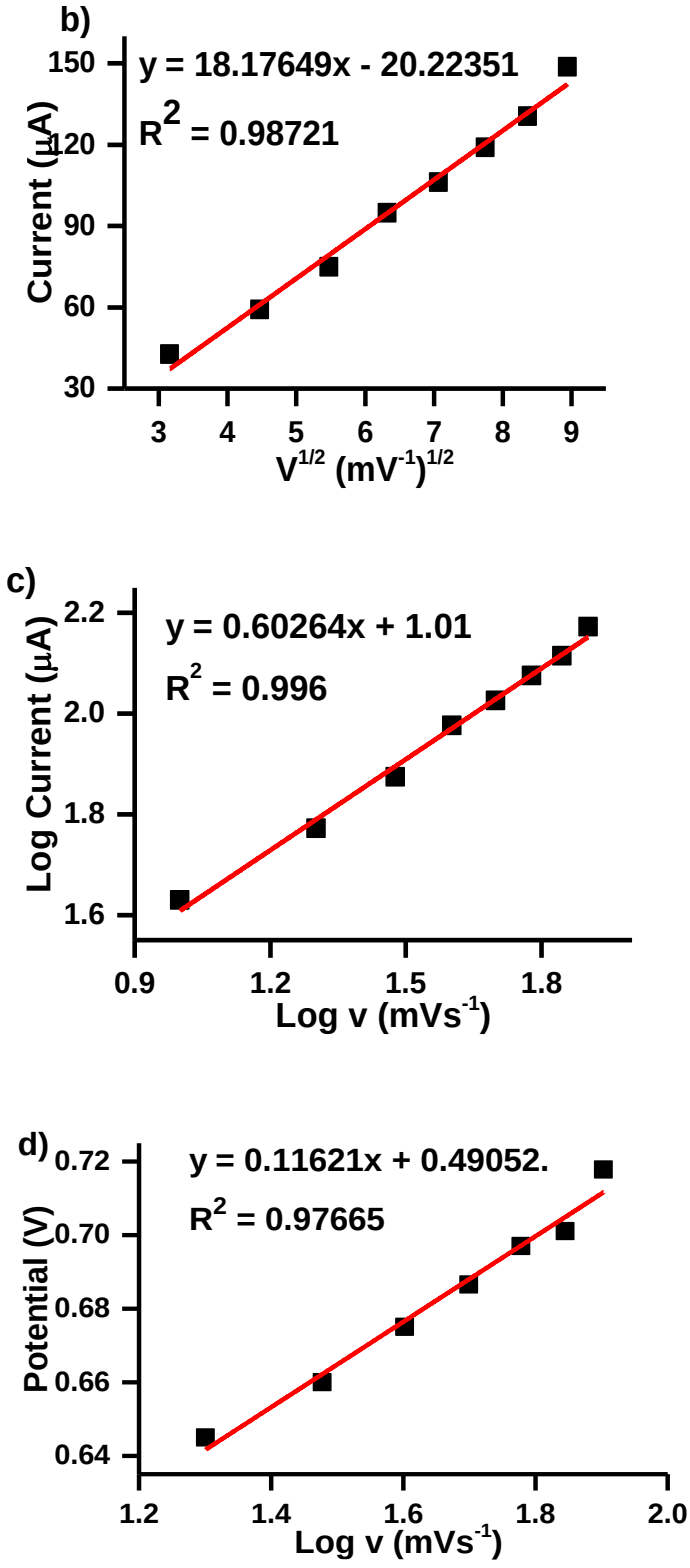

Figure 5.11: (a) cyclic voltammograms obtained in 1 mM catechol (in 0.1 M pH 7 PBS) at varied scan rates, (b) plot of oxidation peak current vs the square root of the scan rate, (c) log of oxidation peak current vs log of scan rate and (d) plot of oxidation peak potential vs log of scan rate. All plots were generated from **2-Co**.

From the data obtained from the CV scans in Figures 5.11(a) and 5.12(a), linear plots of the square root of the scan rate against the oxidation peak current were obtained, (Figures 5.11(b) and 5.12(b)). The linearity observed in these plots is attributed to the electrooxidation of catechol by the electrocatalysts at the electrode surface being diffusion-controlled [195,229].

Figures 5.11(c) and 5.12(c) are linear plots of the log of the current against the log of the scan rate that was used to confirm whether the reaction processes between catechol and the electrocatalysts at the electrode surface are indeed diffusion controlled. The gradients obtained from the cobalt series, nanomaterials and their respective hybrids materials were above 0.5. Thus, indicating that the reaction processes at the electrode surface are adsorption and not diffusion-controlled [230,246,247]. The contradictory results from Figures 5.11(b and c) suggest that a mixture of reactions might have occured at the electrode surfaces. The gradients obtained for the CuPc series were below 0.5, confirming the results from Figure 5.12(b), suggesting that the reaction processes occurring at the electrode surface are diffusion-controlled [229,230].

Tafel slopes were determined using data extrapolated from Figures 5.11(d). These figures represent the oxidation current against the log of the scan rate. The data obtained from these linear plots were fitted into Equation 5.11 to calculate the Tafel slope values in Table 5.3. The Tafel slopes obtained in this work range between 230 mV decade^{-1} and 888 mV decade^{-1}. These values are well above the range with kinetic meaning (60 – 120 mV decade^{-1}) [233].

Equation 5.11 is generally used to calculate Tafel slopes for a one-electron processes. The electrooxidation of catechol involves two electrons. High values are attributed to the by-products from the two-step reaction being adsorbed at the electrode surface [236,248].

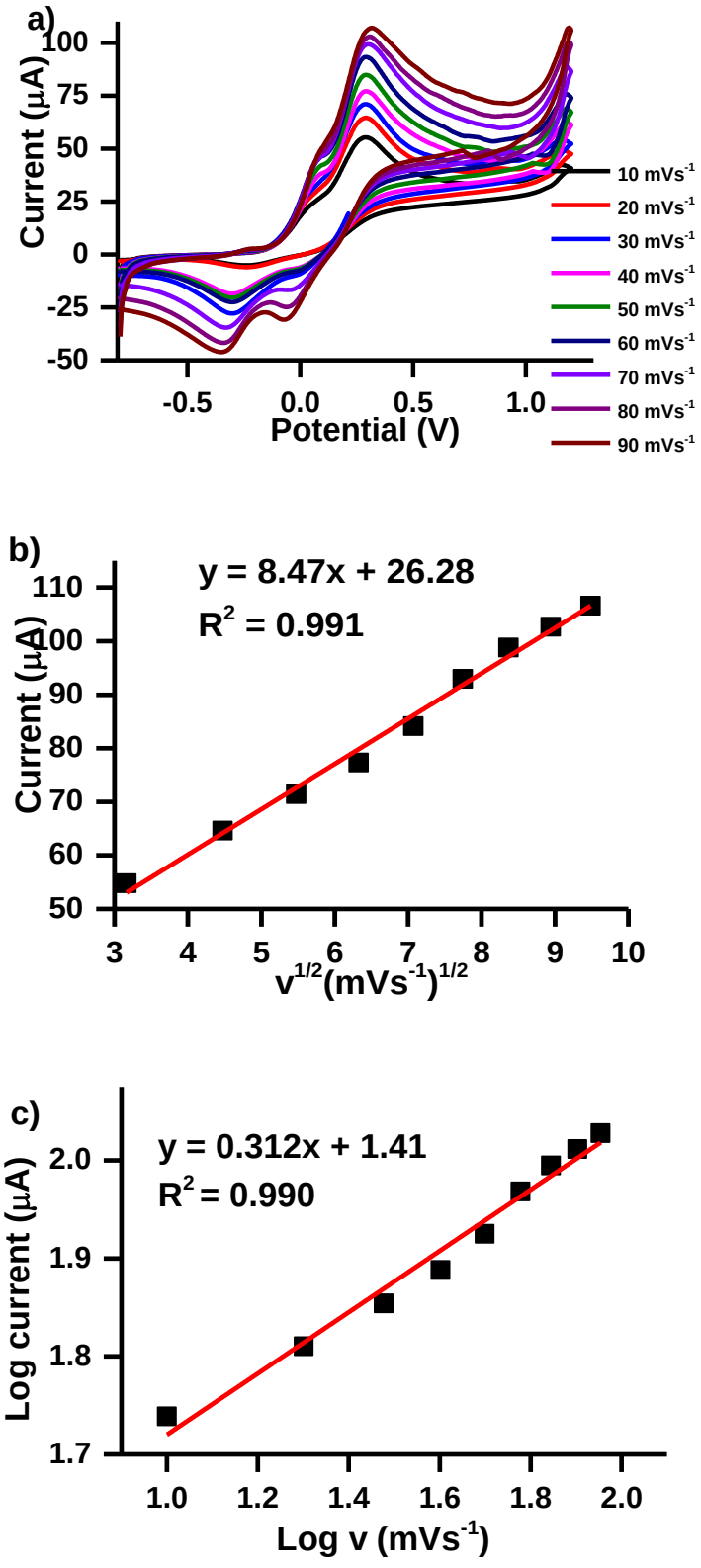

Figure 5.12: (a) cyclic voltammograms obtained in 1 mM catechol (in 0.1 M pH 7 PBS) at varied scan rates, (b) plot of oxidation peak current vs the square root of the scan rate, (c) log of oxidation peak current vs log of scan rate. All plots were generated from **6-Cu**

These high values are an indication of tight binding between catechol and the electrocatalysts, hence they are attributed to adsorption at the electrode surface [236,248]. This, among other factors (elaborated in *section 5.1.2*), could be why relatively high Tafel slopes were obtained in this study.

Table 5.3: Summary of data of the studied electrocatalysts in 1 mM catechol (0.1 M pH 7 PBS)

	Ep (V)	**Background corrected oxidation peak current (µA)**	**Tafel slope (mV decade^{-1})**
GCE	0.61	146	-
GQDs	0.56	177	240
SWCNTs	0.51	175	888
2-Co	0.72	167	-
2-CoπGQDs	0.60	145	232
2-CoπSWCNTs	0.57	176	431
3-Co	0.40	140	240
3-CoπGQDs	0.33	104	320
3-CoπSWCNTs	0.35	120	254
4-Cu-As	0.21	15	-
5-Cu	0.23	48	-
6-Cu	0.29	108	-
7-Cu	0.37	145	-

5.2.3 Sensitivity and Detection Limits Studies

Chronoamperometric studies were conducted to determine the; (i) sensitivity of the electrocatalysts towards the detection of catechol, (ii) limits of detection and (iii) catalytic rate constants.

Figures 5.13(a) and 5.14(a) are examples of the chronoamperograms obtained from varied catechol concentrations (0 mM – 1 mM) for 30 sec (each scan). Figure 5.13(a) shows the chronoamperograms obtained for **2-CoπGQDs**, and 5.14(a) was obtained from **5-Cu**. The insert in these figures are the calibration plots of catechol concentration against the corresponding currents. The calibration plots were used to calculate the LoDs (Table 5.4) using Equation 5.12.

The detection limits obtained in this work range between 0.057 µM and 0.77 µM (Table 5.4). The detection limits and sensitivities obtained herein are comparable with those obtained in literature [97,145,249–252] (Table 5.4). The following observations were made:

i. The nanomaterials exhibited relatively lower detection limits than the MPc complexes alone. Incorporating nanomaterials into **2-Co** and **3-Co** enhanced the detection limits and sensitivities of the electrocatalysts.

ii. **GQDs** and their MPc hybrids exhibited relatively lower detection limits compared to **SWCNTs** and their hybrids.

iii. The formation of Schiff bases enhanced the detection of catechol, resulting in lower detection limits and sensitivities. Electrocatalyst complexes **6-Cu** and **7-Cu** had lower LODs compared to their precursor **5-Cu**.

iv. The low LoDs obtained for **3-CoSWCNTs** (0.057 µM) can be attributed to its higher loading.

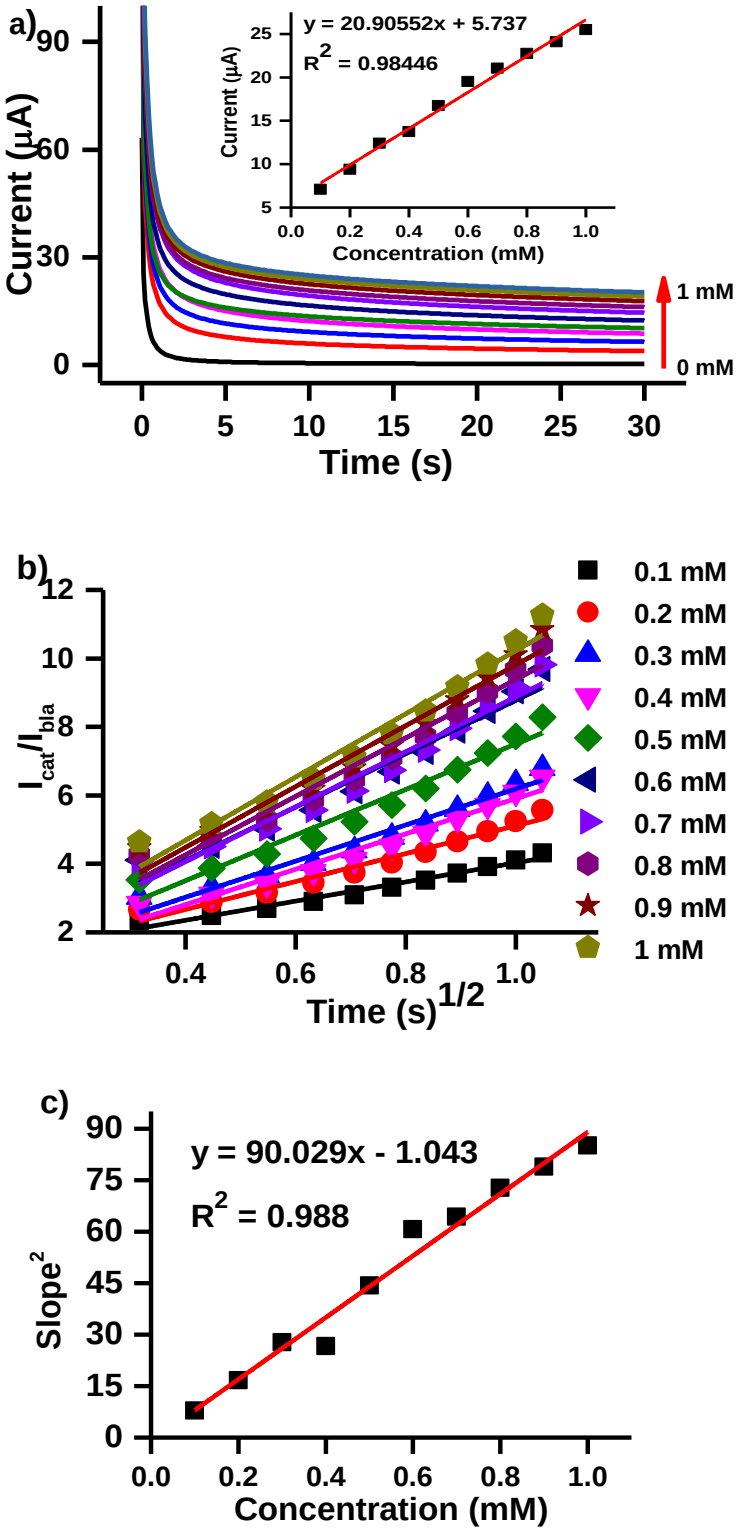

Figure 5.13: (a) Chronoamperograms obtained at varied catechol concentrations (in 0.1 M pH 7 PBS). Insert: calibration curve of the catechol concentration vs the oxidation current, (b) plots of (I_{cat}/I_{bla}) vs the square root of time and (c) plot of the square root of the slopes vs catechol concentrations. All plots were generated from **2-CoπGQDs**.

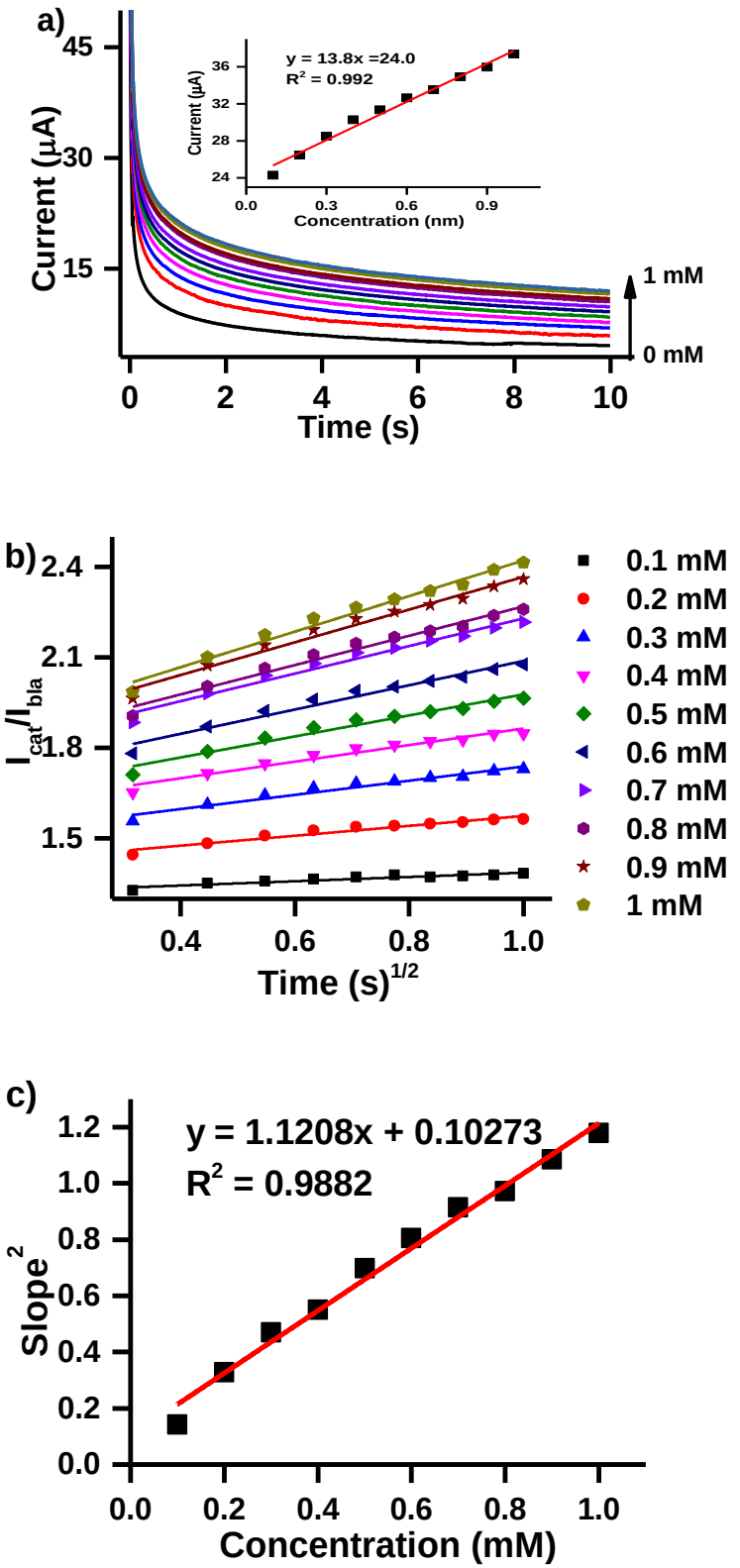

Figure 5.14: (a) Chronoamperograms obtained at varied catechol concentrations (in 0.1 M pH 7 PBS). Insert: calibration curve of the catechol concentration vs the oxidation current, (b) plots of (I_{cat}/I_{bla}) vs the square root of time and (c) plot of the square root of the slopes vs catechol concentrations. All plots were generated from **5-Cu**.

Catalytic rate constants were calculated using data obtained from Figures 5.13(b and c) and 5.14(b and c). Figures 5.13(b) and 5.14(b) represent plots of the ratio between the oxidation currents at the studied in catechol concentrations (I_{cat}) and of the buffer/blank (I_{bla}) against the square root of time lapsed. The catalytic rate constants were calculated according to a method described in literature using Equations 5.13 and 5.14 [239,240]. The squares of the slopes obtained from Figures 5.11(b) and 5.12(b) were plotted against their respective concentrations resulting in the plots shown in Figures 5.13(c) and 5.14(c). The slopes of the linear plots in Figures 5.13(c) and 5.14(c) were used to calculate the catalytic rate constants of the studied electrocatalysts. The linear regressions are represented by Equations 5.16 (i) to (viii):

From the results obtained it can be observed that cobalt phthalocyanine complexes exhibited relatively higher catalytic rate constants compared to the copper complexes with the exception of the asymmetric complex, **4-Cu-As**. This could be attributed to the fact that cobalt generally has better electrocatalytic activity compared to copper. It can also be noted that the addition of nanomaterials to the MPc complexes did not enhance their electrocatalytic rate constants.

$$y = slope\ (catechol\ concentration)\frac{s^{-1}}{mM} + constant \quad (\mathbf{5.16})$$

GQDs: (i)

y = 809.36x -62.21 (R^2 = 0.997)

SWCNTs: (ii)

y = 816.82x -50.34 (R^2 = 0.980)

2-Co: (iii)

y =3.33x - 0.513 (R^2 = 0.910)

2-CoπGQDs: (iv)

y = 90.03x – 1.04 (R^2 = 0.988)

2-CoπSWCNTs: (v)

y = 103.35x – 1.58 (R^2 = 0.987)

3-Co: (vi)

y= 151.92x – 21.04 (R^2 = 0.992)

3-CoπGQDs: (vii)

y = 212.623x – 32.59 (R^2 = 0.980)

3-CoπSWCNTs: (viii)

y = 854.51x – 40.6 (R^2 = 0.993)

4-Cu-As: (ix)

y = 3.07x + 0.525 (R^2 = 0.983)

5-Cu: (x)

y = 1.12x + 0.103 (R^2 = 0.988)

6-Cu: (xi)

y = 2.03x + 0.167 (R^2 = 0.989)

7-Cu: (xii)

y = 6.68x + 0.147 (R^2 = 0.981)

Table 5.4: Comparative sensitivities, LoDs and catalytic rates for catechol (in 0.1 M pH 7 PBS)

	Sensitivity ($\mu A.mM^{-1}$)	LoD	Catalytic rate k ($M^{-1}s^{-1}$)	Reference
GQDs	32.8	0.17	-	This work
SWCNTs	94.1	0.14	258	This work
2-Co	18.3	0.77	260	This work
2-CoπGQDs	20.9	0.56	1.06	This work
2-CoπSWCNTs	36.2	0.27	28.7	This work
3-Co	61.1	0.15	32.9	This work
3-CoπGQDs	82.9	0.064	48.1	This work
3-CoπSWCNTs	110	0.057	67.7	This work
4-Cu-As	18.0	0.28	272	This work
5-Cu	13.8	0.48	0.64	This work
6-Cu	43.1	0.20	2.12	This work
7-Cu	35.0	0.16	0.98	This work
[a] (MtPcCo/ErGO)10/GCE	-	0.53	-	[97]
[a]LB FePc + DMPA	1.21	0.43	-	[145]
[a]LB $LuPc_2$ + DMPA	1.04	0.33	-	[145]
[a]TACoPc/PANI/AgNPs	-	0.46	-	[249]
[a]CoPcNRs/FA-rGO	2.18	0.65	-	[250]
[a]CoPc-CPEs-Tyr	8.88	7.5	-	[251]
[a]Tyr/AA/$LuPc_2$	0.162	2.1	-	[252]

[a]MtPcCo = methylated tetra-β-(N,N- diethylaminoethoxy)phthalocyanine cobalt, ErGo = electrochemically reduced graphene oxide, PANI = conducting polyaniline, AgNPs = silver nanoparticles, NRs = nanorods, FA = fulvic acid, rGO = reduced graphene oxide, CPEs = carbon paste electrodes, Tyr = tyrosinase, AA = arachidic acid, LB = Langmuir–Blodgett, DMPA = dimyristoyl phosphatidic acid

5.2.4 Stability Studies

Stability studies were conducted using cyclic voltammetry (Figure 5.15) to determine the stability of the studied electrocatalysts. The stability of the electrocatalysts studied in this work was conducted in 1 mM catechol (0.1 M PBS pH 7) at a scan rate of 100 mVs^{-1}. Fifteen scans were run consecutively for each electrocatalyst.

A decrease in the oxidation peak current was observed after the first few scans for **2-CoπGQDs** (Figure 5.15(a)). However, the electrode stabilised after the 10^{th} scan and very insignificant change in the oxidation peak current was observed; a slight shift in the peak potential was also observed. The oxidation peaks became more resolved with each scan, which made detection more accurate.

Figures 5.15(b and c) illustrate the cyclic voltammograms obtained when conducting stability and repeatability studies for asymmetric **4-Cu-As** and the symmetric Schiff base precursor complex, **5-Cu**. As observed in Figure 5.15(b and c), copper complexes **4-Cu-As** and **5-Cu** were both very stable electrocatalysts.

All electrocatalysts employed in this work proved to be stable in catechol as they could be used several times over a couple of days without their respective peaks disappearing completely or the oxidation peak potentials changing. The change in the current for all electrocatalysts was below 50%.

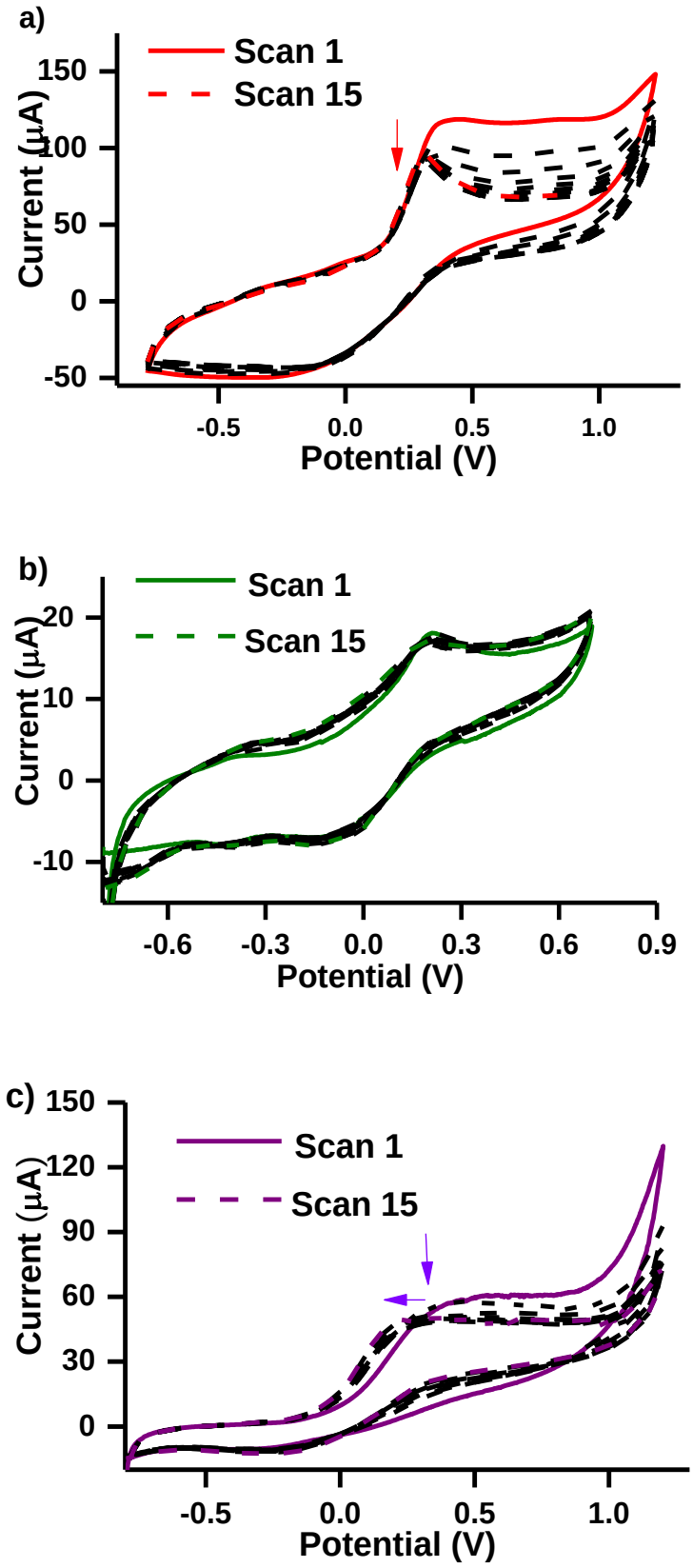

Figure 5.15: Repetitive cyclic voltammograms of a) **2-CoπGQDs**, b) **4-Cu-As,** and c) **5-Cu** in 1 mM catechol (PBS pH 7) Scan rate = 100 mVs^{-1}.

5.2.5 Interference Studies

Catechol interference studies were conducted to determine the selectivity and sensitivity of the studied electrocatalyst (**2-CoπGQDs**) in the presence of hydroquinone, and resorcinol (Figure 5.16). These three analytic species co-exist in the environment and have been detected simultaneously due to the similarities in their structure, physiochemical properties and overlapping oxidation peaks [250,253,254].

Figure 5.16 is an illustration of the differential pulse voltammograms obtained for this study. From the figure it can be observed that **2-CoπGQDs** was able to detect all three analytes as expected. This indicates that the studied electrocatalysts were not selective toward catechol as it could detect the interferants. However, it is important to note that catechol exhibited the highest oxidation peak current compared to the interferants suggesting that the electrocatalyst was sensitive toward catechol.

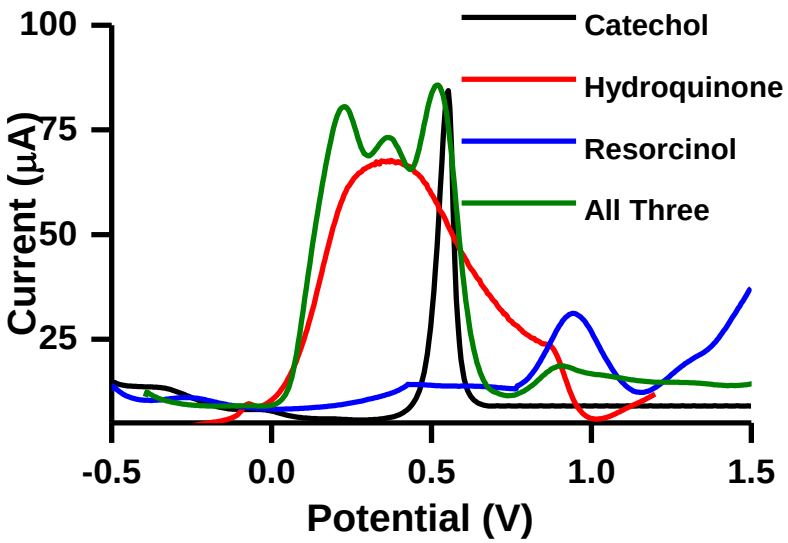

Figure 5.16: Differential pulse voltammograms of **2-CoπGQDs** in the presence of catechol, hydroquinone, resorcinol and a mixture of all three analytes in 0.1 M pH 7 PBS buffer.

In the mixed sample matrix it can be observed that the catechol oxidation peak current was not affected by the presence of the interferents. The change in oxidation peak potential was also insignificant. However, significant increase in the currents of the interferents were observed.

5.3 Dopamine

5.3.1 Comparative Cyclic voltammetry

Figure 5.17 illustrates the cyclic voltammograms obtained for the GCE electrodes modified with **1-Co**, **1-Co-As**, **NGQDs**, **1-CoπNGQDs** and **1-Co-AsπNGQDs**.

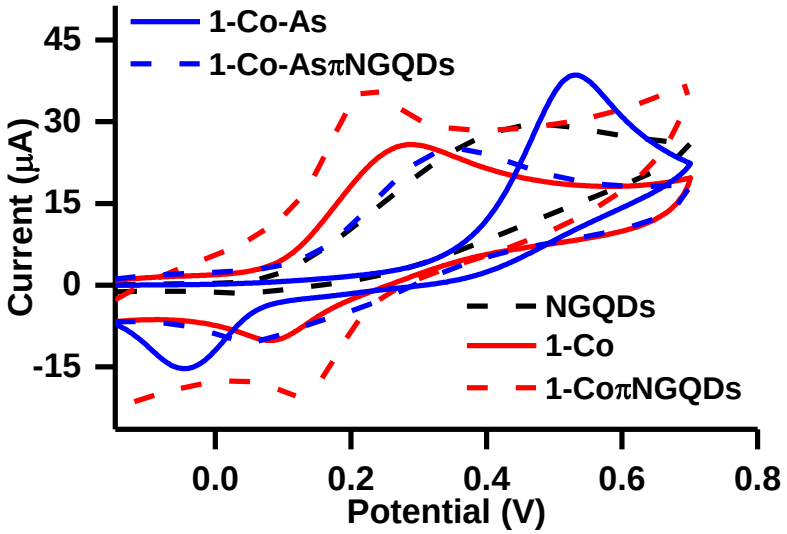

Figure 5.17: Cyclic voltammograms of **1-Co**, **1-Co-As**, **NGQDs**, **1-CoπNGQDs** and **1-Co-AsπNGQDs**. 1 mM dopamine in 0.1 M pH PBS. Scan rate = 100 mVs^{-1}

From Figure 5.17, it can be observed that all the studied electrocatalysts showed dopamine oxidation peaks. No oxidation peak was observed for the bare electrode. Each electrocatalyst exhibited unique dopamine detection properties; the oxidation peak potentials and currents obtained herein are tabulated in Table 5.5. The following observations were made:

i. The symmetric MPc electrocatalyst; **1-Co** exhibited a lower and more desirable oxidation peak potential (0.28 V) compared to the asymmetric MPc electrocatalyst, **1-Co-As** (0.53 V, highest in Table 5.5). This suggests that lowering

the symmetry of an MPc complex does not necessarily enhance its electrocatalytic properties, especially not toward the detection of dopamine.

The hybridised complexes showed a similar trend, where **1-CoπNGQDs** displayed a more favourable dopamine oxidation peak potential relative to **1-Co-AsπNGQDs.**

ii. Although **1-Co-As** exhibited a relatively high oxidation peak potential, it had the highest oxidation peak current (38.4 μA), rendering it the most dopamine-sensitive electrocatalyst in this specific analysis.

iii. The incorporation of nanomaterials to the MPcs decreased the oxidation peak potentials, with **1-CoπNGQDs** showing the lowest oxidation peak potential.

iv. The obtained oxidation peak potentials can be ranked as follows with regard to their favourability **1-CoπNGQDs** > **1-Co** > **1-Co-AsπNGQDs** > **NGQDs** > **1-Co-As**.

v. The results based on the oxidation peak currents were inconclusive. They were ranked as follows: **1-Co-As** > **1-CoπNGQDs** > **NGQDs** > **1-Co** > **1-Co-AsπNGQDs**

5.3.2 Mechanism and Kinetics Studies

The general mechanism for the oxidation of dopamine is described as the ECE (electron transfer, chemical reaction, electron transfer) method (Scheme 5.2) [255,256]. Dopamine exists in a cationic form in neutral environments [137]. The electrochemical oxidation of dopamine occurs via a two-proton and two-electron process yielding *o*-dopaminoquinone (*o*-DQ), this step is known as the E step and is reversible. The chemical reaction (C step) occurs under neutral or basic conditions. Where the amine group in *o*-DQ is deprotonated, and cyclisation occurs, forming leucodopaminochrome. The two-electron, two-proton process

further oxidises leucodopaminochrome at relatively lower potentials resulting in the formation of dopaminochrome.

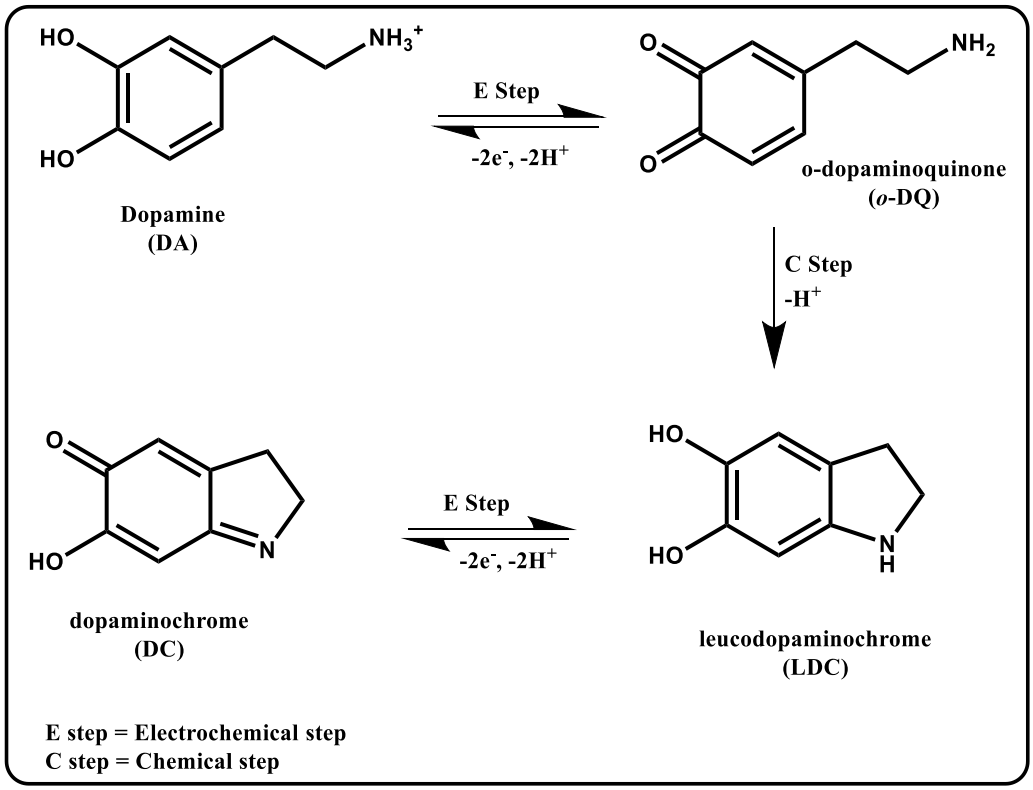

Scheme 5.2: Electrochemical oxidation of dopamine

Kinetic studies for the detection of dopamine were conducted using cyclic voltammetry at varied scan rates (10 mVs^{-1} to 100 mVs^{-1}) using a fixed dopamine concentration (Figure 5.18). These studies were conducted to determine the catalysed reaction's reversibility and calculate the Tafel slopes of the studied electrocatalysts in the presence of dopamine. Figure 5.18(a) shows the cyclic voltammograms obtained for **1-CoπNGQDs** at different scan rates. The oxidation peak potential slightly shifts towards more positive values (increases) as the scan rate increases. This is indicative of the irreversibility of the reduction of dopamine. It can

also be observed that the peak current also increases with the increase in the scan rate. A similar trend was observed for all the electrocatalysts studied herein.

Table 5.5: Summary of the dopamine electrooxidation properties obtained in 1 mM dopamine in 0.1 M pH 7 PBS

	Ep (V)	**Background corrected Oxidation peak current (μA)**	**Tafel slope (mV decade^{-1})**
GCE	-	-	-
NGQDs	0.44	28.6	144
1-Co	0.28	23.6	250
1-CoπNGQDs	0.21	29.0	281
1-Co-As	0.53	38.4	160
1-Co-AsπNGQDs	0.34	21.3	185

The linear relationship between the oxidation peak current and the square root of the scan rate (Figure 5.18(b)) suggests that the oxidation of dopamine is predominantly diffusion-controlled. A similar pattern was observed for all the electrocatalysts studied in this work, suggesting that the oxidation of dopamine using **1-Co**, **1-Co-As**, **1-Co-AsπNGQDs**, **1-Co-AsπNGQDs** and **NGQDs** was diffusion-controlled.

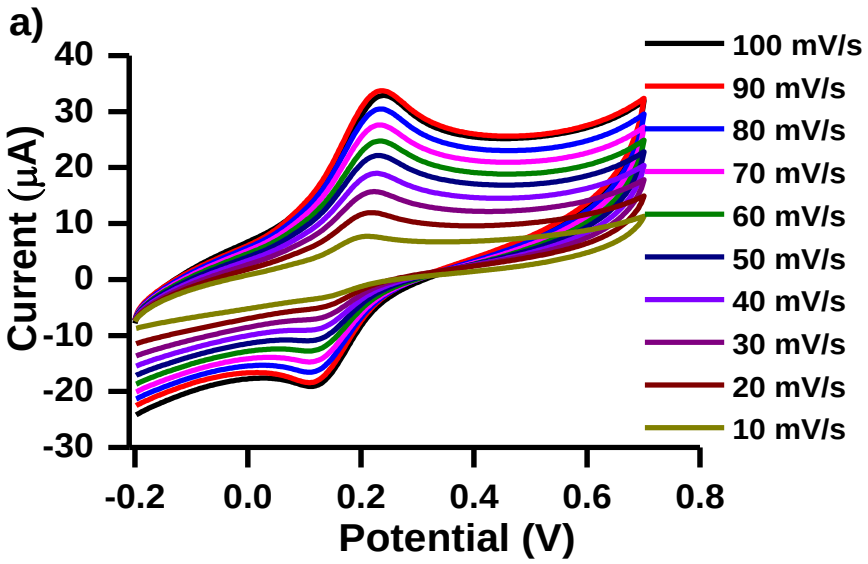
a)
Current (μA)
Potential (V)
100 mV/s
90 mV/s
80 mV/s
70 mV/s
60 mV/s
50 mV/s
40 mV/s
30 mV/s
20 mV/s
10 mV/s

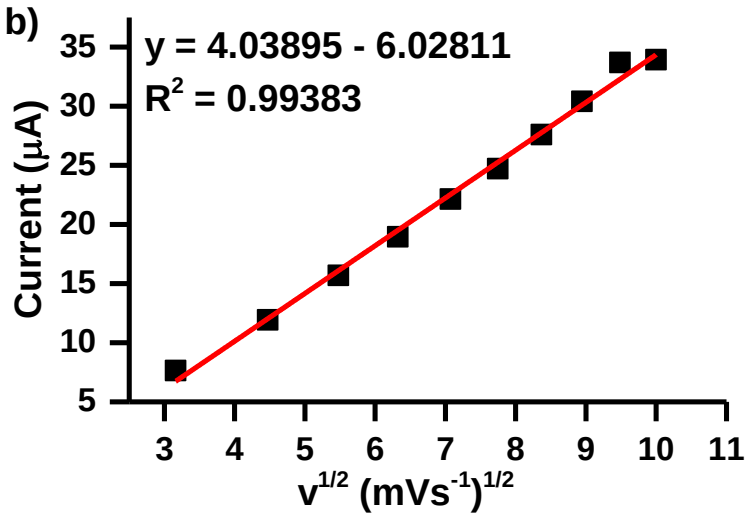
b)
y = 4.03895 - 6.02811
R2 = 0.99383
Current (μA)
v1/2 (mVs-1)1/2

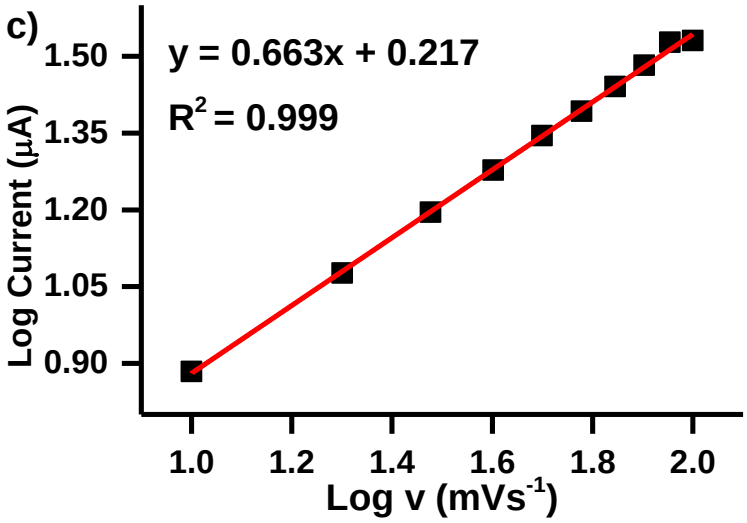
c)
y = 0.663x + 0.217
R2 = 0.999
Log Current (μA)
Log v (mVs-1)

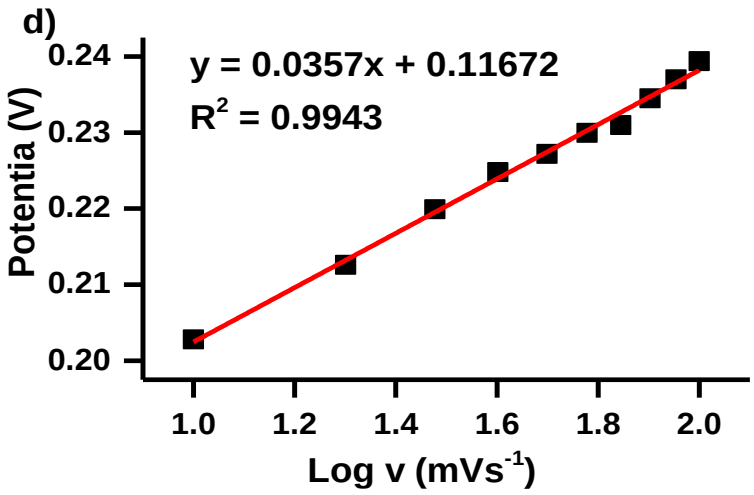

Figure 5.18: (a) Cyclic voltammograms obtained in 1 mM dopamine (in 0.1 M pH 7 PBS) at varied scan rates, (b) plot of oxidation peak current vs the square root of the scan rate, (c) log of oxidation peak current vs log of scan rate and (d) plot of oxidation peak potential vs log of scan rate. All plots were generated from **1-CoπNGQDs**.

Figure 5.18(c) was used to confirm these results. The gradient of the linear plots of the log of the oxidation peak current and log of the scan rate were used to determine whether the reaction processes between the electrocatalysts and the analyte are either diffusion or adsorption-controlled. The gradients obtained in this work were above 0.5, suggesting that the reaction processes were adsorption-controlled [230,246,247]. The conflicting results from the data obtained from Figures 5.18(b) and (c) indicate that there could be a mixture of reactions (both adsorption and diffusion) occurring at the electrode surface.

The Tafel slopes were calculated using Equation 5.11 with data obtained from Figure 5.18(d). Tafel slopes higher than 120 mVdecade^{-1} have no kinetic meaning and are due to adsorption on the electrode surface.

The Tafel slopes obtained herein were above 120 mVdecade^{-1}, ranging between 144 and 300 mVdecade^{-1} (Table 5.5). These high Tafel slope values suggest that the electroactive species were adsorbed at the electrode surface. This is consistent with the results obtained from

Figure 5.17(c). High Tafel slopes are also associated with the superimposition of two or more electron transfer reactions, which is the case with the electrooxidation of dopamine, as illustrated in Scheme 5.2. High values are attributed to the by-products from the two-step reaction being adsorbed at the electrode surface [236,248]. These high values are an indication of tight binding between the substrate (dopamine) and the electrocatalysts, hence they are attributed to adsorption at the electrode surface [236,248].

5.3.3 Sensitivity and Detection Limits Studies

Herein, chronoamperometry was used to determine three key detection parameters; limit of detection, sensitivity and catalytic rate constants (Figure 5.19).

Figure 5.19(a) is an illustration of the chronoamperograms obtained at varied dopamine concentrations (0 – 1000 µM) for **1-CoπNGQDs**. While the insert shows, the linear calibration curve plotted from the concentration of dopamine and the corresponding current obtained at a specific time. Using this plot and Equation 5.12, the LoDs of the electrocatalysts studied in this section were calculated and tabulated in Table 5.6.

The LoDs obtained for the hybrid materials, **1-CoπNGQDs** and **1-Co-AsπNGQDs,** were relatively lower than those of their respective MPcs showing that the incorporation of nanomaterials had a positive effect on the dopamine detection properties. The LoDs obtained in this work are an improvement compared to literature values based on other phthalocyanines (Table 5.6) [137].

The electrocatalytic rate constants of the detection of dopamine using the studied electrocatalysts were calculated using Equations 5.13 and 5.14 with the data obtained from

Figures 5.19(b and c). Linear regressions used to calculate the catalytic rates are expressed in Equations 5.17 (i-v), and the results are tabulated in Table 5.6.

$$y = slope\ (dopamine\ concentration)\frac{s^{-1}}{mM} + constant \quad \textbf{(5.17)}$$

NGQDs: (i)

y = 1.10x -0.375 (R^2 = 0.985)

1-Co: (ii)

y = 0.674x - 0.00264 (R^2 = 0.965)

1-CoπNGQDs: (iii)

y = 1.22x + 0.0426 (R^2 = 0.976)

1-Co-As: (iv)

y= 0.352x + 0.649 (R^2 = 0.9431)

1-Co-AsπNGQDs: (v)

y = 1.07x - 0.72 (R^2 = 0.985)

NGQDs alone obtained the highest rate constant. While the symmetric complex, **1-Co**, exhibited relatively higher rate constant compared to the asymmetric complex, **1-Co-As**. From the data obtained it can be observed that the incorporation of nanomaterials did not improve the electrocatalytic rate constant.

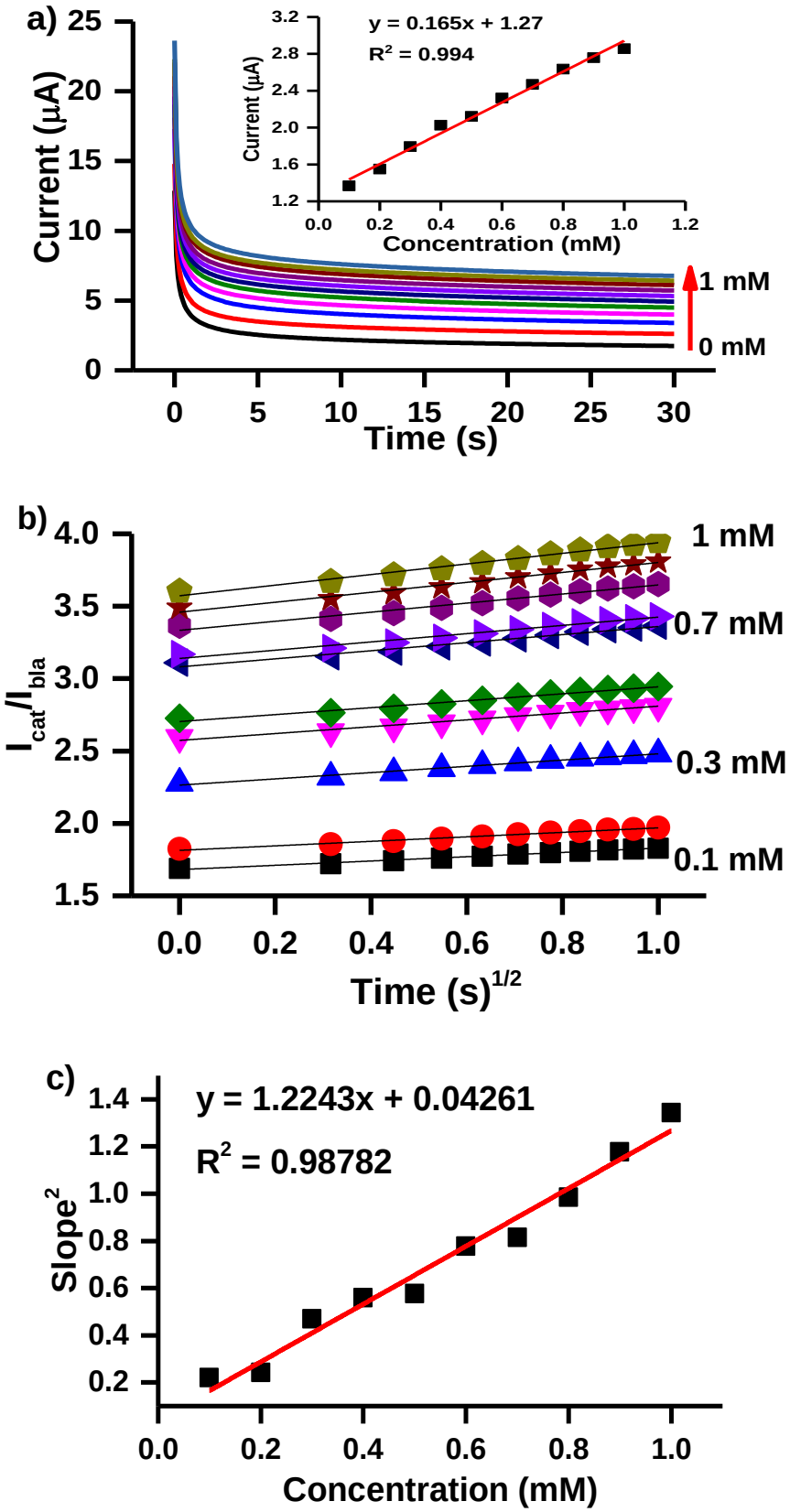

Figure 5.19: (a) Chronoamperograms obtained at varied dopamine concentrations (in 0.1 M pH 7 PBS). Insert: calibration curve of the dopamine concentration vs the oxidation current, (b) plots of (I_{cat}/I_{bla}) vs the square root of time and (c) plot of the square root of the slopes vs dopamine concentrations. All plots were generated from **1-CoπNGQDs**.

Table 5.6: Summary of the dopamine (in 0.1 M pH 7 PBS) detection parameters

	Sensitivity ($\mu A.mM^{-1}$)	**LoD (µM)**	**k ($mM^{-1}s^{-1}$)**	**Reference**
NGQDs	-	0.21	3.51×10^1	This work
1-Co	4.96	0.19	2.08×10^1	This work
1-CoπNGQDs	1.65	0.12	3.84×10^1	This work
1-Co-As	5.15	0.35	1.09×10^1	This work
1-Co-AsπNGQDs	2.42	0.25	3.45×10^1	This work
[a]MWCNT/Fe_3O_4/2,3-Nc	7.21	1.77		[137]
[a]MWCNT/Fe_3O_4/29H,31H-Pc	-	1.35	-	[137]
[a]MWCNT/ZnO/2,3-Nc	-	2.34	-	[137]
[a]MWCNT/ZnO/29H,31H-Pc	-	0.75	-	[137]

[a]MWCNTs = Multiwalled carbon nanotubes, 2,3-Nc = 2,3-Naphthalocyanine, 29H,31H-Pc = 29H,31H-Phthalocyanine.

5.3.4 Stability Studies

For a sensor to be regarded and used practically, it needs to be stable and consequently produce reproducible results. In this work, stability studies of the electrocatalysts in 1 mM dopamine (0.1 M pH 7 PBS) were conducted by running 20 CV scans consecutively (Figure 5.20). The stability of electrocatalysts is generally characterised by little or no change in the oxidation peak potential and currents.

A decrease in the peak current was observed for **1-Co** (Figure 5.20(a)). However, the electrode had stabilised by the 10^{th} scan. Minimal (below 25%) changes in the oxidation peak currents were observed, and a slight shift in the oxidation peak potential (< 5%) was also observed. An increase in the peak current was observed for **1-CoπNGQDs** (Figure 5.20(b)), and no change

was observed in the oxidation peak potential. The incorporation of NGQDs seems to have improved the stability of the MPcs toward the detection of dopamine.

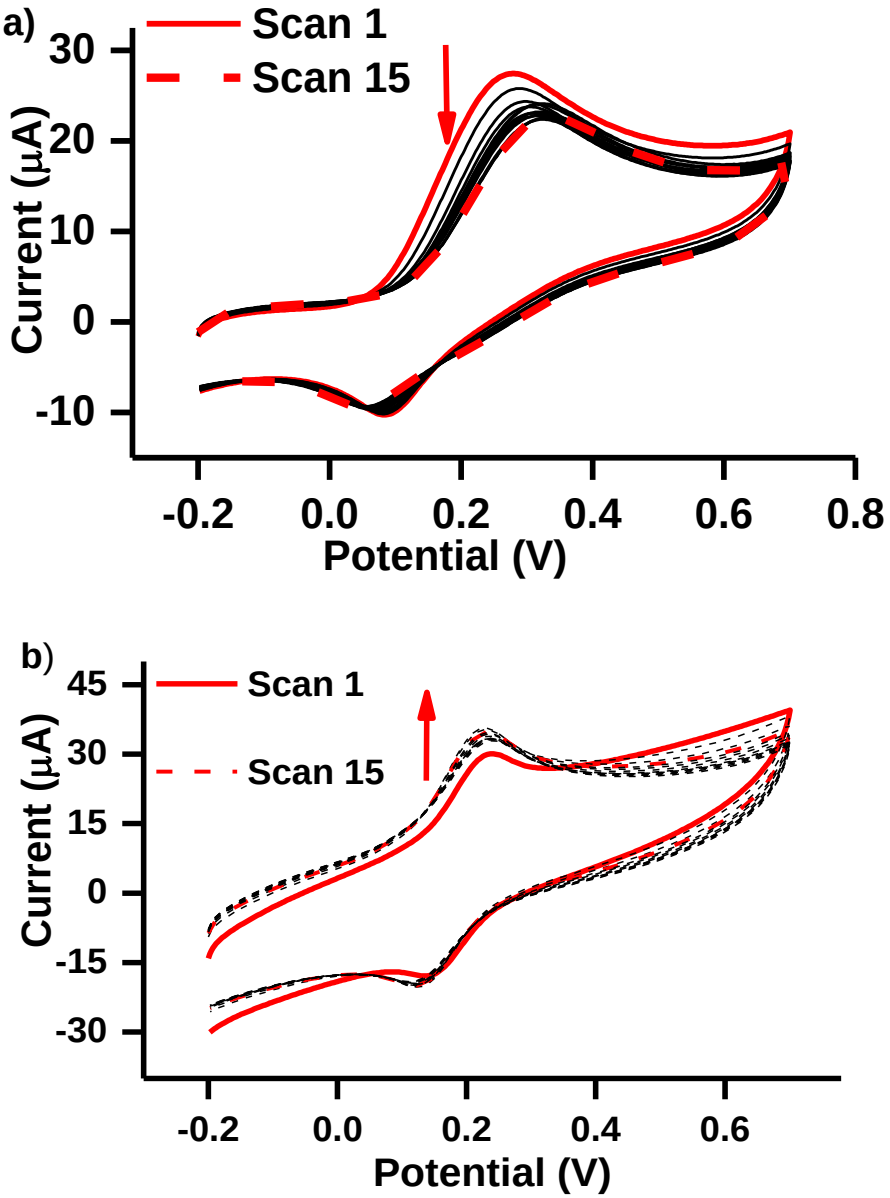

Figure 5.20: Repetitive cyclic voltammograms of a) **1-Co** and b) **1-Co-AsπNGQDs** in 1 mM dopamine in 0.1 M PBS. At a scan rate of 100 mVs^{-1}.

The relative standard deviation (RSD) of the peak currents in the stability studies were calculated to determine the precision and the reproducibility (stability) of the electrocatalysts studied in this work. The RSD values calculated ranged between 2.05 % and 7.64%. The overall decrease in the oxidation peak current was below 40%. All electrocatalysts employed herein proved to be stable as they could be used several times without the respective peaks disappearing completely or the oxidation peak potentials changing, indicating that the results are reproducible.

5.4 Conclusions

This chapter focused on the electrocatalysis of three test analytes; nitrite, catechol and dopamine. Herein, the synthesised phthalocyanine complexes, nanomaterials and their respective hybrids were employed as electrocatalysts in the electrochemical detection of these analytes.

It was observed that the glassy carbon electrode did not exhibit good detection properties for all three test analytes, either not detecting the analyte in the studied potential window or displaying an oxidation peak at high potentials and relatively lower currents. The decrease in oxidation peak potentials and increase in oxidation peak currents upon modification of the GCE shows the importance of electrode modification in electrochemical sensing.

The limits of detection, sensitivities and catalytic rate constants were determined for each analyte per studied electrocatalyst using chronoamperometry and various electrochemical principles and equations. The reaction kinetics and stability studies were conducted using cyclic voltammetry and stipulated equations.

Nitrite: Numerous MPc complexes, nanomaterials and hybrids were used in the detection of nitrite. Asymmetric complex **4-Co-As** was outperformed by all studied complexes (except for **8-Ni**), in terms of LoD, it did not exhibit good nitrite detection properties compared to its symmetric counterpart. The incorporation of nanomaterials to **4-Co-As** enhanced its nitrite detection properties, in terms of the LoD for all hybrid materials expect for **4-Co-AsπNGQDs** (sensitivity). Schiff base complexes **10-Mn** and **11-Mn** also exhibited good nitrite detection properties.

Catechol: A combination of copper and cobalt phthalocyanine complexes were used to detect catechol. The cobalt complexes were further used with nanomaterials (forming hybrid materials) to study the effect of nanomaterials on the electrochemical detection of catechol. Although **3-Co** had the lowest catechol detection limit (0.15 µM), copper complexes showered overall favorable (relatively lower) detection limits compared to the cobalt complexes. An improvement in the detection properties was observed upon the formation of Schiff bases (comparing Schiff base complexes **6-Cu** and **7-Cu** to their precursor **5-Cu**). With regard to the cobalt phthalocyanine complexes, **2-Co**, **3-Co** and, their associated nanomaterials and hybrids it can be concluded that the nanomaterials alone showed more favourable detection properties compared to the MPcs alone.

Dopamine: Symmetric MPc complex **1-Co** and asymmetric MPc complex **1-Co-As** and their respective **NGQDs** hybrids were used as electrocatalyst to detect dopamine. The stability studies conducted proved that the electrocatalysts were stable. Decreases in the peak potentials and the detection limits were observed upon hybridisation, indicating that the incorporation of nanomaterials enhanced the dopamine detection properties of the MPcs. The lowest and most favourable oxidation peak potential and detection limit were obtained

for **1-CoπNGQDs**. This suggests that lowering the symmetry of an MPc does not always enhance its electrochemical properties.

Comparing the test analytes: Although different MPc complexes were used, the following comparisons were drawn:

i. Dopamine and catechol exhibited lower oxidation peak potentials compared to nitrite.

ii. Lower detection limits were obtained for catechol and dopamine relative to nitrite.

iii. Generally higher oxidation peak currents were obtained for the detection of catechol compared to those obtained for dopamine and nitrite detection. This suggests that MPc complexes are more sensitive towards catchol detection.

iv. The overall results obtained herein are comparable to those obtained in literature. The results suggest that nitrite was more difficult to detect compared to dopamine and catechol. This could be attributed to nitrite not having π electrons which makes oxidation easier.

CHAPTER 6

CONCLUSIONS AND RECOMMENDATIONS

Preface: This chapter gives an overview and concludes the work conducted throughout this dissertation. It also provides recommendations (where necessary) for work that could be done to better the work done herein and possibly contribute more to the topics explored.

6. CONCLUSIONS AND RECOMMENDATIONS

6.1 Conclusions

The proposed symmetric and asymmetric phthalocyanine complexes were successfully synthesised using various metals and substituents. These complexes were characterised using various analytical techniques such as; UV-Vis absorption, FT-IR and mass spectroscopy.

Graphene quantum dots, nitrogen-doped quantum dots, bismuth tungsten oxide and nickel tungsten oxide nanoparticles were also successfully synthesised using the bottom-up approach. The synthesis of these nanomaterials was validated by characterising them using various analytical techniques such as XRD, DLS and AFM. Single-walled carbon-nanotubes purchased from Nanolab. However, they were characterised using the same techniques used for the other nanomaterials. Some of the MPc complexes were linked to the nanomaterials forming hybrid materials, the hybridisation/linkage was confirmed using the above-mentioned analytical techniques.

The complexes and materials synthesised (or formed) herein, were employed as electrocatalysts and successfully used in the electrochemical sensing of nitrite, catechol and or dopamine. Overall, the electrocatalysts studied here in showed promising results as electrocatalysts in the electrochemical detection of these analytical species, the results obtained were comparable with those cited in literature using similar materials. Nanomaterials, especially GQDs and Bi_2WO_6 showed better electrocatalytic properties compared to the MPc complexes. A general improvement in the electrocatalytic properties was observed for most complexes upon the incorporation of the nanomaterials

6.2 Recommendations

The following recommendations were made based on the results obtained in this work.

i. More studies/research need(s) to be done on the use of metal oxide nanomaterials (Bi_2WO_6 and $NiWO_4$) as electrocatalysts. These nanomaterials exhibited good electrocatalytic properties and they are not well studied in electrochemical sensing nor is their mechanism known.

ii. Studies need to be conducted to better understand how the morphology and structure of nanomaterials affect their electrocatalytic properties.

iii. The effect of symmetry on the electrocatalytic activity of MPc complexes was inconclusive, more studies need to be conducted to understand the effect of lowered MPc symmetry and whether its properties are solely based on the symmetry being reduced, or the type of substitutes used together.

REFERENCES

1. J. Mack, N. Kobayashi, Low symmetry phthalocyanines and their analogues, Chem. Rev. 111 (2011) 281.

2. H. Isago, Optical spectra of phthalocyanines and related compounds, (2015) Springer, Japan, Tokyo.

3. P. Gregory, Steamrollers, sports cars and security: phthalocyanine progress through the ages, J. Porphyr. Phthalocyanines 3 (1999) 468.

4. J.M. Robertson, R.P. Linstead, C.E. Dent, Molecular weights of the phthalocyanines, Nat. 135 (1935) 506.

5. R.P.J. Linstead, Phthalocyanines. Part I. A new type of synthetic colouring matters, J. Chem. Soc. (1934) 1016.

6. A.M. Schmidt, M.J.F. Calvete, Phthalocyanines: an old dog can still have new (photo)tricks!, Molecules 26 (2021) 2823.

7. K. Sakamoto, E. Ohno-Okumura Syntheses and functional properties of phthalocyanines, Materials 2 (2009) 1127.

8. V.N. Nemykin, E.A. Lukyanets, Synthesis of substituted phthalocyanines, Rev. Accounts (2010) 136.

9. T. Furuyama, K. Satoh, T. Kushiya, N. Kobayashi, Design, synthesis, and properties of phthalocyanine complexes with main-group elements showing main absorption and fluorescence beyond 1000 nm, J. Am. Chem. Soc. 136 (2013) 765.

10. T. Nyokong, Effects of substituents on the photochemical and photophysical properties of main group metal phthalocyanines, Coord. Chem. Rev. 251 (2007) 1707.

11. R. Medyouni, B. Hallouma, L. Mansour, S. Al-Quraishy, N. Hamdi, DBU-catalysed synthesis of metal-free phthalocyanines and metallophthalocyanines containing 2(3,4-dimethoxyphenyl)ethanol and 4-hydroxybenzaldehyde groups: characterisation, antimicrobial properties and aggregation behaviour, J. Chem. Res. 41 (2017) 291.

12. S. Bai, X. Sun, X. Chen, X. Yu, Q. Zhang, Synthesis and properties of a thioether bonded phthalonitrile resin, Mater. Today Commun. 24 (2020) 101352.

13. J. Wang, C. Chen, X. Chen, H. Wang, X. Yu, Y. Ma, K. Naito, Q. Zhang, Synthesis and properties of a novel naphthyl-containing self-promoted phthalonitrile polymer, High Perform. Polym. 30 (2018) 1114.

14. B.I. Kharisov, U. Ortiz Méndez, J.L. Almaraz Garza, J.R. Almaguer Rodríguez, Synthesis of non-substituted phthalocyanines by standard and non-standard techniques. Influence of solvent nature in phthalocyanine preparation at low temperature by UV-treatment of the reaction system, New J. Chem. 29 (2005) 686.

15. T.N. Lomova, E.Y. Tyulyaeva, New trends in the direct synthesis of phthalocyanine/porphyrin complexes, In: B. Kharisv (Eds) Direct synthesis of metal complexes. (2018) 239, Elsevier, Mexico.

16. A. Shaabani, R. Maleki-Moghaddam, A. Maleki, A.H. Rezayan, Microwave assisted synthesis of metal-free phthalocyanine and metallophthalocyanines, Dye. Pigm. 74 (2007) 279

17. H. Tomoda, S. Saito, S. Ogawa, S. Shiraishi, Synthesis of phthalocyanines from phthalonitrile with organic strong bases, Chem. Lett. 9 (2006) 1277.

18. I.M. Denekamp, F.L.P. Veenstra, P. Jungbacker, G. Rothenberg, A simple synthesis of symmetric phthalocyanines and their respective perfluoro and transition-metal complexes, Appl. Organomet. Chem. 33 (2019) e4872.

19. A. Wang, L. Long, C. Zhang, Synthesis of unsymmetrical phthalocyanines: a brief overview, Tetrahedron 68 (2012) 2433.

20. V.N. Nemykin, S. V. Dudkin, F. Dumoulin, C. Hirel, A.G. Gürek, V. Ahsen, Synthetic approaches to asymmetric phthalocyanines and their analogues, Rev. Accounts 2014 (2014) 142.

21. G. De La Torre, C.G. Claessens, T. Torres, Phthalocyanines: the need for selective synthetic approaches, European J. Org. Chem. 16 (2000) 2821.

22. E. Fazio, J. Jaramillo-García, G. De La Torre, T.T. Torres, Efficient synthesis of ABAB functionalized phthalocyanines, Org. Lett. 18 (2014) 4706.

23. I. Chambrier, M.J. Cook, S.J. Cracknell, J. Mcmurdo, Synthesis and characterisation of some non-uniformly substituted mesogenic phthalocyanines, J. Mater. Chem. 3 (1993) 841.

24. G. De la Torre, T. Torres, Synthetic advances in phthalocyanine chemistry, J. Porphyr. Phthalocyanines 6 (2002) 274.

25. M. Salih Ağirtaş, C. Karataş, S. Özdemir, Synthesis of some metallophthalocyanines with dimethyl 5-(phenoxy)-isophthalate substituents and evaluation of their antioxidant-antibacterial activities, Spectrochim. Acta Part A Mol. Biomol. Spectrosc. 135 (2015) 20.

26. H. Tomoda, S. Saito, S. Shiraishi, Synthesis of metallophthalocyanines from phthalonitrile with strong organic bases, Chem. Lett. 12 (1983) 313.

27. H. Karaca, S. Sezer, Ş. Özalp-Yaman, C. Tanyeli, Concise synthesis, electrochemistry and spectroelectrochemistry of phthalocyanines having triazole functionality, Polyhedron 72 (2014) 147.

28. P. Sen, S.Z. Yildiz, Substituted manganese phthalocyanines as bleach catalysts: synthesis, characterization and the investigation of de-aggregation behavior with LiCl in solutions, Res. Chem. Intermed. 42 (2019) 687.

29. J. Mack, M.J. Stillman, Assignment of the optical spectra of metal phthalocyanines through spectral band deconvolution analysis and ZINDO calculations, Coord. Chem. Rev. 219 (2001) 993.

30. C.G. Claessens, U.W.E. Hahn, T. Torres, Phthalocyanines: From outstanding electronic properties to emerging applications, Chem. Rec. 8 (2010) 75.

31. H. Ogata, R. Higashi, N. Kobayashi, Electronic absorption spectra of substituted phthalocyanines in solution and as films, J. Porphyr. Phthalocyanines 7 (2003) 551.

32. M. Gouterman, Spectra of porphyrins, J. Mol. Spectrosc. 6 (1961) 138.

33. P. Gregory, Industrial applications of phthalocyanines, J. Porphyr. Phthalocyanines 4 (2000) 432.

34. M.A. Dahlen, A new class of synthetic pigments and dyes, Ind. Eng. Chem. 31 (1939) 839

35. A.B. Sorokin, Phthalocyanine metal complexes in catalysis, Chem. Rev. 113 (2013)

8152.

36. L. Fernández, V.I. Esteves, Â. Cunha, R.J. Schneider, J.P.C. Tomé, Photodegradation of organic pollutants in water by immobilized porphyrins and phthalocyanines, J. Porphyr. Phthalocyanines 20 (2016) 150.

37. S.L. Wang, Y.F. Fang, Y. Yang, J.Z. Liu, A.P. Deng, X.R. Zhao, Y.P. Huang, Catalysis of organic pollutant photodegradation by metal phthalocyanines immobilized on TiO_2@SiO_2, Chinese Sci. Bull. 56 (2011) 969.

38. D. Gounden, N. Nombona, W.E. van Zyl, Recent advances in phthalocyanines for chemical sensor, non-linear optics (NLO) and energy storage applications, Coord. Chem. Rev. 420 (2020) 213359.

39. A. Kumar, V. Kumar Vashistha, D. Kumar Das, Recent development on metal phthalocyanines based materials for energy conversion and storage applications, Coord. Chem. Rev. 431 (2021) 213678.

40. M. Urbani, M.E. Ragoussi, M.K. Nazeeruddin, T. Torres, Phthalocyanines for dye-sensitized solar cells, Coord. Chem. Rev. 381 (2019) 1.

41. J. Oni, K.I. Ozoemena, Phthalocyanines in batteries and supercapacitors, J. Porphyr. Phthalocyanines 16 (2012) 754.

42. G. de la Torre, P. Vázquez, F. Agulló-López, T. Torres, Role of structural factors in the nonlinear optical properties of phthalocyanines and related compounds, Chem. Rev. 104 (2004) 3723.

43. M. Yahya, Y. Nural, Z. Seferoğlu, Recent advances in the nonlinear optical (NLO) properties of phthalocyanines: A review, Dye. Pigm. 198 (2022) 109960.

44. M.A. Díaz-García, Nonlinear optical properties of phthalocyanines and related compounds, J. Porphyr. Phthalocyanines 13 (2012) 652.

45. A. Anas, J. Sobhanan, K.M. Sulfiya, C. Jasmin, P.K. Sreelakshmi, V. Biju, Advances in photodynamic antimicrobial chemotherapy, J. Photochem. Photobiol. C Photochem. Rev. 49 (2021) 100452.

46. T. Nyokong, Desired properties of new phthalocyanines for photodynamic therapy, Pure Appl. Chem. 83 (2011) 1763.

47. M. Wainwright, Photodynamic antimicrobial chemotherapy (PACT), J. Antimicrob. Chemother. 42 (1998) 13.

48. D. Mukherjee, R. Manjunatha, S. Sampath, A.K. Ray, Phthalocyanines as sensitive materials for chemical sensors, Mater. Chem. Sens. (2016) 165.

49. E. Demir, H. Silah, B. Uslu, Phthalocyanine modified electrodes in electrochemical analysis, Crit. Rev. Anal. Chem. 52 (2020) 425

50. S. Srinivasan, H. Wroblowa, J.O.M. Bockris, Electrocatalysis, Adv. Catal. 17 (1967) 351.

51. M. Gara, K.R. Ward, R.G. Compton, Nanomaterial modified electrodes: evaluating oxygen reduction catalysts, Nanoscale 5 (2013) 7304.

52. A.M. Abdel-Aziz, H.H. Hassan, I.H.A. Badr, Glassy carbon electrode electromodification in the presence of organic monomers: electropolymerization versus activation, Anal. Chem. 92 (2020) 7947.

53. A. Leniart, M. Brycht, B. Burnat, S. Skrzypek, An application of a glassy carbon electrode and a glassy carbon electrode modified with multi-walled carbon nanotubes in

electroanalytical determination of oxycarboxin, Ionics 24 (2018) 2111.

54. E. Desimoni, B. Brunetti, Glassy Carbon Electrodes Film-Modified with Acidic Functionalities. A Review, Electroanalysis 24 (2012) 1481.

55. A.R. Guadalupe, H.D. Abruña, Electroanalysis with chemically modified electrodes, Anal. Chem. 57 (1985) 142.

56. J.-M. Zen, A.S. Kumar, D.-M. Tsai, Recent updates of chemically modified electrodes in analytical chemistry, Electroanalysis 15 (2003) 1073.

57. N. Sandhyarani, Surface modification methods for electrochemical biosensors, in: A.A. Ensafi (Ed), Electrochemical Biosensensors, (2019) 45, Elsevier, Iran.

58. T. Nyokong, S. Khene, Modification of electrode surfaces with metallophthalocyanine nanomaterial hybrid, in: Z.J. H, F. Bedioui (Eds.), N4-Macrocyclic Metal Complexes, (2006) 225, Springer, United States of America.

59. J.H. Zagal, Metallophthalocyanines as catalysts in electrochemical reactions, Coord. Chem. Rev. 119 (1992) 89.

60. L. Ding, J. Qiao, X. Dai, J. Zhang, J. Zhang, B. Tian, Highly active electrocatalysts for oxygen reduction from carbon-supported copper-phthalocyanine synthesized by high temperature treatment, Int. J. Hydrogen Energy 37 (2012) 14103.

61. T. V. Basova, A.K. Ray, V. Basova, Tamara, K. Ray, Asim, Hybrid materials based on phthalocyanines and metal nanoparticles for chemiresistive and electrochemical sensors: a mini-review, ECS J. Solid State Sci. Technol. 9 (2020) 061001.

62. J.H. Zagal, S. Griveau, J.F. Silva, T. Nyokong, F. Bedioui, Metallophthalocyanine-based

molecular materials as catalysts for electrochemical reactions, Coord. Chem. Rev. 254 (2010) 2755.

63. N. Baig, I. Kammakakam, W. Falath, I. Kammakakam, Nanomaterials: a review of synthesis methods, properties, recent progress, and challenges, Mater. Adv. 2 (2021) 1821.

64. J.K. Patra, K.H. Baek, Green Nanobiotechnology: Factors Affecting Synthesis and Characterization Techniques, J. Nanomater. 2014 (2014) 417035.

65. T.R. Pisanic, Y. Zhang, T.H. Wang, Quantum dots in diagnostics and detection: Principles and paradigms, Analyst 139 (2014) 2968.

66. J. Singh, T. Dutta, K.H. Kim, M. Rawat, P. Samddar, P. Kumar, 'Green' synthesis of metals and their oxide nanoparticles: applications for environmental remediation, J. Nanobiotechnology, 16 (2018) 1.

67. D. Titus, E. James Jebaseelan Samuel, S.M. Roopan, Nanoparticle characterization techniques, in: A.K. Shukla, S. Iravani (Eds.), Green synthesis, characterisation and applications of nanoparticles, (2019) 303, Elsevier, Netherlands.

68. M.M. Modena, B. Rühle, T.P. Burg, S. Wuttke, M.M. Modena, E. Zurich, B. Rühle, T.P. Burg, S. Wuttke, Nanoparticle Characterization: What to Measure?, Adv. Mater. 31 (2019) 1901556.

69. M. Azizi-Lalabadi, H. Hashemi, J. Feng, S.M. Jafari, Carbon nanomaterials against pathogens; the antimicrobial activity of carbon nanotubes, graphene/graphene oxide, fullerenes, and their nanocomposites, Adv. Colloid Interface Sci. 284 (2020) 102250.

70. P.V. Sharma, U. Sharma, M. Chattopadhyay, V.N. Shukla, Advance Applications of

Nanomaterials: A Review, Mater. Today Proc. 5 (2018) 6376.

71. L.A. Kolahalam, I. V. Kasi Viswanath, B.S. Diwakar, B. Govindh, V. Reddy, Y.L.N. Murthy, Review on nanomaterials: Synthesis and applications, Mater. Today 18 (2019) 2182.

72. V. Georgakilas, M. Otyepka, A.B. Bourlinos, V. Chandra, N. Kim, K.C. Kemp, P. Hobza, R. Zboril, K.S. Kim, Functionalization of graphene: Covalent and non-covalent approaches, derivatives and applications, Chem. Rev. 112 (2012) 6156.

73. C.M. Tîlmaciu, M.C. Morris, Carbon nanotube biosensors, Front. Chem. 3 (2015) 00059.

74. Y. Zhou, Y. Fang, R.P. Ramasamy, Non-Covalent Functionalization of Carbon Nanotubes for Electrochemical Biosensor Development, Sensors 19 (2019) 392.

75. N. Saifuddin, A.Z. Raziah, A.R. Junizah, Carbon Nanotubes: A Review on Structure and Their Interaction with Proteins, J. Chem. (2013) 676815.

76. C. Gao, Z. Guo, J.H. Liu, X.J. Huang, The new age of carbon nanotubes: An updated review of functionalized carbon nanotubes in electrochemical sensors, Nanoscale, 4 (2012) 1948.

77. D. Maiti, X. Tong, X. Mou, K. Yang, Carbon-Based Nanomaterials for Biomedical Applications: A Recent Study, Fonteirs Pharmacol. 9 (2019) 1401.

78. M.S. Mauter, M. Elimelech, Environmental applications of carbon-based nanomaterials, Environ. Sci. Technol. 42 (2008) 5843.

79. J. Zhang, Z. Xia, L. Dai, Carbon-based electrocatalysts for advanced energy conversion and storage, Sci. Adv. 1 (2015) e1500564.

80. M. Coroş, F. Pogăcean, L. Măgeruşan, C. Socaci, S. Pruneanu, A brief overview on

synthesis and applications of graphene and graphene-based nanomaterials, Front. Mater. Sci. 13 (2019) 23.

81. C.I.L. Justino, A.R. Gomes, A.C. Freitas, A.C. Duarte, T.A.P. Rocha-Santos, Graphene based sensors and biosensors, TrAC - Trends Anal. Chem. 91 (2017) 53.

82. M.M. Kaur, M.M. Kaur, V.K. Sharma, Historical perspective nitrogen-doped graphene and graphene quantum dots: A review on synthesis and applications in energy, sensors and environment, Adv. Colloid Interface Sci. 259 (2018) 44.

83. Z. Liu, F. Li, Y. Luo, M. Li, G. Hu, X. Pu, T. Tang, J. Wen, X. Li, W. Li, Size effect of graphene quantum dots on photoluminescence, Molecules 26 (2021) 1.

84. X. Yan, X. Cui, L.S. Li, Synthesis of large, stable colloidal graphene quantum dots with tunable size, J. Am. Chem. Soc. 132 (2010) 5944.

85. H. Wang, T. Maiyalagan, X. Wang, Review on recent progress in nitrogen-doped graphene: Synthesis, characterization, and its potential applications, ACS Catal. 2 (2012) 781.

86. A. Chen, S. Chatterjee, Nanomaterials based electrochemical sensors for biomedical applications, Chem. Soc. Rev. 42 (2013) 5425.

87. K.S. Ibrahim, Carbon nanotubes-properties and applications: a review Review Articles, Carbon Lett. 14 (2013) 131.

88. A. Kasperski, A. Weibel, L. Datas, E. De Grave, A. Peigney, C. Laurent, Large-diameter single-wall carbon nanotubes formed alongside small-diameter double-walled carbon nanotubes, J. Phys. Chem. C. 119 (2015) 1524.

89. A.J. Saleh Ahammad, J.J. Lee, M.A. Rahman, Electrochemical sensors based on carbon nanotubes, Sensors 9 (2009) 2289.

90. Q. Zhao, Z. Gan, Q. Zhuang, Electrochemical sensors based on carbon nanotubes, Electroanalysis 14 (2002) 1609.

91. C. Luhana, I. Moyo, K. Tshenkeng, P. Mashazi, In-sera selectivity detection of catecholamine neurotransmitters using covalent composite of cobalt phthalocyanine and aminated graphene quantum dots, Microchem. J. 180 (2022) 107605.

92. B.S. Jilani, C.D. Mruthyunjayachari, P. Malathesh, Mounesh, T.M. Sharankumar, K.R.V. Reddy, Electrochemical sensing based MWCNT-Cobalt tetra substituted sorbaamide phthalocyanine onto the glassy carbon electrode towards the determination of 2-Amino phenol: A voltammetric study, Sensors Actuators B Chem. 301 (2019) 127078.

93. E.N. Kaya, T. Basova, M. Polyakov, M. Durmuş, B. Kadem, A. Hassan, Hybrid materials of pyrene substituted phthalocyanines with single-walled carbon nanotubes: structure and sensing properties, RSC Adv. 5 (2015) 91855.

94. R. Nkhahle, K.E. Sekhosana, S. Centane, T. Nyokong, Electrocatalytic activity of asymmetrical cobalt phthalocyanines in the presence of n doped graphene quantum dots: the push-pull effects of substituents, Electroanalysis 31 (2019) 891.

95. E. Jubete, K. Elechowska, O.A. Loaiza, P.J. Lamas, E. Ochoteco, K.D. Farmer, K.P. Roberts, J.F. Biernat, Derivatization of SWCNTs with cobalt phthalocyanine residues and applications in screen printed electrodes for electrochemical detection of thiocholine, Electrochim. Acta 56 (2011) 3988.

96. N. Diab, D.M. Morales, C. Andronescu, M. Masoud, W. Schuhmann, A sensitive and

selective graphene/cobalt tetrasulfonated phthalocyanine sensor for detection of dopamine, Sensors Actuators B Chem. 285 (2019) 17.

97. H. Wu, Z. Chen, L. Guo, Y. Wang, S. Du, Y. Wu, Z. Ren, Direct coupling of phthalocyanine cobalt(ii) and graphene via self-driven layer-by-layer assembly for efficient electrochemical detection of catechol, J. Electrochem. Soc. 167 (2020) 027533.

98. A.J. Shnoudeh, I. Hamad, R.W. Abdo, L. Qadumii, A.Y. Jaber, H.S. Surchi, S.Z. Alkelany, Synthesis, characterization, and applications of metal nanoparticles, in: R.K. Tekade (Ed.), Biomaterial and bionanotechnology: advances in pharmaceutical product development and research, (2019) 527, Academic Press, Gandhinagar, India.

99. P. Makvandi, C.C.C. Wang, E. Nazarzadeh Zare, A. Borzacchiello, L.L. Niu, F.R. Tay, Metal-based nanomaterials in biomedical applications: antimicrobial activity and cytotoxicity aspects, Adv. Funct. Mater. 30 (2020) 1910021.

100. H. Xu, H. Shang, C. Wang, Y. Du, H. Xu, H. Shang, C. Wang, Y. Du, Low-dimensional metallic nanomaterials for advanced electrocatalysis, Adv. Funct. Mater. . 30 (2020) 2006317.

101. K.L. Kelly, E. Coronado, L.L. Zhao, G.C. Schatz, The optical properties of metal nanoparticles: The influence of size, shape, and dielectric environment, J. Phys. Chem. B. 107 (2003) 668.

102. J. Ke, M. Adnan Younis, Y. Kong, H. Zhou, J. Liu, L. Lei, Y. Hou, Nanostructured ternary metal tungstate-based photocatalysts for environmental purification and solar water splitting: a review, Nano-Micro Lett. 10 (2018) 69.

103. H. Yi, L. Qin, D. Huang, G. Zeng, C. Lai, X. Liu, B. Li, H. Wang, C. Zhou, F. Huang, S. Liu, X.

Guo, Nano-structured bismuth tungstate with controlled morphology: Fabrication, modification, environmental application and mechanism insight, Chem. Eng. J. 358 (2019) 480.

104. S.M. Pourmortazavi, M. Rahimi-Nasrabadi, M. Khalilian-Shalamzari, M.M. Zahedi, S.S. Hajimirsadeghi, I. Omrani, Synthesis, structure characterization and catalytic activity of nickel tungstate nanoparticles, Appl. Surf. Sci. 263 (2012) 745.

105. S.M. M Zawawi, R. Yahya, A. Hassan, H.N.M.E. Mahmud, M.N. Daud, Structural and optical characterization of metal tungstates (MWO_4; M=Ni, Ba, Bi) synthesized by a sucrose-templated method, Chem. Cent. J. 7 (2013) 1.

106. L. Yu, B. Yu Xia, X. Wang, X. Wen Lou, L. Yu, B.Y. Xia, X. Wang, X.W. Lou, General formation of M–MoS_3 (M = Co, Ni) hollow structures with enhanced electrocatalytic activity for hydrogen evolution, Adv. Mater. 28 (2016) 92.

107. A. Thomas, C. Janáky, G.F. Samu, M.N. Huda, P. Sarker, J.P. Liu, V. Van Nguyen, E.H. Wang, K.A. Schug, K. Rajeshwar, Time- and energy-efficient solution combustion synthesis of binary metal tungstate nanoparticles with enhanced photocatalytic activity, Chem. Sus. Chem. 8 (2015) 1652.

108. H. Eranjaneya, P.S. Adarakatti, A. Siddaramanna, C.G. Thimmanna, Nickel tungstate nanoparticles: synthesis, characterization and electrochemical sensing of mercury(II) ions, J. Mater. Sci. Mater. Electron. 30 (2019) 3574.

109. X.X. Wang, Y. Li, M.C. Liu, L. Bin Kong, Fabrication and electrochemical investigation of MWO_4 (M = Co, Ni) nanoparticles as high-performance anode materials for lithium-ion batteries, Ionics 24 (2018) 363.

110. L. Zhang, Y. Zhu, A review of controllable synthesis and enhancement of performances of bismuth tungstate visible-light-driven photocatalysts, Catal. Sci. Technol. 2 (2012) 694.

111. H.K. Kroupova, J. Machova, Z. Svobofva, Nitrite influence on fish: a review, Vet. Med. 50 (2005) 461.

112. W.E.J. Phillips, Naturally occurring nitrate and nitrite in foods in relation to infant methaemoglobinaemia, Food Cosmet. Toxicol. 9 (1971) 219.

113. N.S. Bryan, D.D. Alexander, J.R. Coughlin, A.L. Milkowski, P. Boffetta, Ingested nitrate and nitrite and stomach cancer risk: An updated review, Food Chem. Toxicol. 50 (2012) 3646.

114. R. Walker, Naturally occurring nitrate/nitrite in foods., J. Sci. Food Agric. 26 (1975) 17351742.

115. M.J. Moorcroft, J. Davis, R.G. Compton, Detection and determination of nitrate and nitrite: a review, Talanta 54 (2001) 785.

116. M. Gilchrist, A.C. Shore, N. Benjamin, Inorganic nitrate and nitrite and control of blood pressure, Cardiovasc. Res. 89 (2011) 492.

117. K.L. Jonvik, J. Nyakayiru, P.J. Pinckaers, J.M. Senden, L.J. Van Loon, L.B. Verdijk, Nitrate-rich vegetables increase plasma nitrate and nitrite concentrations and lower blood pressure in healthy adults, J. Nutr. 146 (2016) 986.

118. N.S. Bryan, M.B. Grisham, Methods to detect nitric oxide and its metabolites in biological samples, Free Radic. Biol. Med. 43 (2007) 645.

119. H. Trachtman, B. Gauthier, R. Frank, S. Futterweit, A. Goldstein, J. Tomczak, Increased urinary nitrite excretion in children with minimal change nephrotic syndrome, J. Pediatr. 128 (1996) 173

120. Y. Ueki, S. Miyake, Y. Tominaga, K. Eguchi, Increased nitric oxide levels in patients with rheumatoid arthritis., J. Rheumatol. 23 (1996) 230.

121. M.A. Kuiper, J.J. Visser, P.L.M. Bergmans, P. Scheltens, E.C. Wolters, Decreased cerebrospinal fluid nitrate levels in Parkinson's disease, Alzheimer's disease and multiple system atrophy patients, J. Neurol. Sci. 121 (1994) 46.

122. Q.H. Wang, L.J. Yu, Y. Liu, L. Lin, R. gang Lu, J. ping Zhu, L. He, Z.L. Lu, Methods for the detection and determination of nitrite and nitrate: A review, Talanta 165 (2017) 709.

123. Z. Yilong, Z. Dean, L. Daoliang, Electrochemical and other methods for detection and determination of dissolved nitrite: a review, Int. J. Electrochem. Sci. 10 (2015) 1144.

124. P. Singh, M.K. Singh, Y.R. Beg, G.R. Nishad, A review on spectroscopic methods for determination of nitrite and nitrate in environmental samples, Talanta 191 (2019) 364.

125. M.L.A.V. Heien, A.S. Khan, J.L. Ariansen, J.F. Cheer, P.E.M. Phillips, K.M. Wassum, R.M. Wightman, Real-time measurement of dopamine fluctuations after cocaine in the brain of behaving rats, Proc. Natl. Acad. Sci. 102 (2005) 10023.

126. S.D. Iversen, L.L. Iversen, Dopamine: 50 years in perspective, Trends Neurosci. 30 (2007) 188.

127. R. Pivonello, D. Ferone, G. Lombardi, A. Colao, S.W.J. Lamberts, L.J. Hofland, Novel insights in dopamine receptor physiology, Eur. J. Endocrinol. 156 (2007) 13.

128. J.N.J. Reynolds, B.I. Hyland, J.R. Wickens, A cellular mechanism of reward-related learning, Nat. 413 (2001) 67.

129. N. Matsumoto, T. Hanakawa, S. Maki, A.M. Graybiel, M. Kimura, Nigrostriatal dopamine system in learning to perform sequential motor tasks in a predictive manner, J. Neurophysiol. 82 (1999) 978.

130. R.A. Wise, Dopamine, learning and motivation, Nat. Rev. Neurosci. 56 (2004) 483.

131. M. Lakshmanakumar, N. Nesakumar, A.J. Kulandaisamy, J.B.B. Rayappan, Principles and recent developments in optical and electrochemical sensing of dopamine: A comprehensive review, Measurement 183 (2021) 109873.

132. X. Wei, Z. Zhang, Z. Wang, A simple dopamine detection method based on fluorescence analysis and dopamine polymerization, Microchem. J. 145 (2019) 55.

133. P.A. Rasheed, J.S. Lee, Recent advances in optical detection of dopamine using nanomaterials, Microchim. Acta 184 (2017) 1239.

134. S.M. Siddeeg, Electrochemical detection of neurotransmitter dopamine: a review, Int. J. Electrochem. Sci. 15 (2020) 599.

135. N. Baig, M. Sajid, T.A. Saleh, Recent trends in nanomaterial-modified electrodes for electroanalytical applications, TrAC Trends Anal. Chem. 111 (2019) 47.

136. K. Jackowska, P. Krysinski, New trends in the electrochemical sensing of dopamine, Anal. Bioanal. Chem. 405 (2012) 3753.

137. N.G. Mphuthi, A.S. Adekunle, O.E. Fayemi, L.O. Olasunkanmi, E.E. Ebenso, Phthalocyanine doped metal oxide nanoparticles on multiwalled carbon nanotubes

platform for the detection of dopamine, Sci. Reports 71 (2017) 1.

138. C. Karuppiah, R. Devasenathipathy, S.M. Chen, D. Arulraj, S. Palanisamy, V. Mani, V.S. Vasantha, Fabrication of nickel tetrasulfonated phthalocyanine functionalized multiwalled carbon nanotubes on activated glassy carbon electrode for the detection of dopamine, Electroanalysis 27 (2015) 485.

139. J. Sedõ, J. Saiz-Poseu, F. Busqué, D. Ruiz-Molina, Catechol-based biomimetic functional materials, Adv. Mater. 25 (2013) 653.

140. J. He, R. Qiu, W. Li, S. Xing, Z. Song, Q. Li, S. Zhang, A voltammetric sensor based on eosin Y film modified glassy carbon electrode for simultaneous determination of hydroquinone and catechol, Anal. Methods 6 (2014) 6494.

141. F. Karim, A.N.M. Fakhruddin, Recent advances in the development of biosensor for phenol: A review, Rev. Environ. Sci. Biotechnol. 11 (2012) 261.

142. D. Gonçalves, G. Alves, P. Soares-da-Silva, A. Falcão, Bioanalytical chromatographic methods for the determination of catechol-O-methyltransferase inhibitors in rodents and human samples: A review, Anal. Chim. Acta 710 (2012) 17.

143. S. Dong, L. Chi, Z. Yang, P. He, Q. Wang, Y. Fang, Simultaneous determination of dihydroxybenzene and phenylenediamine positional isomers using capillary zone electrophoresis coupled with amperometric detection, J. Sep. Sci. 32 (2009) 3232.

144. J.A. Ribeiro, P.M.V. Fernandes, C.M. Pereira, F. Silva, Electrochemical sensors and biosensors for determination of catecholamine neurotransmitters: A review, Talanta 160 (2016) 653.

145. P. Alessio, F.J. Pavinatto, O.N. Oliveira, J.A. De Saja Saez, C.J.L. Constantino, M.L.

Rodríguez-Méndez, Detection of catechol using mixed Langmuir-Blodgett films of a phospholipid and phthalocyanines as voltammetric sensors, Analyst 135 (2010) 2591.

146. O.J. Achadu, T. Nyokong, Interaction of graphene quantum dots with 4-acetamido-2,2,6,6-tetramethylpiperidine-oxyl free radicals: a spectroscopic and fluorimetric study, J. Fluoresc. 26 (2016) 283.

147. D. Qu, M. Zheng, P. Du, Y. Zhou, L. Zhang, D. Li, H. Tan, Z. Zhao, Z. Xie, Z. Sun, Highly luminescent S, N co-doped graphene quantum dots with broad visible absorption bands for visible light photocatalysts, Nanoscale 5 (2013) 12272.

148. S.F. Anis, B.S. Lalia, A.O. Mostafa, R. Hashaikeh, Electrospun nickel–tungsten oxide composite fibers as active electrocatalysts for hydrogen evolution reaction, J. Mater. Sci. 52 (2017) 7269.

149. B.K. Bansod, T. Kumar, R. Thakur, S. Rana, I. Singh, A review on various electrochemical techniques for heavy metal ions detection with different sensing platforms, Biosens. Bioelectron. 94 (2017) 443.

150. L. Zhang, J. Huang, L. Ren, M. Bai, L. Wu, B. Zhai, X. Zhou, Synthesis and evaluation of cationic phthalocyanine derivatives as potential inhibitors of telomerase, Bioorganic Med. Chem. 16 (2008) 303.

151. J.G. Young, W. Onyebuaga, Synthesis and characterization of di-disubstituted phthalocyanines, J. Org. Chem. 55 (1990) 2155.

152. Y.I. Openda, P. Sen, M. Managa, T. Nyokong, Acetophenone substituted phthalocyanines and their graphene quantum dots conjugates as photosensitizers for photodynamic antimicrobial chemotherapy against Staphylococcus aureus,

Photodiagnosis Photodyn. Ther. 29 (2020) 101607.

153. X. Zhang, W. Lin, H. Zhao, R. Wang, Raman spectra study of p-tert-butylphenoxy-substituted phthalocyanines with different central metal and substitution positions, Vib. Spectrosc. 96 (2018) 26.

154. P. Sen, A.Y Göknur, A. Erdoğmuş, N. Dege, H. Genç, Y. Atalay, S.Z. Yildiz, The synthesis, characterization, crystal structure and photophysical properties of a new meso-bodipy substituted phthalonitrile, J. Fluoresc. 25 (2015) 1225.

155. H. Karaca, B. Çayeɬil, S. Sezer, Synthesis characterization and metal sensing applications of novel chalcone substituted phthalocyanines, Synth. Met. 215 (2016) 134.

156. S.A. Majeed, N. Nwaji, J. Mack, T. Nyokong, S. Makhseed, Nonlinear optical responses of carbazole-substituted phthalocyanines conjugated to graphene quantum dots and in thin films, J. Lumin. 213 (2019) 88.

157. N. Li, W. Lu, K. Pei, W. Chen, Interfacial peroxidase-like catalytic activity of surface-immobilized cobalt phthalocyanine on multiwall carbon nanotubes, RSC Adv. 5 (2015) 9374.

158. J. Rusanova, M. Pilkington, S. Decurtins, A novel fully conjugated phenanthroline - appended phthalocyanine : synthesis and characterisation, Chem. Commun. 19 (2002) 2236.

159. T. Nyokong, Electronic spectral and electrochemical behavior of near infrared absorbing metallophthalocyanines, in: J. Jiang (Ed.), Functional phthalocyanine molecular materials. structure and bonding (2010) 45. Springer, Berlin, Heidelberg

160. S.Ç. Yazici, S. Kahraman, S.Z. Yildiz, M.D. Yilmaz, Peripherally substituted soluble nickel

phthalocyanines: Synthesis, characterization, aggregation behavior and antioxidant properties, J. Porphyr. Phthalocyanines 23 (2019) 1478.

161. M.N. Abbas, A. Lattief, A.L. Radwan, P. Bühlmann, M.A. Abd, E. Ghaffar, Solid-Contact Perchlorate Sensor with Nanomolar Detection Limit Based on Cobalt Phthalocyanine Ionophores Covalently Attached to Polyacrylamide, Am. J. Anal. Chem. 02 (2011) 820.

162. C.C. Leznoff, L.S. Black, A. Hiebert, P.W. Causey, D. Christendat, A.B.P. Lever, Red manganese phthalocyanines from highly hindered hexadecaalkoxyphthalocyanines, Inorganica Chim. Acta 359 (2006) 2690.

163. L. Meng, K. Wang, Y. Han, Y. Yao, P. Gao, C. Huang, W. Zhang, F. Xu, Synthesis, structure, and optical properties of manganese phthalocyanine thin films and nanostructures, Prog. Nat. Sci. Mater. Int. 27 (2017) 329.

164. J. Ryu, E. Lee, S. Lee, J. Jang, Fabrication of graphene quantum dot-decorated graphene sheets via chemical surface modification, Chem. Commun. 50 (2014) 15616.

165. O.J. Achadu, T. Nyokong, Fluorescence “turn-ON” nanosensor for cyanide ion using supramolecular hybrid of graphene quantum dots and cobalt pyrene-derivatized phthalocyanine, Dye. Pigment 160 (2019) 328.

166. Y. Sun, S. Wang, C. Li, P. Luo, L. Tao, Y. Wei, G. Shi, Large scale preparation of graphene quantum dots from graphite with tunable fluorescence properties, Phys. Chem. Chem. Phys. 15 (2013) 9907.

167. X.F. Zhang, X. Shao, π–π binding ability of different carbon nano-materials with aromatic phthalocyanine molecules: Comparison between graphene, graphene oxide and carbon nanotubes, J. Photochem. Photobiol. A Chem. 278 (2014) 69.

168. Z. de Liu, H.X. Zhao, C.Z. Huang, Obstruction of photoinduced electron transfer from excited porphyrin to graphene oxide: a fluorescence turn-on sensing platform for iron (iii) ions, PLoS One. 7 (2012) e50367.

169. M.H.V. Reddy, R.M. Al-Shammari, N. Al-Attar, S. Lopez, T.E. Keyes, J.H. Rice, Optical properties of porphyrin: graphene oxide composites, Nanostructured Thin Film. VII. 9172 (2014) 91720P.

170. R. Prabakaran, R. Kesavamoorthy, G.L.N. Reddy, F.P. Xavier, structural investigation of copper phthalocyanine thin films using X-Ray Diffraction, raman scattering and optical absorption measurements, Phys. Status Solidi Basic Res. 229 (2022) 1175.

171. R. Das, S. Bee Abd Hamid, M. Eaqub Ali, S. Ramakrishna, W. Yongzhi, Carbon nanotubes characterization by X-ray powder diffraction- a review, Curr. Nanosci. 11 (2015) 23.

172. F.H. Abdulrazzak, A.F. Alkiam, Hussein. Falah Hasan, Behavior of X-ray analysis of carbon nanotubes, in: H.E.-D., Saleh, S.M.M. El-Sheikh (Eds.), Perspective of Carbon Nanotubes (2019) 109, InTechOpen, London, UK.

173. D.Y. Kim, S. Kim, M. Kang, Synthesis of Bi_2WO_6 nanometer sheet shaped and approach to the photocatalysis, Bull. Korean Chem. Soc. 30 (2009) 630.

174. S.H. Yu, B. Liu, M.S. Mo, J.H. Huang, X.M. Liu, Y.T. Qian, General synthesis of single-crystal tungstate nanorods/nanowires: a facile, low-temperature solution approach, Adv. Funct. Mater. 13 (2003) 639.

175. Y. Chen, Y. Zhang, C. Liu, A. Lu, W. Zhang, Photodegradation of malachite green by nanostructured Bi_2WO_6 visible light-induced photocatalyst, Int. J. Photoenergy (2012) 510158.

176. A.C. Ferrari, J. Robertson, Interpretation of Raman spectra of disordered and amorphous carbon, Phys. Rev. B. 61 (2000) 14095.

177. S.M. Bose, S. Gayen, S.N. Behera, Theory of the tangential G-band feature in the Raman spectra of metallic carbon nanotubes, Phys. Rev. B. 72 (2005) 153402.

178. L. Song, J. Shi, J. Lu, C. Lu, Structure observation of graphene quantum dots by single-layered formation in layered confinement space, Chem. Sci. 6 (2015) 4846.

179. A.R. Monteiro, M. Graça, P.M.S. Neves, T. Trindade, Functionalization of graphene oxide with porphyrins: synthetic routes and biological applications, Chem. Plus. Chem. 85 (2020) 1857.

180. M.S. Dresselhaus, G. Dresselhaus, R. Saito, A. Jorio, Raman spectroscopy of carbon nanotubes , Phys. Reports 409 (2005) 47.

181. I. Childres, L.A. Jauregui, W. Park, H. Cao, Y.P. Chen, Raman spectroscopy of graphene and related materials, In: J.I Jang (Eds) New developments in photon and materials research (2013) 382, Nova Publishers, Binghamton, New York.

182. O. Bajjou, M. Khenfouch, M. Baïtoul, B. Mothudi, M. Dhlamini, E. Faulques, M. Maaza, Vibrational and optical properties of Meso-tetrakis(4-phenylsulfonica-acid) porphyrin decorated with graphene oxide., Mater. Sci. Eng. 186 (2017) 012003.

183. D.K. Singh, P.K. Iyer, P.K. Giri, Diameter dependence of interwall separation and strain in multiwalled carbon nanotubes probed by X-ray diffraction and Raman scattering studies, Diam. Relat. Mater. 19 (2010) 1281.

184. J.-B. Wu, M.-L. Lin, X. Cong, H.-N. Liu, P.-H. Tan, Raman spectroscopy of graphene-based materialsand its applications in related devices, Chem. Soc. Rev. 47 (2018) 1822.

185. A.J. Rondinone, M. Pawel, D. Travaglini, S. Mahurin, S. Dai, Metastable tetragonal phase CdWO4 nanoparticles synthesized with a solvothermal method, J. Colloid Interface Sci. 306 (2007) 281.

186. E.I. Ross-Medgaarden, I.E. Wachs, Structural determination of bulk and surface tungsten oxides with UV-vis diffuse reflectance spectroscopy and raman spectroscopy, J. Phys. Chem. C. 111 (2007) 15089.

187. F.D. Hardcastle, I.E. Wachs, Determination of the molecular structures of tungstates by Raman spectroscopy, J. Raman Spectrosc. 26 (1995) 397.

188. A. Ragunathan, R. Krishnan, B. Ameen Kamaludeen, Stability of tungsten oxide nanoparticles in different media, J. Chem. Res. 39 (2015) 622.

189. F. Farivar, P.L. Yap, K. Hassan, T.T. Tung, D.N.H. Tran, A.J. Pollard, D. Losic, Unlocking thermogravimetric analysis (TGA) in the fight against “Fake graphene” materials, Carbon 179 (2021) 505.

190. K. Gulati, M.S. Aw, D. Losic, Nanoengineered drug-releasing Ti wires as an alternative for local delivery of chemotherapeutics in the brain, Int. J. Nanomed. 7 (2012) 2069.

191. K. Šafářová, A. Dvořák, R. Kubínek, M. Vůjtek, A. Rek, Usage of AFM, SEM and TEM for the research of carbon nanotubes, In: A.M. Villas, J. Diaz (eds), Modern Research and Educational Topics in Microscopy 2 (2007) 513 Formatex, Badajoz, Spain.

192. S. Umrao, P. Sharma, A. Bansal, R. Sinha, R.K. Singh, A. Srivastava, Multi-layered graphene quantum dots derived photodegradation mechanism of methylene blue, RSC. Adv. 5 (2015) 51790.

193. A. Kaliyaraj Selva Kumar, Y. Zhang, D. Li, R.G. Compton, A mini-review: How reliable is

the drop casting technique?, Electrochem. Commun. 121 (2020) 106867.

194. F.R. Simões, M.G. Xavier, Electrochemical sensors, in: A.L. Da Róz, M.L.G. Ferreira, F. de Lima Leite, O.N. de Oliveira (Eds.), Nanoscience and its applications (2016) 155, William Andrew, Oxford, United Kingdom.

195. N. Elgrishi, K.J. Rountree, B.D. McCarthy, E.S. Rountree, T.T. Eisenhart, J.L. Dempsey, A Practical beginner's guide to cyclic voltammetry, J. Chem. Educ. 95 (2018) 197.

196. C. Sandford, M.A. Edwards, K.J. Klunder, D.P. Hickey, M. Li, K. Barman, M.S. Sigman, H.S. White, S.D. Minteer, A synthetic chemist's guide to electroanalytical tools for studying reaction mechanisms, Chem. Sci. 10 (2019) 6404.

197. A.A. Bojang, H.S. Wu, Characterization of electrode performance in enzymatic biofuel cells using cyclic voltammetry and electrochemical impedance spectroscopy, Catalysts 10 (2020) 782.

198. P.T. Kissinger, W.R. Heineman, Cyclic voltammetry, J. Chem. Educ. 60 (1983) 702.

199. J.J. Gooding, V.G. Praig, E.A.H.H. Hall, Platinum-catalyzed enzyme electrodes immobilized on gold using self-assembled layers, Anal. Chem. 70 (1998) 2396.

200. A.H. Suroviec, Determining surface coverage of self-assembled monolayers on gold electrodes, Chem. Educ. 17 (2012) 83.

201. A.J. Bard, G. Denuault, C. Lee, D. Mandler, D. 0 Wipf, Scanning electrochemical microscopy: a new technique for the characterization and modification of surfaces, Acc. Chem. Res. 23 (1990) 357.

202. A.J. Bard, F.R.F. Fan, D.T. Pierce, P.R. Unwin, D.O. Wipf, F. Zhou, Chemical imaging of

surfaces with the scanning electrochemical microscope, Science 254 (1991) 68.

203. M. V. Mirkin, W. Nogala, J. Velmurugan, Y. Wang, Scanning electrochemical microscopy in the 21st century. Update 1: five years after, Phys. Chem. Chem. Phys. 13 (2011) 21196.

204. C. Zoski, Review-Advances in Scanning electrochemical microscopy (SECM), J. Electrochem. Soc. 163 (2016) H2088.

205. C.G. Zoski, B. Liu, A.J. Bard, Scanning electrochemical microscopy: theory and characterization of electrodes of finite conical geometry, Anal. Chem. 76 (2004) 3646.

206. D. Polcari, P. Dauphin-Ducharme, J. Mauzeroll, Scanning electrochemical microscopy: a comprehensive review of experimental parameters from 1989 to 2015, Chem. Rev. 116 (2016) 13234.

207. Engineering ToolBox, (2008). *Electrical Conductivity - Elements and other Materials*. [online] Available at: https://www.engineeringtoolbox.com/conductors-d_1381.html Accessed [August. 2022].

208. H.S. Magar, R.Y.A. Hassan, A. Mulchandani, Electrochemical impedance spectroscopy (eis): principles, construction, and biosensing applications, Sensors 21 (2021) 6578.

209. B.Y. Chang, S.M. Park, Electrochemical impedance spectroscopy, Annu. Rev. Anal. Chem. 3 (2010) 207.

210. B.A. Mei, O. Munteshari, J. Lau, B. Dunn, L. Pilon, Physical interpretations of nyquist plots for edlc electrodes and devices, J. Phys. Chem. C 122 (2018) 194.

211. J. Zhang, Z. Chen, H. Wu, F. Wu, C. He, B. Wang, Y. Wu, Z. Ren, An electrochemical

bifunctional sensor for the detection of nitrite and hydrogen peroxide based on layer-by-layer multilayer films of cationic phthalocyanine cobalt(ii) and carbon nanotubes, J. Mater. Chem. B 4 (2016) 1310.

212. C. Wang, R. Yuan, Y. Chai, S. Chen, Y. Zhang, F. Hu, M. Zhang, Non-covalent iron(III)-porphyrin functionalized multi-walled carbon nanotubes for the simultaneous determination of ascorbic acid, dopamine, uric acid and nitrite, Electrochim. Acta 62 (2012) 109.

213. B. Sanna Jilani, P. Malathesh, C. Mruthyunjayachari, K.R. Venugopala Reddy, Cobalt (II) tetra methyl-quinoline oxy bridged phthalocyanine carbon nano particles modified glassy carbon electrode for sensing nitrite: A voltammetric study, Mater. Chem. Phys. 239 (2020) 121920.

214. R. Nkhahle, T. Nyokong, Assessing the electrocatalytic activity of a localized push-pull system in cobalt phthalocyanine/graphene quantum dot hybrids, Mater. Chem. Phys. 280 (2022) 125842.

215. S. Lu, M. Hummel, S. Kang, Z. Gu, Selective voltammetric determination of nitrite using cobalt phthalocyanine modified on multiwalled carbon nanotubes, J. Electrochem. Soc. 167 (2020) 046515

216. Z.H. Wen, T.F. Kang, Determination of nitrite using sensors based on nickel phthalocyanine polymer modified electrodes, Talanta 62 (2004) 351.

217. V. Mani, A.P. Periasamy, S.M. Chen, Highly selective amperometric nitrite sensor based on chemically reduced graphene oxide modified electrode, Electrochem. Commun. 17 (2012) 75.

218. X. Song, L. Gao, Y. Li, L. Mao, J.H. Yang, A sensitive and selective electrochemical nitrite sensor based on a glassy carbon electrode modified with cobalt phthalocyanine-supported Pd nanoparticles, Anal. Methods 9 (2017) 3166.

219. S. Lu, H. Jia, M. Hummel, Y. Wu, K. Wang, X. Qi, Z. Gu, Two-dimensional conductive phthalocyanine-based metal-organic frameworks for electrochemical nitrite sensing, RSC Adv. 11 (2021) 4472.

220. Y. Wang, E. Laborda, R.G. Compton, Electrochemical oxidation of nitrite: Kinetic, mechanistic and analytical study by square wave voltammetry, J. Electroanal. Chem. 670 (2012) 56.

221. R. Guidelli, F. Pergola, G. Raspi, voltammetric behavior of nitrite ion on platinumin neutral and weakly acidic media, Electroanal Chem, J. 44 (1972) 745.

222. B. Piela, P.K. Wrona, Oxidation of nitrites on solid electrodes, J. Electrochem. Soc. 149 (2002) E55.

223. T. Nyokong, Electrodes modified with monomeric M– N_4 catalysts for the detection of of environmentally important molecules In: N_4-Macrocyclic Metal Complexes, J.H. Zagal, F. Bedioui, J-P, Dodelet (Eds) (2006) 331, Springer, New York.

224. N. Chebotareva, T. Nyokong, interactions of cobalt(ii) tetrasulfophthalocyanine with nitrite in the presence of nitrate and perchlorate ions, J. Coord. Chem. 46 (1999) 433.

225. L. Cui, T. Pu, Y. Liu, X. He, Layer-by-layer construction of graphene/cobalt phthalocyanine composite film on activated GCE for application as a nitrite sensor, Electrochim. Acta 88 (2013) 559.

226. B. Agboola, T. Nyokong, Comparative electrooxidation of nitrite by electrodeposited Co

(II), Fe (II) and Mn (III) tetrakis (benzylmercapto) and tetrakis (dodecylmercapto) phthalocyanines on gold electrodes, Anal. Chim. Acta 587 (2007) 116.

227. F. Matemadombo, N. Sehlotho, T. Nyokong, Effects of the number of ring substituents of cobalt carboxyphthalocyanines on the electrocatalytic detection of nitrite, cysteine and melatonin, J. Porphyr. Phthalocyanines. 13 (2009) 986.

228. B.O. Agboola, K.I. Ozoemena, T. Nyokong, Electrochemical properties of benzylmercapto and dodecylmercapto tetra substituted nickel phthalocyanine complexes: Electrocatalytic oxidation of nitrite, Electrochim. Acta 51 (2006) 6470.

229. T. Kim, W. Choi, H.-C. Shin, J.-Y. Choi, J.M. Kim, M.-S. Park, W.-S. Yoon, Applications of Voltammetry in Lithium Ion Battery Research, J. Electrochem. Sci. Technol. 11 (2020) 14.

230. L. Gaolatlhe, R. Barik, S.C. Ray, K.I. Ozoemena, Voltammetric responses of porous Co3O4 spinels supported on MOF-derived carbons: Effects of porous volume on dopamine diffusion processes, J. Electroanal. Chem. 872 (2020) 113863.

231. T. Shinagawa, A.T. Garcia-Esparza, K. Takanabe, Insight on Tafel slopes from a microkinetic analysis of aqueous electrocatalysis for energy conversion, Sci. Rep. 5 (2015) 1.

232. A. Salimi, K. Abdi, Enhancement of the analytical properties and catalytic activity of a nickel hexacyanoferrate modified carbon ceramic electrode prepared by two-step sol-gel technique: Application to amperometric detection of hydrazine and hydroxyl amine, Talanta 63 (2004) 475.

233. C.A. Caro, F. Bedioui, J.H. Zagal, Electrocatalytic oxidation of nitrite on a vitreous carbon

electrode modified with cobalt phthalocyanine, Electrochim. Acta 47 (2002) 1489.

234. N. Sato, Electrochemistry at metal and semiconductor electrodes, 1998, Elsevier, Sapporo, Japan.

235. H. Li, K. Lee, J. Zhang, Electrocatalytic H_2 oxidation reaction, In: J. Zhang (Eds) PEM fuel cell electrocatalysts and catalyst layers: fundamentals and applications (2008) 135, Springer, London.

236. Y.H. Fang, Z.P. Liu, Tafel kinetics of electrocatalytic reactions: From experiment to first-principles, ACS Catal. 4 (2014) 4364.

237. N. Uwitonze, D. Zhou, J. Lei, W. Chen, X.Q. Zuo, J. Cai, Y.X. Chen, The high Tafel slope and small potential dependence of activation energy for formic acid oxidation on a Pd electrode, Electrochim. Acta 283 (2018) 1213.

238. S. Lu, H. Jia, M. Hummel, Y. Wu, K. Wang, X. Qi, Z. Gu, Two-dimensional conductive phthalocyanine-based metal–organic frameworks for electrochemical nitrite sensing, RSC Adv. 11 (2021) 4472.

239. M. Abdul Aziz, A.N. Kawde, Gold nanoparticle-modified graphite pencil electrode for the high-sensitivity detection of hydrazine, Talanta 115 (2013) 214.

240. X. Gu, X. Li, S. Wu, J. Shi, G.G. Jiang, G.G. Jiang, S. Tian, A sensitive hydrazine hydrate sensor based on a mercaptomethyl-terminated trinuclear Ni(ii) complex modified gold electrode, RSC Adv. 6 (2016) 8070.

241. D. Kaniansky, I. Zelenský, A. Hybenová, Anna, F.I. Onuska, Determination of chloride, nitrate, sulfate, nitrite, fluoride, and phosphate by on-line coupled capillary isotachophoresis-capillary zone electrophoresis with conductivity detection, Anal.

Chem. 66 (1994) 4258.

242. W. D'Alessandro, S. Bellomo, F. Parello, P. Bonfanti, L. Brusca, M. Longo, R. Maugeri, Nitrate, sulphate and chloride contents in public drinking water supplies in Sicily, Italy Environ. Monit. Assess. 84 (2012) 2845.

243. R.A.S. Lapa, J.L.F.C. Lima, I.V.O.S. Pinto, Simultaneous determination of fluoride, chloride, nitrite, bromide, nitrate, phosphate and sulfate in aqueous solutions at 10−9 to 10−8% level by ion chromatography, J. Chromatogr. B 800 (2004) 321.

244. D. Nematollahi, H. Goodarzi, E. Tammari, Mechanism of electrochemical oxidation of catechol and 3-substituted catechols in the presence of barbituric acid derivatives. Synthesis of new dispiropyrimidine derivatives, J. Chem. Soc. Perkin Trans. 2 (2002) 829.

245. R. Madhu, S. Palanisamy, S.M. Chen, S. Piraman, A low temperature synthesis of activated carbon from the bio waste for simultaneous electrochemical determination of hydroquinone and catechol, J. Electroanal. Chem. 727 (2014) 84.

246. N. Hashemzadeh, M. Hasanzadeh, N. Shadjou, J. Eivazi-Ziaei, M. Khoubnasabjafari, A. Jouyban, Graphene quantum dot modified glassy carbon electrode for the determination of doxorubicin hydrochloride in human plasma, J. Pharm. Anal. 6 (2016) 235.

247. S. Corona-Avendaño, M.T. Ramírez-Silva, M. Romero-Romo, A. Rojas-Hernández, M. Palomar-Pardavé, Influence of the $HClO_4$ concentration on the β-CD electropolimerization over a carbon paste electrode and on dopamine's electrochemical response, Electrochim. Acta 89 (2013) 854.

248. J.M. Zen, A. Senthil Kumar, M.R. Chang, Electrocatalytic oxidation and trace detection of amitrole using a Nafion/lead–ruthenium oxide pyrochlore chemically modified electrode, Electrochim. Acta 45 (2000) 1691.

249. S.M. Sudhakara, M.C. Devendrachari, H. Makri, N. Kotresh, F. Khan, Silver nanoparticles decorated phthalocyanine doped polyaniline for the simultaneous electrochemical detection of hydroquinone, catechol, J. Electroanal. Chem. (2021) 115071.

250. Y. Zhang, X. Qiang, Z. Xia, G. Gui, F. Deng, Q. Xie, Z. Xia, G. Gui, F. Deng, X. Qiang, Z. Xia, G. Gui, F. Deng, Q. Xie, Z. Xia, G. Gui, F. Deng, Fulvic acid reduced go and phthalocyanine nanorods as reaction platform for simultaneous determination of catechol, hydroquinone, phenol and p -nitrophenol , J. Electrochem. Soc. 166 (2019) B1293.

251. M. Ozsoz, A. Erdem, E. Kilinc, L. Gokgunnec, Mushroom-based cobalt phthalocyanine dispersed amperometric biosensor for the determination of phenolic compounds, Electroanalysis 8 (1996) 147.

252. C. Apetrei, P. Alessio, C.J.L. Constantino, J.A. de Saja, M.L. Rodriguez-Mendez, F.J. Pavinatto, G.R. Fernandes, V. Zucolotto, O.N. Oliveira, Biomimetic biosensor based on lipidic layers containing tyrosinase and lutetium bisphthalocyanine for the detection of antioxidants, Biosens. Bioelectron. 26 (2011) 2513.

253. R. Cesana, J.M. Gonçalves, R.M. Ignácio, M. Nakamura, V.M. Zamarion, H.E. Toma, T.C. Canevari, Synthesis and characterization of nanocomposite based on reduced graphene oxide-gold nanoparticles-carbon dots: electroanalytical determination of dihydroxybenzene isomers simultaneously, J. Nanoparticle Res. 22 (2020) 336.

254. M.U. Hossain, M.T. Rahman, M.Q. Ehsan, Simultaneous detection and estimation of catechol, hydroquinone, and resorcinol in binary and ternary mixtures using electrochemical techniques, Int. J. Anal. Chem. (2015) 862979.

255. M.A. Kamyabi, M.A. Shafiee, Electrocatalytic oxidation of dopamine, ascorbic acid and uric acid at poly2,6diaminopyridine on the surface of carbon nanotubes/gc electrodes, J. Braz. Chem. Soc. 23 (2012) 593.

256. M.D. Hawley, S. V. Tatawawadi, S. Piekarski, R.N. Adams, Electrochemical studies of the oxidation pathways of catecholamines, J. Am. Chem. Soc. 89 (1967) 447.